

# Fast Longitudinal Diagnostics for the HERA Proton Ring

**Dissertation**  
**zur Erlangung des Doktorgrades**  
**des Fachbereichs Physik**  
**der Universität Hamburg**

vorgelegt von  
Elmar Vogel  
aus Waiblingen

Hamburg  
2002

DESY report:  
DESY-THESIS-2002-010  
March 2002

Gutachter der Dissertation: Prof. Dr. P. Schmüser  
Dr. A. Gamp

Gutachter der Disputation: Prof. Dr. P. Schmüser  
Dr. F. Willeke

Datum der Disputation: 28. Februar 2002

Dekan des Fachbereichs  
Physik und Vorsitzender  
des Promotionsausschusses: Prof. Dr. F.-W. Büßer

# Abstract

After the luminosity upgrade of the electron proton collider HERA, the proton bunch length will become relevant for the achievable luminosity. New, strong focussing, superconducting magnets inside the detectors H1 and ZEUS lead to smaller cross sections at the interaction regions and with that, to higher luminosity. Due to the strong focussing, the beta function and the bunch length have a comparable magnitude. This enhances the effective cross section, ‘hour-glass-effect’ [1]. A reduction of the bunch length would result in smaller effective cross sections and so further increase the luminosity.

Even at HERA energies of 920 GeV, protons do not lose a significant amount of energy, due to synchrotron radiation, because of their large rest mass. Hence, there is no natural damping of unwanted beam oscillations, as is the case for electrons or positrons. Coherent oscillations of the proton beam lead to an increase of the beam dimensions. Shorter bunch lengths at high energy are achievable by suppressing the coherent oscillations at injection and during acceleration.

For an investigation of the origin of coherent oscillations, powerful longitudinal diagnostic tools are indispensable. Therefore, a fast longitudinal diagnostic system was developed, which permits real time measurements of bunch phase and length for all 180 bunches during one turn. Beam loading transients and the accelerating voltages can be examined with a fast cavity field diagnostic. The vacuum system of the HERA proton ring was carefully designed to keep the impedance, which could drive beam oscillations, as low as possible. Therefore, measures are needed to suppress the oscillations. The fast longitudinal diagnostic system provides the signals, needed for a RF feedforward and a coupled-bunch feedback.

The new diagnostic system permits novel observations and experiments at HERA. One can observe coupled-bunch oscillations during acceleration, which are correlated with an increase in the longitudinal emittance. The impact of bunch oscillations on the beam loading transients can be demonstrated. Measurements of the longitudinal beam transfer function and measurements of decoherence times, together with beam echoes, yields important beam dynamical parameters. Since a further reduction of the all over impedance is not easily achievable, the suppression of coupled-bunch oscillations must be done by active systems. The results obtained in this thesis, provide the necessary information for the design of a coupled-bunch feedback system, whose task is the preservation of the longitudinal emittance.





# Zusammenfassung

Nach der Erhöhung der Luminosität der Hadron, Elektron Ring Anlage HERA spielt die Länge der Teilchenpakete (Bunche) der Protonen eine Rolle bei der erreichbaren Luminosität. Neue, stark fokussierende supraleitende Magnete in den Detektoren H1 und ZEUS führen zu kleineren Strahlquerschnitten in den Wechselwirkungsbereichen und damit zu mehr Luminosität. Wegen der starken Fokussierung haben die Betafunktion und die Bunchlänge vergleichbare Werte. Das erhöht wiederum die effektive Strahlquerschnittfläche, ‘Sanduhreffekt’ [1]. Eine Reduktion der Bunchlänge würde kleinere effektive Strahlquerschnittflächen ergeben und so die Luminosität weiter erhöhen.

Selbst bei HERA Energien von 920 GeV verlieren Protonen, aufgrund ihrer hohen Ruheenergie, nur unbedeutend Energie durch Abstrahlung von Synchrotronstrahlung. Damit existiert auch keine natürliche Dämpfung von Strahlschwingungen, wie das bei Elektronen oder Positronen der Fall ist. Kohärente Schwingungen von Protonenstrahlen führen zu einer Aufweitung der Strahlen. Kürzere Bunche bei hoher Energie sind durch das Unterdrücken der kohärenten Schwingungen, bei der Injektion und während der Beschleunigung, zu erreichen.

Zur Ermittlung einer Ursache für die kohärenten Schwingungen sind leistungsfähige Diagnosewerkzeuge unerlässlich. Deshalb wurde ein schnelles longitudinales Diagnosesystem entwickelt, das Messungen der Phasen und Längen aller 180 Bunche in Echtzeit und innerhalb eines Umlaufs gestattet. Transientes ‘Beam-Loading’ und die Beschleunigungsfelder können mit der Diagnose der Hochfrequenzfelder in den Hohlraumresonatoren (Cavities) untersucht werden. Das HERA Vakuumsystem wurde sorgfältig entworfen, um alle Impedanzen, welche zu Strahlschwingungen führen, so klein wie möglich zu halten. Deshalb sind Maßnahmen notwendig, um Schwingungen zu unterdrücken. Das schnelle Diagnosesystem stellt die Eingangssignale bereit, die für ein HF Feedforward und ein Multibunch-Feedback notwendig sind.

Das neue Diagnosesystem ermöglicht neuartige Beobachtungen und Experimente bei HERA. Man kann gekoppelte Schwingungen aller Bunche während der Beschleunigung von der Injektionsenergie zur Speicherenergie beobachten, die mit einer Zunahme der longitudinalen Emittanz einhergehen. Der Einfluß der Bunchschwingungen auf die transienten Beam-Loading Felder ist nachweisbar. Messungen der longitudinalen Strahl Transferfunktion und Messungen der Dekohärenzzeiten, zusammen mit Strahlechos, liefern wichtige strahldynamische Parameter. Weil eine weitere Reduktion der Gesamtimpedanz nicht einfach realisierbar ist, muß die Unterdrückung von gekoppelten Schwingungen durch aktive Systeme erfolgen. Die Resultate dieser Dissertation stellen die Informationen zur Verfügung, die für den Entwurf eines Multibunch Feedback Systems notwendig sind. Die Aufgabe eines solchen Systems ist die Erhaltung der longitudinalen Emittanz.



# Contents

<b>Abstract</b>	<b>iii</b>
<b>Zusammenfassung</b>	<b>v</b>
<b>1 Introduction</b>	<b>1</b>
1.1 HERA - a collider for two different kinds of particles . . . . .	1
1.2 The luminosity upgrade . . . . .	3
1.3 Longitudinal proton emittance dilution . . . . .	5
1.4 Fast longitudinal diagnostics . . . . .	7
1.5 Examinations on the longitudinal stability . . . . .	9
<b>I Existing RF Installation</b>	<b>11</b>
<b>2 Existing Longitudinal Beam Diagnostics</b>	<b>13</b>
2.1 Resistive gap monitor . . . . .	13
2.2 Narrow band phase measurements . . . . .	14
2.3 Longitudinal bunch shape measurements . . . . .	15
<b>3 Radio Frequency System</b>	<b>17</b>
3.1 Frequency control . . . . .	17
3.2 Control systems for the cavities . . . . .	20
3.3 Narrow band beam phase feedback systems . . . . .	22
<b>II Fast Longitudinal Diagnostics</b>	<b>25</b>
<b>4 Real Time Measurements of Single Bunch Phase and Length</b>	<b>27</b>
4.1 Bunch phase . . . . .	27
4.2 Bunch length . . . . .	31
<b>5 Measurement of Multi-Bunch Oscillations</b>	<b>37</b>
5.1 Timing . . . . .	37
5.2 Data acquisition . . . . .	37
5.3 First experimental results . . . . .	38
5.4 Emittance blow up . . . . .	40
5.5 Synchrotron frequency during acceleration . . . . .	43
<b>6 Fast Cavity Field Diagnostic</b>	<b>47</b>
6.1 Generator field and transient . . . . .	47
6.2 Measurement principle . . . . .	48
6.3 Timing and data acquisition . . . . .	53
6.4 Transient modulations with the synchrotron frequency . . . . .	53
6.5 Phase drift between the references of the double harmonic RF system . . . . .	54

<b>III</b>	<b>Examination of the Longitudinal Stability</b>	<b>57</b>
<b>7</b>	<b>Modal Analysis of Coupled bunch Oscillations</b>	<b>59</b>
7.1	On coupled bunch oscillations . . . . .	59
7.2	Analysis of steady state modes . . . . .	62
7.3	Modal spectrum of a multi-bunch oscillation . . . . .	63
7.4	Coupled bunch modes and emittance dilution . . . . .	65
7.5	A coupled bunch instability . . . . .	68
7.6	Estimations of the instability growth rates . . . . .	69
7.7	Analysis of the transient behavior of modes . . . . .	70
7.8	Transient modal spectrum of multi-bunch oscillations . . . . .	72
7.9	Results . . . . .	74
<b>8</b>	<b>Consideration of the Beam Response</b>	<b>75</b>
8.1	Frequency spread within a bunch . . . . .	75
8.2	Impulse response . . . . .	78
8.3	Response to harmonic excitation . . . . .	79
8.4	Beam echoes . . . . .	82
8.5	Expectations on response measurements . . . . .	85
<b>9</b>	<b>Beam Transfer Function</b>	<b>87</b>
9.1	Measurement setup . . . . .	87
9.2	Performed measurements . . . . .	89
9.3	Phase error in the measurements . . . . .	94
9.4	Results . . . . .	94
<b>10</b>	<b>Decoherence and Beam Echoes</b>	<b>97</b>
10.1	RF kick production . . . . .	97
10.1.1	52 MHz RF cavity control system . . . . .	98
10.1.2	208 MHz RF cavity control system . . . . .	99
10.2	Timing . . . . .	101
10.3	Errors of measured signals . . . . .	101
10.4	Observed beam echoes . . . . .	101
10.5	Decoherence . . . . .	105
10.6	Echo strength depending on kick delay . . . . .	107
10.7	Echo strength depending on RF noise . . . . .	109
10.8	Results . . . . .	109
<b>IV</b>	<b>Putting it All Together</b>	<b>111</b>
<b>11</b>	<b>Causes of Beam Instability</b>	<b>113</b>
11.1	The concept of effective impedances . . . . .	113
11.2	Which is the driving impedance? . . . . .	115
11.2.1	Space charge impedance . . . . .	115
11.2.2	Resistive wall impedance . . . . .	116
11.2.3	Cavity impedances at fundamental frequencies . . . . .	117
11.2.4	Broad band impedances . . . . .	118
11.2.5	Other impedances . . . . .	120
11.3	Is there sufficient Landau damping? . . . . .	120

---

<b>12 Active Measures against Emittance Dilution</b>	<b>123</b>
12.1 Increase of coherent synchrotron frequency spread . . . . .	123
12.2 Landau damping cavity . . . . .	124
12.3 Reduction of cavity impedance by RF feedforward . . . . .	124
12.4 Coupled bunch feedback . . . . .	125
<b>Conclusion and Outlook</b>	<b>127</b>
<b>Appendix</b>	<b>129</b>
A.1 Notation . . . . .	129
A.1.1 Radio frequency waves, phasors and vectors . . . . .	129
A.1.2 Other notation and expressions . . . . .	131
A.2 Derivation of the luminosity reduction factor . . . . .	132
A.3 Microwave instability . . . . .	134
A.4 Details on the phase locked loop for injections . . . . .	134
A.5 Details on the ep-synchronization . . . . .	136
A.6 Stability investigations on the narrow band beam phase feedback systems . . .	139
A.6.1 The beam transfer function used for investigations . . . . .	139
A.6.2 Phase loop I . . . . .	139
A.6.3 Phase loop II . . . . .	142
A.7 Picture gallery . . . . .	147
<b>Bibliography</b>	<b>156</b>
<b>Acknowledgments</b>	<b>163</b>



# 1 Introduction

In 1955, the form factor of the proton was determined by R. Hofstadter and his colleagues from Stanford University by shooting electrons from a linear accelerator on protons and measuring the electron deflection [2, 3]. These experiments showed that the proton has a finite size. Since that time many experiments were undertaken to determine the inner structure of the proton. In the late 1960's, the deep inelastic electron proton scattering at SLAC revealed that the nucleon consists of nearly point like objects, called partons. The experiments H1 and ZEUS - installed in the Hadron Elektron Ring Anlage (HERA) at DESY - started to operate in 1992 and permit the deepest insight into the proton structure by measuring the collision fragments of a 27.5 GeV electron beam colliding with a 920 GeV proton beam<sup>1</sup>. For a comprehensive overview of the physics at HERA, see [4, 5]. A more in-depth description can be found in [6, 7, 8].

For a study of the large  $Q^2$  regime and a search of rare events by the experiments H1 and ZEUS, the luminosity has to be increased. Therefore, new, focussing quadrupole magnets are mounted inside the detectors H1 and ZEUS for a further reduction of the beam cross-sections at the interaction points. This is called the 'luminosity upgrade'. But the focussing takes place within only two meters. Hence, the proton bunch length of about 50 cm becomes relevant for the 'effective' beam cross-sections. For long bunches they are larger than the cross-sections at the interaction point. In contrast, the electron bunch length of about 2.5 cm plays no role.

During acceleration, the proton bunches suffer from a longitudinal emittance growth. If one is able to suppress this dilution, one will get shorter bunches at high energy and with that about 20% more luminosity. The desire for shorter bunches defines an ambitious research program. It consists of the setup of sufficient diagnostic tools which are also able to serve as monitors for future feedback loops. The properties of the proton beam have to be examined to find instabilities and technical deficiencies. Active measures have to be implemented to counteract the emittance growth, for instance a Landau damping cavity, a RF feedforward or a coupled bunch feedback.

This thesis addresses many of these subjects, except for the implementation of active measures. The main task was first to design, build and commission the diagnostic tools. Secondly, studies have been carried out on coupled bunch oscillations, beam transfer functions, decoherence times, Landau damping and beam echoes.

## 1.1 HERA - a collider for two different kinds of particles

HERA is the only high energy accelerator in the world, which collides protons with either electrons or positrons. The two different kinds of particles require two completely separate high energy storage rings. They are both mounted in a common 6.3 km long ring tunnel, 12 m below ground. Both beams collide at two interaction points inside the H1 and ZEUS detectors.

The HERA electron ring accelerates electrons or positrons, injected from the pre-accelerator PETRA, from 12 GeV to 27.5 GeV. It consists of 456 normal conducting bending magnets. Their field of 0.19 Tesla is sufficient to keep the electrons on the circular trajectory, because of the relatively small momentum of the electrons. Due to the small rest mass, electrons lose

---

<sup>1</sup>This asymmetric design results in a center of mass energy of 320 GeV.

50 MeV per revolution, because of synchrotron radiation in the bending magnets. To compensate these losses, 82 normal conducting and 16 superconducting 500 MHz radio frequency (RF) cavities re-accelerate the electron beam. This leads to a damping of unwanted beam oscillations. Parasitic modes in the RF cavities are responsible for coupled bunch instabilities which would limit the beam current to about 3 mA. These instabilities are suppressed by transverse and longitudinal coupled bunch feedback systems [9], which allow more than 50 mA of beam current to be stored.

A special feature of the HERA electron beam is its longitudinal polarization of about 60%. To generate and preserve the polarization, the spin must be vertically oriented in the arcs of the storage ring. The spin is ‘rotated’ in a special magnet arrangement into the longitudinal direction at the interaction regions.

The second storage ring accelerates 40 GeV protons, also injected from PETRA, to 920 GeV. This is a energy gain of 23, which is more than at comparable rings<sup>2</sup>. To force the 920 GeV proton beam on the 6.3 km long circle, the bending magnets have to provide a magnetic field of more than 5 Tesla. Such high fields can only be reached with superconducting magnets. In the HERA proton ring 224 superconducting bending magnets are installed and cooled with liquid helium at 4.4 K. The 422 quadrupole magnets for focussing and a large number of correction magnets are also superconducting.

The superconducting dipoles and quadrupoles are connected in series and operated with one power supply, providing a maximum current of 8000 A at a voltage of 500 V. The voltage limits the maximum possible field change in the magnets, needed for the acceleration from 40 GeV to 920 GeV. The acceleration ‘ramp’ requires about 20 minutes. All normal- and superconducting correction magnets and the RF cavities are synchronized to the dipole field, which is measured in real-time in two reference magnets. These reference magnets are installed outside the ring, but are connected in series with the main magnets.

At energies up to 920 GeV, protons do not lose a significant amount of energy by synchrotron radiation, because of their large rest mass. Therefore, only moderate RF power is needed to accelerate and store the proton beam. In HERA, a double harmonic RF system, consisting of two 52 MHz and four 208 MHz cavities, is installed. At the injection energy of 40 GeV, the longitudinal focussing is provided by the 52 MHz cavities. During ramping to 920 GeV, the 208 MHz cavities take over. The reasons for this double RF are the accommodation of the long proton bunches, injected from PETRA [10, 11], and the longitudinal compression of the bunches by the steeper potential of the 208 MHz system at high energy.

The study of rare events in high energy experiments requires sufficiently high interaction rates, given by luminosity<sup>3</sup> times the cross section. The luminosity decreases when coherent oscillations of the proton beam are excited. The reason is: there is no natural damping of unwanted beam oscillations, as for electrons or positrons, because of the missing synchrotron radiation. Coherent oscillations of the proton beam lead to an increase of the beam emittance. Hence, the luminosity decreases, because it is proportional to the effective width of the colliding beams.

A larger beam also loses protons more rapidly, via collision with the vacuum chamber. The high energy particles generated produce background radiation in the experiments.

<sup>2</sup>The TEVATRON at Fermilab accelerates from 150 GeV to 980 GeV, that is a gain of 6.5.

<sup>3</sup>The peak luminosity  $\mathcal{L}$  by the year 2000 was up to  $2 \cdot 10^{31} \text{ cm}^{-2} \text{ s}^{-1}$ .



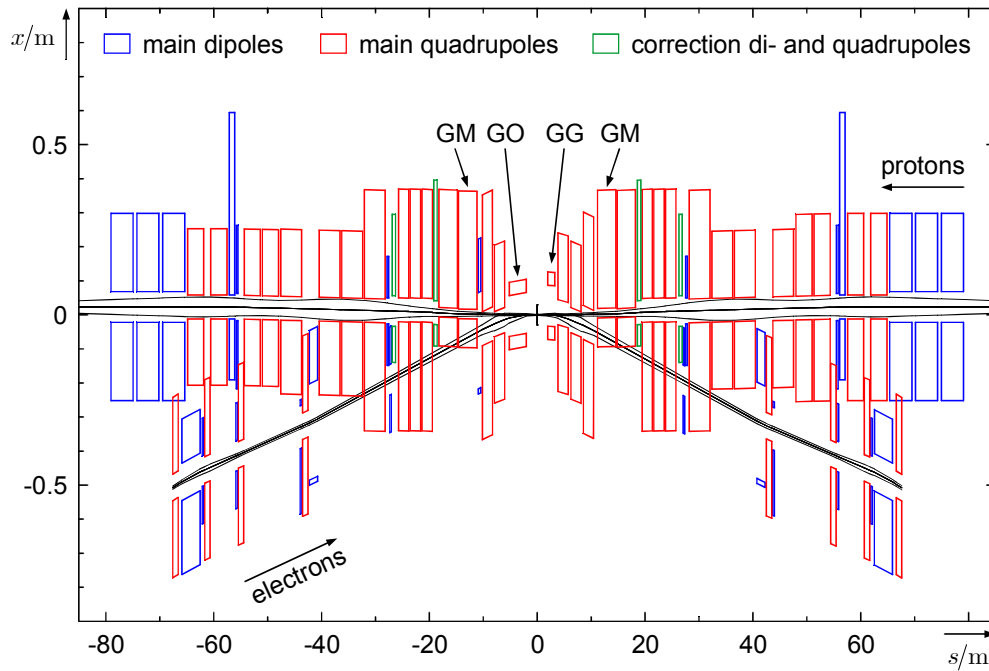


Figure 1.1: Interaction region optics after the luminosity upgrade: GO and GG are superconducting quadrupoles, mounted inside the detectors, GM are the half quadrupole magnets with mirror plates. The  $10\sigma$  envelopes of the electron and proton beam are also shown.

## 1.2 The luminosity upgrade

To increase the luminosity of HERA by a factor of about four, new optical components were installed in the interaction sections of the two collider experiments. This is called the ‘luminosity upgrade’. Before this upgrade, the nearest quadrupole magnets to focus the beams at the interaction points (IPs) were mounted 5.8 m from the IPs in the electron case and 27 m in the proton case. These magnets were located outside the detectors H1 and ZEUS. For the further increase of the focussing, these magnets have been replaced by sophisticated new ones, located partly inside the detectors. The closest electron quadrupoles are now only 2 m away from the IPs. In order to conform with the tight space constraints inside the detectors, they are realized as superconducting magnets. At 11 m from the IPs, the nearest proton quadrupoles are installed. They are half magnets, equipped with mirror plates. This mirror plate design was needed, since the electron and the proton beams are only separated by 65 mm at this distance from the IPs.

Until summer 2000, only the HERMES<sup>4</sup> experimental zone was equipped with spin rotators. As a part of the luminosity upgrade, spin rotator magnets have been also mounted in the straight sections around the collider experiments H1 and ZEUS.

The vertical  $\beta$ -function of the proton ring is  $\beta_y^* = 0.18$  m at the IPs. While the bunch length of  $\sigma_s = 0.204$  m exceeds this value, the effective cross section is larger than the cross section at the IPs. This is equivalent to a loss in luminosity. A reduction of the proton bunch length is therefore of high interest. Within the old optics this effect was negligible, because of the larger  $\beta$ -functions<sup>5</sup>.

To discuss the dependence of the luminosity on the  $\beta$ -function and the bunch length in more detail, the relevant design parameters [12] of HERA after the luminosity upgrade are given in table 1.1.

<sup>4</sup>The experiment HERMES examines the spin composition of nucleons with the polarized electron beam.

<sup>5</sup> $\beta_x^* = 7$  m and  $\beta_y^* = 0.5$  m

Parameters	e-ring	p-ring
$E$ (GeV)	27.5	920
$I$ (mA)	58	140
$\beta_x^*$ (m)	0.63	2.45
$\beta_y^*$ (m)	0.26	0.18
$\epsilon_x$ (nm)	20	5.1
$\epsilon_y / \epsilon_x$	0.17	1
$\sigma_x$ ( $\mu\text{m}$ )	112	112
$\sigma_y$ ( $\mu\text{m}$ )	30	30
$\sigma_s$ (mm)	10.3	204
$l_{FWHM}$ (ns)	0.081	1.6

Table 1.1: Design parameters of HERA after the luminosity upgrade

The luminosity per bunch crossing for very short bunches ( $\sigma_s \ll \beta^*$ ) is in good approximation

$$\mathcal{L}_{col,0} = \frac{N_p N_e}{2 \pi \sqrt{(\sigma_{px}^{*2} + \sigma_{ex}^{*2})(\sigma_{py}^{*2} + \sigma_{ey}^{*2})}}, \quad (1.1)$$

with  $N$  the total number of particles in a bunch and  $\sigma^*$  the r.m.s bunch size at the interaction point<sup>6</sup>. The vertical  $\beta$ -function  $\beta_y^*$  of the proton storage ring and the proton bunch length  $\sigma_s$  have comparable magnitude. The horizontal  $\beta$ -function  $\beta_x^*$  is about three times larger, hence, we can neglect its influence. Considering only the vertical plane, the reduction of luminosity can be calculated analytically

$$R(u_y) = \frac{\mathcal{L}_{col,0}}{\mathcal{L}_{col}} = \frac{u_y}{\sqrt{\pi}} \exp\left(-\frac{u_y^2}{2}\right) K_0\left(\frac{u_y^2}{2}\right) \quad (1.2)$$

with

$$u_y^2 = \frac{2(\sigma_{py}^{*2} + \sigma_{ey}^{*2})}{(\sigma_{ps}^2 + \sigma_{es}^2) \left( \frac{\sigma_{py}^{*2}}{\beta_{py}^{*2}} + \frac{\sigma_{ey}^{*2}}{\beta_{ey}^{*2}} \right)}. \quad (1.3)$$

The luminosity per collision is

$$\mathcal{L}_{col} = R \mathcal{L}_{col,0}. \quad (1.4)$$

For the derivation of these expressions see [1] and appendix A.2.

Figure 1.2 shows the luminosity gain, scaled from the design value as a function of the vertical proton  $\beta$ -function and the bunch length<sup>7</sup>.

The values were calculated by keeping the value of the vertical electron  $\beta$ -function constant, and matching the vertical electron beam size to the proton beam size

$$\sigma_{py}^* = \sqrt{\epsilon_p \beta_{py}^*} \stackrel{!}{=} \sigma_{ey}^* = \sqrt{\left(\frac{\epsilon_{ey}}{\epsilon_{ex}}\right) \epsilon_{ex} \beta_{ey}^*}, \quad (1.5)$$

<sup>6</sup>‘\*’ denotes a value at the interaction point

<sup>7</sup>Here we quote bunch length in the time domain. Since  $\beta = \frac{v}{c} \geq 0.9997$  at HERA, the spatial lengths are given by multiplication with  $c$ . The conversion between FWHM bunch lengths in the time domain and the spatial  $\sigma$ -bunch length is:  $\frac{\sigma_s}{\text{m}} = 0.1273 \frac{l_{FWHM}}{\text{ns}}$

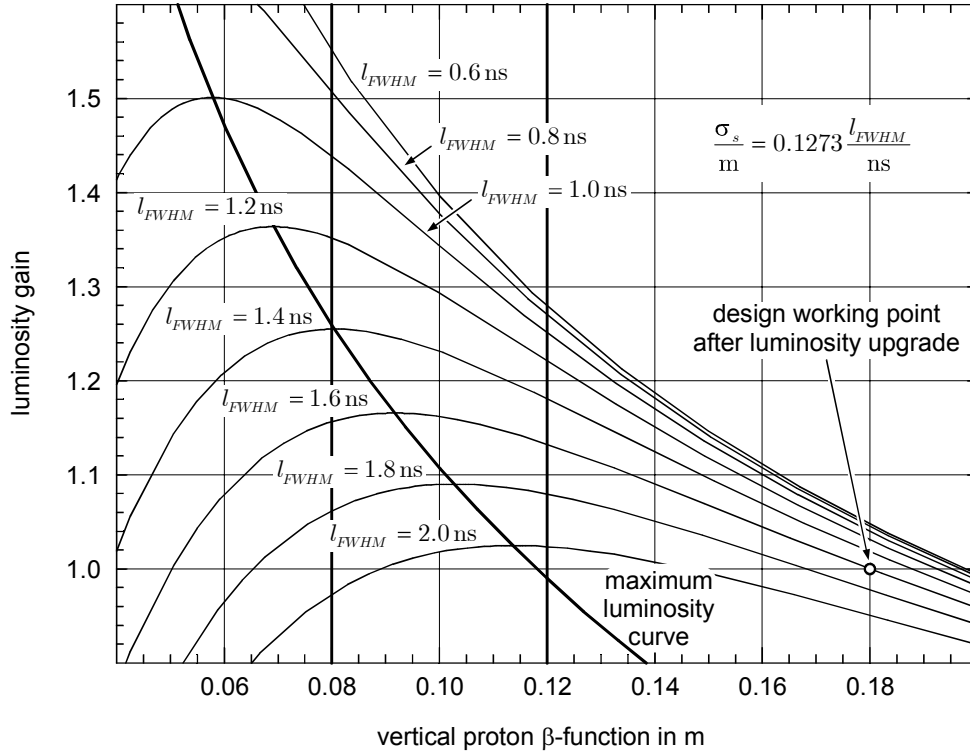


Figure 1.2: Dependence of the luminosity gain on the vertical proton  $\beta$ -function and the bunch length. ( $\mathcal{L}_{design} \approx 7 \cdot 10^{31} \frac{1}{\text{cm}^2 \text{s}}$ )

by choosing the coupling factor between the vertical and horizontal electron emittances  $\epsilon_{ey} / \epsilon_{ex}$  such that

$$\left( \frac{\epsilon_{ey}}{\epsilon_{ex}} \right) = \frac{\epsilon_p}{\epsilon_{ex} \beta_{ey}^*} \beta_{py}^* = \frac{0.98}{\text{m}} \beta_{py}^*. \quad (1.6)$$

In practice, the change of the coupling factor is controlled by the magnetic field strength of a quadrupole, rotated by  $45^\circ$ .

Starting from the design working point, in figure 1.2, the reduction of the  $\beta$ -function at a constant bunch length of  $\sigma_s = 0.204 \text{ m}$  ( $l_{FWHM} = 1.6 \text{ ns}$ ) leads to a maximum luminosity at  $\beta_{py}^* = 0.0916 \text{ m}$ . At shorter bunch length, this maximum is reached for a lower  $\beta_{py}^*$  and the luminosity gain is higher. So, a working point should be as close as possible to the ‘maximum luminosity curve’, shown in figure 1.2.

The geometrical aperture of the proton storage ring, especially in the half quadrupole magnets with mirror plates, gives an additional lower limit for  $\beta_{py}^*$ . For commissioning  $\beta_{py}^* = 0.18 \text{ m}$  was chosen to have enough safety margin. The safety margin from the last HERA operation period, using the old optics, allow  $\beta_{py}^* = 0.12 \text{ m}$ . A further reduction is a challenge, the lowest possible limit seems to be  $\beta_{py}^* = 0.08 \text{ m}$  [14].

### 1.3 Longitudinal proton emittance dilution

There are two main bunch lengthening effects: On the one hand, the bunch length can be increased during the transfer from PETRA to HERA, due to transient beam loading effects, and on the other hand by beam oscillations of any kind during acceleration.

Before this work, it was not clear which effect was more relevant. But it was possible to measure one longitudinal bunch shape every second, recorded with a 12.5 GHz digital oscilloscope. From these measurements we know: Typical FWHM bunch lengths after injection are 2.4 ns, during ramping, the lengths are reduced to 1.6 ns by the compression of the 208 MHz RF system and by adiabatic damping. Under the assumption of emittance conservation, one would expect a bunch length of  $l_{920 \text{ GeV}} \approx 0.27 l_{40 \text{ GeV}}$  i.e.  $\approx 0.6 \text{ ns}$  at 920 GeV. This means, that there are processes during the ramp which increase the longitudinal emittance.

HERA is operated with 180 bunches<sup>8</sup>, stored in the proton ring and 189 bunches, stored in the electron ring. The HERA proton storage ring has 220 possible bunch positions 96 ns apart. A schematic picture of the accelerator and its bunch structure is shown in figure 1.3. To inject

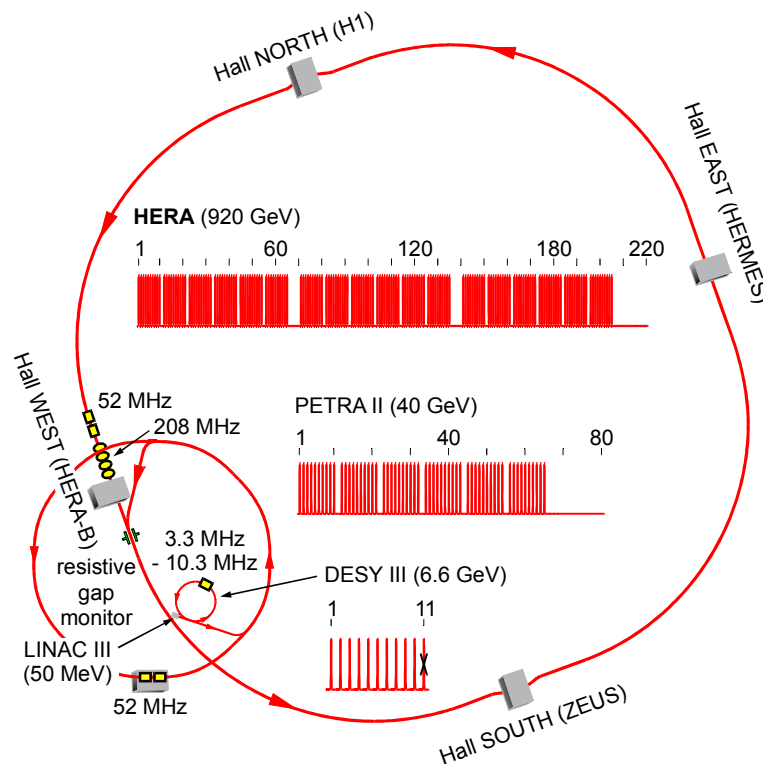


Figure 1.3: The proton accelerator complex at DESY with the various RF-Systems and the positions occupied by bunches. The gaps between the three bunch trains are needed for the build up of the fields in the injection and the dump kicker magnets.

180 proton bunches into HERA, three PETRA fillings of 60 proton bunches are transferred. The rise time of the injection kickers requires a gap of 5 bunch positions (480 ns) between the successive trains of 60 bunches. After the third 60 bunch train, there is a gap of 15 bunch positions, needed for the dump kicker at 920 GeV<sup>9</sup>.

The observation of the longitudinal bunch shapes showed that bunch oscillations took place during acceleration. Different types of instabilities or technical defects are conceivable. A single bunch instability leads to an emittance dilution, which is independent of the presence of the other bunches in the ring. In contrast, at a coupled bunch instability all bunches together form oscillation states, also causing an emittance dilution. The microwave instability is the most

<sup>8</sup>Each bunch contains  $10^{10}$  to  $10^{11}$  particles.

<sup>9</sup>The rise time of the injection kickers is 200 ns. To build up the magnetic field of the dump kicker 800 ns are needed [13].

likely single bunch instability<sup>10</sup>. First suspicions that it could play a role were not confirmed, see appendix A.3. Then, coupled bunch instabilities, a loss of damping, or technical problems were obvious.

Since the fast oscilloscope is only able to sample once per second and one bunch at a time, nothing was known about the time evolution of these oscillations, nor about the behavior of the other bunches at the same time. So, we could not confirm multi-bunch oscillations. The use of a spectrum analyzer for this purpose is only possible for equilibrium conditions. In addition, it is not suitable as sensor of potential feedback systems.

Available narrow band beam phase<sup>11</sup> measurements yielded also ambiguous results.

The fixed target experiment HERA-*B* suffers from high energetic protons, which are not trapped in the RF buckets, the so called ‘coasting beam’. These coasting protons may hit the HERA-*B* wire targets and generate reaction products. Since this occurs continually and not synchronized with the bunched beam, it seriously complicates the data taking of the HERA-*B* detector.

For these reasons, it appeared necessary to develop new diagnostic tools, which measure the longitudinal position and the length of every bunch, and the transient RF signals of all RF cavities. These diagnostic should also serve as the sensor of feedback systems.

## 1.4 Fast longitudinal diagnostics

Normally, one determines coupled bunch oscillations by measuring the beam frequency spectrum with a broad band monitor [16]. Coupled bunch oscillation modes are visible as sidebands. But inhomogeneous bunch patterns complicate the interpretation. If the bunches differ in their charge, shape and distance between each other, sidebands are observed with similar frequencies to those caused by coupled bunch oscillations.

The new diagnostic system should avoid this problem and permit the observation of transient effects, for example during injection. Hence, it had to work in the time domain and be able to observe the time evolution of the phase and length of every single bunch quasi simultaneously. Similar capabilities may be found in digital feedback systems used at electron and positron storage rings [17]. They also permit the observation of bunch phases. In contrast, there is no bunch length available only the bunch current instead.

To be suitable as a sensor for future feedback systems, the devices must permit real time measurements. An essential value for a coupled bunch feedback is the minimum voltage of the longitudinal kicker. This voltage depends on the minimum detectable bunch oscillation. Hence, a highly sensitive and noise free sensor leads to a cost reduction for a feedback kicker system.

For checking the functioning and automated adjustment of a possible RF feedforward, measurements of the transient cavity fields are of paramount importance. During acceleration from low to high energy, the RF transients change their shapes due to the transition of the bucket potential<sup>12</sup> from 52 MHz to 208 MHz. A possible RF feedforward has to consider this automatically. Therefore, the beam loading transients must be measurable in real time and with high accuracy.

In my thesis, I designed and set-up a real time measurement system of the proton bunches. It is able to determine, from a monitor signal, the phase and length of each bunch before the arrival of the next bunch, 96 ns later. Additionally, I designed and set up a cavity field diagnostics permitting the recording of the accelerating and transient fields in each cavity. Depending

<sup>10</sup>Other single bunch instabilities are the negative mass instability and the longitudinal head-tail instability [15].

<sup>11</sup>Beam phase means: Phase of RF when a bunch passes a cavity.

<sup>12</sup>this is observable with an oscilloscope

on the specific measurement task, different timing schematics have to be used to preselect the large amount of data. Therefore, I designed, specified and commissioned a remotely controllable timing system, providing the trigger and clock signals for the analog to digital converters (ADCs). For data recording and presentation software was necessary. In part, I specified and commissioned it, earlier versions I wrote by myself. Figure 1.4 gives an overall view of the fast longitudinal diagnostic system as implemented.

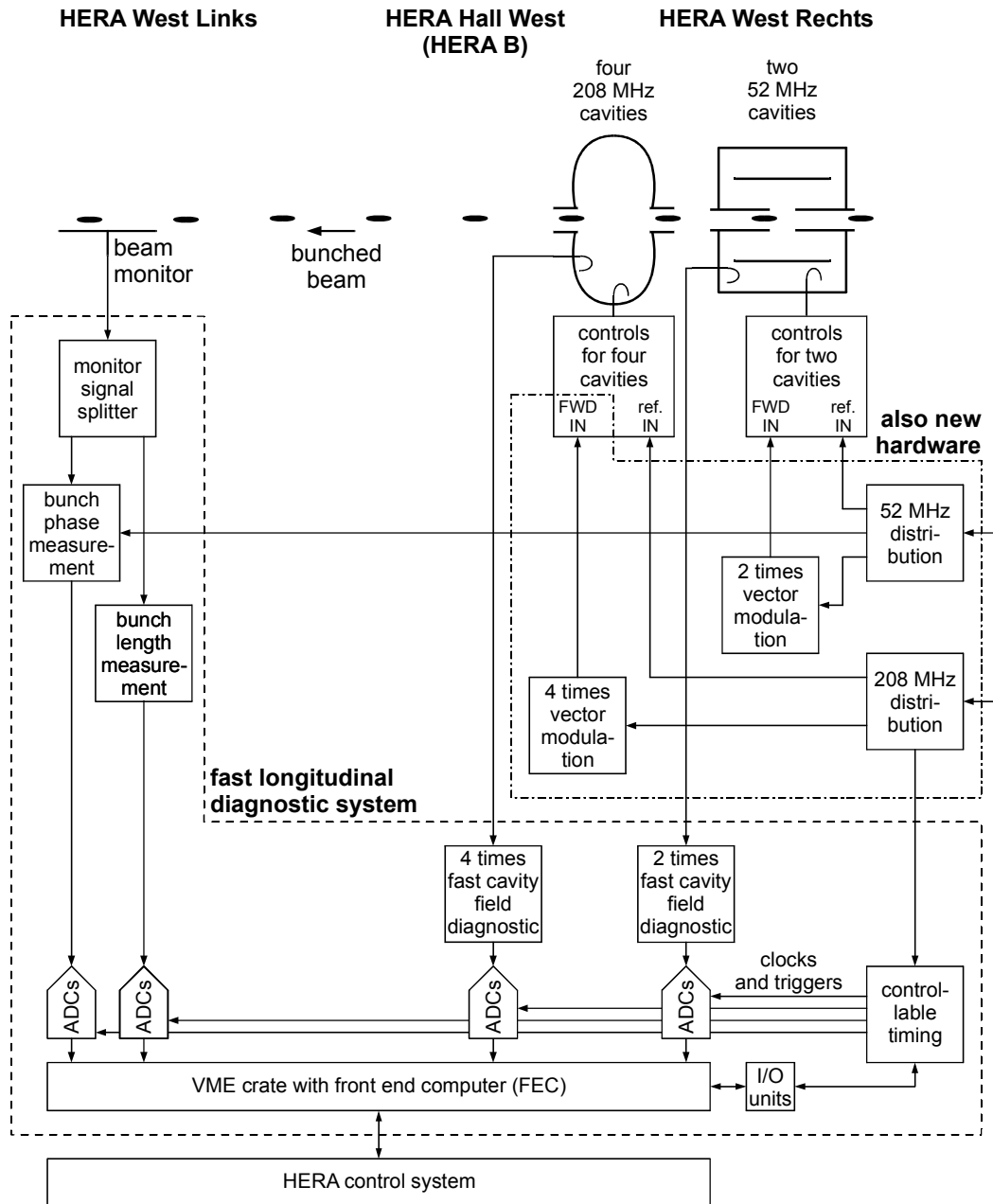


Figure 1.4: An overall view on the fast longitudinal diagnostic system for the HERA proton ring and the new hardware.

Vector modulation units for future applications are included. They can be used for control of the cavity fields and for correction of the transients in the cavities.

Together with the new diagnostic system several improvement of the existing RF system have been made, in particular I redesigned the RF signal distribution.

## 1.5 Examinations on the longitudinal stability

The new diagnostics permits different measurements of the HERA beam and RF signals which were not previously available.

With the new diagnostic system, I started to examine the longitudinal stability in more detail. These examinations are the subject of the third part of this thesis.

Chapter 7 summarizes Sacherer's formulae describing coupled bunch instabilities [18]. Based on these, a modal analysis of the multi-bunch oscillations which are observed during a typical acceleration period is presented. Whether HERA suffers from coupled bunch instabilities or not will be discussed applying Sacherer's rules. The order of magnitude of growth rates is estimated. A transient modal analysis is applied, similar to that done at electron / positron storage rings with digital coupled bunch feedback systems.

The above measurements do not influence the beam. A deeper insight into the longitudinal stability is offered by measurements of the beam response to particular excitations. An overview of such measurements and their results will be given.

Since the hardware setup was still under development, W. Kriens and U. Hurdelbrink from DESY provided parts of the electronics used. We started to establish measurements of the longitudinal beam transfer function, the decoherence time, Landau damping and longitudinal bunched beam echoes. These measurements are treated in chapters 9 and 10. The first results allow conclusions to be drawn on the longitudinal stability of the HERA proton beam. For comparison with complex theories, additional measurements may be done with the new diagnostics system in the future.

In part four of the thesis, possible causes for the emittance dilution during acceleration are discussed. In this context, the concept of effective impedances is used [19]. A discussion whether there is sufficient Landau damping in the HERA proton ring follows. Finally, chapter 12 contains a survey on possible active measures against the longitudinal emittance dilution in the HERA proton ring.





**Part I**

**Existing RF Installation**



## 2 Existing Longitudinal Beam Diagnostics

For the development of the new fast longitudinal beam diagnostic system, the different abilities and disadvantages of the present diagnostic systems had to be considered. These systems are described in this chapter. All systems use the broad band signals supplied by the resistive gap monitors. For a cross-check and calibration of the new diagnostic system, results from the present systems are used.

### 2.1 Resistive gap monitor

Two identical resistive gap monitors [20] in the HERA proton storage ring are used for all the longitudinal beam diagnostics. The monitors deliver time signals of the longitudinal density distribution of the bunches, with a time resolution of approximately 200 ps. For a photograph of a resistive gap monitor see figure A.27 in the appendix.

In figure 2.1, the working principle of a resistive gap monitor [21] is shown.

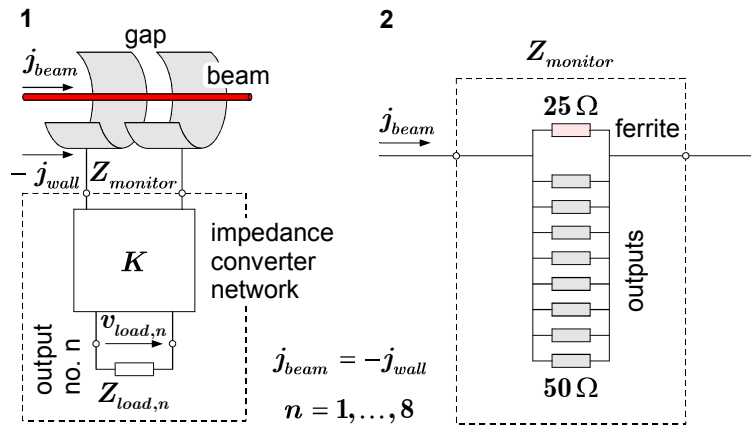


Figure 2.1: (1) Working principle of a resistive gap monitor, and (2) the equivalent network for calculation of the impedance as seen by the beam.

A beam with current  $j_{beam}$  induces for  $v = c$  the wall current  $j_{wall} = -j_{beam}$  in a smooth cylindrical vacuum chamber. The vacuum chamber is electrically separated by a small cylindrical gap, so that the wall current has to flow through an intermediate impedance converter network  $K$ . At the output no.  $n$  the network supplies the voltage signal  $v_{load,n}$  to a load resistor  $\text{Re}(Z_{load,n})$ . This signal is related by the monitor sensitivity factor  $S_n$  to the beam current  $j_{beam}$ :

$$v_{load,n} = S_n j_{beam} \quad (2.1)$$

When passing the monitor, the beam loses the power  $P_{monitor} = j_{beam}^2 \text{Re}(Z_{monitor})$  and the network supplies the power  $P_{load,n} = v_{load,n}^2 / \text{Re}(Z_{load,n})$  at the output  $n$ . Hence, the

sensitivity is

$$S_n = \sqrt{\operatorname{Re}(Z_{load,n}) \operatorname{Re}(Z_{monitor}) \frac{P_{load,n}}{P_{monitor}}}. \quad (2.2)$$

In figure 2.2, the assembly of the monitor is shown. Eight  $50 \Omega$  outputs are arranged around the gap. The end of a coaxial structure enclosing the vacuum chamber is loaded with ferrites to suppress reflections over a wide range of frequencies. The impedance of the ferrites is  $25 \Omega$ . This results in the equivalent network shown in figure 2.1, and the impedance, seen by the

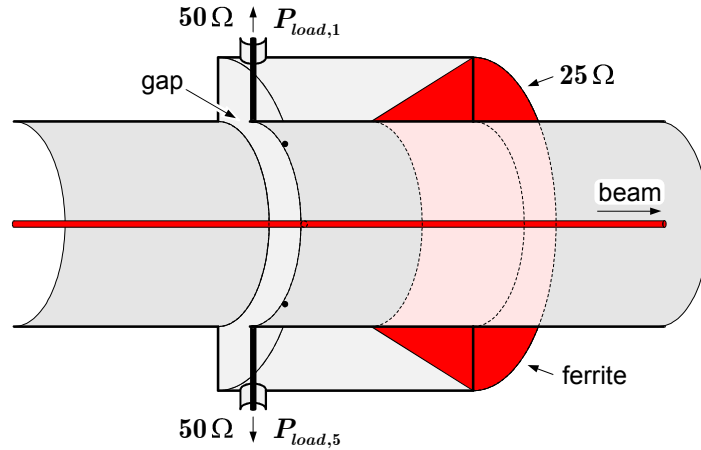


Figure 2.2: Resistive gap monitor

beam, is  $Z_{monitor} = 5 \Omega$ . At each output the power  $P_{load} = \frac{1}{10} P_{monitor}$  is supplied, therefore the sensitivity factor is

$$S_n = \sqrt{50 \Omega \cdot 5 \Omega \cdot \frac{1}{10}} = 5 \Omega. \quad (2.3)$$

The signals at the individual outputs depend on the horizontal and vertical beam position. This dependence can be suppressed by combining four outputs with resistive power combiners cross-wise [22]. Resistive power combination results in a power loss of 50% in each combiner, i.e. the combination of four outputs yields the same power as a single output. Therefore, the sensitivity is again  $5 \Omega$ .

## 2.2 Narrow band phase measurements

Several narrow-band systems for measuring the beam phase are implemented in HERA. The principle is shown in figure 2.3.

The bunched beam passes one of the resistive gap monitors and induces signals which excite oscillations in a band pass filter whose center frequency is identical to the RF reference. The phase between these oscillations and the RF reference is equal to the beam phase. It is measured with a phase detector. High accuracy in the phase measurement is obtained by averaging over many bunches, this is achieved either by a narrow band width of the band pass filter or by using low pass filters at the output. These systems are inadequate for the observation of multi-bunch oscillations. In particular, the signal may even vanish if bunches perform synchrotron oscillations with different phases.

Two control loops are installed to damp synchrotron oscillations in HERA [23, 24, 25]. Both loops have phase detection units as described above.



$\pm 50$  ps, the maximum phase error is  $\pm 3.6^\circ$  with respect to a 208 MHz RF bucket, which is too imprecise.

The dead time problem can be solved by using a fast frame oscilloscope, which is triggered on the same bunch every 100th revolution, see e.g. [10]. This technique is also often used for phase space tomography [26, 27, 28]. However, with the fast frame oscilloscope there is no easy way to implement the simultaneous observation of all bunches in HERA. Hence, a new diagnostic tool was required.

## 3 Radio Frequency System

To achieve optimal performance in the longitudinal diagnostics and to counteract the emittance dilution, requires consideration of the whole radio frequency system. An overview of the actual RF system of the HERA proton ring follows.

### 3.1 Frequency control

In a high energy storage ring, the orbit length  $2\pi R$  of the beam depends on the energy of the synchronous particle  $E_s$  and the frequency  $f_{RF}$  of the RF-system

$$2\pi R = \frac{v}{f_{rev}} = \frac{hc\beta}{f_{RF}} = \frac{hc}{f_{RF}} \sqrt{1 - \frac{1}{\gamma^2}} = \frac{hc}{f_{RF}} \sqrt{1 - \left(\frac{E_0}{E_s}\right)^2}, \quad (3.1)$$

where  $v$  is the particle velocity,  $f_{rev}$  the revolution frequency,  $h = f_{RF} / f_{rev}$  the harmonic number and  $E_0 = m_p c^2$  the proton rest mass. At the HERA proton storage ring, the energy is ramped from 40 GeV to 920 GeV. In the case of a fixed frequency, the orbit length would increase from the design value  $2\pi R = 6335.825$  m to 6337.586 m and the average orbit radius  $R$  would increase by 28 cm. The beam pipe in HERA has a typical diameter of 5.5 cm. Since the beam should always be centered inside the beam pipe with a constant orbit length,  $f_{RF}$  has to be changed as  $E_s$  changes. Figure 3.1 shows the necessary frequency change for the energy ramp.

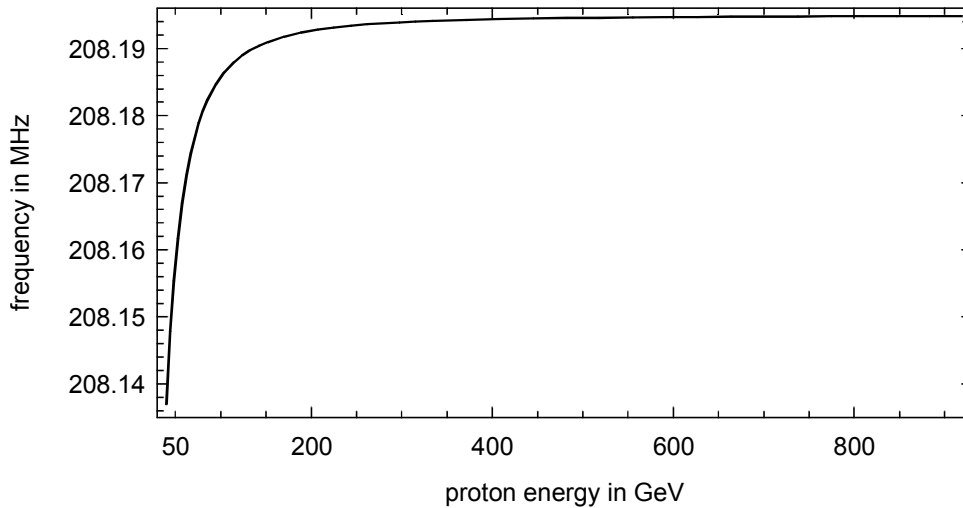


Figure 3.1: Necessary RF frequency change for proton acceleration.

The momentum  $p_s$  and the energy of the synchronous particle  $E_s$  are defined by the magnetic field  $B$  in the dipole magnets and the orbit radius in the magnets  $\rho$

$$\beta E_s = c p_s = c e \rho B. \quad (3.2)$$

From the measurement of the magnetic field  $B$  in a reference dipole magnet, connected in series to the dipole magnets of the storage ring, the required RF frequency is obtained from

$$f_{RF} = \frac{hc}{2\pi R} \frac{1}{\sqrt{1 + \left(\frac{E_0}{ce\rho B}\right)^2}}. \quad (3.3)$$

In figure 3.2 the principle of the technical setup for the frequency generation is shown. The

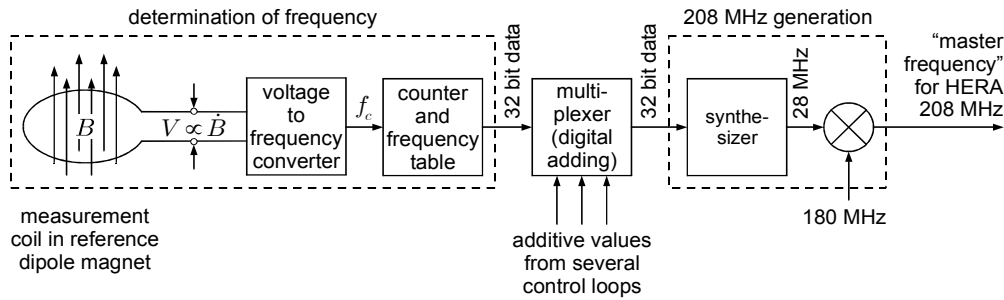


Figure 3.2: Principle of frequency generation for the HERA proton storage ring.

change of the magnetic field in the reference magnet induces a voltage in the measurement coil, located inside the reference magnet. For the signal transport, this voltage is converted into a frequency. A counter counts the waves of this frequency. The number of counts in a period of time is proportional to the time derivative of the magnetic field. This information, together with knowledge of the magnetic field at injection, measured by nuclear magnetic resonance (NMR), is converted to a digital frequency value by a table generated according to (3.3). Afterwards, correction values from several control loops are added in a multiplexer. From the sum value, a synthesizer generates a variable frequency of 28 MHz without phase jumps. Mixing this frequency with 180 MHz result in 208 MHz.

A phase locked loop, see figure 3.3, locks the second HERA frequency of 52 MHz to 208 MHz. First, 208 MHz is divided by four. The resulting 52 MHz signal is mixed with the output

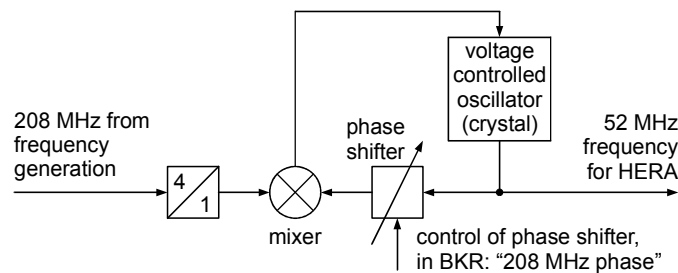


Figure 3.3: A phase locked loop locks the 52 MHz to the 208 MHz frequency.

signal of the voltage controlled oscillator (VCO). Phase deviations of both signals lead to a non-zero voltage at the mixer output, which changes the frequency of the VCO until the phase deviation is zero. The controllable phase shifter in one signal path enables a remote shift of the phase between 208 MHz and 52 MHz.

During injection, the RF systems of PETRA and HERA must be phase-locked to ensure that the bunches, ejected from PETRA, are injected into the planned bucket positions in HERA. The injection scheme is shown in figure 3.4. The 'injection logic', see figure 3.4, consisting





synchronization. From the 208 MHz reference signal, a 500 MHz signal is obtained by a phase locked loop. Mixing with the 500 MHz from the electron storage ring delivers the difference frequency. Since the harmonic number of 500 MHz with respect to the revolution frequency is 10560, every 10560th count ( $N$  in figure 3.5) of the difference frequency waves, the same buckets of both rings hit each other. For locking the buckets, the proton frequency is changed by the additive value  $f_{corr}$  as long as  $\Delta f > 250$  Hz. Afterwards, the minimum remaining time for synchronization  $t_R = \frac{N}{\Delta f}$  is observed until it is about 30 s. By changing  $f_{corr}$ , this time is then kept constant, resulting in a smooth approach of both accelerator frequencies. Values of  $\Delta f < 5$  Hz lead to a release of the synchronization start signal and the variation of  $f_{corr}$  is stopped. Reaching the next  $N = 0$ , the phase locked loop, acting on the electron frequency, is closed. For a more detailed description of this procedure, see appendix A.5.

Revolution trigger signals during standard operation, locked on the bunch filling scheme, are obtained at both rings by counting the 500 MHz signals. This leads to a trigger time position resolution of  $\frac{1}{500 \text{ MHz}} = 2$  ns. This is too coarse, but a more precise alignment is possible with adjustable delays. After a technical failure, the revolution trigger signals and the counter start of the ep-synchronization have to be restored manually.

For more details on the frequency control in HERA see [25] and [29].

## 3.2 Control systems for the cavities

The RF signals are generated near the control room and transferred over a distance of about 600 m to the HERA Hall West, where the cavity controls are located. Signal splitters divide the signals to several diagnostic units, to timing units and to each single control of the two 52 MHz and four 208 MHz cavities. These splitters had to be replaced by new ones, to improve the signal quality for the new longitudinal diagnostic system.

Figure 3.6 shows the components of one 52 MHz cavity control system. For a minimal

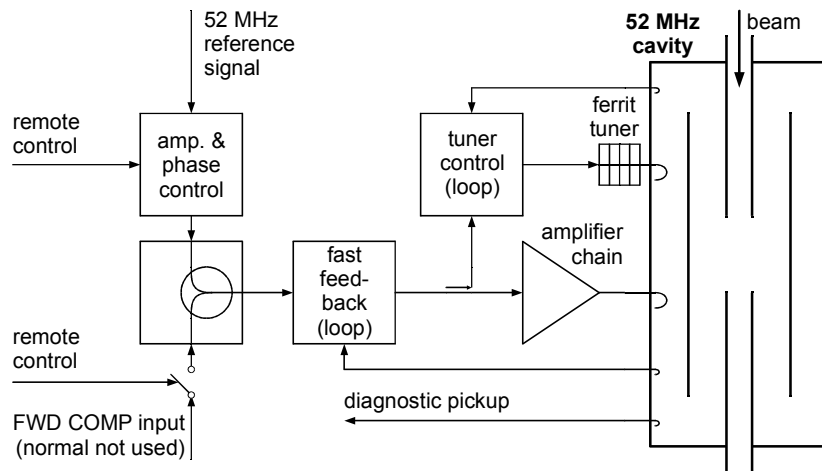


Figure 3.6: Control system for a single 52 MHz cavity.

signal propagation time, the components are installed near the cavity in the HERA tunnel. Via the amplitude and phase regulation unit, the amplitude and phase of the cavity are set remotely. This unit does not check the fields in the cavity. A remotely switchable feedforward compensation input, named 'FWD COMP' in figure 3.6, permits the addition of an RF signal e.g. for beam loading compensation. In the fast feedback loop, the cavity signal is subtracted from the drive signal and afterwards amplified. In this way, the suppression of an error signal in the

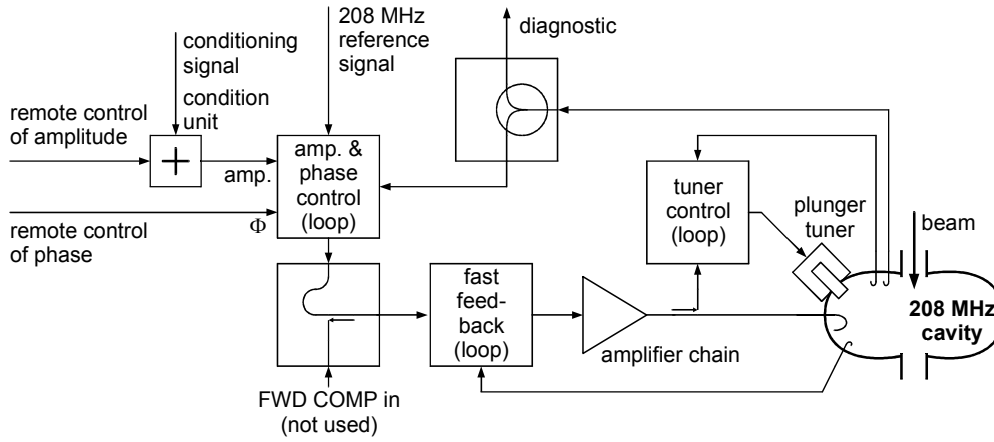


Figure 3.7: The control system of a single 208 MHz cavity.

Parameter	52 MHz cavity & control	208 MHz cavity & control
Harmonic number:	1100	4400
No. of cavities:	2	4
Drive frequency from 40 GeV to 920 GeV:	52.0342 MHz 52.0485 MHz	208.137 MHz 208.194 MHz
Max. gradient with beam after conditioning:	120 kV / cavity	190 kV / cavity
Max. possible gradient:	200 kV / cavity [30]	800 kV / cavity [32]
Signal propagation through amplitude and phase control:	open loop control	$(3 \pm 0.5) \mu\text{s}$ [33]
Signal propagation time through fast feedback:	$(200 \pm 10) \text{ ns}$ [33]	$(250 \pm 10) \text{ ns}$ [33]
Gain of fast feedback:	adjustable from 1 to 50 [30]	fixed at 100 [30, 23]
Bandwidth of amplifier chain:	unknown	$(3.5 \pm 0.1) \text{ MHz}$ (3 dB) [31]
Final stage amplifier:	tetrode (50 kW) [34] EMAC 4 CW 50 000 E [31]	transmitter tetrode (60 kW) Siemens RS 2058 [32]
$Q_0 (= Q_L)$ of cavity:	9600 [34]	27000 [23]
$R / Q_0 = \sqrt{L/C}$ of cavity:	120 $\Omega$ [34]	8 M $\Omega$ / 27000 [35]
$\tau_{cav} = 2Q_0 / \omega_{cav}$ :	59 $\mu\text{s}$	41 $\mu\text{s}$
Time const. of tuning loop:	approx. 1 s [30]	approx. 1 s [30]
Tuning range:	$f_{center} \pm 10 \text{ kHz}$ [34]	$f_{center} \pm 200 \text{ kHz}$ [32]

Table 3.1: Parameters of the cavities in the HERA proton storage ring and their controls.

cavity starts after the signal propagation time through the loop. In case of a deviation between the drive frequency and the cavity eigen-frequency, the tuner control loop measures a phase deviation between the drive RF and the cavity RF. By changing the strength of the magnetic field in the ferrite tuner, the permeability of the ferrites and consequently the frequency in the tuner cavity is changed. Via the coupling of both cavities, this also changes the frequency of the accelerating cavity. In this way, the loop electronics minimizes the frequency deviation between drive RF and cavity RF.

Figure 3.7 shows the control of a 208 MHz cavity. Except for the fast feedback loop, located in the HERA tunnel, these components are installed in an electronic room 300 m away for easier maintenance. The phase and amplitude control unit compares the cavity voltage and phase with the desired values and adjusts them if necessary. A feedforward compensation input is available. The working principle of the fast feedback loop is similar to the one at a 52 MHz cavity. A stepper motor moves a plunger, reaching inside the cavity, affecting the eigen-frequency. It is steered by the tuner control loop.

Table 3.1 contains the most relevant parameters for the cavities and their control systems.

Figures A.28 and A.29 in the appendix are photographs of the 52 MHz and 208 MHz cavities. A photograph of the 208 MHz cavity control is figure A.30.

### 3.3 Narrow band beam phase feedback systems

For damping synchrotron oscillations of the proton beam, two narrow band beam phase feedback systems are installed in HERA.

Figure 3.8 shows the phase loop I. Implementing a differential controller, this loop leads to

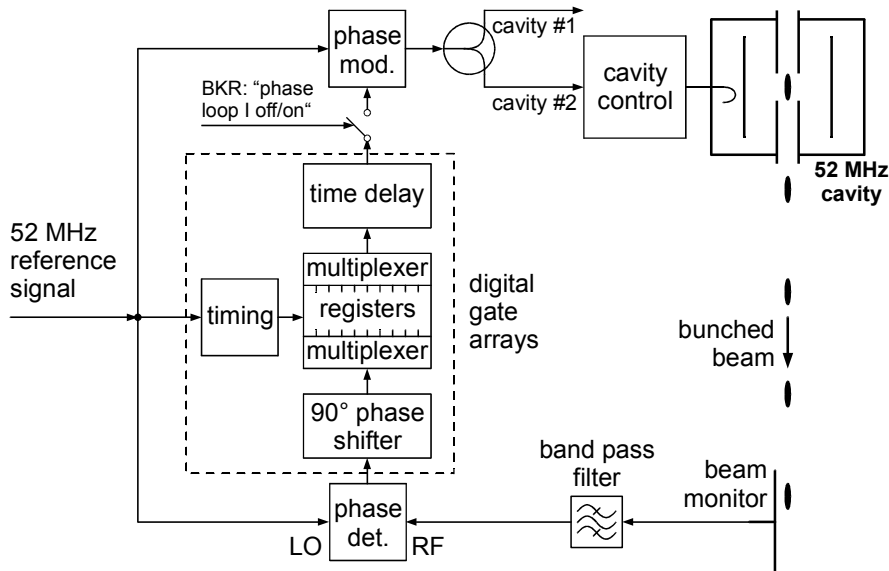


Figure 3.8: Working principle of the phase loop I.

a damping term  $2\delta \frac{d(\Delta\phi)}{dt}$  for synchrotron oscillations

$$\frac{d^2(\Delta\phi)}{dt^2} + 2\delta \frac{d(\Delta\phi)}{dt} + \omega_s^2(\Delta\phi) = 0. \quad (3.4)$$

This can be understood as follows: Since the beam phase<sup>1</sup> obeys

$$\Delta\phi = \Delta\phi_{\max} \cos[\sqrt{\omega_s^2 - \delta^2} t + \varphi] e^{-\delta t}, \quad (3.5)$$

a shift of  $\Delta\phi$  by  $90^\circ$  i.e.  $\frac{\omega_s}{4}$  is proportional to the time derivative of  $\Delta\phi$  and with it the damping term. Therefore, feeding back the beam phase, shifted by  $90^\circ$ , damps synchrotron oscillations.

The beam phase is determined by measuring the phase between the oscillation of a 52 MHz band pass filter, excited by the beam signal, and the 52 MHz reference signal (compare section 2.2). After digitizing the phase every 962 ns, the values are shifted by  $90^\circ$  and stored in a register. Twenty two correction values are available, each for a batch of ten bucket positions. After a time delay and a digital to analog conversion, the values vary the phase of the common drive signal for the 52 MHz cavities via a phase modulator; the 208 MHz cavities are not influenced. The time delay ensures the separate damping of each batch.

Unlike the phase loop I, phase loop II damps synchrotron oscillations by influencing the frequency generation (section 3.1), it acts as an integral controller. Figure 3.9 shows the essential components: The beam phase  $\Delta\phi$  is measured using the previously described standard

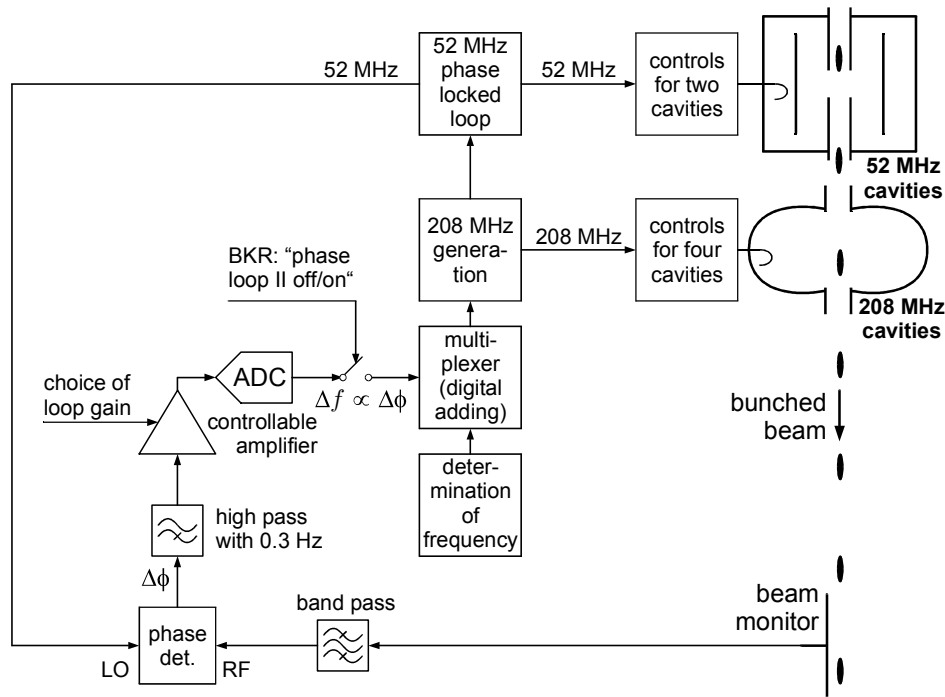


Figure 3.9: Working principle of the phase loop II.

method. Since the synchrotron oscillations should be damped without disabling the frequency ramp (figure 3.1), a high pass filter is used which transmits the phase signals caused by synchrotron oscillations with typical frequencies of 30 Hz but suppresses the phase signals caused by the changing RF during ramping. The filtered phase signal is amplified by a controllable amplifier and sampled with an ADC. The addition of the ADC output to the digital frequency value, calculated from the magnetic field of the reference dipole, leads to a frequency change

<sup>1</sup>In longitudinal beam dynamics the bunch phase is usually denoted by  $\phi$ . The phase with respect to the bucket minimum at  $\phi_s$  is  $\Delta\phi = \phi - \phi_s$ .

$\Delta\omega \propto \Delta\phi$  and with it to a phase change  $\Delta\varphi(t) \propto \Delta\phi$  of the RF

$$\begin{aligned}
 v_{RF}(t) &= V_{RF}(t) \sin [(\omega_{RF} + \Delta\omega) t + \varphi_{RF}] \\
 &= V_{RF}(t) \sin [\omega_{RF} t + \Delta\omega t + \varphi_{RF}] \\
 &= V_{RF}(t) \sin [\omega_{RF} t + \Delta\varphi(t) + \varphi_{RF}].
 \end{aligned} \tag{3.6}$$

Since the reference signal for the beam phase measurement is also changed, this mechanism leads to a damping of synchrotron oscillations independent of any particular synchrotron frequency, without danger of instabilities. Converting the phase error  $\Delta\phi$  to a correction frequency  $\Delta\omega$  results in the integral control behavior of the loop.

Appendix A.6 contains details of the stability of both phase loops.

## **Part II**

# **Fast Longitudinal Diagnostics**





## 4 Real Time Measurements of Single Bunch Phase and Length

One of the main features of the new fast longitudinal diagnostic system is the capability to measure the phase and length of each individual bunch in real time, i.e. within the time two bunches successively pass a monitor. This measurement is based on the signals provided by the resistive gap monitor, located behind the injection point near the Hall West, where the proton beam is transferred from PETRA to HERA. A future feedforward system for beam-loading compensation at injection will need a monitor in this position.

In this chapter, the main principles and technical specifications are presented. In addition, the measurement errors of the setup are estimated and the values obtained by the fast bunch length measurement and longitudinal bunch shape measurements, described in section 2.3, are compared.

A main goal of this setup was to enable measurements of synchrotron oscillations with oscillation amplitudes smaller than  $0.5^\circ$ , to decrease the requirements on a longitudinal feedback kicker, probably needed in the future. This is due to the minimal detectable oscillation is proportional to the minimum necessary RF voltage for a kicker, compare section 12.4.

### 4.1 Bunch phase

The ‘bunch phase’ is the difference, in RF phase, between the bunch center and the bucket center. The goal is to determine this phase for every bunch in a long train.

This can be achieved with a band-pass filter which has a decay time well below the 96 ns separation between two bunches. An IQ demodulator is used to obtain the phase in the full range from  $-180^\circ$  to  $180^\circ$ . The IQ demodulator requires two analog-to-digital converters (ADCs). Successive data points correspond to the real and imaginary part of the phasor of the signal, therefore complex multiplication can be used for evaluation.

To understand the functioning and advantages of an IQ demodulator, the principle of a phase detector is described first.

In electrical engineering, the convention is to represent a RF voltage  $v_{RF}(t)$  by a phasor<sup>1</sup>  $\mathbf{v}(t)$

$$v_{RF}(t) = \text{Im} [\mathbf{v}(t) e^{i\omega_{RF}t}] = V(t) \sin [\omega_{RF}t + \varphi(t)], \quad (4.1)$$

where  $V(t)$  is the amplitude and  $\varphi(t)$  the phase of the RF signal. Table 4.1 shows the action of the RF components, that are used in phase detectors and IQ demodulators, in terms of phasors.

The RF components of a phase detector are a limiter, a low pass filter, a controllable phase shifter and a frequency mixer, see figure 4.1. The output signal of the phase detector should depend only on the phase shift between the RF wave and the local oscillator (LO) wave, but not on the amplitude of the RF wave. For this reason, the amplitude of the RF signal is first limited to a constant value. Higher harmonics generated by the limiter are damped by a low pass filter.

---

<sup>1</sup>For the phasor representation of a RF wave see appendix A.1.1.

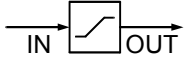
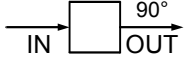
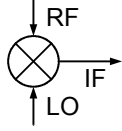
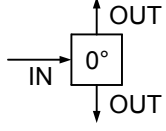
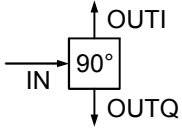
limiter:		$V_{OUT}(t) = \begin{cases} V_{lim} & \text{for } V_{IN}(t) > V_{lim} \\ -V_{lim} & \text{for } V_{IN}(t) < -V_{lim} \\ V_{IN}(t) & \text{else} \end{cases}$
90° phase shift:		$\mathbf{v}_{OUT}(t) = -i \mathbf{v}_{IN}(t)$
mixer:		$\mathbf{v}_{IF}(t) = \frac{1}{2} \mathbf{v}_{LO}(t) \mathbf{v}_{RF}^*(t)$
two way 0° power splitter:		$\mathbf{v}_{OUT}(t) = \frac{1}{\sqrt{2}} \mathbf{v}_{IN}(t)$
two way 90° power splitter:		$\mathbf{v}_{OUTI}(t) = \frac{1}{\sqrt{2}} \mathbf{v}_{IN}(t)$ $\mathbf{v}_{OUTQ}(t) = -\frac{i}{\sqrt{2}} \mathbf{v}_{IN}(t)$

Table 4.1: Mode of action of RF components used in phase detectors and IQ demodulators.

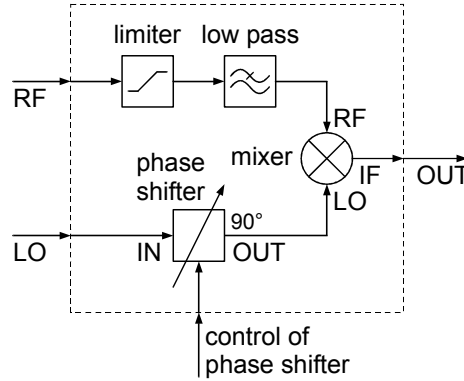


Figure 4.1: Principle of a phase detector.

The resulting signal is mixed with the LO signal in a frequency mixer. Before doing this, the phase of the LO signal is shifted by 90° using a controllable phase shifter.

We obtain the output signal

$$v_{OUT}(t) = \frac{1}{2} V_{LO} V_{lim} \sin [(\omega_{LO} - \omega_{RF})t + (\varphi_{LO} - \varphi_{RF}(t))] . \quad (4.2)$$

The LO frequency is set equal to the RF frequency  $\omega_{LO} = \omega_{RF}$  and for small phase deviations  $|\varphi_{LO} - \varphi_{RF}(t)| \ll 1$  the sine function is linearized:

$$v_{OUT}(t) \approx \frac{1}{2} V_{LO} V_{lim} [\varphi_{LO} - \varphi_{RF}(t)] \quad (4.3)$$

Phase measurements with a phase detector suffer from several sources of errors. In practice, the phase  $\varphi_{LO} - \varphi_{RF}(t)$  consists of a constant and a time varying part. As one is only interested in the time varying part, the constant part is first subtracted by tuning the phase shifter. Large phase deviations lead to errors because of the replacement of the sine by its argument. A limiter also contains capacitive components which lead to a phase shift of the output signal, varying with the input amplitude. Finally, one has to measure  $\frac{1}{2}V_{LO} V_{lim}$  for calibration. Phase measurements with an IQ demodulator avoid these problems.

An IQ demodulator consists of two frequency mixers, a two way  $0^\circ$  power splitter, and a two way  $90^\circ$  power splitter, see figure 4.2.

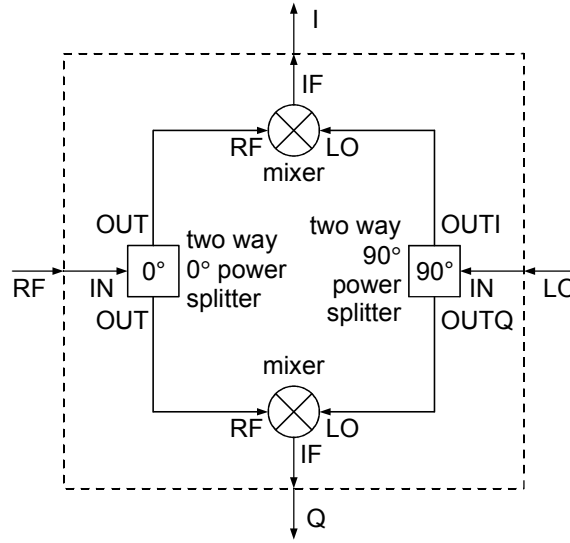


Figure 4.2: Principle of an IQ demodulator.

The demodulator outputs are

$$v_Q(t) = \frac{1}{2\sqrt{2}} V_{LO} V_{RF}(t) \sin [(\omega_{LO} - \omega_{RF})t + (\varphi_{LO} - \varphi_{RF}(t))] \quad (4.4)$$

$$v_I(t) = \frac{1}{2\sqrt{2}} V_{LO} V_{RF}(t) \cos [(\omega_{LO} - \omega_{RF})t + (\varphi_{LO} - \varphi_{RF}(t))] . \quad (4.5)$$

In the special case  $\omega_{LO} = \omega_{RF}$ , one speaks of down-conversion to the base band. We get full information about the amplitude  $V_{RF}(t)$  and phase  $\varphi_{RF}(t)$  of the RF signal  $v_{RF}(t)$  at the demodulator outputs.

After this short excursion on phase detectors and IQ demodulators, we now come back to the beam diagnostic where an IQ demodulator is used, see figure 4.3.

The beam monitor signal of a single bunch excites an oscillation in a broadband 52 MHz band pass filter, which is analyzed with an IQ demodulator by down-conversion to the base band, using the RF frequency as a local oscillator. Before sampling the I and Q signals with two ADC channels, they are smoothed with low pass filters.

The correct sampling time is given by the condition that the expression  $\sqrt{(v_I(t))^2 + (v_Q(t))^2}$  assumes its maximum. In this case we get the 52 MHz Fourier component of the bunch signal by

$$A_{52, meas} = \max \left[ \sqrt{(v_I(t))^2 + (v_Q(t))^2} \right] \equiv \sqrt{(v_{I, max})^2 + (v_{Q, max})^2} \quad (4.6)$$

$$A_{52} = C_{52} A_{52, meas} \quad (4.7)$$

and the phase<sup>2</sup> by

$$\Delta\phi = \arctan \frac{v_{Q,\max}}{v_{I,\max}} + \Delta\phi_{\text{offset}}. \quad (4.8)$$

where  $C_{52}$  is the overall gain in the circuit and  $\Delta\phi_{\text{offset}}$  the phase offset between RF and LO inputs.

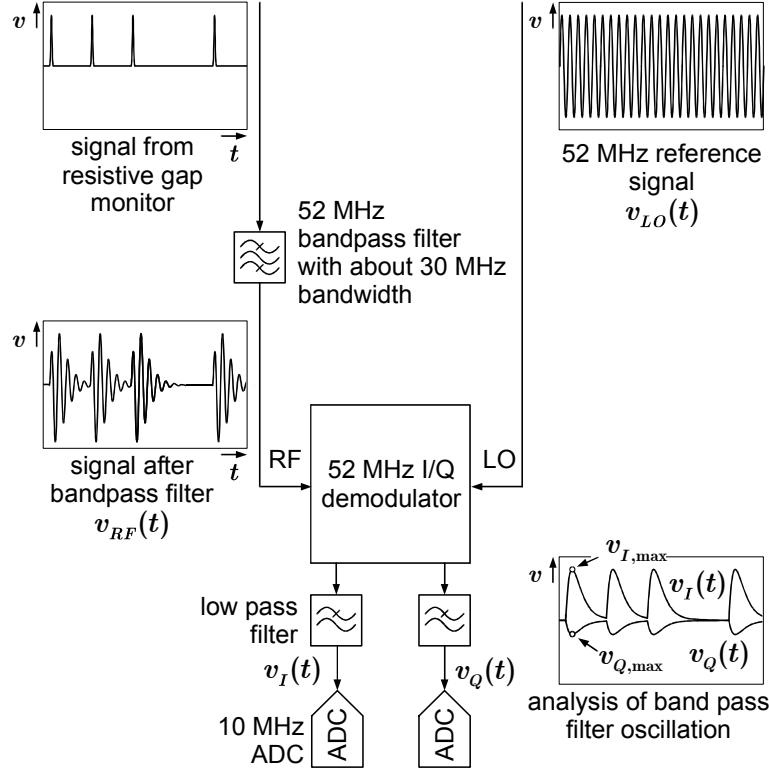


Figure 4.3: Measurement principle of the phase and amplitude of the 52 MHz Fourier component of a single bunch signal: The signal from the resistive gap monitor excites an oscillation in a band pass filter, which decays before the next bunch passes the monitor. The IQ demodulator determines the in-phase (I) and out-of-phase resp. quadrature (Q) components of the bunch induced oscillation, with respect to the 52 MHz reference frequency.

The following contradictory conditions must be fulfilled by the band pass filter:

1. The remaining RF oscillation in the filter must be small when the next pulse arrives. This means, the decay time of the RF signal in the filter has to be sufficiently small e.g. the bandwidth has to be large.
2. After the IQ demodulator and the low pass filters a certain time is necessary for the sampling at the signal maximum. For slowly varying signals the analog-digital conversion is less sensitive to jitter in the ADC timing signals. For this reason, larger decay times of the RF signal in the filter are desirable which imply a small bandwidth of the filter.
3. In order to obtain useful phase information, the filter should not ring and the cycle duration should be constant. To have no ringing effects in a filter, the progression of the phase over the frequency has to be a monotone and smooth function.

<sup>2</sup>In longitudinal beam dynamics the bunch phase is usually denoted by  $\phi$ . We measure the phase  $\Delta\phi = \phi - \phi_s$  with respect to the phase of the bucket minimum, which is equal to the phase of the synchronous particle  $\phi_s$ .

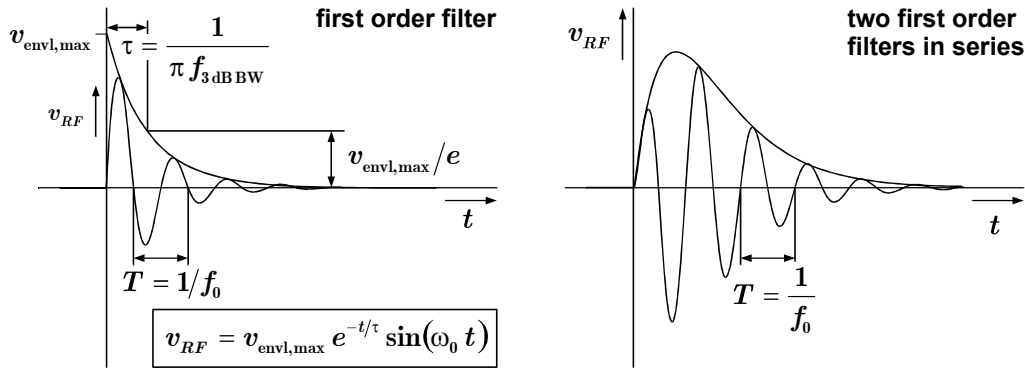


Figure 4.4: Response of an ideal 52 MHz band pass filter and of two band pass filters connected in series, each of first order, to an impulse excitation.

center frequency:	52.041 MHz
design type:	series connection of two first order Butterworth filters, a constant cycle duration is important
bandwidth (6 dB):	25 MHz
input frequency:	DC to 4.2 GHz
pass band ripple:	$< \pm 0.2$ dB
impedance:	$50 \Omega$ at in- and output
insertion loss:	$< 1$ dB
dynamic range:	$< -80$ dBm to $> 0$ dBm
operating temperature:	$-10$ °C to $85$ °C
connectors:	SMA

Table 4.2: Properties of 52 MHz band pass filter.

Simulations based on measured bunch shapes showed that two Butterworth filters of first order in series fulfill these criteria. The filter specification is given in table 4.2. The filter was custom designed, according to these specifications.

In figure 4.3, some technical details have been omitted: Amplifiers for increasing signal levels and attenuators to suppress signal reflections are also needed. Figure A.20, in the appendix, shows a photograph of RF parts for the bunch phase measurement.

An example for the bunch phase measurement is shown in figure 4.5. Here, 10 bunches are taken without noticeable synchrotron oscillation and the phase values, measured during a 0.52 s time period, are plotted in a histogram, subtracting the individual time-averaged phase of each bunch. A Gaussian distribution is observed, with a FWHM of  $0.19^\circ$ , with respect to the 52 MHz radio frequency. This number is an upper limit for the resolution of the detection system, since the phase noise of the bunched proton beam itself is included in the data.

## 4.2 Bunch length

Two typical bunch shapes at 40 GeV and 499 GeV, as recorded with the fast oscilloscope, are shown in figure 4.6 and 4.7. An almost Gaussian shape is observed, even during strong synchrotron oscillations at 499 GeV. Under the assumption of a Gaussian bunch shape, the experimental setup, described here, permits a bunch length determination in real time.

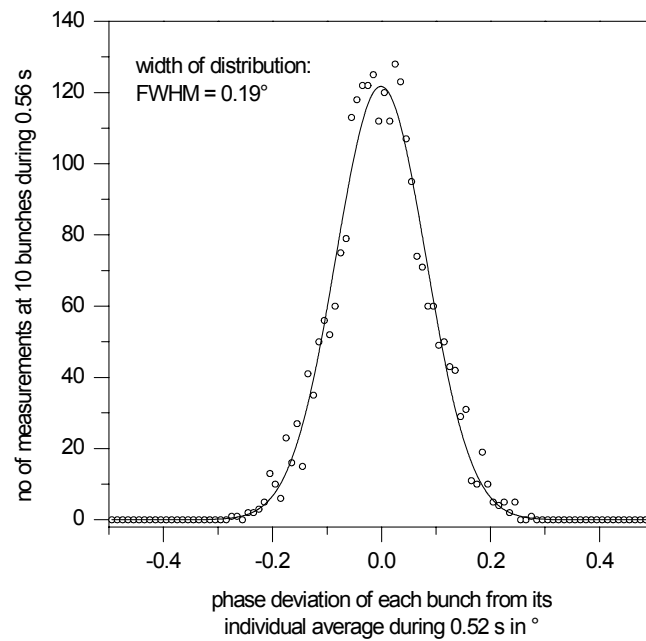


Figure 4.5: Relative measurement errors of single shot phase measurements.

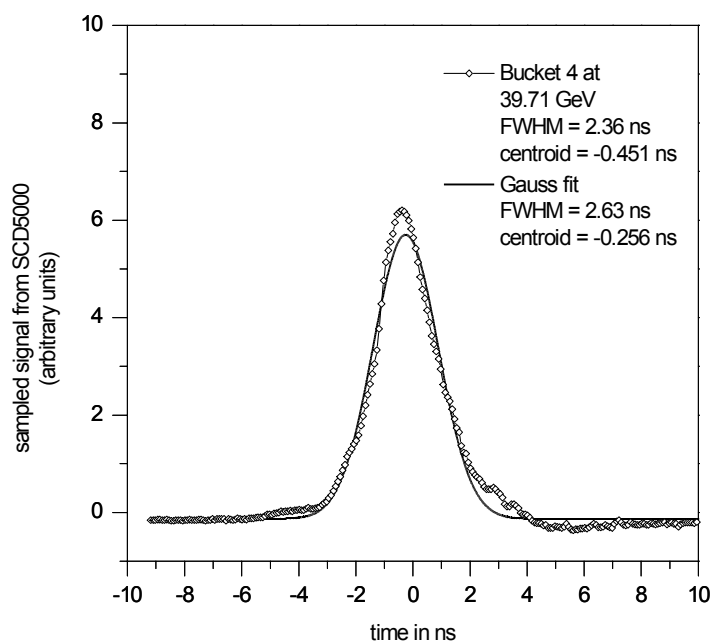


Figure 4.6: Bunch shape at 40 GeV.

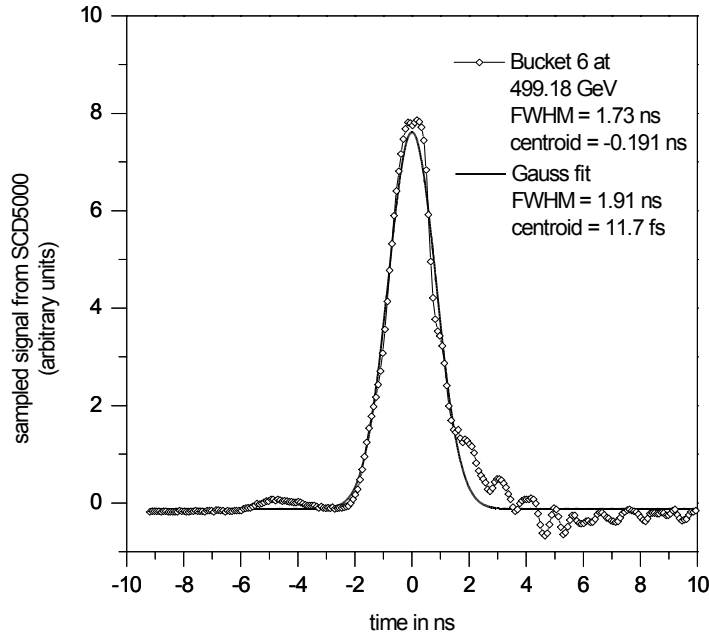


Figure 4.7: Bunch shape during synchrotron oscillations at 499 GeV.

If we measure at least two Fourier coefficients at different frequencies, we are able to calculate the bunch length:

Consider the monitor signal of a Gaussian bunch

$$A(t) = \frac{1}{\sqrt{2\pi}\sigma} e^{-\frac{1}{2}\frac{t^2}{\sigma^2}} \quad (4.9)$$

with the bunch length  $l_{FWHM} = \beta c \sqrt{\ln 4} \cdot 2\sigma$ . The Fourier component is

$$A(\omega) = \frac{1}{\sqrt{2\pi}} \int_{-\infty}^{\infty} dt e^{-i\omega t} A(t) = \frac{1}{\sqrt{2\pi}} e^{-\frac{1}{2}\sigma^2\omega^2}. \quad (4.10)$$

The bunch length (in the time domain) is obtained from the ratio  $\frac{A_1}{A_2} \equiv \frac{A(\omega_1)}{A(\omega_2)}$

$$l_{FWHM} = \beta 2 \sqrt{\ln 4} \sqrt{\frac{2}{\omega_2^2 - \omega_1^2}} \sqrt{\ln \frac{A_1}{A_2}}. \quad (4.11)$$

In HERA, the proton velocity is  $v \approx c$ , for simplification one can set  $\beta = \frac{v}{c}$  to 1.

From the phase measurement described in section 4.1, one obtains not only the bunch phase but also the amplitude of the 52 MHz Fourier coefficient of the longitudinal bunch signal. The natural choice for the second frequency is 208 MHz at HERA.

To measure the 208 MHz Fourier component, a band pass filter is used whose specifications are identical to those given in table 4.2, except for the central frequency of 208 MHz. In figure 4.8, the Bode diagrams of both band pass filters are shown.

The output signal of the filter is detected by a RF diode, smoothed by a low pass filter, and then digitized by an ADC. Figure 4.9 shows the setup.

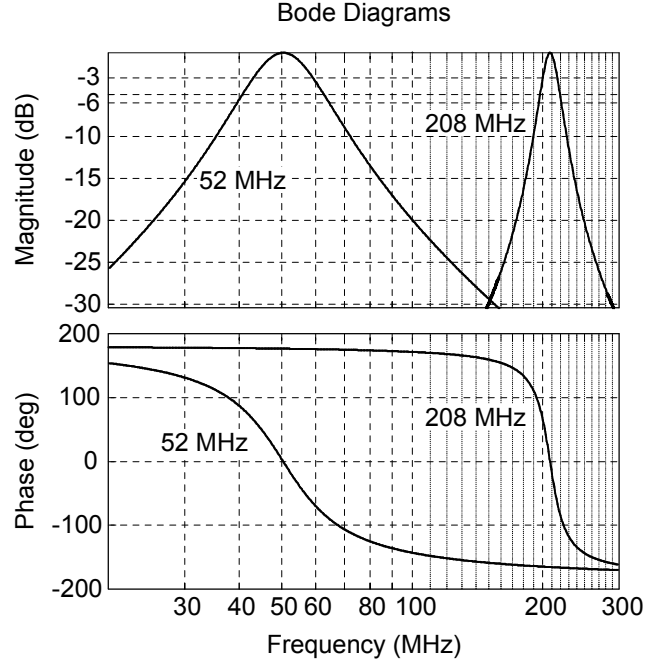


Figure 4.8: The Bode diagrams of the 52 MHz and 208 MHz band pass filters.

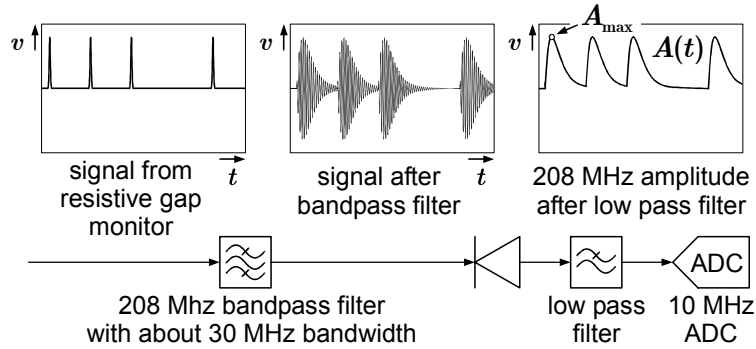


Figure 4.9: Principle of 208 MHz Fourier component measurement.

Taking into account the characteristic curve of the diode  $F_{\text{diode}}(A_{\text{max}}) \propto A_{\text{max}}^2$  and the different overall gains  $C_{52}$  and  $C_{208}$  in the 52 MHz and 208 MHz, the bunch length is given by

$$l_{FWHM} = 2.63175 \text{ ns} \sqrt{\ln \frac{A_{52}}{A_{208}}} \quad (4.12)$$

$$\frac{A_{52}}{A_{208}} = \frac{C_{52}}{C_{208}} \frac{A_{52, \text{meas}}}{A_{208, \text{meas}}}. \quad (4.13)$$

In practice, the ratio  $C_{52}/C_{208}$  is determined by comparing the results of this method with direct FWHM measurements using the TEK SCD5000 oscilloscope.

For long bunches the 208 MHz Fourier coefficient is small and the signal to noise ratio becomes unfavorable.

At a bunch length of 1.8 ns, the measurement error of the single shot measurement is less than 5.2 ps, see figure 4.10.

Figure 4.11 shows the correlation of the average bunch length during a time interval of 0.56 s, derived from the 52 MHz and 208 MHz Fourier components and the determination of



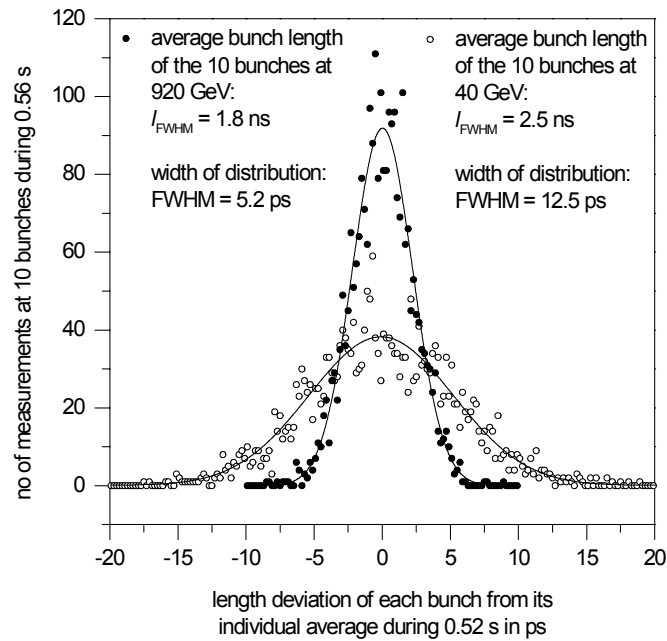


Figure 4.10: Length measurements of bunches with no observable oscillations.

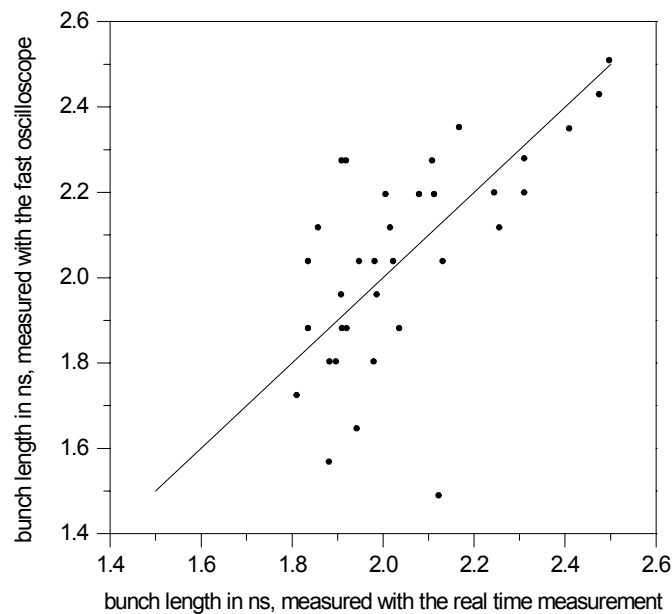


Figure 4.11: Correlation between real-time bunch length measurements and the FWHM determination with the fast oscilloscope.

the FWHM bunch length by analyzing the bunch shapes, recorded with the fast oscilloscope. A reasonable correlation is observed. The spread is mainly caused by multi-bunch oscillations during acceleration from 40 GeV to 920 GeV, where bunch length oscillations are always present. Therefore, the results from the fast oscilloscope depend on the particular measurement times. The FWHM determination from the fast oscilloscope only uses the center peak and disregards the population in the head and tail of the bunch, while the real time method takes account of these particles. The disadvantage of the real time method is, that particles spilling over into the neighboring 208 MHz RF buckets enhance the 208 MHz Fourier component and therefore reduce the calculated value of the bunch length (4.12).

The measurement of the bunch length, using two Fourier coefficients of the longitudinal charge distribution, was attempted independently by [36].

# 5 Measurement of Multi-Bunch Oscillations

The previous diagnostic systems in the HERA proton ring were neither able to observe multi-bunch oscillations nor single bunch oscillations. The new diagnostic system is able to observe multi-bunch oscillations in the time domain. Particular clock and trigger signals, controlling the ADCs, are used to obtain phase and length for each bunch, supplied by the real time measurement as described in chapter 4.

In this chapter, the electronics generating the clock and trigger signals is described. It is called the ‘timing’ system. The data acquisition and processing methods, which are used to display typical multi-bunch oscillations, measured during standard operation of the accelerator, are mentioned.

The calculation of the longitudinal emittance from the bunch length and the RF field strength shows whether multi-bunch oscillations and emittance dilution are simultaneous.

By means of a particular data presentation, changes in the synchrotron frequency and possible disturbing frequencies from technical components can be displayed over long time periods of the order of hours. Using this method, beam oscillation data, taken during a complete acceleration, can be viewed.

## 5.1 Timing

For the detection of multi-bunch oscillations, the clock and trigger signals must be delivered to the ADC boards in a special way.

The clock signals are rectangular signals with a frequency of 10.4 MHz, the bunch repetition frequency, deduced from the RF reference by counting RF waves with ECL gate arrays. The clock signals can be shifted under remote control in steps of 500 ps, to ensure that the ADCs sample the signal maxima.

Because of the low synchrotron frequency, 20 Hz to 60 Hz, it is not necessary to measure the bunch parameters on every turn. One synchrotron oscillation cycle would fill the ADC memory of 64 k (65536) samples per channel. However, the ADC boards used, are able to start several times a measurement cycle with an eligible number of samples, 256 samples for each cycle are selected. Measuring every 104th revolution has turned out to be a good compromise between time and frequency resolution. A trigger signal is provided every 104th revolution by dividing the beam revolution trigger (47.310 kHz) by 104. In this way, the phase and amplitude of an individual bunch are sampled with a frequency of 455 Hz, fast enough for the observation of bunch phase oscillations (20 Hz to 60 Hz) and length oscillations (40 Hz to 120 Hz). The total recording time is 0.56 s.

## 5.2 Data acquisition

Ground loops at the signal path which carry high frequency are suppressed by using DC blocks. After down-conversion the DC blocks cannot be used any more. Background noise is removed

by using sampled values from unoccupied bunch positions for an offset correction [37]. The dump gap consisting of 15 bunch positions was used for this purpose. Since the revolution frequency is 47.310 kHz, we suppress every unwanted signal modulation in the technical setup with a frequency lower than 47 kHz. Errors, caused by mains frequency (50 Hz) and ground loops, are suppressed rather well.

Several measurements were made with incomplete filling of the ring. To remove unoccupied bunch positions from the data, a minimum value of the 52 MHz Fourier component was required.

### 5.3 First experimental results

The bucket minima are not equidistant. This is caused by the beam loading transients and results

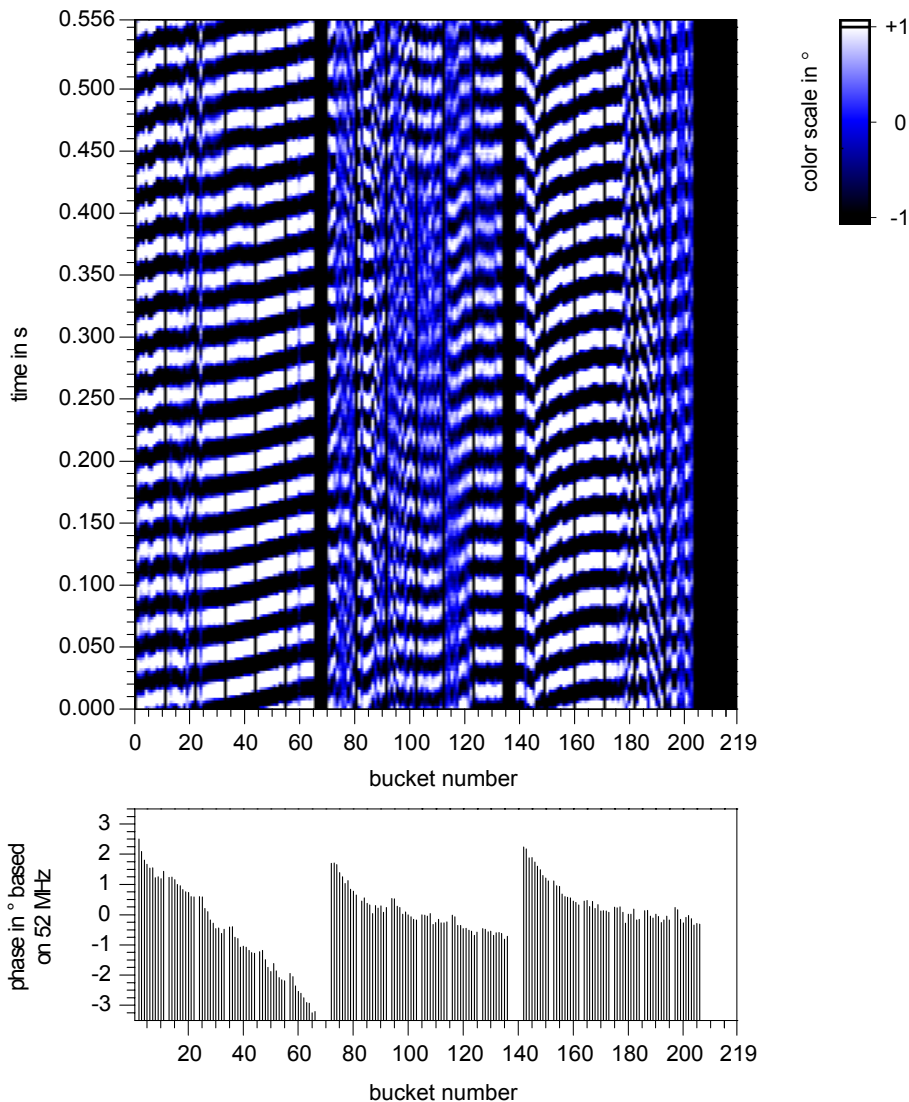


Figure 5.1: Lower graph: The average phase of each bunch during the measurement time of 0.56 s at 499 GeV. Upper graph: Multi-bunch phase oscillation. The axes are the bucket position and time. The phase deviation from the average bunch phase with respect to 52 MHz is given by the pixel color.

in a shift of the bunch phasing with respect to the RF reference signal from one bunch to the

next. Thus, the first step for data presentation is the calculation of the average phase of each bunch during the measurement time of 0.56 s. The data are shown in the lower graph in figure 5.1. A systematic variation of the phase is seen along the three trains of 60 bunches.

During multi-bunch oscillations, a single bunch carries out phase oscillations with a typical amplitude of  $2^\circ$  about its average value. For a graphical representation only the phase deviations of each bunch from its average phase, during the observation time, are presented, using a colored pixel plot. The two axes in the upper graph in figure 5.1 are the bucket position and time, while the phase deviation from the average is indicated by the pixel color<sup>1</sup>.

The presentation of bunch lengths is done in the same way, figure 5.2.

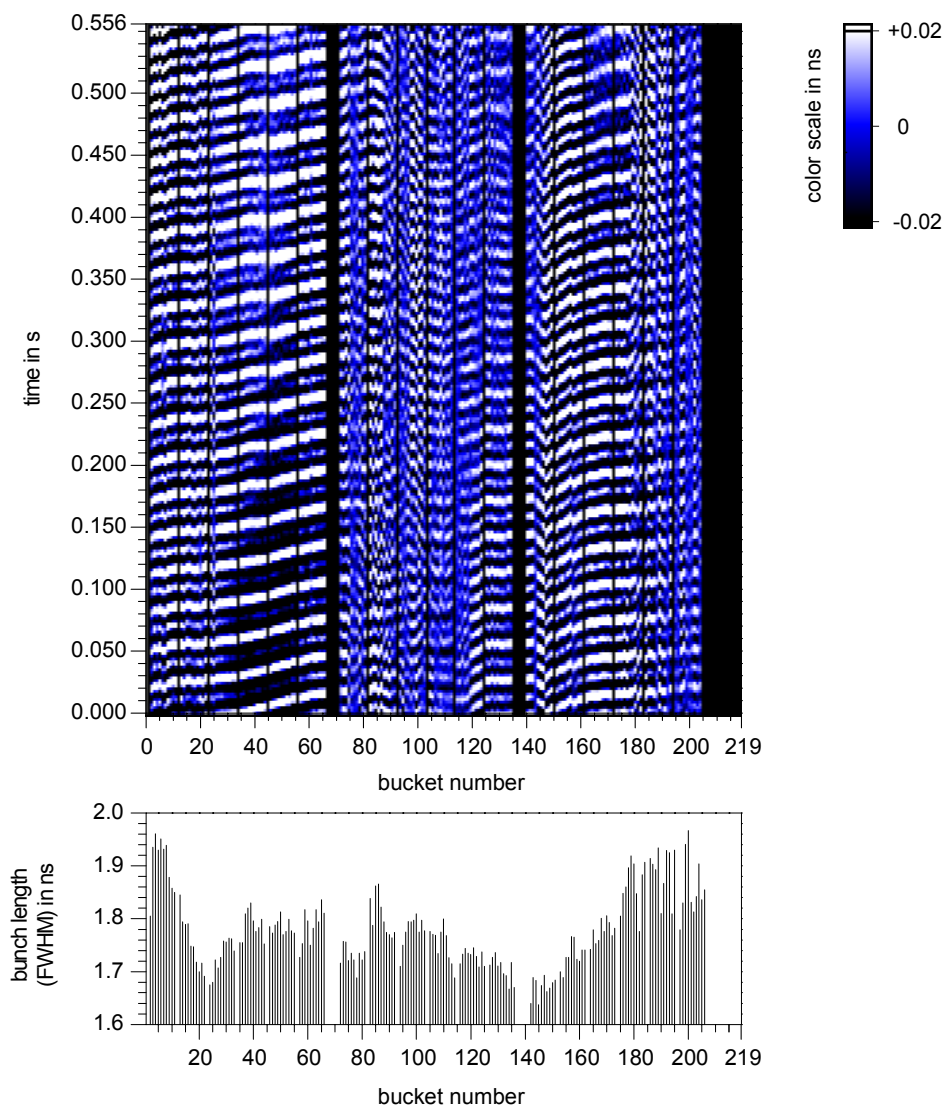


Figure 5.2: Lower graph: The average length of each bunch at 499 GeV during a measurement time of 0.56 s. Upper graph: Multi-bunch length oscillation.

With this diagnostic tool, one observes multi-bunch oscillations during every ramp of the proton storage ring. The most impressive oscillations are seen at energies above 300 GeV. Usually they persist up to 920 GeV. In the stored 920 GeV beam, the multi-bunch oscillations decay within half an hour. Then, the pattern shown in figure 5.3 is obtained, which is characteristic of a beam without measurable multi-bunch oscillations, remaining quiet for the rest of the

<sup>1</sup>Similar graphic representations have already been used at Fermilab.

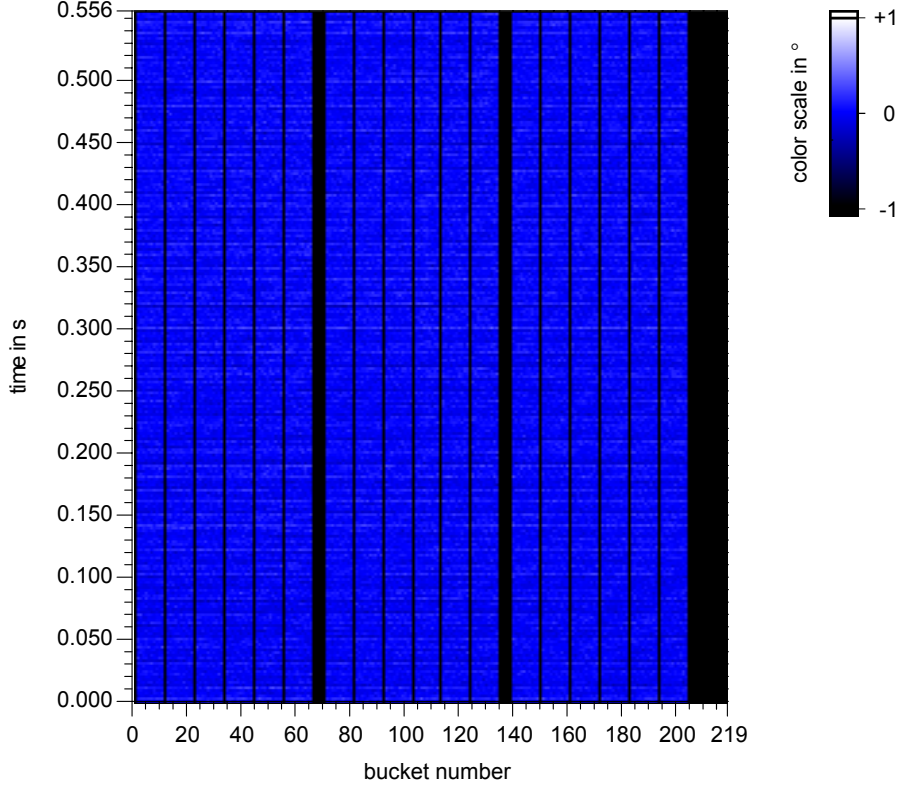


Figure 5.3: Quiet beam during a luminosity run at 920 GeV.

luminosity run.

## 5.4 Emittance blow up

In figure 5.4, the average length of all bunches is plotted versus time together with the energy. At the injection energy of 40 GeV, one observes discontinuities related to the injection of the second and third train from the preaccelerator PETRA. On the ramp from 40 GeV to 920 GeV, the optics is changed at various intermediate energies: 70 GeV, 150 GeV, 300 GeV and 675 GeV. The steps in the energy ramp are correlated with small changes in the average bunch length and with multi-bunch oscillations.

In a storage ring, the longitudinal emittance is theoretically conserved. A FWHM bunch length of 2.4 ns after injection should result in a FWHM bunch length of 0.6 ns at 920 GeV, compare section 1.3. This is due to the bunch compression by the steeper bucket potential of the 208 MHz cavities. With this in mind, we observe a bunch lengthening of 1 ns = 1.6 ns – 0.6 ns during acceleration. This bunch lengthening is indicated much better by calculating the longitudinal emittance. The longitudinal emittance,  $\epsilon_{FWHM}$  is given by [38]

$$\epsilon_{FWHM} = \pi \Delta t_{FWHM} \Delta E_{FWHM} \quad (5.1)$$

with [39]

$$\Delta t_{FWHM} = \frac{1}{2} l_{FWHM} = \frac{\Delta \phi_{FWHM}}{\omega_{RF}} \quad (5.2)$$

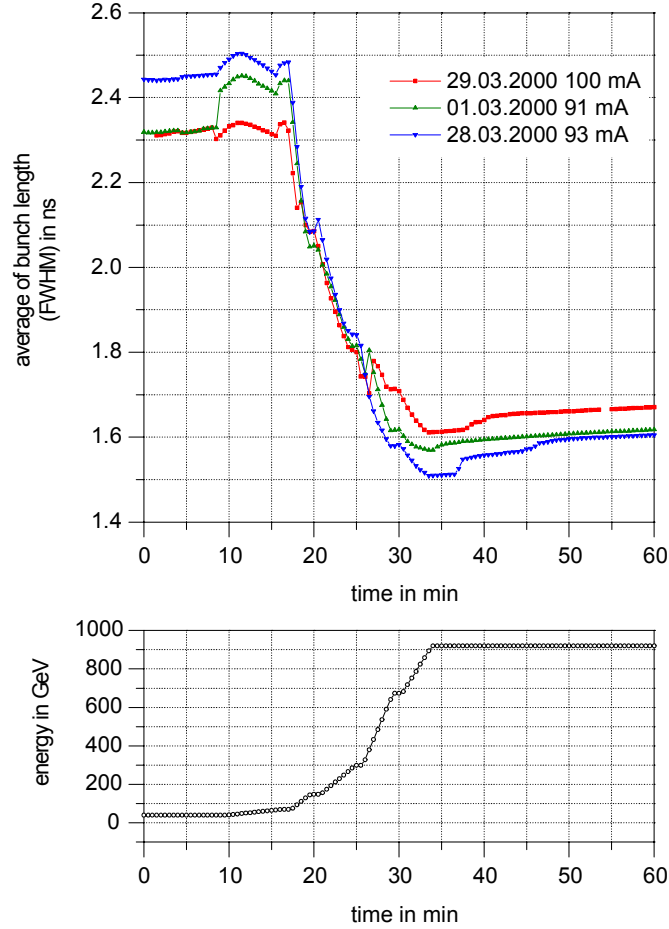


Figure 5.4: The change of the average bunch length during ramping from 40 GeV to 920 GeV, see text.

(note:  $[l_{FWHM}] = \text{s}$ ) and

$$\Delta E_{FWHM} = \beta \sqrt{\frac{2 E_s}{\eta}} \sqrt{U (\Delta \phi_{FWHM})}. \quad (5.3)$$

where  $\Delta E_{FWHM}$  is the energy deviation,  $\Delta t_{FWHM}$  the time deviation of a particle with phase deviation  $\Delta \phi_{FWHM}$ ,  $\beta = \frac{v}{c}$ ,  $E_s$  the energy of the synchronous particle and  $\eta = \frac{1}{\gamma_t^2} + \frac{1}{\gamma^2}$  the slip factor with  $\gamma_t = 27.74$  and  $\gamma = \frac{E_s}{E_0}$ .

The voltage of the double harmonic RF System

$$V = V_{52} \sin \phi + V_{208} \sin 4 \phi \quad (5.4)$$

creates the bucket potential

$$U(\Delta \phi) = \frac{e V_{52}}{2\pi h_{52}} (\sin \phi_s (\phi_s - \Delta \phi) + \cos \phi_s - \cos \Delta \phi) + \frac{e V_{208}}{2\pi 4 h_{52}} (\sin 4 \phi_s (4 \phi_s - 4 \Delta \phi) + \cos 4 \phi_s - \cos 4 \Delta \phi). \quad (5.5)$$

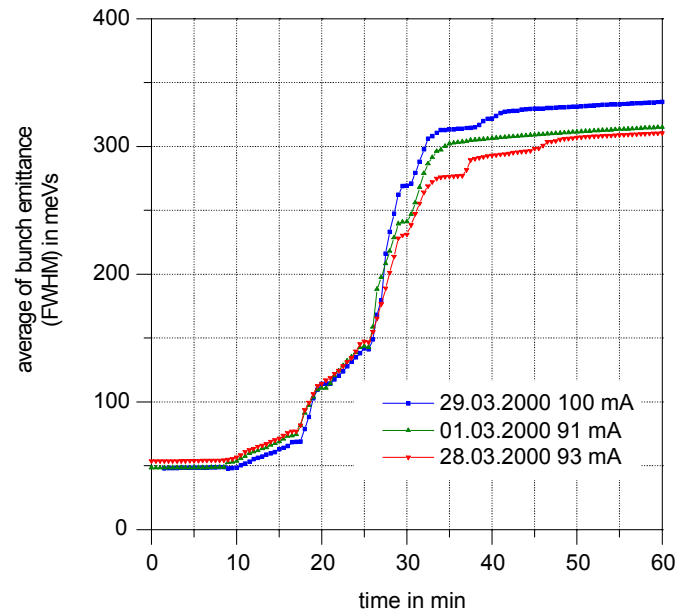


Figure 5.5: Evolution of the longitudinal emittance (FWHM) during the energy ramp from 40 GeV to 920 GeV.

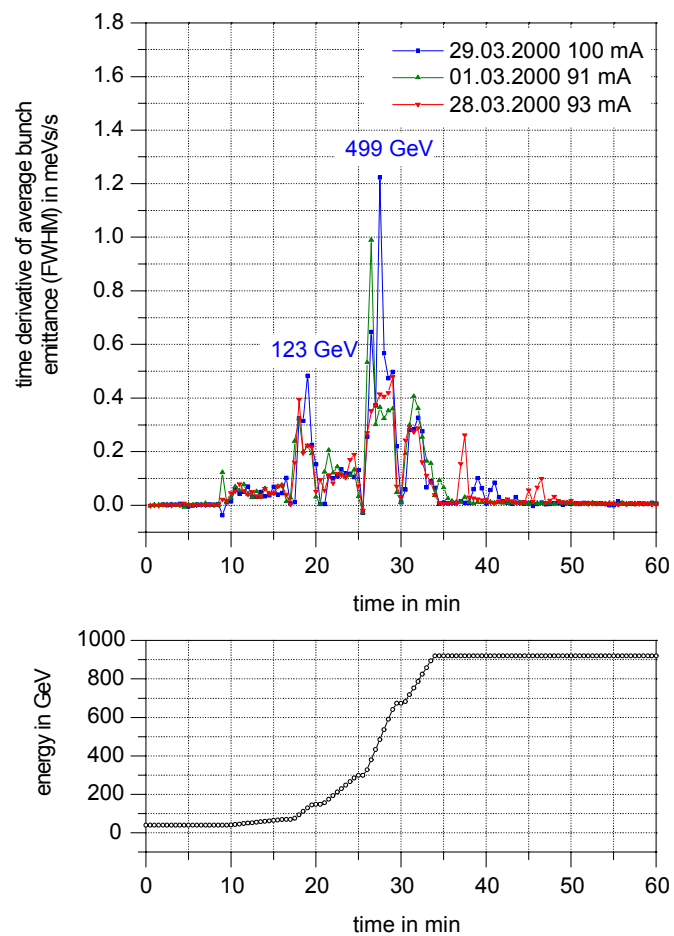


Figure 5.6: The time derivative of the longitudinal emittance as a measure of emittance blow up.



where  $\phi_s$  is the synchronous phase and  $\Delta\phi$  the phase deviation. To simplify the calculation of the longitudinal emittance, using (5.1), (5.2), (5.3) and (5.5), the synchronous phase  $\phi_s$  was set to zero. The time-evolution of the emittance is plotted in figure 5.5.

One observes a strong increase in the emittance from 40 GeV to 920 GeV. To provide more insight, the time derivative of the emittance is plotted in figure 5.6. It exhibits strong maxima at 123 GeV and 499 GeV. These are associated with multi-bunch oscillations of large amplitude. A close look at figure 5.6 reveals, that the stepwise increase in the emittances does not occur during the optics change at fixed energy, but rather in the acceleration periods in between optic changes.

This indicates, that an optics change at constant energy does not cause multi-bunch oscillations. Possible reasons for the excitation of oscillations during acceleration are chromaticity effects, errors in the tracking between the field in the superconducting bending magnets and the radio frequency, and the effects of passive impedances, or of active impedances such as the RF feed-back systems.

A modal analysis for coupled bunch oscillations is performed in chapter 7.

## 5.5 Synchrotron frequency during acceleration

After acceleration it is helpful, to review the beam oscillations which took place. The data presentation described in section 5.3 does not achieve this, because one has to look at all recorded multi-bunch pictures one after the other.

Neglecting the phase relations of the various multi-bunch modes, one can calculate the amplitude of the fast Fourier transformation (FFT) of each bunch oscillation. Adding the resulting values from all bunches and then dividing by the number of bunches yields an average spectrum of all bunch oscillations. Figure 5.7 shows two average spectra, one obtained at 299 GeV, and the second at 499 GeV.

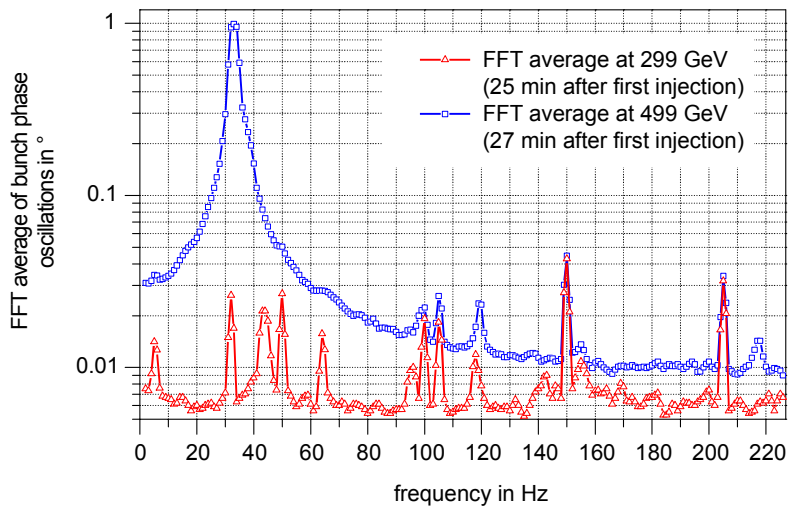


Figure 5.7: Bunch oscillation spectra, obtained by averaging the absolute values from the FFTs of all individual bunch oscillations, measured during 0.556 s.

These synchrotron oscillation spectra are not visible with a spectrum analyzer. One can measure the spectrum, available at the output of the narrow band phase measurements (described in section 2.2) with a spectrum analyzer. However, during multi-bunch oscillations,

many bunches oscillate against each other. The resulting phase signals compensate each other, and the information is lost. With the method described above, this problem is avoided.

In order to examine the time evolution of the spectra, one can plot them one after the other against time, encoding the amplitude values for the particular frequencies with a color scale. In this way we obtain a two dimensional colored pixel plot, as shown in figure 5.8.

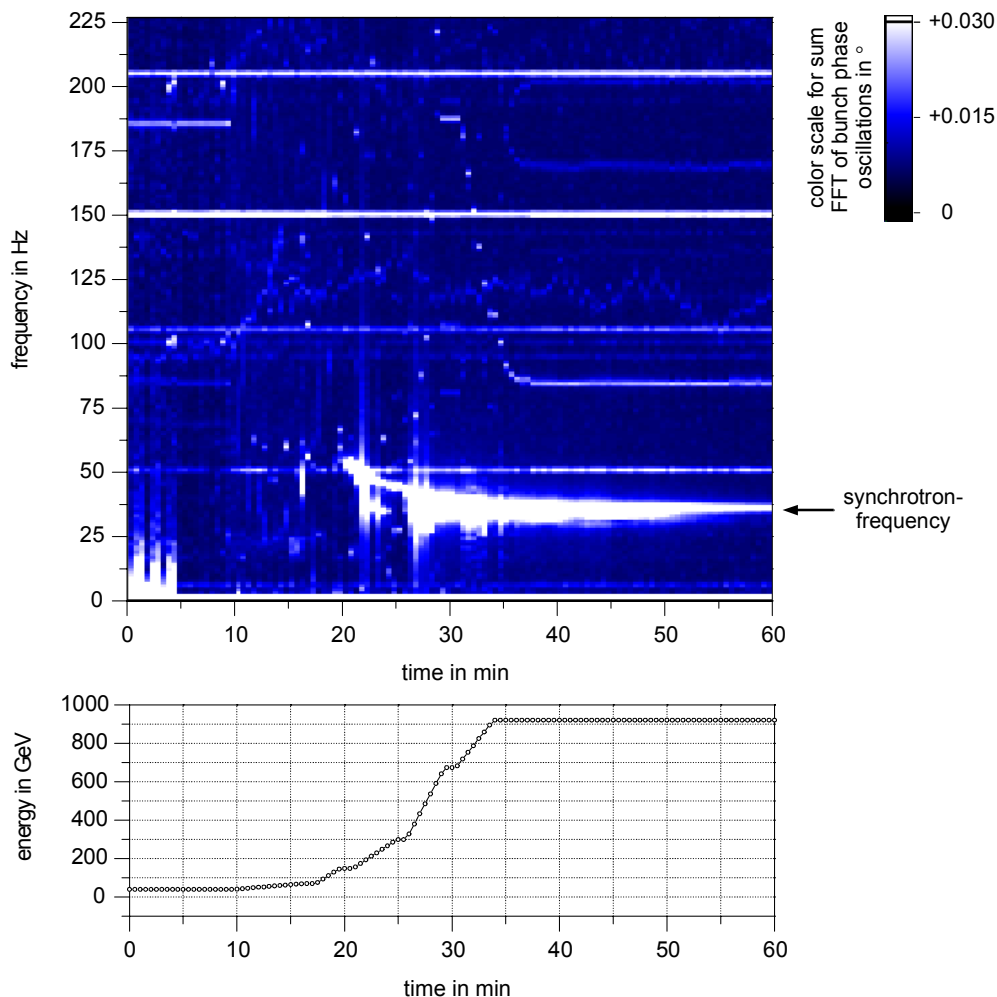


Figure 5.8: FFT average of all bunch phase oscillations during a ramp on 1. March 2000.

The recorded bunch length data can be dealt with in the same way, as shown in figure 5.9.

Interestingly, the synchrotron frequency is above the mains frequency of 50 Hz at energies from 70 GeV up to 200 GeV, without problems occurring as this frequency is crossed. At 499 GeV one observes the biggest FFT values, fitting well with the largest emittance dilution, previously discussed.

The pictures shown, provide more information. A lot of additional and in principle unwanted frequencies can be observed. Some of those frequencies are fixed, like the mains frequency of 50 Hz and its harmonics, such as 100 Hz and 150 Hz. Other frequencies show a clear dependence on the accelerator energy and the mode of operation.

One prominent frequency appeared near 185 Hz, as 600 GeV was passed, and decreased to about 85 Hz after 920 GeV was reached. When we first saw this behavior, we assumed the synchronization loop of the electron and proton storage ring was the source. When the data were taken, the RF frequency of the proton storage ring was still locked to the RF frequency of the electron storage ring. This motivated the change of the synchronization philosophy. Since

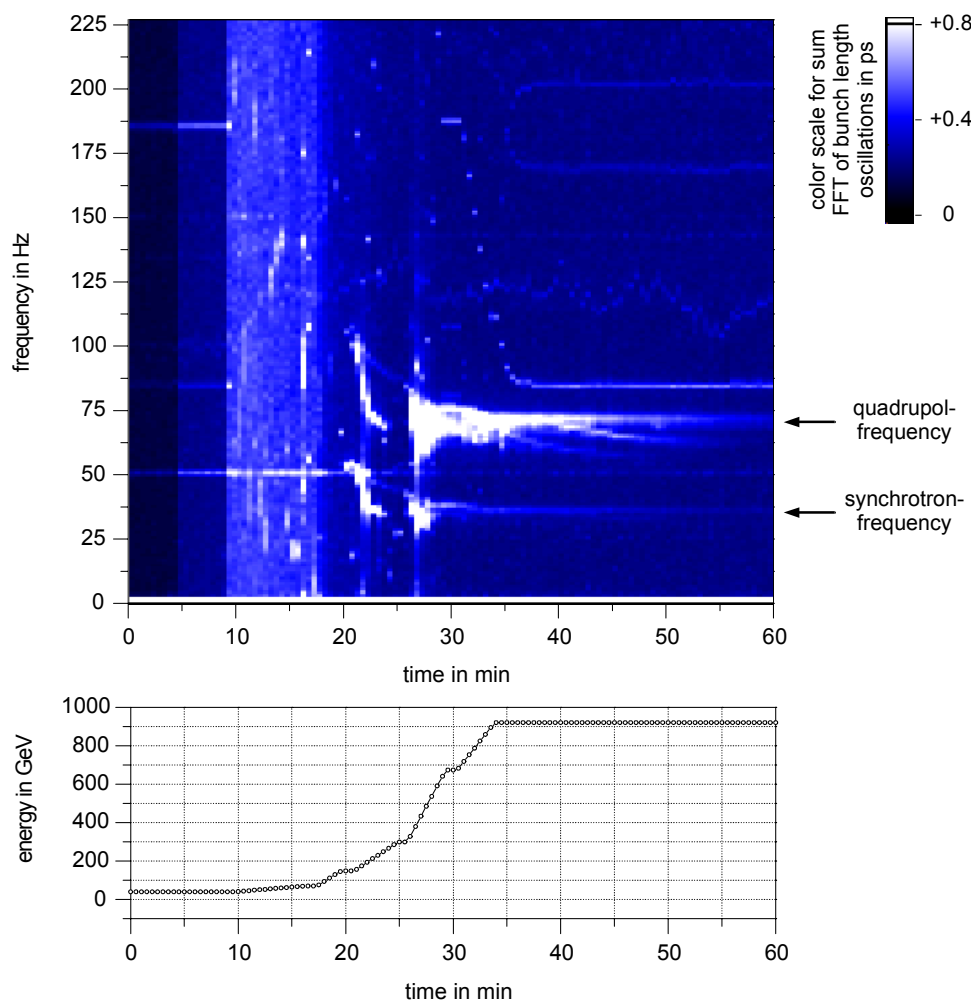


Figure 5.9: FFT average of all bunch length oscillations during a ramp on 1. March 2000.

Spring 2000, the electron storage ring is locked to the proton storage ring, as described in section 3.1, in order to influence the proton frequency generation as little as possible. Unfortunately, one can still observe this frequency and the longitudinal emittance blow-up was not reduced by this change.

The data presentation, discussed in this section, will be useful in the search for possible technical defects, causing the emittance dilution.



## 6 Fast Cavity Field Diagnostic

Bunches passing the RF cavities in a storage ring, are not only focussed longitudinally by the RF voltage, they also deposit RF voltage in the cavities themselves. This beam-loading leads to an unwanted change of the RF phase in the cavities for subsequent bunches. Several methods are suitable to reduce this effect, such as detuning the cavities and the use of RF fast-feedback loops [23].

If one considers RF fast-feedback loops in the frequency domain, then they reduce the cavity impedance seen by the beam. This is only possible down to a certain threshold, see section 12.3. For a further decrease of the effective cavity impedance, or the beam loading transients, a RF feedforward is indispensable. For checking the functioning and automated adjustment of such a system, the transient cavity fields have to be measured. During acceleration from low to high energy the RF transients change their shape due to the transition of the bucket potential from 52 MHz to 208 MHz. A RF feedforward has to consider this automatically.

In the HERA proton storage ring, the time constants of the fast-feedback loops and the beam loading of each single proton bunch determine the transient behavior of the cavity voltages. In order to learn more about this time behavior, it is necessary to measure and visualize the transients in the time domain.

In this chapter, the main points of beam loading are discussed. Then, the measurement principle and the timing are explained, followed by experimental results.

Finally, the last section deals with the measurement of the phase between both RF reference frequencies in the HERA hall west and the observed phase drifts.

### 6.1 Generator field and transient

Figure 6.1 shows the cavity voltage, compound of the generator voltage and the transient voltage which is deposited by a passing bunch: Without beam, the cavity voltage is generated by the final stage amplifier

$$v_{gen}(t) = \text{Im} [\mathbf{v}_{gen} e^{i\omega_{RF} t}] = V_{gen} \sin[i\omega_{RF} t] \quad (6.1)$$

with the phasor<sup>1</sup>

$$\mathbf{v}_{gen} = V_{gen}. \quad (6.2)$$

In the following, we denote this voltage as the generator voltage.

A bunch passing the cavity at  $t_{pass} = 1/4\pi\omega_{RF}$  induces the voltage  $V_{bunch}$  oscillating with the cavity frequency  $\omega_{cav}$  and decaying with the cavity time constant  $\tau_{cav}$

$$\begin{aligned} v_{bunch}(t) &= \text{Im} [\mathbf{v}_{bunch}(t) e^{i\omega_{cav} t}] \\ &= V_{bunch} \Theta(t - t_{pass}) e^{-(t-t_{pass})/\tau_{cav}} \text{Im} \left[ e^{i(\omega_{cav} t - \frac{\pi}{2})} \right] \\ &= V_{bunch} \Theta(t - t_{pass}) e^{-(t-t_{pass})/\tau_{cav}} \text{Im} \left[ e^{i(\omega_{RF} t + \Delta\omega t - \frac{\pi}{2})} \right]. \end{aligned} \quad (6.3)$$

---

<sup>1</sup>For the phasor representations of a RF wave, see appendix A.1.1.

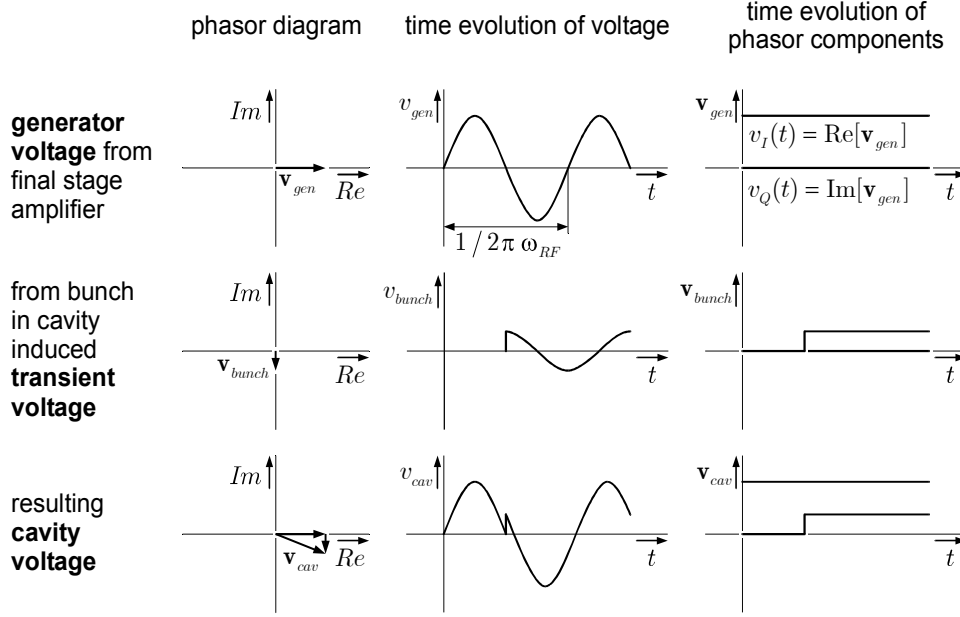


Figure 6.1: Beam-loading in a storage ring. In the first column the voltages  $v(t)$  are presented by their phasors  $\mathbf{v}(t)$ , the second column shows the time evolution of the voltages, and the third shows the time evolution of the components  $v_I(t) = \text{Re}[\mathbf{v}(t)]$  and  $v_Q(t) = \text{Im}[\mathbf{v}(t)]$  of the phasors, measured e.g. with an IQ demodulator.

Here, the difference frequency determined by the cavity tuning is  $\Delta\omega = \omega_{cav} - \omega_{RF}$ , and the phasor of the beam loading voltage becomes

$$\mathbf{v}_{bunch}(t) = -i \Theta(t - t_{pass}) V_{bunch} e^{i\Delta\omega t} e^{-(t-t_{pass})/\tau_{cav}}. \quad (6.4)$$

We used the Heavyside step function  $\Theta$ , a definition is given in appendix A.1.2. The voltage in the cavity is the phasor addition of these two voltages

$$\mathbf{v}_{cav}(t) = \mathbf{v}_{gen} + \mathbf{v}_{bunch}(t) = V_{gen} - i \Theta(t - t_{pass}) V_{bunch} e^{i\Delta\omega t} e^{-(t-t_{pass})/\tau_{cav}}. \quad (6.5)$$

A fast feedback loop leads to a fast reduction of the beam-loading voltage, in this case one has to replace the cavity time constant  $\tau_{cav}$  by the fast-feedback time constant  $\tau_{ff}$ , neglecting the loop delay time. In normal operation, with 180 proton bunches circulating in HERA, the phasor of the cavity voltage is given by  $\mathbf{v}_{cav}(t) = \mathbf{v}_{gen} + \mathbf{v}_{trans}(t)$  with the phasor of the transient voltage

$$\mathbf{v}_{trans}(t) = \sum_{\text{all revolutions}} \sum_{\text{all bunches}} \mathbf{v}_{bunch}(t). \quad (6.6)$$

Since the voltage  $v_{trans}(t) = \text{Im}[\mathbf{v}_{trans}(t) e^{i\omega_{RF}t}]$  is caused by the transient beam loading, it will also be denoted with beam loading voltage.

## 6.2 Measurement principle

The measurement device has to cover the full range of the generator voltage. At a 208 MHz cavity, the design value of the maximum generator voltage is 800 kV. Using a 14 bit ADC, we can divide the measuring range of  $\pm 800$  kV into  $2^{14}$  intervals and get a resolution of 100 V. A

small value for the DC-current of a single proton bunch<sup>2</sup> in HERA is 0.15 mA. This leads to a beam loading voltage of  $V_{bunch} \approx 2 R_s I_{bunch} = 2400$  V. If we measure the cavity voltage directly with ADCs, we get a resolution of 4.2%. Noise leads to a further reduction of the resolution. Any finer details of the beam loading voltage are not measurable in this way. Hence, a more suitable method to measure the beam loading voltage is needed.

At the injection energy of 40 GeV, the RF buckets are provided by the 52 MHz cavities, the vector sum of the 208 MHz cavities is zero. During ramping to 920 GeV, the 208 MHz cavities take over and the voltage of the 52 MHz cavities is reduced. This means that the generator voltage is changed in all cavities during acceleration on a time scale of minutes or slower. In contrast, the transient voltage (6.6) is determined by the bunch length and bunch current, the cavity tuning, the fast-feedback time constant and the revolution frequency. The transient voltage is independent of the generator voltage. In HERA, the transient voltage typically shows the same behavior on each revolution. Every bunch contributes to the transient voltage. This means, in Fourier space the phasor of the transient voltage can be expressed by harmonics with frequencies between 47 kHz and 10.4 MHz. This enables an analogue separation of generator field from the transient after an IQ demodulation of the cavity field by duplexing filters. Separate pre-amplifiers permit an optimum use of the ADC resolution. Four ADC channels are needed for each cavity. It is an advantage that it is not necessary to match the signal cable length, for separation of the signal component, in phase with the LO wave (I), from that out of phase (Q). Instead, the ADC channels contain a mixture. Multiplication with a rotation matrix allows separation of the phasor components.

Figure 6.2 shows the technical setup of the fast cavity field diagnostic. A duplexing filter consists of a low pass (LP) filter and a high pass (HP) filter with a common input. The upper 3 dB frequency of the low pass filter is equal to the lower 3 dB frequency of the high pass filter. The duplexing filters used have to fulfill the following conditions:

1. The low pass band transmits DC and slowly varying signals of the components of the generator voltage phasor.
2. The high pass band transmits only the rapidly varying signals of the mixed components of the transient voltage phasor. This means, that the lower frequency of the high pass band has to be sufficiently smaller than the revolution frequency  $f_{rev} \approx 47$  kHz and the upper frequency has to be well above the bunch repetition frequency  $f_{rep} \approx 10.4$  MHz. The frequency response has to be smooth.

Simulations based on the transient shapes, measured with a digital oscilloscope, show that Butterworth filters of first order fulfill these criteria. The minimum upper frequency should be  $3 f_{rep} \approx 30$  MHz and the separating 3 dB point should be smaller than  $f_{rev} / 25 \approx 1.9$  kHz. It is technically demanding to realize duplexing filters with a smooth frequency response at the high pass, for a frequency range covering four orders of magnitude. The duplexer specification is given in table 6.1.

The required 12 filters were custom-designed by a company, according to these specifications. The production ensured a matched behavior of all filters.

Figure 6.3 shows some typical transients, taken from the high pass outputs of the duplexing filters. Each picture represents the average of 256 successive transients acquired over 0.56 s. The gaps between subsequent batches of ten bunches, and the larger ones between the bunch trains of 60 bunches leave noticeable steps in the beam loading voltage. The timing of the ADCs was adjusted to the bunch crossings at the resistive gap monitor, located about 300 m

<sup>2</sup>The DC-current of a single bunch is the time integral over one revolution of the bunch charge density per unit of time.

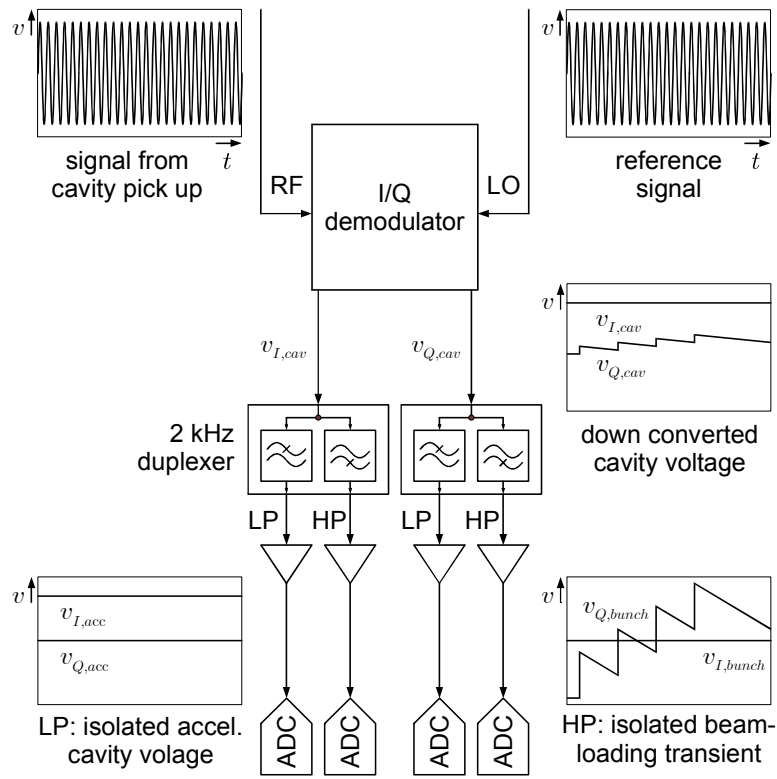


Figure 6.2: Technical setup of the fast cavity field diagnostic. Duplexing filters enable a separate pre-amplification for the measurement of accelerating voltage and the beam-loading transient. Some technical details have been omitted, such as low pass filters and attenuators for suppression of signal reflections.

defined frequency range:	DC to 30 MHz
separating 3 dB point:	$(1.9 \pm 0.1)$ kHz
input frequency:	DC to 60 MHz
pass band ripple:	$< \pm 0.2$ dB
impedance:	50 $\Omega$ at in- and output
insertion loss:	$< 1$ dB
dynamic range:	$< -75$ dBm to $> 5$ dBm
operating temperature:	$-10$ $^{\circ}\text{C}$ to $85$ $^{\circ}\text{C}$
connectors:	SMA

Table 6.1: Properties of duplexing filters.



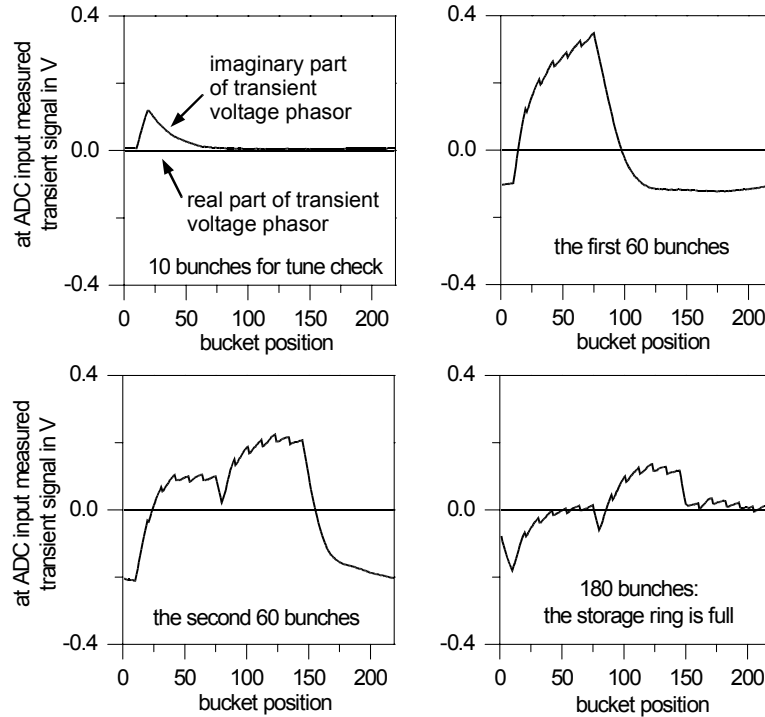


Figure 6.3: Average beam-loading transients, taken at the 208 MHz cavity No. 2, during a standard proton filling procedure of HERA.

downstream of the RF cavities. Therefore, the transients are shifted by 10 bucket positions. If the transients are sampled at a rate of 100 MHz, instead of 10.4 MHz, an additional sawtooth structure, caused by the single bunches, is visible [41].

To estimate the accuracy, transients are recorded for a time interval of 0.56 s, taking bunches without observable synchrotron oscillations. The fluctuations of the individual values around the average represent an upper limit of the measurement error, because the values contain also noise of the beam. Figure 6.4 shows such a measurement of the transient of 120 bunches. The FWHM deviation of the imaginary part of the phasor is approximately double the real part. Possible reasons are a different noise behavior of the preamplifiers in front of the ADCs or more phase noise than amplitude noise of the proton beam. The measurement accuracy is given by  $\sqrt{\text{FWHM}_I^2 + \text{FWHM}_Q^2} / (V_{trans,max} - V_{trans,min}) = 2.6\%$ .

A resolution for the measurement of the generator voltage can be estimated by recording the duplexer low pass signals over a period of time, for example 90 ms. Figure 6.5 shows such a measurement. The dominant error signal is a 150 Hz modulation. At the moment, the source is not known. The steps in the signals shown, are caused by a restriction of the digits in the data acquisition software and not by the ADCs. In future, we plan to use more digits. For the relative measurement accuracy we get  $\Delta V_{gen} / V_{gen} = 0.6\%$ . The absolute calibration is a complex task. One has to determine, among other things, the cavity quality factor, the coupling between the final stage amplifier and the cavity, the coupling of the pick up antenna and thermal losses by measuring the cooling water temperature. Another method is to measure the beam small amplitude synchrotron frequency for given voltage settings on the cavities. With this data, one can determine calibration values. Such calibration measurements were not yet performed.

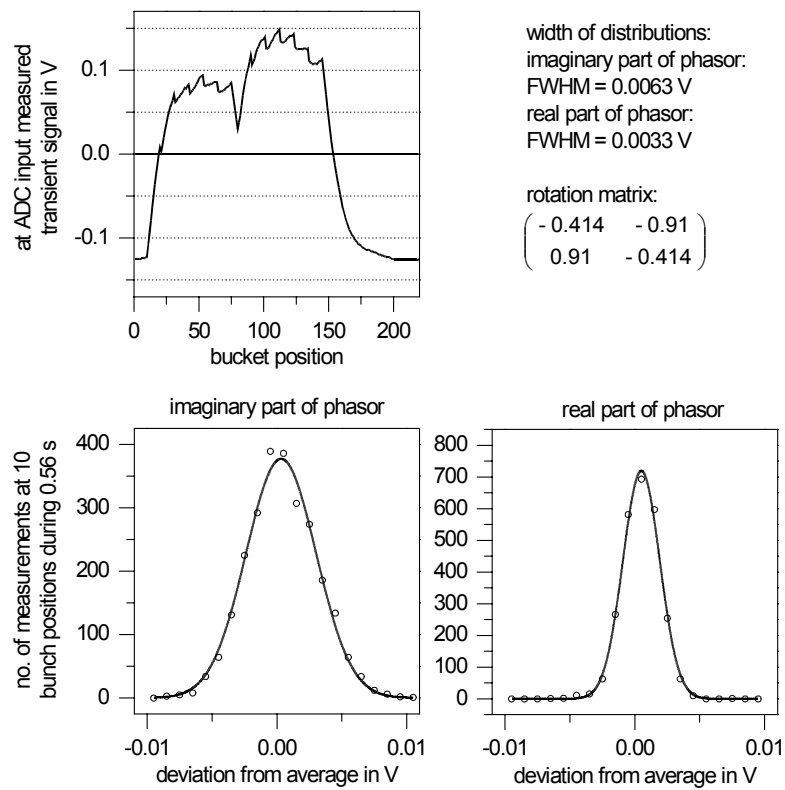


Figure 6.4: Measurement of beam loading transients in 208 MHz cavity no. 2 for an accuracy estimation.

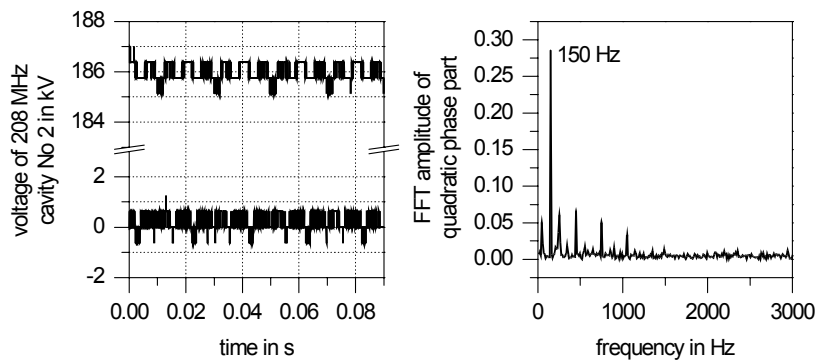


Figure 6.5: Measurement of the accelerating voltage of 208 MHz cavity no. 2 for a resolution estimation.

Throughout this thesis, where specific voltages are quoted, they have been acquired from the cavity phase and amplitude controls, described in section 3.2.

### 6.3 Timing and data acquisition

A proton bunch circulating in HERA samples the cavity voltage with the revolution frequency. The time constant of the longitudinal beam dynamic is given by the cycle time of synchrotron oscillations. To examine the connection between the cavity transients and the longitudinal bunch dynamics, it is natural to sample first the transients at fixed bunch positions. This may be done, using the sampling scheme already described for the measurement of multi-bunch oscillations, see chapter 5.1. Modulations of the RF, seen by the single bunches, are sampled with a frequency of 455 Hz.

Since the lower cut off frequency of the duplexer high-pass band is 2 kHz, signal modulation at the mains frequency of 50 Hz does not appear on the transient voltage measurement. Several components of the HERA RF system use intermediate frequencies above 2 kHz. There is no simple way to eliminate the modulation they cause.

By using DC blocks in front of the down conversion of the RF signals with the IQ demodulator, modulation at the mains frequency is reduced in the generator voltage measurement. A further reduction of this modulation by software is not simple.

The rotation matrix for the separation of the real and imaginary parts of the phasor

$$\mathbf{v}_{gen} = \mathbf{M}_{rot} \mathbf{v}_{gen,meas} \quad (6.7)$$

is obtained from measured values  $v_{I,gen,meas}$  and  $v_{Q,gen,meas}$  without beam by

$$\mathbf{M}_{rot} = \frac{1}{\sqrt{v_{I,gen,meas}^2 + v_{Q,gen,meas}^2}} \begin{pmatrix} v_{I,gen,meas} & v_{Q,gen,meas} \\ -v_{Q,gen,meas} & v_{I,gen,meas} \end{pmatrix}. \quad (6.8)$$

This matrix is also used for separating the real and imaginary parts of the transient voltage phasor  $\mathbf{v}_{I,trans,meas}$ .

### 6.4 Transient modulations with the synchrotron frequency

The appearance of the beam loading transients in HERA is similar for each revolution, except during the injection process. During a revolution, the development depends on the bunch filling scheme as shown in figure 6.3. This means that the buckets are determined by both, the generator voltage and the individual mean value of the beam loading voltage at the bucket position. This leads to unequal separation of the bucket centers, as already mentioned in section 5.3. A bunch performing synchrotron oscillations causes oscillating beam loading voltage around the mean value. This voltage oscillation can be presented by plotting the deviation at each bucket position from its mean value in a colored pixel plot, like the bunch phase and bunch length deviations in section 5.3.

Figure 6.6 shows a typical transient modulation during acceleration. One can see modulation at the synchrotron frequency. During the bunch passage, the phasor of the induced transient voltage is purely imaginary, see figure 6.1. Therefore, one would expect to measure bigger oscillations on the imaginary part. Figure 6.6 shows the opposite. A possible reason could be the detuning  $\Delta\omega$  of the cavity together with a shift of the sample times against the bunch crossing times. Another reason could be a technical failure in a control loop.

For the sake of completeness, figure 6.7 shows a modulation picture of the transient at a beam without observable synchrotron oscillations.

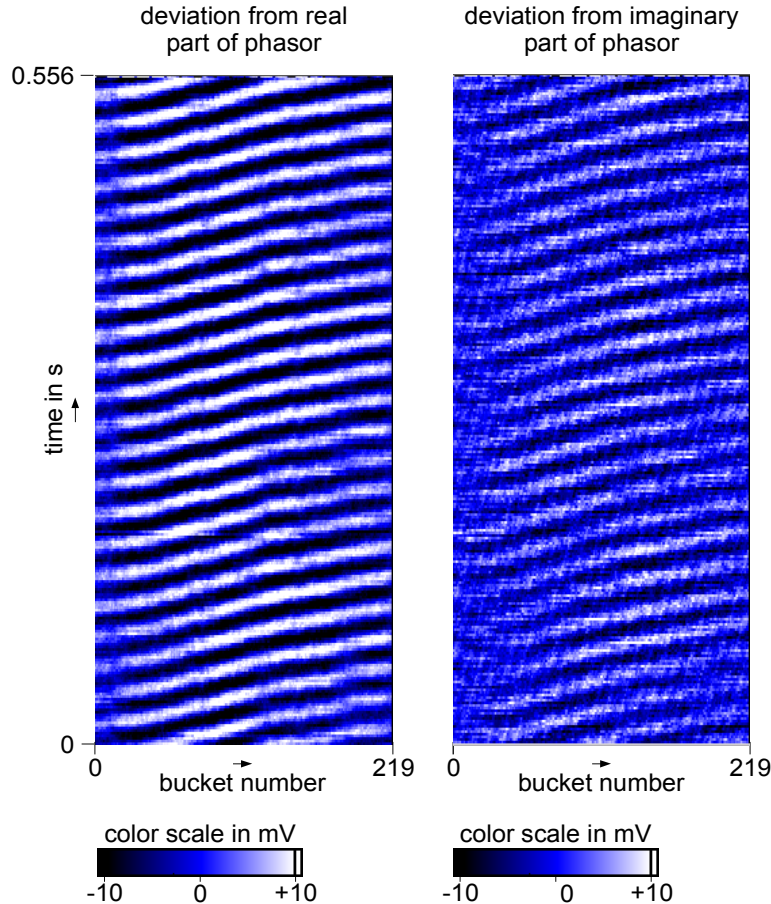


Figure 6.6: Transient modulation of 208 MHz cavity no. 2 during acceleration. The picture was taken at 416 GeV. Note: the color scale refers to the ADC input voltage.

## 6.5 Phase drift between the references of the double harmonic RF system

The fast diagnostic of a single cavity is done with an IQ demodulator. For this purpose a reference signal is needed. Since a double harmonic RF system is installed in the HERA proton storage ring, we deal with two different reference signals. For the determination of the phasing between the 52 MHz cavities and the 208 MHz cavities, we have to measure the phasing of the two reference signals, used.

Figure 6.8 shows how the relative phase between both used RF reference signals is measured in the HERA hall west. A frequency doubler provides not only the double frequency, but also higher harmonics. Using a band pass filter, we select the 208 MHz frequency and detect it by an IQ demodulator with the 208 MHz reference as local oscillator signal. Calculating the inverse tangent of the sampled values supplies the phasing between both RF reference signals. One can also deduce a correction matrix, needed for the determination of the phasing between the 208 MHz and 52 MHz cavities.

Figure 6.9 shows phasing, measured with an early hardware version, over a time period of one week. The large phase jumps appeared when the energy of the storage ring was reduced from 920 GeV to 40 GeV, to inject a new proton beam. The frequencies are ramped with the energy. No phase error compensation was installed at that time. Since the HERA hall west is more than 600 m away from the phase locked loop near the control room, both reference

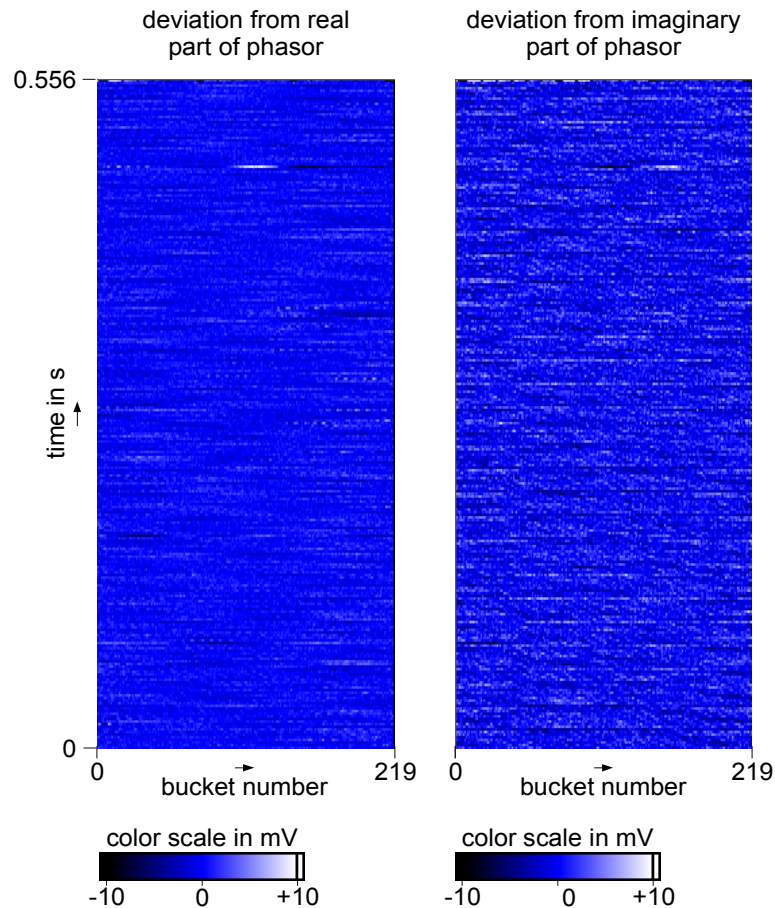


Figure 6.7: Without observable synchrotron oscillations one observes no transient modulations.

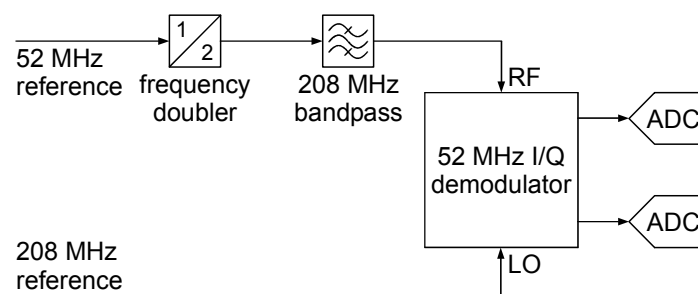


Figure 6.8: Measurement of the phasing between both RF reference signals in the HERA hall west.

frequencies suffer a phase change due to the length of the cables. From time to time this caused beam loss during acceleration. After this first observations, more detailed examinations by J. Baran and the installation of a control by R. Wagner removed this problem. This presented a first success of measures within the framework of reducing the proton bunch length. In fact, the bunch length was not influenced, but the reliability of the storage ring was increased, and with that the integrated luminosity.

In addition, one can observe temperature effects on the phasing. Between night and day a phase change of  $5^\circ$  is observable. The biggest change always appeared in the afternoons, caused by cable lengthening due to the heating by solar radiation. Until now, this effect has not been

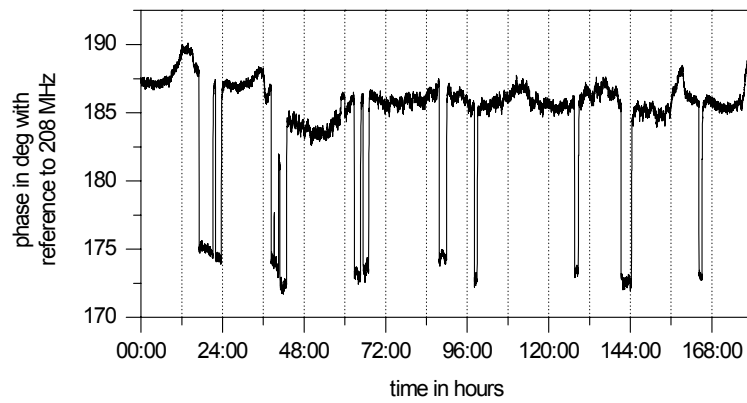


Figure 6.9: Phasing between the two reference frequencies 208 MHz and 52 MHz in the HERA hall west. The data was taken in August 1999.

compensated.

## **Part III**

# **Examination of the Longitudinal Stability**





# 7 Modal Analysis of Coupled bunch Oscillations

Bunches, passing an impedance in a storage ring, leave electromagnetic fields behind. These fields influence subsequent bunches. Depending on the strength and frequency response of the impedance, this mechanism leads to a coupling of bunch oscillations. This is only expected when the synchrotron frequencies of the individual bunches have similar values [18].

A coupling between the oscillations of individual bunches leads to common oscillations of all bunches together. Any multi-bunch oscillation pattern can be developed in a series of eigen-oscillations, called modes. If the multi-bunch oscillation pattern is assembled by only a few modes, coupling is present. According to the properties of the coupling impedance, some modes are unstable. A growing oscillation amplitude, together with an emittance blow up, is evidence for a coupled bunch instability. In the case of non coupled bunches, the multi-bunch oscillation is made up of a random distribution of all modes.

In this chapter, we test the recorded multi-bunch oscillations for coupled bunch oscillations exemplary at the recorded data of an arbitrary chosen ramp. Therefore, an overview on the well-known results of coupled bunch oscillation theory is given, following Sacherer [18].

One possibility to analyze multi-bunch oscillation patterns is to expand them in a series of all modes. The result is a steady state modal spectrum. We will discuss the modes appearing together with the emittance blow up, the coherent frequency spread and the frequency shift.

An other possibility to look at the recorded data is to analyze the phase relation between the bunches at a fixed time. Since every mode has its characteristic phase advance, we get a mode spectrum at a given time. Performing this for a complete data record, reveals the transient behavior of the modes. This method is ambiguous with respect to the mode numbers but permits examinations of the time behavior. Growing unstable modes are in principle directly visible.

## 7.1 On coupled bunch oscillations

Any multi-bunch oscillation of  $M$  equally spaced bunches can be developed in a series of  $M$  modes [42]

$$x_{j,m}(t) = \sum_{l=0}^{M-1} \hat{c}_l \eta_{l,j} e^{i\omega_{m,l} t}. \quad (7.1)$$

$x_{j,m} = x_{j,m}(t)$  is the oscillation of the bunch no.  $j$ . The index  $m$  denotes the single bunch oscillation type. For  $m = 1$  the bunch performs oscillations of its center called phase oscillations, dipole oscillations or rigid-bunch oscillations,  $m = 2$  stands for bunch length or quadrupole oscillations and so forth. In (7.1),  $\hat{c}_l$  is the amplitude of the coupled bunch mode  $l$ ,  $\eta_l$  is the mode vector describing the oscillation amplitude and phase of each bunch and  $\omega_{m,l}$  is the oscillation frequency.

The mode vectors are independent of the particular coupling mechanism. They are always the same because the eigenvalue problem has always the same symmetry, namely the rotation

symmetry resulting in cyclic matrices. The normalized vector of the mode  $l$  is given by

$$\boldsymbol{\eta}_l = \frac{1}{\sqrt{M}} \begin{pmatrix} 1 \\ e^{-\frac{2\pi i l}{M}} \\ e^{-2\left(\frac{2\pi i l}{M}\right)} \\ e^{-3\left(\frac{2\pi i l}{M}\right)} \\ \vdots \\ e^{-(M-1)\left(\frac{2\pi i l}{M}\right)} \end{pmatrix}, \quad l = 0, 1, 2, \dots, M-1. \quad (7.2)$$

The distinctive feature of these vectors is that the sum of all phase advances between adjacent bunches is  $l$  times  $2\pi$ .

Non coupled bunches oscillate with the synchrotron frequencies  $\omega_{s,j}$ , determined by the individual bucket potentials. In the case of identical bucket potentials, all bunches oscillate with the same frequency  $\omega_{s,j} = \omega_s$ . Coupling between bunch oscillations leads to a change of the oscillation frequency, called ‘coherent’ frequency shift  $\Delta\omega_{m,l}$ . This frequency shift is different for the individual modes. Hence, the mode frequency is composed out of  $m$  times the synchrotron frequency plus the coherent frequency shifts  $\Delta\omega_{m,l}$

$$\omega_{m,l} = m\omega_s + \Delta\omega_{m,l} \quad \text{with } \Delta\omega_{m,l} \in \mathbb{C}. \quad (7.3)$$

In accelerator physics the expressions ‘coherent’ and ‘incoherent’ are usually used in the following way: Effects regarding bunch shapes are called ‘coherent’ whereas effects regarding the individual particles within a bunch are called ‘incoherent’. A ‘coherent frequency shift’ is a change of the synchrotron frequency of bunches.

For  $\text{Im}[\Delta\omega_{m,l}] < 0$  the argument of the exponential function in (7.1) contains a positive real part. Then, the mode is unstable and the oscillation amplitude grows with

$$\frac{1}{\tau} = \text{Im}[\Delta\omega_{m,l}]. \quad (7.4)$$

The frequency shift  $\Delta\omega_{m,l}$  depends not only on the coupled bunch mode  $l$  but also on the strength of the coupling impedance. In the case of the impedance as imposed by a resonator, this coherent frequency shift is [18, 42, 44]

$$\Delta\omega_{m,l} = \omega_s \frac{R_s I M D_l F_m (\overline{\Delta\phi})}{2\pi V_{RF} \cos\phi_s B h} \quad (7.5)$$

with

$m$	single bunch oscillation type, $m = 1$ for bunch phase oscillations
$\omega_s$	phase oscillation frequency
$R_s$	shunt impedance of the resonator
$I$	total beam current
$M$	number of bunches
$D_l$	factor which depends on the attenuation of the induced signal between bunches and the coupled bunch mode $l$
$F_m(\omega_{res} l_{full})$	form factor which specifies the efficiency with which the single bunch oscillation ( $m$ ) is driven by the resonator
$\omega_{res}$	resonant frequency of the resonator, responsible for the coupling
$l_{full} = \frac{2l_{FWHM}}{\sqrt{\ln 4}}$	total resp. full bunch length
$l_{FWHM}$	FWHM bunch length
$V_{RF}$	voltage generating the bucket potential

$\phi_s$	phase of synchronus particle
$B = \frac{l_{full}}{t_{rep}}$	bunching factor
$t_{rep} = \frac{1}{M f_{rev}}$	time between subsequent bunches pass a fixed position at the ring
$f_{rev}$	revolution frequency
$h$	harmonic number
$\tau_{res} = \frac{2Q}{\omega_{res}}$	resonator time constant
$Q$	quality factor of resonator.

All these quantities are real values, with the exception of the factor  $D_l$ . The imaginary part of  $D_l$  determines stability. It depends on the attenuation  $e^{-t_{rep}/\tau_{cav}}$  of the signal, induced in the impedance. For a narrow band resonator  $D_l$  is given by

$$D_l \approx \frac{\Delta f_{res}}{f_{res} - N_l f_{rev} - i \Delta f_{res}} \quad \text{for} \quad \frac{t_{rep}}{\tau_{res}} \ll 1. \quad (7.6)$$

$f_{res}$  is the resonant frequency of the impedance,  $\Delta f_{res} = \frac{f_{res}}{2Q}$  the bandwidth,  $f_{rev}$  the revolution frequency and  $N_l$  is an integer number. Since the impedance is at a fixed position in the accelerator, the beam samples the impact with the bunch repetition frequency  $M f_{rev}$ . This sample frequency is modified in the case of a coupled bunch oscillation by  $l f_{rev}$ . Hence, a coupled bunch mode  $l$  is only excited when this sample frequency, or a multiple, hits the resonance frequency of the impedance

$$f_{res} \approx N_l M f_{rev} \pm l f_{rev} \quad \text{with} \quad N_l \in \mathbb{Z}. \quad (7.7)$$

This criterion determines the value of  $N_l$ , needed for calculating  $D_l$  with (7.6).

In the case of a wide band impedance, this factor is

$$D_l \approx -2 \frac{t_{rep}}{\tau_{res}} \exp \left[ -\frac{t_{rep}}{\tau_{res}} \right] \exp \left[ \frac{2\pi i l}{M} \right] \sin \left[ \frac{2\pi f_{res}}{M f_{rev}} \right] \quad \text{for} \quad \frac{t_{rep}}{\tau_{res}} \gg 1 \quad (7.8)$$

and coupled bunch modes near  $l = \frac{M}{4}$  and  $l = \frac{3M}{4}$  are most strongly excited. These modes have a phase difference between bunches of  $\pm \frac{\pi}{2}$ . Remember a driven harmonic oscillator. At phase differences of  $\frac{\pi}{2}$  between the driving force and the oscillator, the oscillator is maximal damped or excited, depending on the sign of the force. Here we have exactly the same situation, one of the modes  $l = \frac{M}{4}$ ,  $\frac{3M}{4}$  is damped and the other one is unstable.

In the general case the factor  $D_l$  is given by

$$D_l = -i \frac{t_{rep}}{\tau_{res}} \left( \frac{1}{1 - e^{x_+}} - \frac{1}{1 - e^{x_-}} \right) \quad \text{where} \quad x_{\pm} = \frac{2\pi i}{M} \left( l \pm \frac{f_{res}}{f_{rev}} \right) - \frac{t_{rep}}{\tau_{res}}. \quad (7.9)$$

For short bunches,  $l_{full} \lesssim 1.5 / 2\pi f_{res}$ , the form factor for dipole oscillations  $F_{m=1}(\omega_{res} l_{full})$  is

$$F_{m=1}(\omega_{res} l_{full}) \approx 2\omega_{res} l_{full} \quad \text{for} \quad l_{full} \lesssim 1.5 / 2\pi f_{res}. \quad (7.10)$$

As already mentioned, coupling between bunch oscillations is only possible when the synchrotron frequencies  $\omega_{s,j}$  of the individual bunches have similar values. A rule-of-thumb for de-coupling is that the r.m.s. spread in individual bunch frequencies  $S_{\omega}$  should exceed the frequency shift due to the coupling:

$$(\text{coherent}) \text{ spread} > \text{shift} \quad (7.11)$$

$$S_{\omega} > |\Delta\omega_{m,l}| \quad \text{for de-coupling.} \quad (7.12)$$

## 7.2 Analysis of steady state modes

With the measurement method for recording multi-bunch oscillations described in chapter 5, we obtained the phase oscillation ( $m = 1$ )

$$x_j(t) = \Delta\phi_j(t) \approx \hat{x}_j e^{i\omega_j t} \quad (7.13)$$

of every bunch  $j$  during 0.556 s. In the case of a coupled bunch oscillation at mode  $l$ , all frequencies  $\omega_j$  are equal

$$\omega_j = \omega_l. \quad (7.14)$$

In practice one observes not only one value but rather a distribution. Therefore, we have to assume for the analysis, the frequencies of the individual bunches have the same values, given by

$$\omega_l = \frac{1}{M} \sum_j \omega_j. \quad (7.15)$$

Then we can rewrite (7.1) to

$$\hat{x}_j e^{i\omega_l t} = \sum_{l=0}^{M-1} \hat{c}_l \eta_{l,j} e^{i\omega_l t} \quad (7.16)$$

$$\hat{x}_j = \sum_{l=0}^{M-1} \hat{c}_l \eta_{l,j}. \quad (7.17)$$

We are interested in the amplitude  $\hat{c}_l$  of the coupled bunch mode  $l$  in the multi-bunch oscillation, described by the complex vector  $\hat{\mathbf{x}}$ . Using orthogonality

$$\sum_{l',j} \eta_{l',j}^* \eta_{l,j} = \delta_{ll'} \quad (7.18)$$

the amplitude can be calculated by the scalar product

$$\hat{c}_{l'} = \sum_{j=0}^{M-1} \eta_{l',j}^* \hat{x}_j = \boldsymbol{\eta}_{l'}^* \hat{\mathbf{x}}. \quad (7.19)$$

In practice we do not have 220 bunches with equal charge and length. Instead we deal with 180 different bunches with slightly varying current and length. Hence, we calculate the mode frequency  $\omega_l$  as follows:

The oscillation frequency spectrum of an individual bunch is obtained by the complex fast Fourier transformation (FFT). It looks similar to the averaged oscillations spectra shown in figure 5.7. In the case of no parasitic frequencies such as the mains frequency and harmonics (50 Hz, 100 Hz and 150 Hz), the oscillation frequency of the bunch is given by the frequency at the maximum amount of the frequency spectrum. For the performed analysis the frequency  $\omega_j$  at the spectrum maximum  $|\hat{x}_j|$  between 10 Hz and 46 Hz is determined. It is used in the analysis when it is larger than the frequency value at the mains frequency of 50 Hz, otherwise it is disregarded for the analysis.

The mean of the frequencies taken is used as mode frequency  $\omega_l$ . The r.m.s. frequency spread is the r.m.s. value of these frequencies.

$$S_f = \frac{\sqrt{\sum (\omega_{j(taken)} - \langle \omega_l \rangle)^2}}{2\pi} \quad (\text{coherent}) \text{ spread between bunches} \quad (7.20)$$

A measure for the incoherent frequency spread within bunches is the r.m.s of the oscillation frequency in the frequency spectrum, determined with:

$$s_f = \frac{\sqrt{\sum (\text{FWHM}(\omega_{j(taken)}))^2}}{4\pi \sqrt{\ln 4}} \quad (\text{incoherent}) \text{ spread within bunches} \quad (7.21)$$

Since the sample frequency of the measurements are  $f_{sample} = \frac{47 \text{ kHz}}{104}$  and 256 samples are taken, the frequency resolutions of the  $\omega_{j(taken)}$  are  $2\pi \cdot 1.7 \text{ Hz}$ . We have to bear this in mind when interpreting the results.

The FFT value of the individual bunch  $j$  at the frequency  $\omega_l$  is the complex vector component  $\hat{x}_j$ . Every multi-bunch oscillation pattern, taken during the measurement time of 0.556 s, is assigned to a vector  $\hat{\mathbf{x}}$ . Before performing the scalar product  $\boldsymbol{\eta}_l^* \hat{\mathbf{x}}$ , we have to normalize this vector  $\hat{\mathbf{x}} \rightarrow \hat{\mathbf{n}} = (\hat{\mathbf{x}}^* \hat{\mathbf{x}})^{-1/2} \hat{\mathbf{x}}$ , taking into account the gaps in the bunch occupation pattern. Then we receive the normalized amplitude  $c_l$ , respectively portion of the coupled bunch mode  $l$ .

$$c_l = \boldsymbol{\eta}_l^* \hat{\mathbf{n}} = \frac{\boldsymbol{\eta}_l^* \hat{\mathbf{x}}}{\sqrt{\hat{\mathbf{x}}^* \hat{\mathbf{x}}}} = \frac{\hat{c}_l}{\sqrt{\hat{\mathbf{x}}^* \hat{\mathbf{x}}}}. \quad (7.22)$$

This method works if only one coupled mode or a few modes with small coherent frequency shifts  $\Delta\omega_l$  are excited. It fails if two or more modes with different mode frequencies  $\omega_l$  are building up the observed multi-bunch oscillation. Then, the approximation (7.15) is invalid.

For a large frequency spread  $S_f$  the approximation (7.14) is not justified. In this case, the described modal analysis results in equally distributed values for the portions  $c_l$ .

Analyzing a 'full machine', with 220 occupied bunch positions, leads to an upper limit examination. Gaps in the occupation pattern always result in a more stable behavior [45].

An analysis assuming a 'full machine' leads to small artificial amplitudes ( $c_l < 0.18$ ) of non-existent coupled bunch modes, due to the gaps. We will discuss this point by means of modal analyses of an artificially constructed mode in section 7.7. Here we state: Modes with normalized amplitudes  $c_l$  smaller than 0.18 should not be considered. We will see in the next sections, this is not a strong restriction on the analysis.

### 7.3 Modal spectrum of a multi-bunch oscillation

Figure 7.1 shows a multi-bunch phase oscillation of a beam of 110 mA at 830 GeV during ramping to 920 GeV over about 20 synchrotron oscillation periods. One can immediately recognize regular patterns. One is a phase shift of  $2\pi$  accumulated over the whole bunch train, e.g. from bunch position 0 to 219. A second phase shift leads to 'lines' from top left to bottom right.

By applying the modal analysis described we obtain the modal spectrum shown in figure 7.2. The multi-bunch oscillation in figure 7.1 consists of 58.6% of mode  $l = 1$  which shows a phase shift of  $2\pi$  from bunch position 0 to 219. The second strong mode is  $l = 163$  with 38.5%. Mode  $l = 163$  is near  $l = \frac{3M}{4}$  and has a phase shift of about  $\frac{3\pi}{4}$ . It is one of the most likely unstable modes, compare section 7.1. Figure 7.3 shows the isolated mode patterns of these two modes.

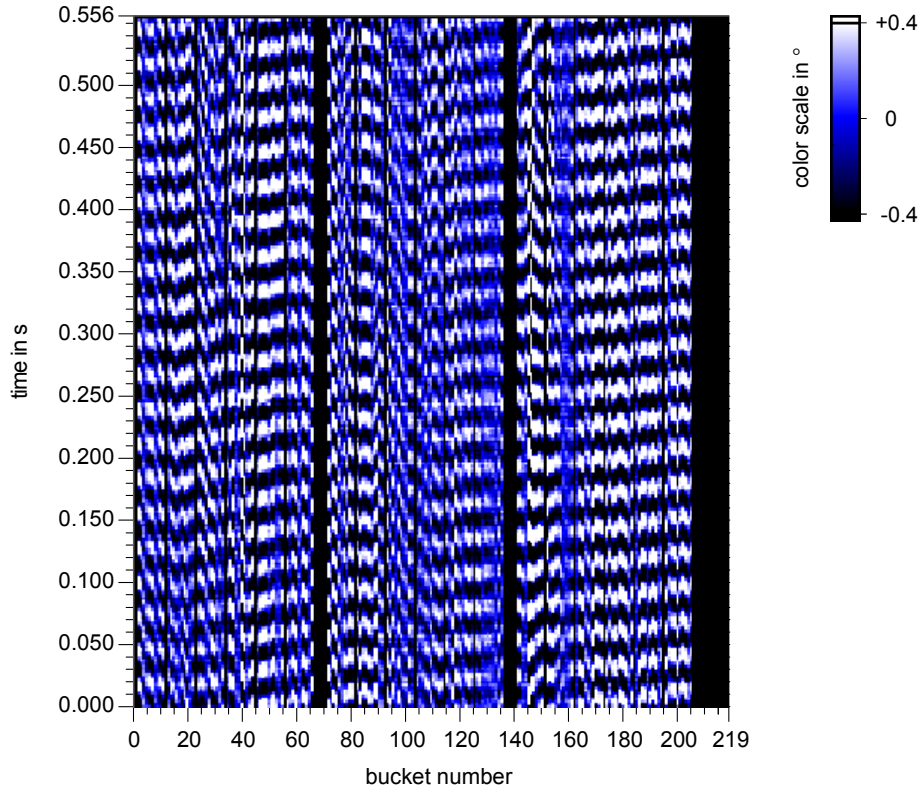


Figure 7.1: Multi bunch phase oscillation during ramping, showing particular modes.

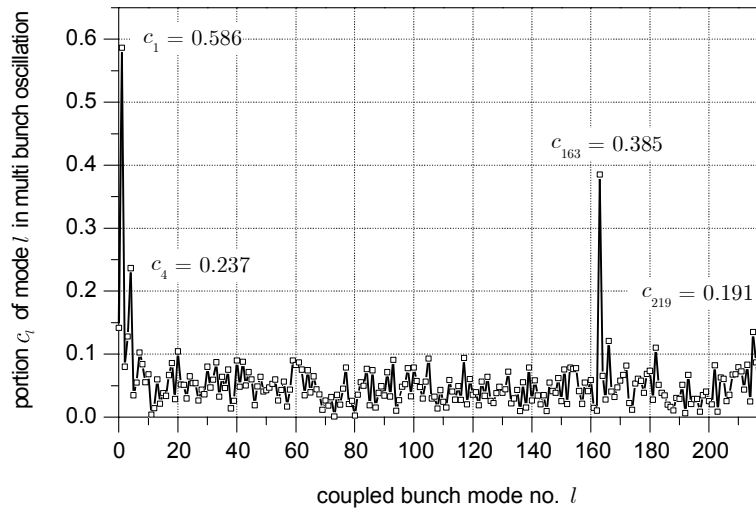


Figure 7.2: Modal spectrum of multi bunch oscillation with  $\omega_l/2\pi \approx 35$  Hz,  $S_f = 1.2$  Hz and  $s_f = 0.81$  Hz.

Modes  $l = 4$  and  $l = 219$  are also excited, but they contribute less to the multi-bunch oscillation pattern.

Half a minute later, at 866 GeV, the frequency spreads increased from  $S_f = 1.2$  Hz and  $s_f = 0.81$  Hz to  $S_f = 1.6$  Hz and  $s_f = 0.89$  Hz. The oscillation frequency  $\omega_l$  has changed from 35 Hz to 32 Hz and the multi-bunch oscillations, shown in figure 7.4, are still present, but the modal analysis fails, see figure 7.5.

Obviously, the bunches are no longer coupled. To learn more about the connection between

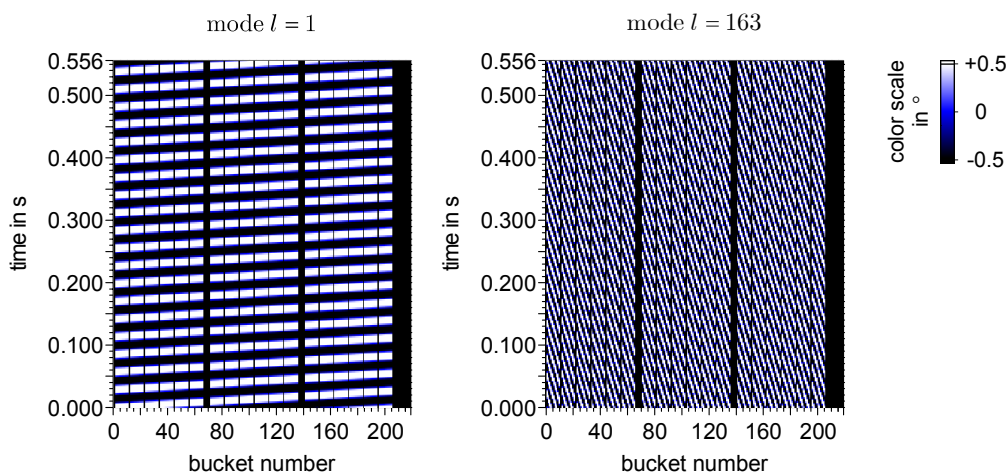


Figure 7.3: Coupled bunch oscillation mode patterns for mode  $l = 1$  and  $l = 163$  with the mode frequency  $\omega_l/2\pi = 35$  Hz.

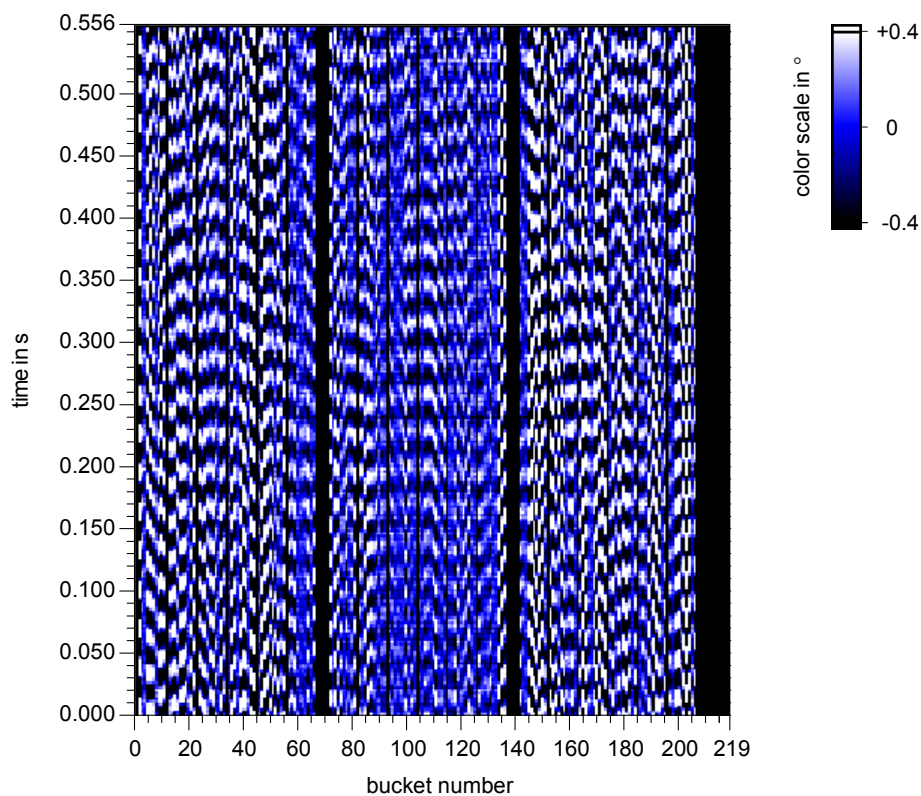


Figure 7.4: Multi bunch phase oscillation during ramping, without recognizable coupled modes.

the different parameters, a more detailed analysis follows in the next section.

## 7.4 Coupled bunch modes and emittance dilution

At the time of the measurements, the fast longitudinal diagnostic system was able to record 0.56 s long periods of multi-bunch oscillations in time steps of 30 s. The analysis in the previous section showed, that the character of the observed multi-bunch oscillation can change completely within 30 s. The question which arises here is: Are these the normal conditions and



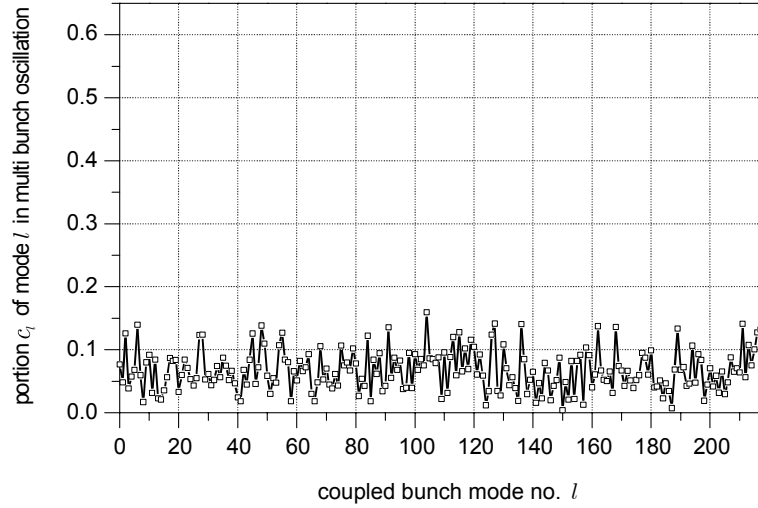


Figure 7.5: The multi bunch oscillation, recorded 30 s later, shows this modal spectrum with  $\omega_l/2\pi \approx 32$  Hz,  $S_f = 1.6$  Hz and  $s_f = 0.89$  Hz.

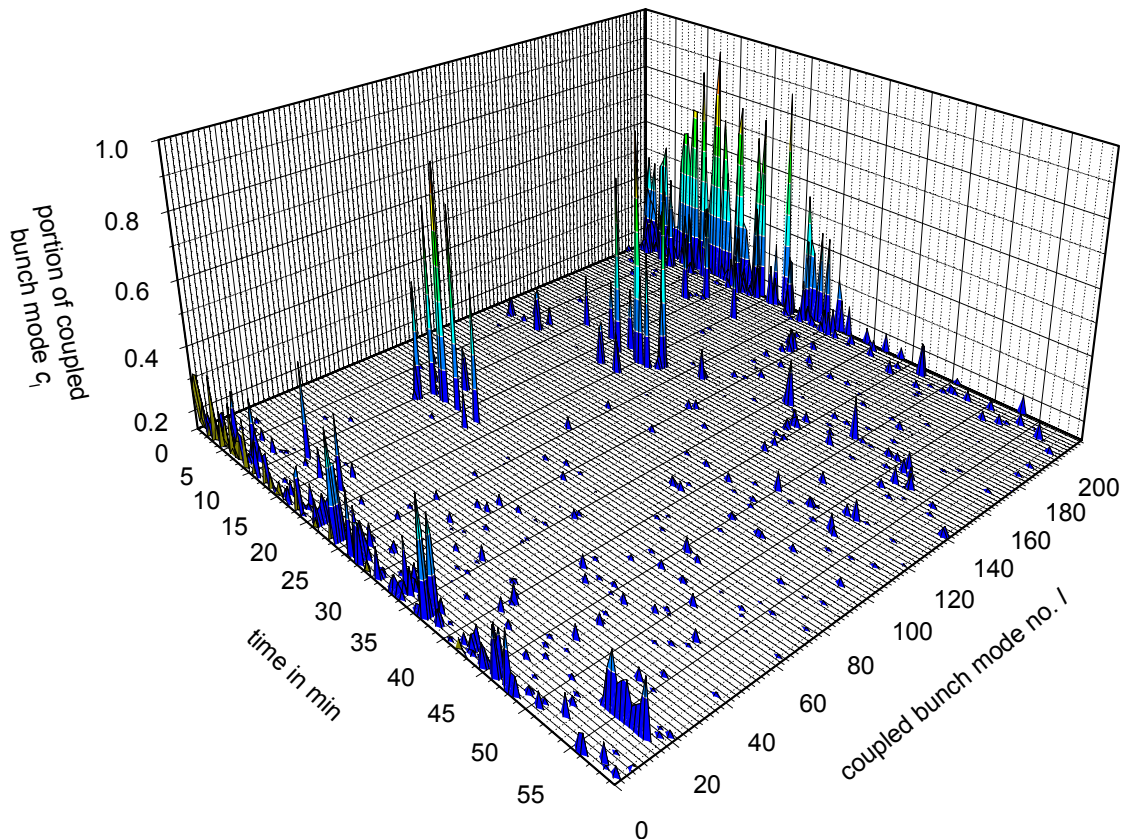


Figure 7.6: Coupled bunch mode spectrum in dependence on the measurement time of the analyzed multi bunch oscillation.

do the particular modes correlate with the emittance dilution described in section 5.4?

First, we can obtain an overview of the coupled bunch mode spectrum, during a ramp from low to high energy, by plotting the mode amplitude as a three dimensional contour plot, using the time as additional axis. Figure 7.6 shows such a coupled bunch mode spectrum.



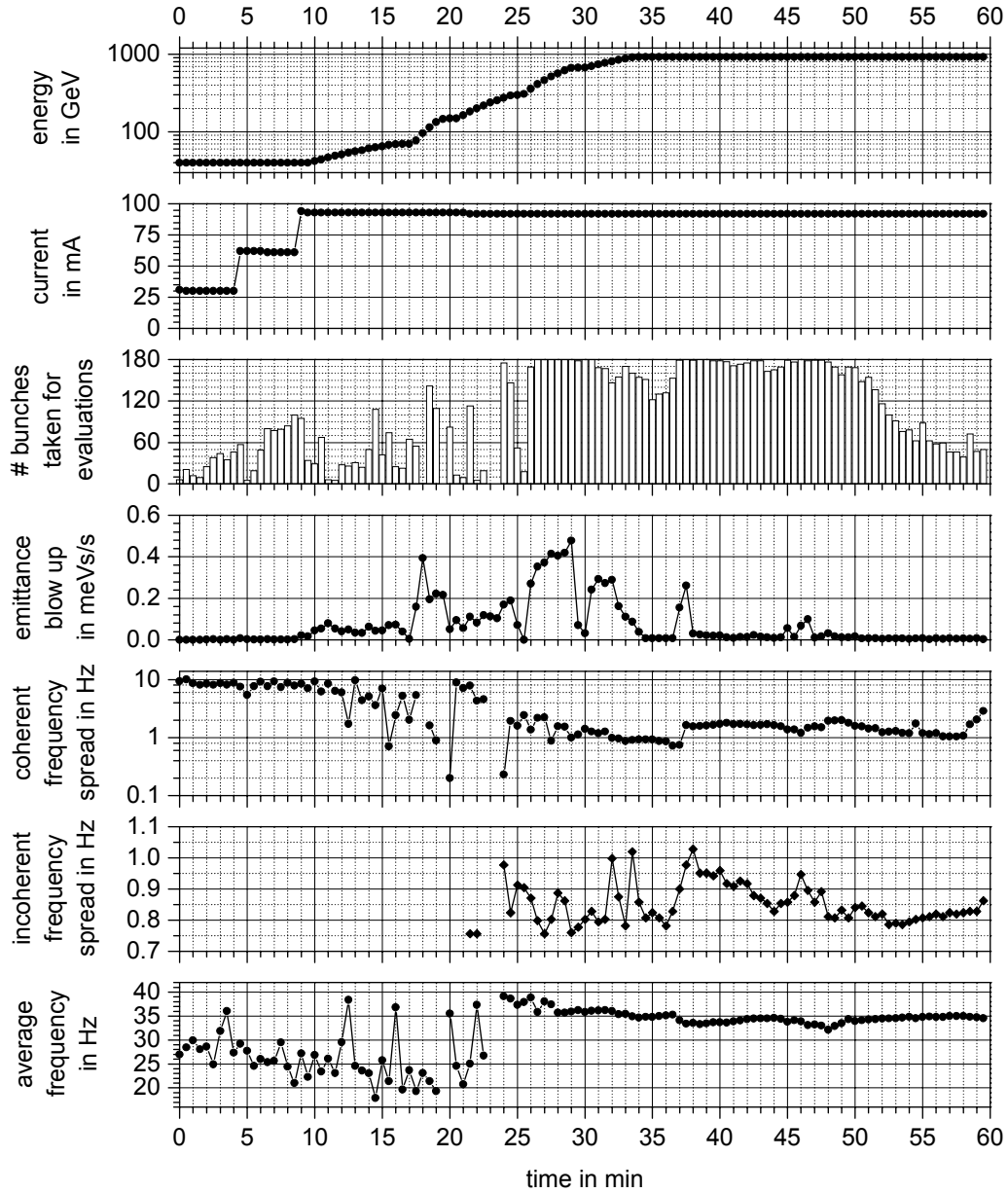


Figure 7.7: Time evolution of various parameters in the HERA proton ring during ramping and steady state operation at 920 GeV. The emittance blow up goes along with changes of the coherent frequency spread  $S_f$ , the incoherent one  $s_f$  and the average frequency used in the analysis as mode frequency  $\omega_l / 2\pi$ . All these values are calculated from the bunches with sufficiently strong synchrotron oscillations. The number of bunches, used for these calculations, are given in the third row.

Only normalized amplitudes of coupled bunch modes above 15% are plotted, to suppress spectra showing no particular modes. This plot can be interpreted together with the parameters shown in figure 7.7:

At the time  $t = 9$  min, the third bunch train is injected at an energy of 40 GeV, leading

to a jump in the beam current from about 60 mA to about 90 mA. This goes along with a tiny emittance blow up. 45 bunches show synchrotron oscillations which are sufficiently strong for a calculation of their coherent frequency spread  $S_f$ . Since the maximum FFT values are not more than twice as large as the noise levels of the FFT values, no incoherent spread  $s_f$  is determined. The average frequency, taken as mode frequency, to calculate the mode spectrum, is 28 Hz. In the mode spectrum shown in figure 7.6, the mode  $l = 6$  is visible.

In this way, we can go through the complete ramp procedure. In the time between 10 min and 16 min HERA is ramped from 40 GeV to 70 GeV. Several times modes around  $l = 74$  are visible going along with an emittance blow up. Mode  $l = 74$  is most excited at 12.5 min where we also discover a reduction of the coherent frequency spread. Half a minute later, the spread increases and the mode disappears.

In the course of the ramp, the visible modes change from modes around  $l = 74$  to modes around  $l = 146$  between 15 min and 23 min. Note: The oscillation phase difference between subsequent bunches at mode  $l = 146$  is the negative of those at mode  $l = 74$ . With this in mind, they are ‘mirrored’ on the mode  $l = 110$ , where subsequent bunches oscillate against each other e.g. with a phase shift of  $\pi$ .

During the whole ramp, modes near  $l = 0$  and  $l = 219$  are visible. These are modes where all bunches oscillate almost in phase. We call them ‘fundamental modes’.

The connection between the coherent frequency spread, appearing coupled bunch modes and the emittance blow up is most evident when we examine the situation after 920 GeV is reached. At 36 min the mode  $l = 163$  is visible and one minute later the modes  $l = 2$  and  $l = 4$ . Previously, no emittance blow up is visible, but together with the arising modes the emittance blows up. This goes along with an increase of the coherent frequency spread from 0.75 Hz to 1.63 Hz and an increase of the incoherent frequency spread. In addition, we observe a small jump of 1.18 Hz in the average frequency.

We can convince ourselves that this correlation is also visible at the times 44 min, 46 min and between 57 min to 57 min.

By analyzing other ramps in the same way, one finds a similar behavior.

## 7.5 A coupled bunch instability

During the HERA energy ramp described, particular modes ( $l = 163, l = 2, l = 4$ ) appear at 36 min, which are accompanied by an emittance dilution. Is this an unstable coupled bunch oscillation, in other words a coupled bunch instability?

First we remember the condition for de-coupling (11.36), respectively coupling:

$$S_f < \frac{|\Delta\omega_{m,l}|}{2\pi} \quad \text{for coupling} \quad (7.23)$$

The measured frequency shift between the state with observable modes and the oscillations without modes is  $\text{Re}[\Delta\omega_{m,l}] / 2\pi = 1.18$  Hz. While we observe the modes, the coherent frequency spread is 0.75 Hz, well below the coherent frequency shift. So, this condition for coupling is fulfilled.

Due to the coupling, the oscillation amplitudes of the bunches increase. By increasing also the emittance, the incoherent and the coherent frequency spread, the beam stabilizes itself. As soon as the coherent frequency spread is 1.63 Hz and thus larger than the frequency shift of  $\Delta\omega_{m,l} / 2\pi = 1.18$  Hz, the oscillation de-couples. As a result of this de-coupling, we no longer observe particular modes and the oscillation frequency changes by the value of the frequency shift, see figures 7.6 and 7.7. All bunches oscillate with their individual synchrotron frequencies.

## 7.6 Estimations of the instability growth rates

We observe modes near  $l = \frac{M}{4} = 55$  and  $l = \frac{3M}{4} = 165$ . This is an indication that there is a broadband impedance driving the instability, because a broadband impedance would preferably drive these modes, see section 7.1. A narrow band impedance is not completely excluded.

If we assume a broadband impedance, then the coherent frequency shifts (7.5) are given by a factor  $|\Delta\omega_m|$ , depending on the single bunch oscillation type  $m$  times a factor, containing the dependence on the coupled bunch modal number  $l$

$$\Delta\omega_{m,l} = |\Delta\omega_m| \exp \left[ \frac{2\pi i l}{M} \right]. \quad (7.24)$$

In the last sections, we discussed an instability showing first the mode  $l = 163$  and one minute later the modes  $l = 2$  and  $l = 4$ . Figure 7.8 shows the frequency shifts in the complex plane.

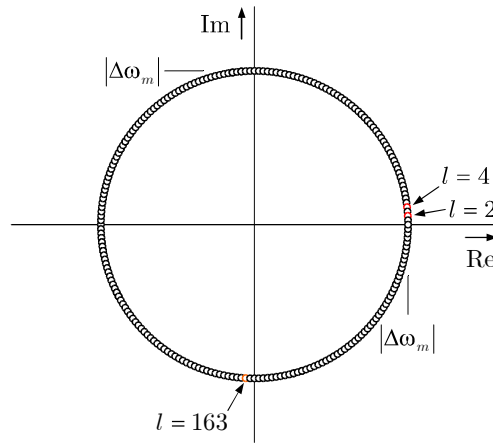


Figure 7.8: Coherent frequency shifts in complex plane.

An observed frequency jump caused by the break up of a coupled bunch oscillation correlates to the real part of the complex frequency shift. If modes near  $l = 0$  or  $l = 110$  disappear, the frequency jump is equal to the frequency shift. Under the assumption that mode  $l = 163$  and modes  $l = 2, 4$  are driven by the same impedance, the amount of the frequency shift would be equal to the observed frequency jump  $|\Delta\omega_m| = 1.18$  Hz, since

$$\Delta\omega_{1,2} = |\Delta\omega_1| \exp \left[ \frac{2\pi i 2}{220} \right] \approx |\Delta\omega_1|. \quad (7.25)$$

This is not a well found assumption, above all no frequency jump is observed by the change from the mode  $l = 163$  to the modes  $l = 2$  and  $l = 4$ . Another problem is the question of the mechanism, causing the change from  $l = 163$  to  $l = 2$  and  $l = 4$ .

However, with this rough assumption we can estimate the instability growth rate for the mode  $l = 163$  with

$$\frac{1}{\tau} = \text{Im} [\Delta\omega_{m,l}] \approx |\Delta\omega_1| \text{Im} \left[ \exp \left[ \frac{2\pi i 163}{220} \right] \right] \approx |\Delta\omega_1|. \quad (7.26)$$

The result corresponds to the frequency jump of about  $\frac{1}{\tau} = 1\frac{1}{s}$ .

Now we look at the mode  $l = 74$  most excited at 12.5 min. This mode number differs significant from the mode numbers  $l = \frac{M}{4} = 55$  and  $l = \frac{3M}{4} = 165$ . This suggest that this

mode is not driven by a broadband impedance. Rather, this is an indication that there is a narrow band impedance. In this case, the coherent frequency shifts are also given by a factor  $|\Delta\omega_m|$ , depending on the single bunch oscillation type  $m$  times a factor containing the dependance on the coupled bunch modal number  $l$

$$\Delta\omega_{m,l} = |\Delta\omega_m| \frac{D_l}{|D_l|} \quad (7.27)$$

where we use (7.9) for the calculation of  $D_l$ . But in this case, we need some idea of what could be the driving impedance. The resonant frequency of this impedance should obey the condition (7.7). It is for example approximately fulfilled by the higher order monopole mode of the 208 MHz system at  $f_{res} = 856.570$  MHz [46]:

$$f_{rev} (N_l M + l) = 47.31034 \text{ kHz} (82 \cdot 220 + 74) = 856.792 \text{ MHz} \quad (7.28)$$

This cavity mode has a quality factor of  $Q = 7403$  which causes a bandwidth of  $\Delta f_{res} = 58.637$  kHz. When we calculate the difference between the expected frequency for mode  $l = 74$  and the frequency of the cavity mode, we find a deviation of 222 kHz, this is about four times the bandwidth. So this cavity mode should not drive mode  $l = 74$ , but rather mode  $l = 65$ . Nevertheless, we will here assume mode  $l = 74$  may be driven by a narrow band impedance with the same quality factor and estimate which instability growth rate we then have to expect: A frequency change would be equal to the real part of the frequency shift caused by the coupling. At the time when the mode vanishes we see a frequency change of 10 Hz. Hence, we can estimate the growth rate of mode  $l = 74$ :

$$\frac{D_l}{|D_l|} \approx 1 + 0.053i \quad \implies \quad \frac{1}{\tau} = |\Delta\omega_{74}| \left| \text{Im} \frac{D_l}{|D_l|} \right| \approx 0.53 \frac{1}{s} \quad (7.29)$$

Both values  $\frac{1}{\tau} = 1 \frac{1}{s}$  for mode  $l = 163$  and  $\frac{1}{\tau} = 0.53 \frac{1}{s}$  for mode  $l = 74$  are of the same order of magnitude. These values may not be correct but are to some extent supported by the available data. Particularly, if we hit with mode  $l = 74$  a narrow band impedance with a lower quality factor than that considered, we have to expect a higher growth rate.

## 7.7 Analysis of the transient behavior of modes

The estimations of the instability growth times in the last section resulted in values of the order of magnitude of  $\tau = 1$  s to  $\tau = 2$  s. Since our recording time of a multi-bunch pattern is 0.556 s, these growth times may be visible in our records.

A much faster, but less selective modal analysis method [47] is based on the fact that the oscillation phase difference between subsequent bunches for the mode  $l$  is

$$\Delta\Phi_l = \frac{2\pi l}{M}. \quad (7.30)$$

Even during one passage of all bunches at the recording monitor, this phase difference can be analyzed. To do that, we take the phase deviation of every bunch from its individual synchronous phase in a number sequence. Zeros are assigned to the gaps in the bunch occupation pattern. Assume mode  $l = 1$  is present, then the number sequence of bunch phases shows one ‘oscillation cycle’, mode  $l = 2$  shows two ‘oscillation cycles’ etc. By applying a complex FFT of the number sequence and dividing the resulting amount values by the number of bunches we

get the oscillation amplitudes of the contained modes. The applied FFT does not distinguish between the modes  $l$  and  $M - l$ . Hence, we restrict our view on the modes  $l = 0$  to  $l = M / 2$ .

In the following, we look at the results of the analysis method by means of an artificially constructed record of a multi-bunch pattern. Figure 7.9 shows as example the mode 180 with linearly growing oscillation amplitude. By performing the fast modal analysis described, we ob-

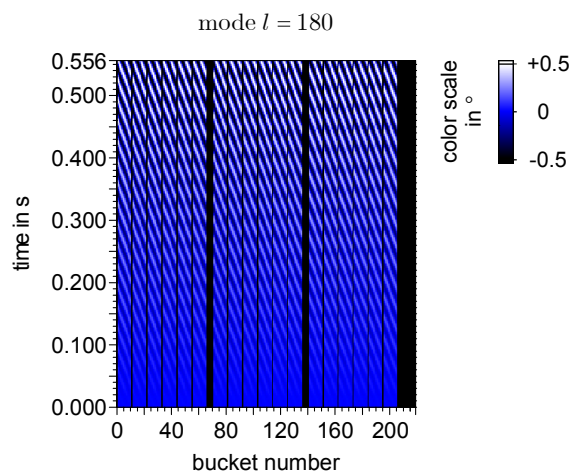


Figure 7.9: Example of an transient mode with linear growing amplitude.

tain the amplitude spectrum of the modes in figure 7.10. It is ambiguous compared to the steady

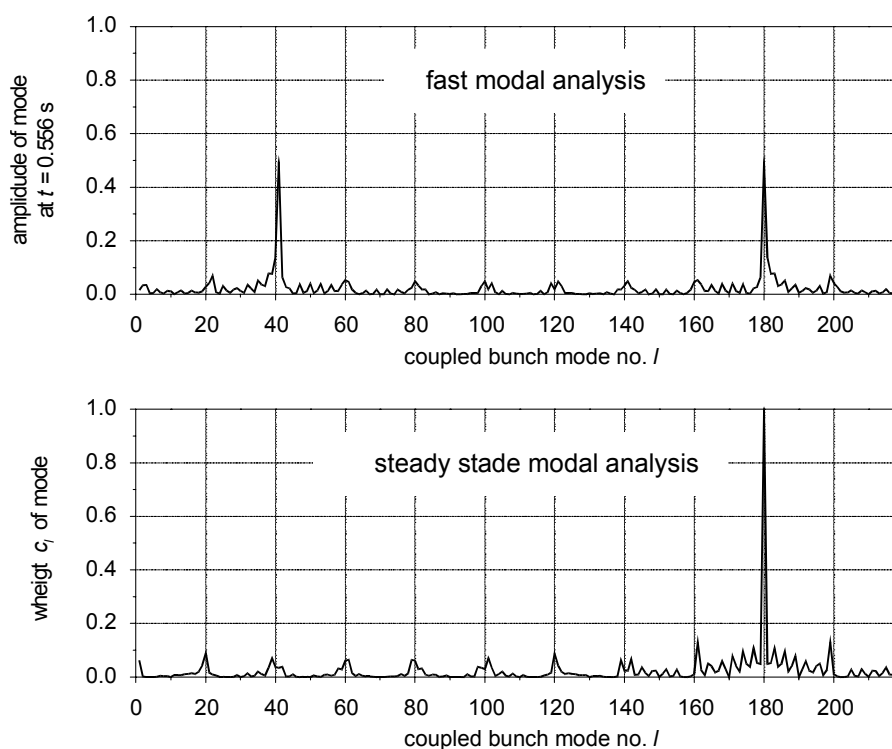


Figure 7.10: Analysis of a synthesized multi bunch oscillation pattern oscillating in mode 180.

state modal analysis. But we can observe the transient behavior of this mode in figure 7.11. Before plotting these data, we performed digital low pass filtering to smooth out modulations of the amplitude in the time domain.

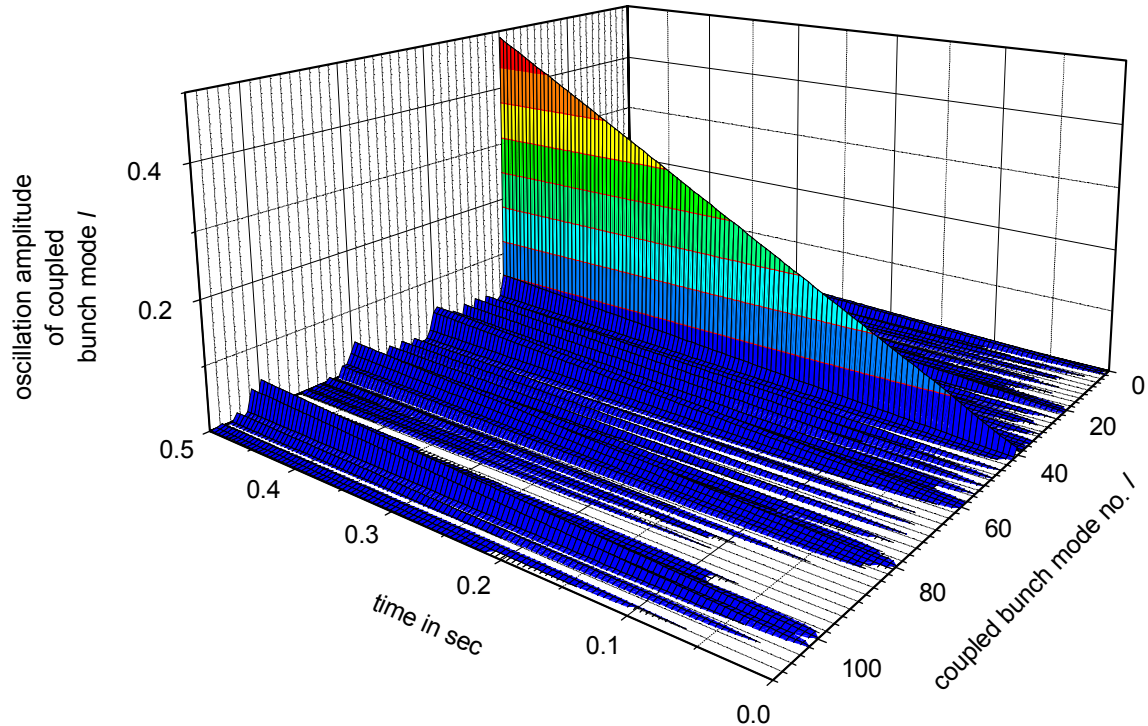


Figure 7.11: Transient behaviour of the constructed mode 180 with growing amplitude.

Note: the gaps in the bunch pattern lead to small artificial amplitudes ( $c_l < 0.18$ ) of other modes in the analysis. Since we can easily identify the mode 180, we can neglect the gaps for further analysis. We have only to take into account, that small amplitudes must not be physically relevant. Furthermore, small amplitudes may also be caused by noise at the measurements.

In the following, a mode spectrum as in figure 7.11 will be referred to as a ‘transient modal spectrum’.

## 7.8 Transient modal spectrum of multi-bunch oscillations

Our records of multi-bunch oscillations span 0.556 s. We estimated instability growth times of  $\tau = 1$  s to  $\tau = 2$  s. Hence, the growth of the coupled bunch instabilities should in principle be visible in the transient modal spectrum. In section 7.6, we estimated the instability growth time  $\tau = 2$  s of mode  $l = 74$  by means of the frequency jump observed between 12.5 min and 13 min.

Figure 7.12 shows the transient modal spectrum at 12.5 min. The mode  $l = 74$  is recognizable. But no exponential behavior is visible. The analyzed situation shows an approximate constant behavior. Therefore, we can assume that a conceivable narrow band impedance driving this mode does not have a sufficiently high quality factor to generate a direct visible growth of the oscillation amplitudes. It is also possible that we observe an active impedance driving a stable mode. Then, the observed frequency jump of 10 Hz would be the difference frequency between the bunch oscillations driven by the active impedance and the ‘free’ bunch oscillations. Remember, we found in section 7.4 that during ramping mode  $l = 74$  is visible several times and later mode  $l = 146$  which is  $l = 74$  ‘mirrored’ on  $l = 110$ . This ‘symmetry’ seems to be a hint that both modes are driven by the same source. In this case, a usual narrow band impedance could not be the source because the condition (7.7) can only be fulfilled by one value for  $N_l = \pm 36$



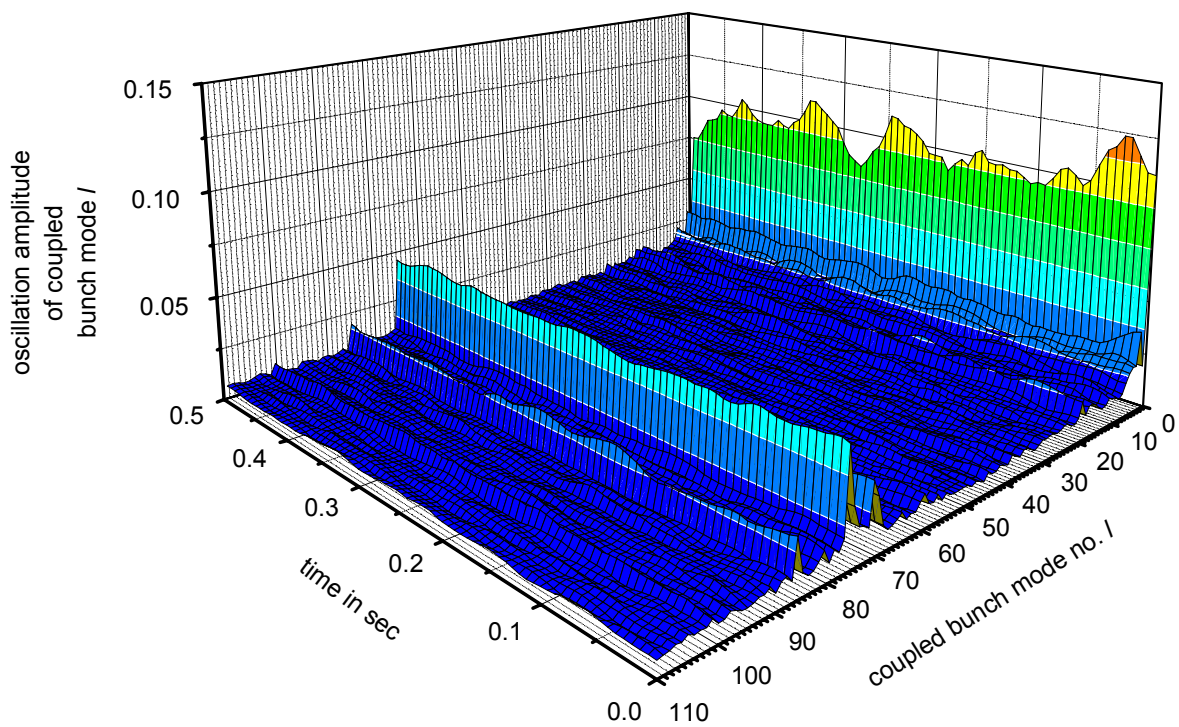


Figure 7.12: Transient mode spectrum at 12.5 min.

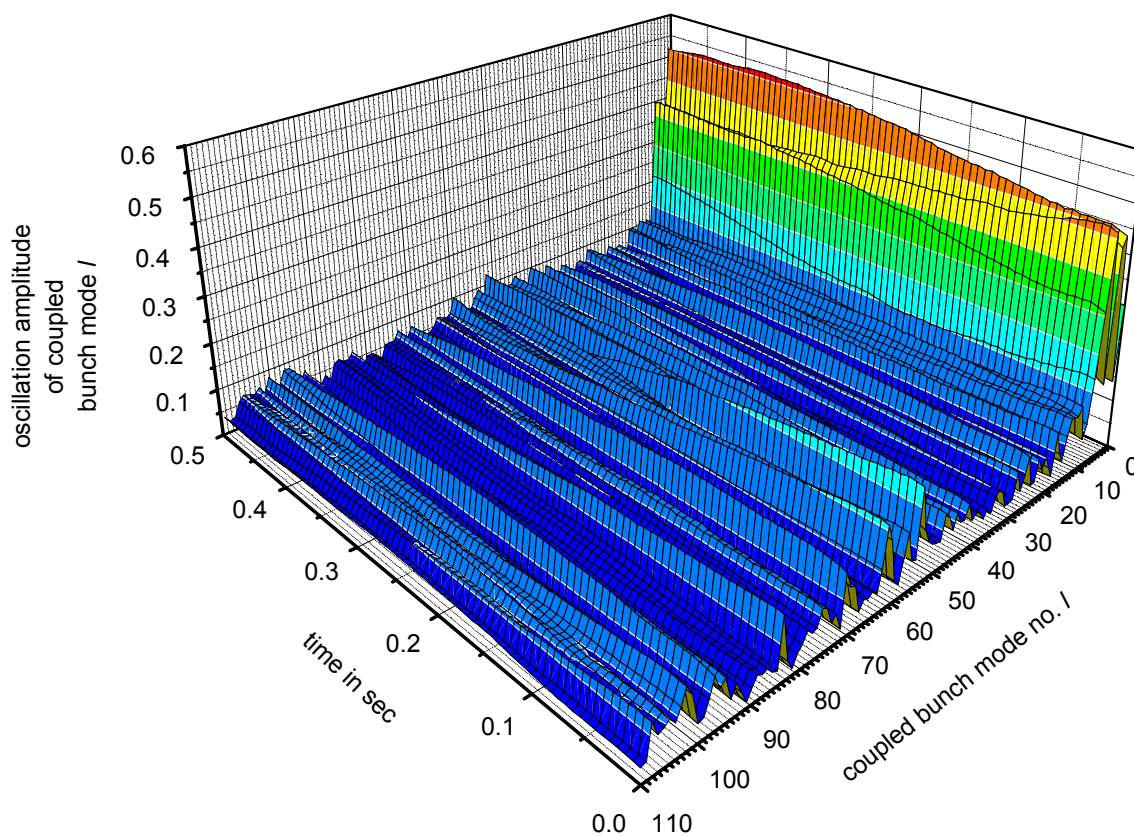


Figure 7.13: Transient mode spectrum at 36.5 min.

to get the same frequency  $f_{res}$  for both modes! This is extremely unlikely. Hence,  $l = 74$  and  $l = 146$  may be the result of a complicated active impedance, respectively a technical damage.

In section 7.6 we also discussed mode  $l = 163$  visible at 36 min. It disappears half a minute later and the modes  $l = 2$  and  $l = 4$  are visible. Figure 7.13 shows the transient mode spectrum at this time. In contrast to the situation just discussed at 12.5 min, growing and decaying modes are visible. But the estimated time constants are about  $\tau = 10$  s, instead of  $\tau = 1$  s. The difference could also be caused by an influence of a damping mechanism, most probably Landau damping.

To get a more detailed insight into the transient behavior of the coupled bunch modes, records of multi-bunch oscillations over a longer period of time are necessary. The periods of observation should be in the order of minutes or longer. This requires either more ADC memory or the use of a DSP system. For instance, the DSP system of a multi-bunch feedback was used to analyze stability of coupled bunch modes at the LBNL Advanced Light Source (ALS) [47]. Until now, none of these possibilities have been available at the HERA proton ring.

## 7.9 Results

There are indications that the HERA proton ring suffers from coupled bunch instabilities. In this chapter, we discussed these indications in detail exemplary at the recorded data of an arbitrary chosen ramp from low to high energy. Other observed ramps behave similarly. We found that certain emerging oscillation modes are going along with an emittance blow up. A detailed analysis of the oscillation frequencies and their spread also fit with the rule-of-thumb for coupling and de-coupling of bunch oscillations.

From the available recorded data of multi-bunch oscillation pattern, we determined frequency shifts of 1 Hz and 10 Hz, particular assumptions yield instability grow times of  $\tau = 1$  s and  $\tau = 2$  s. There are indications that the frequency shift of 10 Hz may also be caused by an active source. The attempt, to verify these growth times by analyzing directly the transient behavior of the modes, was not very satisfactory. A more detailed study in this direction has to be performed. This requires additional new hardware.

The global damping behavior of the storage ring determines whether a coupled bunch instability could take place or not. Measurements of the beam transfer function (BTF) and the de-coherence time give information about the damping behavior. The next chapters are about these subjects.



## 8 Consideration of the Beam Response

The longitudinal stability of the bunched beam in a storage ring can not only be examined by passive observations. Measurements of the beam response to particular excitations offer additional insight. Two complementary methods are kick excitations and harmonic excitations. Kick excitations cover a broad band frequency range, while harmonic excitations are narrow band. In this chapter, the underlying physical principles are explained.

In the first section, we will derive the frequency spread within a short bunch, in the case of a double harmonic RF system, causing a nonlinear longitudinal behavior of a proton bunch. In the subsequent section, we discuss the beam response to single RF phase kicks. Measurements of this impulse response yield the decoherence time and, with that, the frequency spread within a bunch. This incoherent frequency spread can stabilize instabilities, this is called ‘Landau damping’. Hence, one can infer from decoherence measurements whether there is enough incoherent frequency spread available to suppress instabilities.

In contrast to a kick excitation, which has an effect on all protons in a bunch, a harmonic excitation has only an effect on protons with oscillation frequencies near the excitation frequency. The consequences of this selective excitation on the beam response are discussed in the third section. From these measurements, we obtain the so called beam transfer function (BTF), which is the starting point of stability examinations of feedback loops. In appendix A.6, principles of such stability estimations are demonstrated by means of the two narrow band beam feedback loops already mounted in the HERA proton ring.

Another type of beam response is a beam echo. The beam parameters, which can be determined by this method, provide information about diffusive processes. As already mentioned, a RF phase kick leads to a damped collective bunch oscillation because of the incoherent frequency spread. The bunch center oscillation can be partly recovered by performing a suitable RF amplitude kick. After a waiting time of twice the distance between the two RF kicks, a bunch center oscillation reappears. This is called the echo.

### 8.1 Frequency spread within a bunch

The reason for the nonlinear longitudinal behavior of a proton bunch is the spread of the synchrotron frequency within the bunch, called ‘incoherent frequency spread’. The synchrotron frequency of a single proton depends on its oscillation amplitude. This is due to the flattening bucket potential at higher amplitudes, which reduces the frequency.

In this section, we derive the amplitude dependence of the synchrotron frequency for short bunches. For more detail see [48, 49, 50].

The Hamilton function of a proton in a single harmonic RF bucket potential, in the non accelerating case, is given by [39]

$$H = \frac{1}{2} \frac{h^2 \omega_{rev}^2 \eta}{\beta^2 E_s} \left( \frac{\Delta E}{h \omega_{rev}} \right)^2 + \frac{1}{2} \frac{q_p V}{2 \pi h} 2 (1 - \cos \Delta \phi), \quad (8.1)$$

where  $\Delta E$  is the energy deviation,  $\Delta \phi$  is the phase deviation,  $h$  the harmonic number,  $\omega_{rev}$  the revolution frequency,  $\eta = \frac{1}{\gamma_t^2} + \frac{1}{\gamma^2}$  the slip factor with  $\gamma_t = 27.74$  at HERA,  $\gamma = \frac{E_s}{E_0}$ ,  $E_s$  the

energy of the synchronous particle,  $E_0$  the rest energy of a proton,  $q_p$  the proton charge,  $V$  the RF voltage and  $\beta = \frac{v}{c}$ .

Using the abbreviations

$$q = \Delta\phi \quad (8.2)$$

$$f = \frac{q_p V}{2\pi h} \quad (8.3)$$

$$p = \left( \frac{\Delta E}{h\omega_{rev}} \right) \quad (8.4)$$

$$m = \frac{\beta^2 E_s}{h^2 \omega_{rev}^2 \eta} \quad (8.5)$$

it reads

$$H = \frac{p^2}{2m} + \frac{f}{2} 2 (1 - \cos q). \quad (8.6)$$

In the case of a double harmonic RF system and larger oscillation amplitudes, we have to examine the Hamiltonian with a modified potential

$$H = \frac{p^2}{2m} + \frac{f}{2} 2 \left( (1 - \cos q) + \frac{r_{12}}{h_{12}} (1 - \cos h_{12} q) \right) \quad (8.7)$$

$$H = \frac{p^2}{2m} + U(q) \quad (8.8)$$

where  $r_{12} = \frac{V_2}{V_1}$  is the ratio of the RF voltages and  $h_{12} = \frac{h_2}{h_1}$  the ratio of the harmonic numbers.

To examine the simplest approximation, we expand the potential  $U(q)$  in a series up to the order  $\mathcal{O}(q^2)$ :

$$H = \frac{p^2}{2m} + \frac{f(1 + r_{12}h_{12})}{2} q^2 + \mathcal{O}(q^4). \quad (8.9)$$

The second RF system modifies the synchrotron frequency  $\omega_{s0} = \sqrt{f/m}$  for small oscillation amplitudes to

$$\left. \frac{\omega_s}{\omega_{s0}} \right|_{q \rightarrow 0} = \sqrt{1 + r_{12}h_{12}}. \quad (8.10)$$

This approximation does not take into account a decrease of the oscillation frequency at higher amplitudes. Therefore, we will now derive first the frequency in the general case. Following standard procedures [51, 52], we realize the particle has no momentum at the maximum oscillation amplitude  $q_{\max}$ , so that the particle energy is given by

$$E_{q_{\max}} = U(q_{\max}). \quad (8.11)$$

The energy is conserved, hence, we get for any other time

$$E_{q_{\max}} = \frac{m}{2} \left( \frac{dq}{dt} \right)^2 + U(q) \quad \iff \quad dt = \frac{dq}{\sqrt{\frac{2}{m} (U(q_{\max}) - U(q))}} \quad (8.12)$$

and we obtain the cycle period by the integration

$$T = \oint_{\text{one cycle}} \frac{dq}{\sqrt{\frac{2}{m} (U(q_{\max}) - U(q))}}. \quad (8.13)$$

To perform this integration, we develop the potential given in (8.7) up to terms of the order  $\mathcal{O}(q^4)$ . Using integration tables as in [48], or a computer algebra system like *Mathematica*, the integration (8.13) can be performed analytically. We expand the result for  $r_{12} < 1/h_{12}$  in a series. By taking  $\omega_s = 2\pi/T$  into account, we get

$$\frac{\omega_s(q_{\max})}{\omega_{s0}} = \sqrt{1 + r_{12} h_{12}} - \frac{1}{16} \frac{1 + r_{12} h_{12}^3}{\sqrt{1 + r_{12} h_{12}}} q_{\max}^2 + \mathcal{O}(q_{\max}^4), \quad (8.14)$$

respectively

$$\frac{\omega_s(\Delta\phi_{\max})}{\omega_{s0}} \approx \sqrt{1 + r_{12} h_{12}} - \frac{1}{16} \frac{1 + r_{12} h_{12}^3}{\sqrt{1 + r_{12} h_{12}}} \Delta\phi_{\max}^2. \quad (8.15)$$

Note: this is valid for  $r_{12} < 1/h_{12}$ . The quantity

$$s_\omega = -\frac{1}{16} \frac{1 + r_{12} h_{12}^3}{\sqrt{1 + r_{12} h_{12}}} \omega_{s0} \Delta\phi_\sigma^2 \quad (8.16)$$

defines the so called synchrotron frequency spread  $\frac{s_\omega}{2\pi}$  within a bunch.  $\Delta\phi_\sigma$  is the half bunch length expressed in RF radians

$$\Delta\phi_\sigma = \frac{l_{FWHM}}{2\beta c \sqrt{\ln 4}} 2\pi h_1 \omega_{rev} \quad (8.17)$$

with the FWHM bunch length  $l_{FWHM}$  and the RF frequency  $\omega_{RF1} = h_1 \omega_{rev}$ . By the restriction on the quadratic term of the frequency spread (8.16), we make an error. This error can be estimated by numeric integration. At low energy the values for HERA are  $h_{12} = 4$ ,  $r_{12} \leq \frac{1}{4}$  and  $l_{FWHM} = 2.4$  ns, they obey

$$\frac{\Delta s_\omega}{s_\omega} \approx 0.4\% \quad \text{at 40 GeV.} \quad (8.18)$$

At high energy we have  $h_{12} = \frac{1}{4}$ ,  $r_{12} \approx \frac{1}{3}$  and  $l_{FWHM} = 2.4$  ns, this results in an error of

$$\frac{\Delta s_\omega}{s_\omega} \approx 0.2\% \quad \text{at 920 GeV.} \quad (8.19)$$

The response of a bunch for an external excitation depends on the oscillation frequency distribution within the bunch. We evaluate this distribution for a Gaussian bunch moving in a single harmonic RF potential. This treatment can be extended directly to the case of a double harmonic RF system.

The normalized Gaussian distribution of the oscillation amplitudes is given by

$$\rho(\Delta\phi_{\max}) = \frac{1}{\sqrt{2\pi}\Delta\phi_\sigma} \exp\left[-\frac{1}{2} \frac{\Delta\phi_{\max}^2}{\Delta\phi_\sigma^2}\right]. \quad (8.20)$$

We can rewrite (8.16) to

$$\omega_s = \omega_{s0} + s_\omega \frac{\Delta\phi_{\max}^2}{\Delta\phi_\sigma^2} \quad \Leftrightarrow \quad \Delta\phi_{\max}^2 = \frac{\omega_{s0} - \omega_s}{s_\omega} \Delta\phi_\sigma^2 \quad (8.21)$$

and receive the oscillation frequency distribution

$$\rho(\omega_s) = \Theta(\omega_{s0} - \omega_s) \frac{1}{-2s_\omega} \exp\left[-\frac{1}{2} \frac{\omega_{s0} - \omega_s}{s_\omega}\right]. \quad (8.22)$$

We take into account that  $\omega_s \leq \omega_{s0}$ , for all protons in a bunch, by inserting the Heavyside function  $\Theta$ , defined in the appendix. The distribution is normalized to one

$$\int_{-\infty}^{\infty} \rho(\omega_s) d\omega_s = 1. \quad (8.23)$$

In the case of a double harmonic RF system we have to replace  $\omega_{s0}$  by  $\sqrt{1 + r_{12}} h_{12} \omega_{s0}$  in (8.22).

Figure 8.1 shows the distribution (8.22) for two different bunch lengths. A longer relative bunch length implies an increase of the population at lower frequencies.

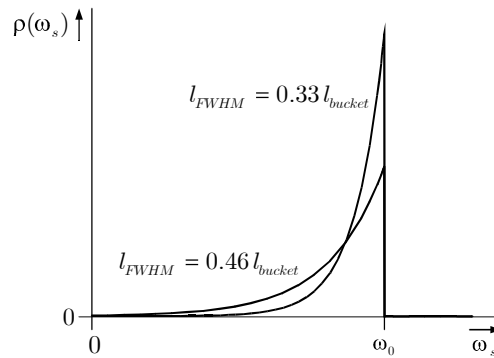


Figure 8.1: Density distribution of protons  $\rho(\omega_s)$  with a specific eigenfrequency  $\omega_s$ .

## 8.2 Impulse response

Error signals in the RF, or intentionally applied signals, can cause jumps in the RF phase of the RF cavities. A sufficiently short jump in the RF phase kicks the protons in a bunch to other trajectories in phase space. For a short while after the kick all protons oscillate in phase and as a result the bunch charge centroid (bunch center) oscillates. Because of the frequency spread, the protons lose their phase relation after a certain time and the bunch center stops oscillating. This damping of the bunch center oscillation is commonly called ‘decoherence’.

In contrast, ‘Landau damping’ commonly denotes the stabilization of a bunch oscillation driven by a coherent instability [38]. In the case of an instability, a force proportional to the deviation of the beam itself drives bunch oscillations. The frequency spread within a bunch stabilizes the unstable behavior.

Both effects are results of the frequency spread within a bunch and belong together. Measurements of the decoherence time allow estimations of the frequency spread, and with that on Landau damping.

A rigorous treatment of decoherence can be found in the references quoted in A. W. Chaos and M. Tigners handbook [15]. Here we will quote only the results used for data interpretation.

A rule-of-thumb for the bunch center oscillation after a kick is that the oscillation amplitude decays with a time constant given by the inverse frequency spread  $|s_\omega|$  [55, 56], namely

$$\langle \Delta\phi(t) \rangle_{\max} = \langle \Delta\phi(0) \rangle \exp[-|s_\omega| t], \quad (8.24)$$

this results in a decoherence time of

$$\tau_d = \frac{1}{|s_\omega|}. \quad (8.25)$$

An exact treatment of the decoherence of a kicked, Gaussian bunch results in the following decay of the oscillation amplitude [15]

$$\langle \Delta\phi(t) \rangle_{\max} = \frac{\langle \Delta\phi(0) \rangle}{1 + (2s_\omega t)^2} \exp \left[ -\frac{(2s_\omega t)^2}{1 + (2s_\omega t)^2} \frac{\Delta l^2}{2l_{FWHM}^2} \right]. \quad (8.26)$$

For small kicks  $\Delta l \ll l_{FWHM}$  the exponential function is about one and the time until the amplitude decays to  $1/e$  of the initial amplitude, is given by

$$\tau_d = \frac{\sqrt{e-1}}{2} \frac{1}{|s_\omega|} \approx \frac{0.655}{|s_\omega|}. \quad (8.27)$$

Apart from the factor 0.655 in the decay times, the decoherence after small kicks is approximately described by an exponential. Figure 8.2 shows the time behavior.

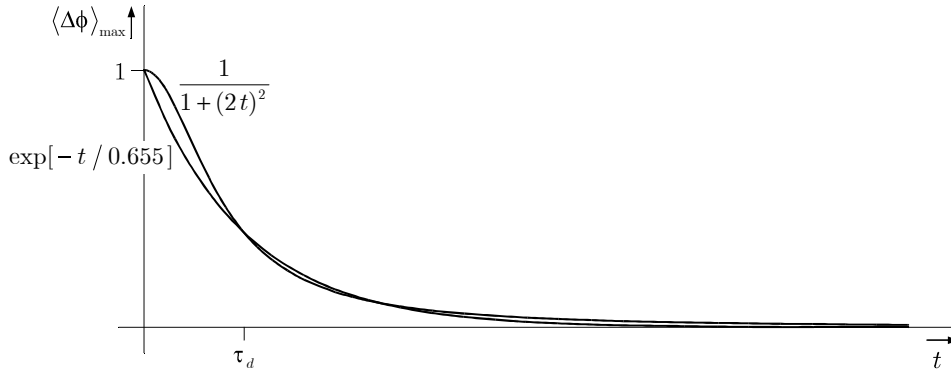


Figure 8.2: The time behavior of the decoherence for a Gaussian bunch and a corresponding exponential decay.

These rules are only approximate, because real bunches are not Gaussian. Particularly if one performs several kicks, one influences the population and decoherence times. In general, the oscillation envelope depends on the bunch shape. (8.26) is valid for a Gaussian bunch, whereas binomial distributions lead to other oscillation envelopes. In this case, S. Koscielniak and H. J. Tran showed the following point [54]: The rate of decoherence depends to first order on the average gradient of the distribution.

The formulae presented are only valid when other damping mechanisms, coming from the cavities tuning or RF control loops, have time constants well above the decoherence time.

### 8.3 Response to harmonic excitation

A harmonic excitation affects only those protons whose oscillation frequencies are near that of the excitation.

First, we neglect rearrangement effects in the density distribution of a bunch. Since only protons with oscillation frequencies near the modulation frequency are excited, Landau damping does not exist. This driven bunch center oscillation is damped when the cavity tuning  $\Delta\omega = \omega_{cav} - \omega_{RF} < 0$  is negative (Robinson damping [58]). Since this damping acts on the bunch center, we expect a response similar to that of a driven, damped harmonic oscillator, with damping constant  $\delta$ , weighted with the oscillation frequency distribution.

We define the beam transfer function (BTF) of a single bunch as its response  $\langle \Delta \phi(t) \rangle$  to an excitation with amplitude  $\Delta \phi_{RF}$  and frequency  $\omega_{\text{mod}}$

$$BTF \equiv \frac{\langle \Delta \phi(t) \rangle}{\Delta \phi_{RF} \exp[i \omega_{\text{mod}} t]} \quad (8.28)$$

Amplitude and phase are

$$A_{BTF} = |BTF| \quad (8.29)$$

$$\varphi_{BTF} = \tan^{-1} \frac{\text{Im } BTF}{\text{Re } BTF} \quad (8.30)$$

Figure 8.3 shows computed BTFs for different bunch lengths and constant damping when we use the frequency distribution (8.22). A longer bunch has a lower maximum BTF amplitude

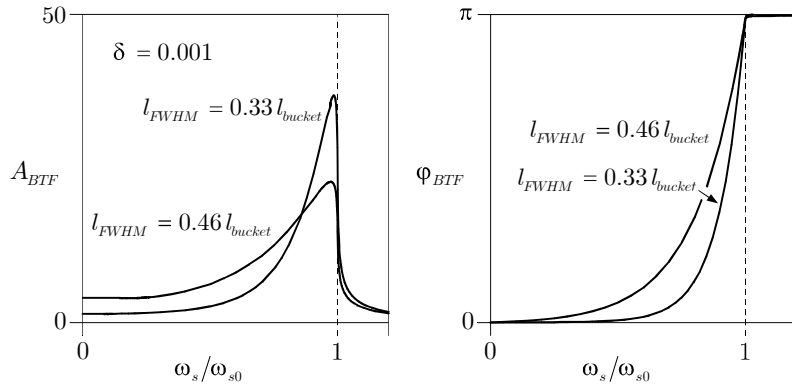


Figure 8.3: BTF at different bunch length but constant damping.

and more asymmetric curves of amplitude and phase. In comparison, figure 8.4 shows the BTFs for different damping constants with constant bunch length. Higher damping leads to a lower

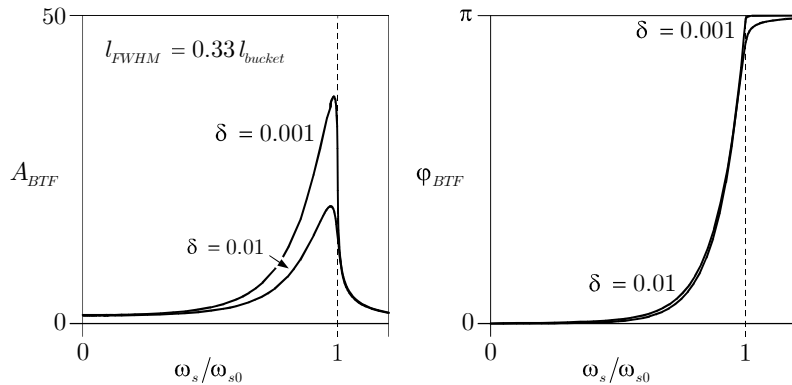


Figure 8.4: BTF at different damping for a fixed bunch length.

maximum BTF amplitude and the symmetry of the BTF curves is less influenced.

From these considerations, we have to expect asymmetric BTFs, whose maximum amplitudes and form of the amplitude and phase curves depend on the bunch length and the damping  $\delta$ .

In practice, we measure the BTF by changing the excitation frequency step by step and acquiring the amplitude and phase response. However, the oscillation amplitude of each proton increases and consequently the eigen-frequency decreases. This leads to an irreversible change of the distribution of the oscillation amplitudes in a bunch and to a bunch lengthening. When we excite with the next frequency, we measure the values from the new population.

Figure 8.5 shows this effect for a single proton, when we change the excitation frequency from higher to lower values, and figure 8.6, when we start at lower frequencies. The observed

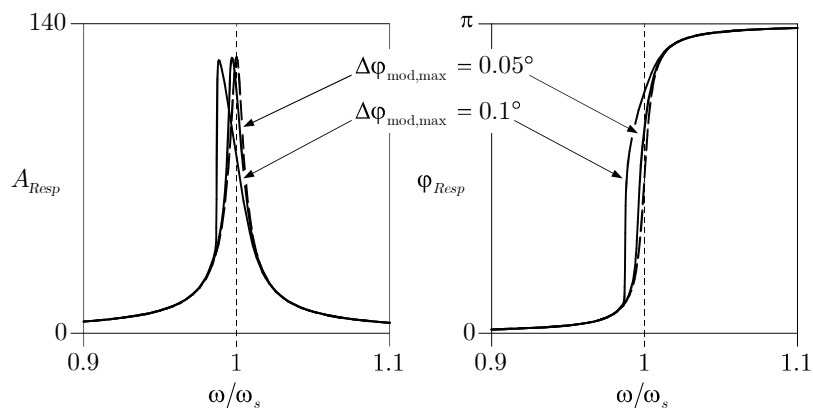


Figure 8.5: Calculated response of a single proton, due to a step by step stimulation, from higher to lower frequencies.

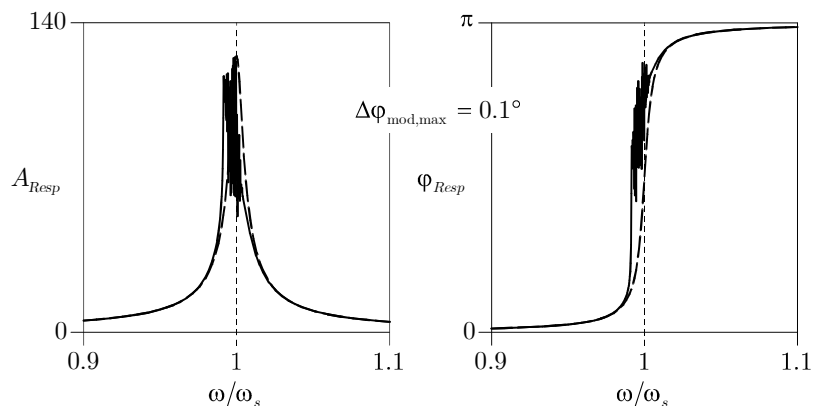


Figure 8.6: Calculated response of a single proton, due to a step by step stimulation, from lower to higher frequencies.

response curves are shifted to lower frequencies compared to the response curve of a single proton, dashed line, depending on the excitation amplitude. The frequency distance to the previous measurement and the duration also influences the observed response curve. The smaller the excitation amplitudes, the smaller is this effect and one can expect tolerable measurement results.

It is also conceivable, that we initiate instabilities with BTF measurements. Then one obtains a growing response amplitude. After some time the oscillation amplitudes increase, so that the proton population with synchrotron frequencies near the actual excitation frequency is massively decreased. This reorganization of the frequency distribution may lead to Landau damping. When the unstable behavior and this damping reaches an equilibrium state, we can

also speak about a beam transfer function, since we defined it by the ratio between the response and the excitation (8.28). But we cannot expect a behavior as shown in figures 8.3 and 8.4.

For a measurement of the BTF, we change the excitation frequency step by step, this means we scan the individual frequencies. Hence, we also have to expect an influence of the scan direction on the measurement results:

Assume we scan from higher to lower frequencies. Then we excite first the particles with the highest eigen-frequencies. These are the particles in the bunch core, having the smallest oscillation amplitudes. By exciting them, they get larger oscillation amplitudes and with that smaller eigen-frequencies. In the next step, we decrease our excitation frequency and excite these particles once more, together with the particles originally having eigen-frequencies at the new excitation frequency. We once again increase the amplitudes of these particles and decrease their eigen-frequencies. In this way, we ‘push’ the particles step by step from higher to lower eigen-frequencies. This results in larger values for the BTF amplitudes.

Assume we scan from lower to higher frequencies. Then, we excite first particles with the lowest eigen-frequencies and highest oscillation amplitudes. We decrease the eigen-frequencies of these particles. In the next step, when we increase the excitation frequency, we do not excite them once more because they already have lower eigen-frequencies. We only excite the particles originally having eigen-frequencies at the new excitation frequency. In contrast to a scan direction from higher to lower frequencies, the particles in the distribution are only excited once.

This should result in a hysteresis of the measured BTF. Landau and Robinson damping is expected to reduce this effect.

More information about BTFs can be found elsewhere [21, 59, 60].

## 8.4 Beam echoes

Normally, in many body systems of identical microscopic particles, one cannot stimulate and measure an individual particle. On the contrary, one always stimulates and measures the response of the ensemble. Provided the behavior of the particles is different, because of varying surroundings, this response is influenced by such deviations. The measured behavior of the ensemble compared to the behavior of a single particle can differ. Echo experiments are used to examine such effects. This technique exists in plasma physics, has become very sophisticated in solid states physics [61], and has been recently used in proton accelerator physics [15, 62, 63].

In the case of a proton bunch, we have the following situation: a sufficiently short jump in the RF phase e.g. a quarter of the synchrotron oscillation period, induces a phase oscillation. Shortly after the kick, all protons oscillate in phase and as a result the bunch center oscillates. Because of the synchrotron frequency spread, the protons lose their phase relation after a certain time and the bunch center stops oscillating. This damping of the bunch center oscillation is called decoherence, see section 8.1 and 8.2.

The individual protons within the bunch still oscillate with the frequencies and amplitudes caused by the phase kick. From a RF amplitude kick, it is possible to reconstruct a part of the initial phase dependence of the protons and thus obtain a bunch center oscillation. This is called the echo.

Some protons change their frequencies and amplitudes after the phase kick, due to scattering processes. Scattering can be caused by RF noise, other particles within the bunch and particles from outside. When there is a long time between the phase kick and the amplitude kick, more scattering processes take place. This influences the echo, it will become smaller.

The phase information can be regained, provided the decoherence time is smaller than the time constant of the scattering processes, which is normally true in a proton accelerator.



One can characterize bunch shape oscillations by the terms, called modes, of a series expansion. The first mode is a bunch center oscillation, called the dipole mode and the second one a bunch length oscillation, called the quadrupole mode. Thus, we refer to the RF phase kick as a dipole kick, because the dipole mode is excited, and to the RF amplitude kick as a quadrupole kick.

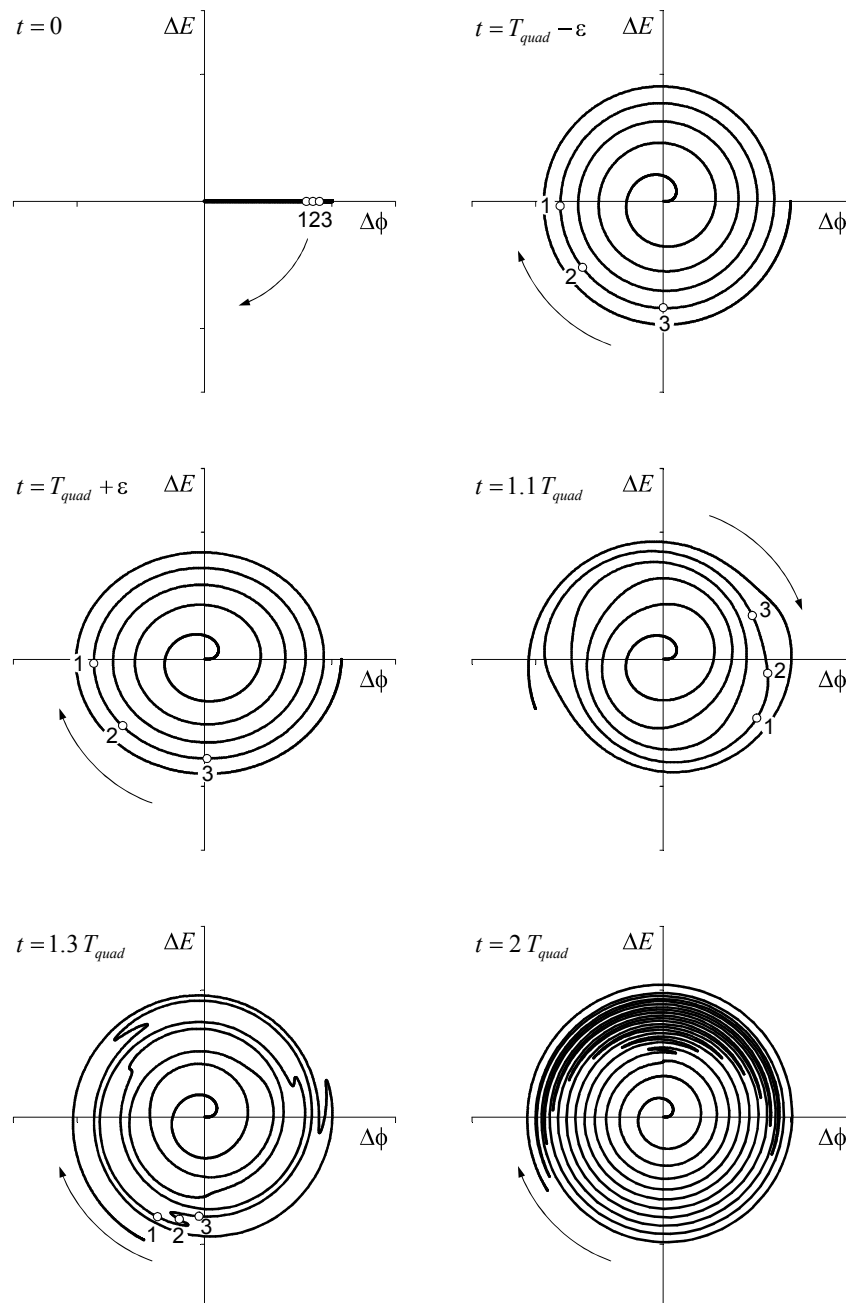


Figure 8.7: Deformation of the filamentation spiral, of an initial line distribution, leads to a wind up of spiral parts. This wind up is observed as the echo signal.

In figure 8.7 simulation results of the echo mechanism are shown, assuming a line distribution in the longitudinal phase space as initial condition. A RF dipole kick leads to a shifted bunch center in phase space, represented by the plotted line distribution at  $t = 0$ . The numbered protons no. 1, 2 and no. 3 oscillate in phase. Each proton moves on a circular trajectory in phase

space. Proton no. 1 has initially a smaller phase amplitude than protons no. 2 and 3,

$$\Delta\phi_{\max,1} < \Delta\phi_{\max,2} < \Delta\phi_{\max,3}. \quad (8.31)$$

It circulates in phase space faster than the other two, because of the steeper bucket potential at smaller amplitudes

$$\omega_{s,1} > \omega_{s,2} > \omega_{s,3}. \quad (8.32)$$

The protons disperse spiral like, see the population at  $t = T_{quad} - \varepsilon$  (with  $\varepsilon \rightarrow +0$ ). A RF quadrupole kick deforms this spiral, shown at  $t = T_{quad} + \varepsilon$ . The amplitude of proton no. 1 is now larger than the amplitudes of the protons no. 2 and 3,

$$\Delta\phi_{\max,1} > \Delta\phi_{\max,2} > \Delta\phi_{\max,3}. \quad (8.33)$$

This leads to an inversion of the frequency ordering for the viewed protons

$$\omega_{s,1} < \omega_{s,2} < \omega_{s,3}. \quad (8.34)$$

Now, proton no. 3 starts to catch up with protons no. 2 and 1, see phase space distributions at  $t = 1.1 T_{quad}$  and  $t = 1.3 T_{quad}$ . After the same amount of time, as between the phase jump and amplitude change,  $t = 2 T_{quad}$ , the maximum wind up of spiral parts is reached. The resultant asymmetric density distribution in phase space is observed as a phase oscillation of the center. This is called the beam echo.

Its worth mentioning that spin echoes in solid state physics comes from an inversion of occupied states  $n$ . The spin alignment, with respect to an external magnetic field, change sign due to the second kick. This can be expressed in changed signs of the Larmor frequencies  $\omega_{l,n} \rightarrow -\omega_{l,n}$ . A complete reconstruction of the original phase alignment of all spins is in principle possible.

At beam echoes, an inversion of the synchrotron frequency ordering of bunch parts is performed, and not of the entire bunch. Therefore, the initial phase dependence lead to an unbalanced condensation of the particle distribution in phase space, after the second kick, seen as reconstructed phase oscillation.

## 8.5 Expectations on response measurements

Putting it all together, we expect qualitatively the following results from beam response measurements:

### Response to harmonic excitations - BTF

The beam transfer functions (BTFs) are expected to be asymmetric, because the particle population has an asymmetric frequency distribution within a bunch. BTFs should depend on the cavity tuning which is causally connected to Robinson damping. We expect a hysteresis effect, depending on the scan direction.

BTF measurements are the starting point to analyze the stability behavior of beam feedback loops. In appendix A.6 principles of such stability estimations are demonstrated by means of the two narrow band beam feedback loops already mounted in the HERA proton ring.

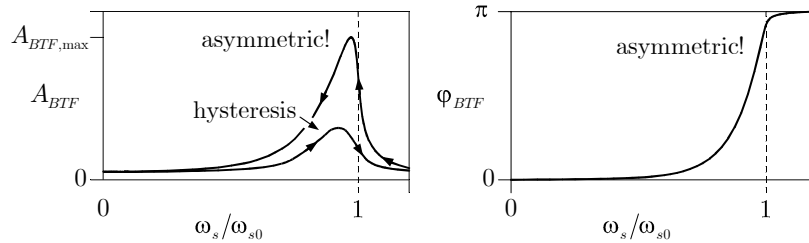


Figure 8.8: General expectations on measurable BTF values.

### Response to single kick excitations - decoherence

The response to phase kicks should lead to oscillation envelopes, decaying exponential or  $1/(1+4t^2)$  like. Since the decoherence time is proportional to the inverse frequency spread  $\tau_d \propto 1/s_\omega$ , it is expected to depend on the bunch length and the particular RF potential, which may be deformed by the second RF system.

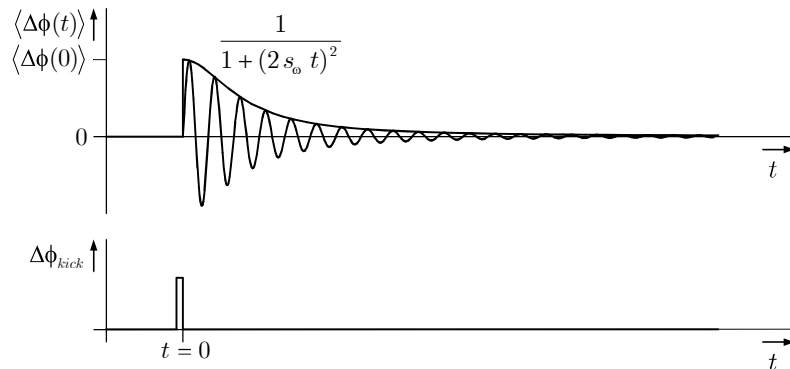


Figure 8.9: General expectations on measurable decoherence due to RF phase kicks.

From measured decoherence times one can estimate the frequency spread within a bunch. Hence, one can state whether there is enough Landau damping available to suppress instabilities.

### Response to double kick excitations - echoes

Measurements of beam echoes should look in general as in figure 8.10. An amplitude kick,

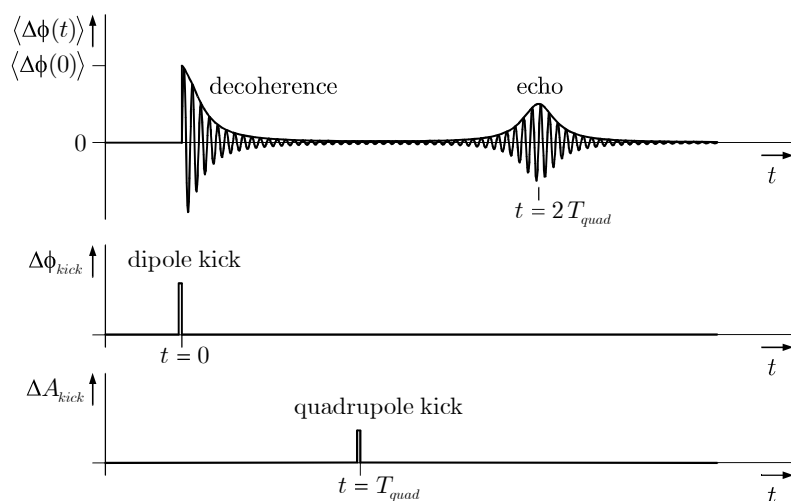


Figure 8.10: General expectations on measurable beam echoes.

some time after the bunch ceased oscillating, initiate an oscillation (echo) after the double time. The strength of the echo depends on the time delay between the two kicks  $T_{quad}$ , on noise in the RF, or on general diffusion processes. More RF noise for example should decrease the echo strength. Echo measurements are an extension of decoherence measurements. So all parameters influencing decoherence should also influence beam echoes, like the bunch length, the bunch shape and particular RF potentials resulting from the double RF system.

From beam echo measurements one can expect to learn something about diffuse processes and the production mechanism of un-bunched beam, so called coasting beam.

# 9 Beam Transfer Function

Before this thesis, no measurements of the BTF were performed at the HERA proton ring. So the goal of the technical setup and measurement results, presented here, was to establish BTF measurements at the HERA proton ring. The required parameters for the excitation had to be marked out together with the area of the BTF values. For theoretical considerations and expectations on beam transfer function measurements, see section 8.3.

Since the hardware setup, described in this thesis, was still under development and not fully available at the time of these measurements, W. Kriens and U. Hurdelbrink from DESY provided the electronics used. This setup has the advantage of a modulation adjustable with high accuracy, but the disadvantage is the low sensitivity and narrow bandwidth of the phase detector. For sufficiently high signal levels, we had to use 180 bunches. Unfortunately the bunches may perform not only synchronous phase oscillations, due to the modulated RF phase, but also multi-bunch oscillations. The interpretation is invalid if multi-bunch oscillations occur. We were able to distinguish between these two conditions since the first version of the multi-bunch detection software, using the real time measurement described, was available as a test version.

## 9.1 Measurement setup

For BTF measurements, one needs to modulate the RF phase in a defined way, and to measure the beam phase in response to this RF phase modulation. Such phase modulation units and phase measurements are available in beam phase feed-backs. So, it is natural to bypass the loop electronics with a measurement setup. We did this at the phase-loop II. This loop is described in chapter 3.3.

Preliminary studies with excitation amplitudes of about  $2^\circ$  caused synchrotron oscillation amplitudes larger than  $15^\circ$ , this is one order of magnitude larger than under normal circumstances. The result was an immediate beam blow up. A sophisticated setup was necessary, to provide well defined excitation amplitudes of about  $0.1^\circ$ . Figure 9.1 shows this setup. The ADC of the phase-loop II and the multiplexer are clocked with 100 kHz. As a result, the generated frequency  $f_{RF}$  can be changed by the offset frequency  $\Delta f$  as a function of the sampled ADC value  $\Delta f = 8 \frac{\text{Hz}}{\text{mV}} \text{ADC}_{IN}$  every  $10 \mu\text{s}$ . If we change the ADC output from zero to a given value for  $10 \mu\text{s}$  only, using the pulse generator with name ‘TEK HFS 9003 Stimulus System’, then the RF phase is changed by

$$\begin{aligned} \Delta\varphi_{\text{step},208} &= \Delta\omega \Delta t = 2\pi 8 \frac{\text{Hz}}{\text{mV}} \frac{A_{\text{mod}}}{31.6} 10 \mu\text{s} = 0.016 \frac{A_{\text{mod}}}{\text{V}} \\ &= 0.917^\circ \frac{A_{\text{mod}}}{\text{V}} \end{aligned} \quad (9.1)$$

$$\Delta\varphi_{\text{step},52} = \frac{\Delta\varphi_{208}}{4} = 0.004 \frac{A_{\text{mod}}}{\text{V}} = 0.23^\circ \frac{A_{\text{mod}}}{\text{V}}. \quad (9.2)$$

Performing such frequency changes at regular intervals of  $1/f_{\text{mod}}$ , one generates a stepwise change of the RF phase, see figure 9.2, which can be expressed as a Fourier series.



and multiplexer. One mode of the HFS 9003 outputs a rectangular signal with programmable level and length, when triggered, and allows a programmable dwell time before the next trigger is accepted. This level  $A_{\text{mod}}$  and the wait time  $1/f_{\text{mod}}$  were controlled via a remote connection (GPIB) from a particular software, running on an UNIX Workstation.

A TEK TDS 684a digital oscilloscope was used, to sample the signal of the beam phase detector, triggered by the output signal of the HFS 9003. This ensures that the response detected at the oscilloscope has the correct phase with respect to the RF modulation. Consideration of the phase detector calibration supplies the amplitude of the beam phase oscillation. Transferring the scope data via GPIB to the workstation, the BTF measurement software carried out a complex fast Fourier transformation. To suppress artificial transformation effects, only the data of the first modulation cycle with duration  $1/f_{\text{mod}}$  was used. The recorded amplitude of the beam phase  $\Delta\phi_{\text{max}}$  divided by the modulation amplitude yields the BTF amplitude. Due to the scope trigger used, the phase value resulted direct in the BTF phase.

## 9.2 Performed measurements

At the injection energy of 40 GeV, the buckets are provided mainly by the 52 MHz cavities. In normal operation it is not possible to operate the storage ring at this energy without any voltage in the 208 MHz cavities, since the tuner control loops always need control signals for proper operation. It is not possible to lock these loops in a controlled way at higher energies without danger of beam loss. So it is interesting to study the influence of the 208 MHz cavities on the damping behavior at low energy.

Figure 9.3 and 9.4 shows measured BTFs under normal conditions, i.e. all cavities and control loops were active. We measured BTF amplitudes of about 100.

Figure 9.5 shows the BTF without closed phase, amplitude and tuner control loops of the 208 MHz cavities. The tuners were held at stand by positions, so that the cavities were tuned off resonance. For beam loading reduction the fast-feedback loops were active. Figure 9.6 shows the same situation, but there we locked the tuners in the normal working position, i.e. tuning for optimum power adjustment between the final stage amplifiers and the cavities. In this situation, we observed much bigger BTF amplitudes and thus less damping, depending on the cavity tuning.

At higher energies, we measured BTFs only in normal operation conditions. Figure 9.7 shows an BTF, measured at 70 GeV. Here we verified a synchrotron frequency above 50 Hz, also noticed in section 5.5. The BTF shown in figure 9.8 was taken at 300 GeV. The measured BTF amplitude collapsed due to the onset of multi-bunch oscillations. As already mentioned, the narrow band phase measurement averages over many bunch phases. The average phase information is suppressed and may be completely destroyed by the presence of such oscillations. Hence, no meaningful measurement is possible.

At 920 GeV, we obtained results such as in figure 9.9 and 9.10. Unfortunately, we always excited multi-bunch oscillations in the scans from higher to lower frequencies. So we can only give a lower limit for the true BTF amplitudes. This limit is at about 100.

An interesting point is the hysteresis effect when we started the scan from lower frequencies. An already discussed explanation (section 8.3) could be: One excites the protons which have eigen-frequencies near the actual excitation frequency. These protons reach higher oscillation amplitudes and therewith lower eigen-frequencies. With a scan from lower frequencies one excites protons only once, whereas with a scan from higher frequencies the same protons are excited several times. This results in larger BTF amplitudes, for scans from higher to lower frequencies.

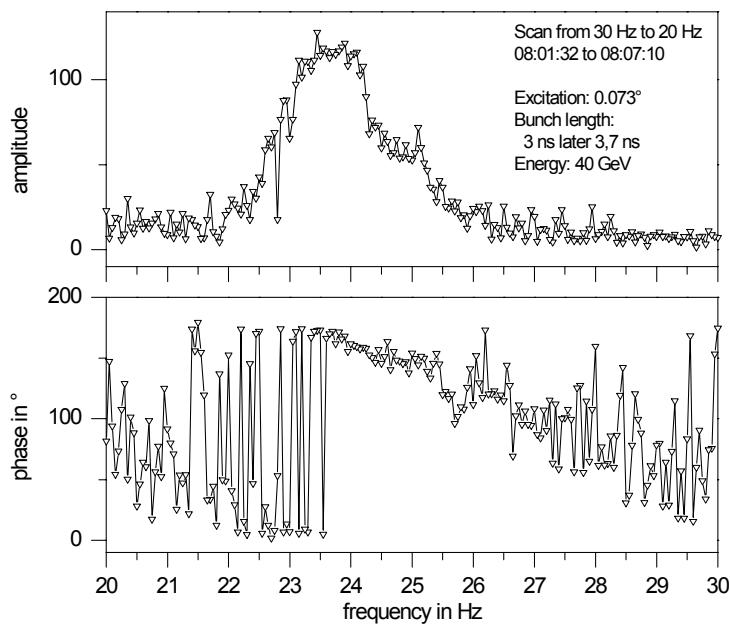


Figure 9.3: Standard situation, i.e. 52 MHz and 208 MHz cavity control systems on. ‘Excitation:  $0.073^\circ$ ’ means  $\Delta\varphi_{\text{mod,max}} = 0.073^\circ$  with respect to 52 MHz.

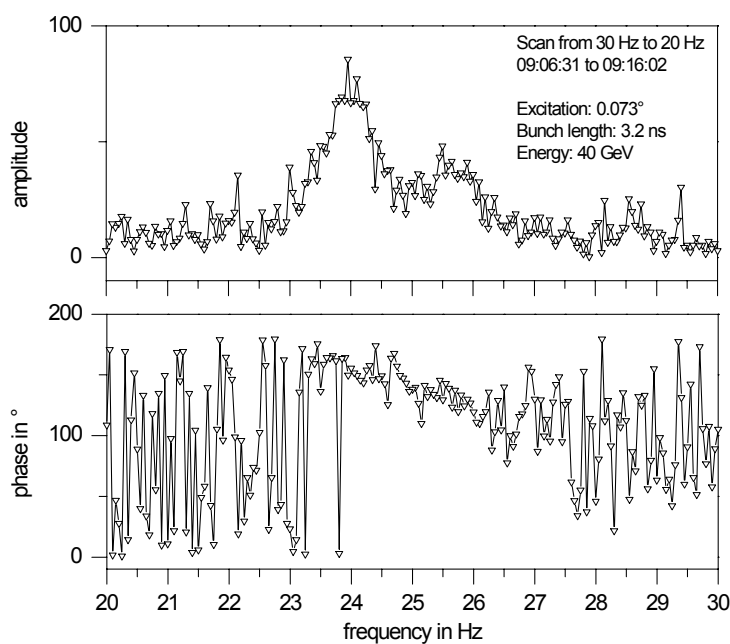


Figure 9.4: Standard situation after a new injection, i.e. 52 MHz and 208 MHz cavity control system on.



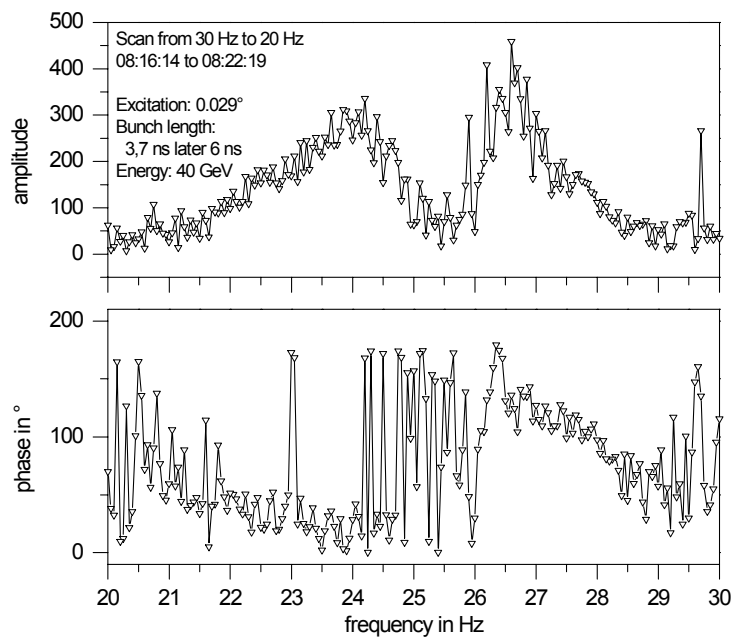


Figure 9.5: BTF with 52 MHz on and 208 MHz system off, but with 208 MHz fast feedback loop in operation. The 208 MHz tuners were in standby positions.

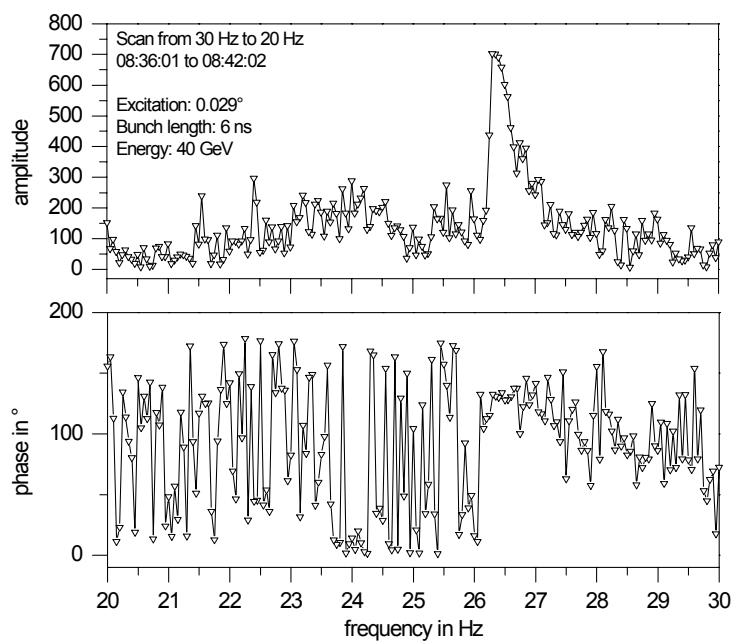


Figure 9.6: BTF with 52 MHz on and 208 MHz system off, but with working 208 MHz fast feedback loop. The 208 MHz tuners were locked in the normal working positions.

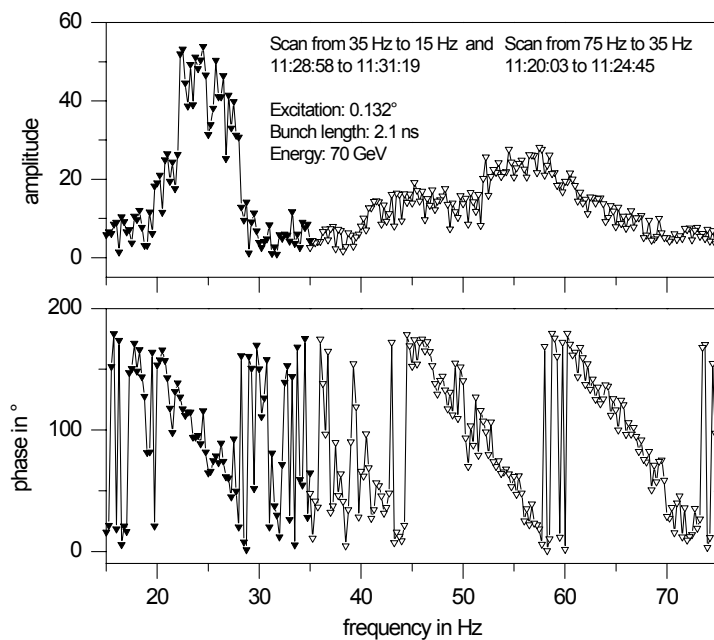


Figure 9.7: Standard situation at 70 GeV. One can see the synchrotron frequency above 50 Hz.

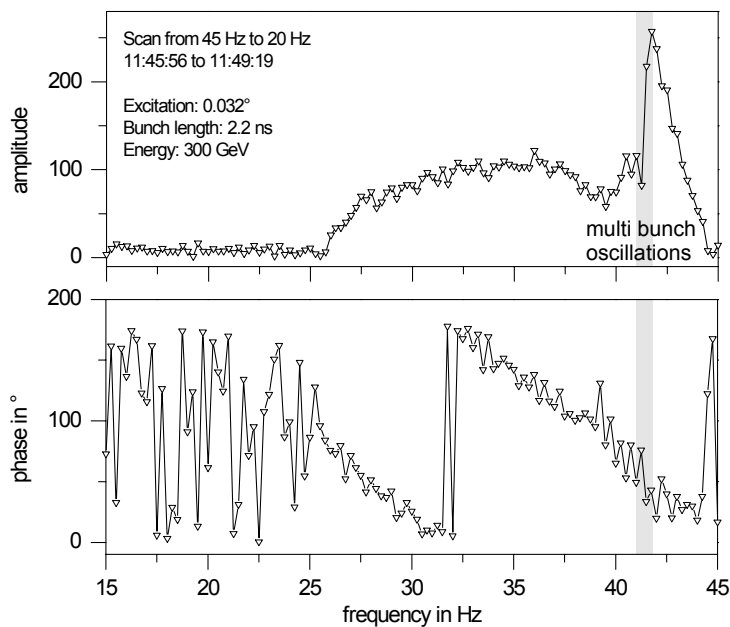


Figure 9.8: Standard situation at 300 GeV with higher multi bunch oscillation modes in the marked area.

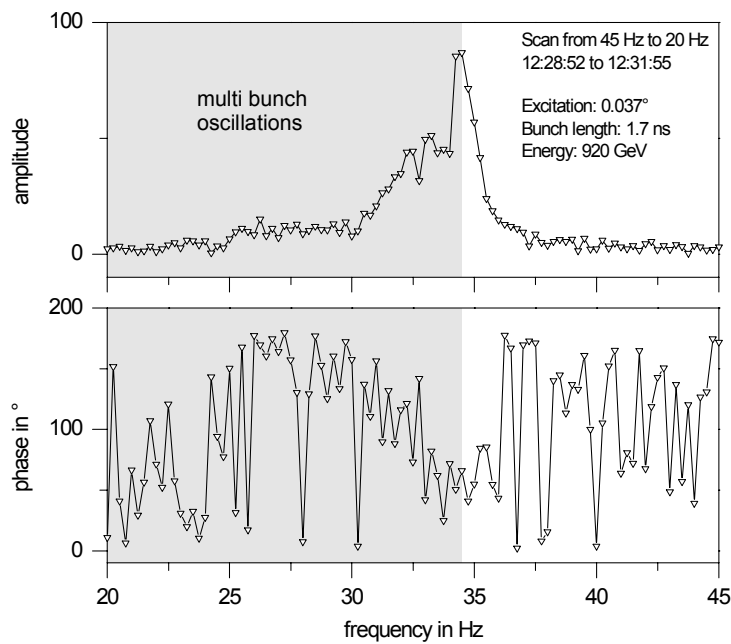


Figure 9.9: Standard situation at 920 GeV. We observed higher multi bunch oscillation modes at the marked area.

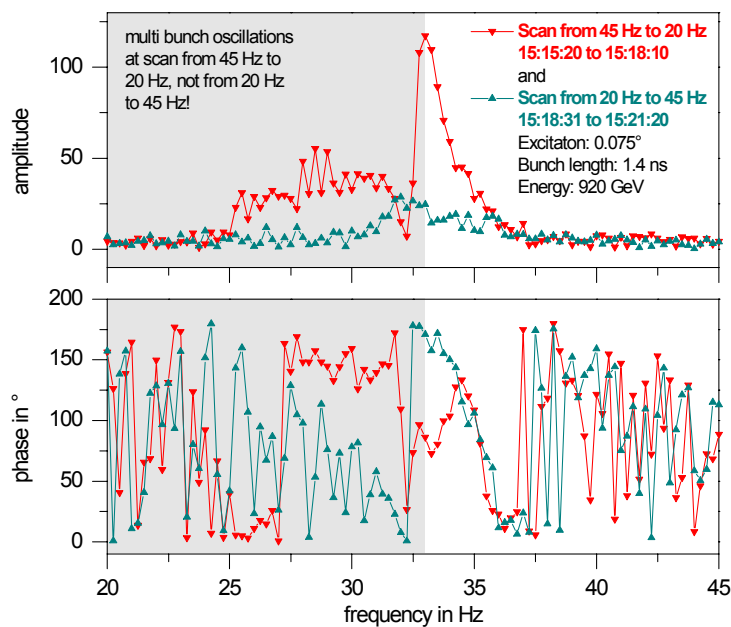


Figure 9.10: A hysteresis effect at different scan directions.

### 9.3 Phase error in the measurements

The precision of a phase value depends on the corresponding amplitude. Phase values, measured at low amplitudes, have a large spread. Such values were rejected by hand for the subsequent

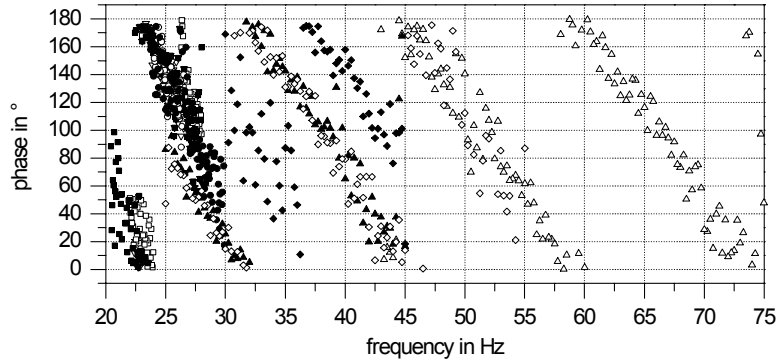


Figure 9.11: The phase values between 20 Hz and 75 Hz, taken from several BTF measurements suggest a systematic phase error in our measurements.

examination. Figure 9.11 shows the remaining phase values for BTF measurements for frequencies from 20 Hz to 75 Hz. The data shows a pattern, suggesting a systematic phase shift independent of the individual BTF measurements. Perhaps, we have a systematic error in our phase measurements. Until now we could not localize it for a correction.

### 9.4 Results

The measurements presented here were a first attempt to measure BTFs at the HERA proton storage ring. The main goal was to get an overview of typical values involved in such measurements and to establish hardware configurations. As suggested in section 8.3, these measurements are difficult to interpret since proton beams are not damped due to synchrotron radiation and therefore one always changes the proton populations in the bunches by the excitation.

Table 9.1 contains the main observed BTF values for the different energies and conditions of the storage ring.

The second difficulty is the narrow band phase measurement with the relatively low level of the output signal,  $\Delta\phi$  in figure 9.1. The signal level is not sufficient for a single bunch measurement, and so we had to work with many bunches. Unfortunately we often encountered multi-bunch oscillations, then the technique is not applicable. By using the real time measurement for bunch phases one may be able to record BTFs for single bunches in the future. The BTF values here obtained may help to optimize a new measurement setup at the HERA proton ring.

Nevertheless, the BTF values obtained may serve for first estimations on achievable damping rates or general technical parameters of a possible future coupled bunch feedback system.

energy	52 MHz cavities & controls	208 MHz cavities & controls	208 MHz tuners	scan direction	BTF amplitude
40 GeV	standard settings	standard settings	standard settings	down	$\approx 100$
40 GeV	standard settings	only fast- feedback on	off resonant fixed	down	$\approx 400$
40 GeV	standard settings	only fast- feedback on	standard settings	down	$\approx 750$
70 GeV	standard settings	standard settings	standard settings	down	$\approx 50$ (23 Hz) $\approx 20$ (55 Hz)
300 GeV	standard settings	standard settings	standard settings	down	$> 250$
920 GeV	standard settings	standard settings	standard settings	down	$> 100$
920 GeV	standard settings	standard settings	standard settings	up	$\approx 50$

Table 9.1: Observed BTF amplitues for the different energies and set ups of the storage ring.



# 10 Decoherence and Beam Echoes

As mentioned, Landau damping and decoherence are results of the incoherent frequency spread and belong together. Measurements of the decoherence time allow conclusions on the frequency spread and, consequently, on the Landau damping and the longitudinal stability. For this reason, we started to establish measurements of the decoherence time at the HERA proton ring. Before this thesis, such measurements were not technically feasible in HERA.

If one performs not only a phase kick for decoherence measurements, but also, after the decoherence time an amplitude kick, one gets a ‘beam echo’. The additional technical effort compared to pure decoherence measurements is small. Echo experiments are a powerful tool for the study of diffuse processes in many body systems. After observation of coasting proton beam production, first seen by the HERA-*B* experiment [64], we started also to establish beam echo measurements.

For theoretical considerations and expectations on decoherence and beam echo measurements, see section 8.2. In this chapter, we will discuss the technical principles used and the measurement results obtained.

W. Kriens and U. Hurdelbrink provided the pulse generator, together with its remote control. For the detection of the RF and the beam response, we used the fast longitudinal diagnostic system. Together, we developed the method to generate the kicks, needed for the measurements of decoherence and echoes. This required some initial tests aimed at demonstrating sufficiently short and powerful RF deflections. We had to take into account the technical characteristics of the RF control systems. Without taking these details into account, several feedback loops would have suppressed the RF deflections. We will discuss this in the first section.

To detect the beam response, we used the real time bunch phase and length measurement with a modified timing scheme. In contrast to the multi-bunch measurements presented in chapter 5, we measured only one bunch, to reach observation times up to 70 ns, due to the relatively high amount of ADC memory available. The required timing is presented, together with determinations of the measurement accuracy, in the second section.

In the subsequent section, ‘pictures’ of longitudinal bunched beam echoes in the HERA proton ring are presented.

In the fourth section, results on the decoherence time at 40 GeV and 920 GeV for different bunch lengths are given. This section contains also the results of measurements of the echo strength, depending on the kick delay.

## 10.1 RF kick production

At 40 GeV, the RF potential is dominated by the voltages in two 52 MHz RF cavities. The necessary RF kicks are therefore most effectively applied by modulating the RF of one of the 52 MHz cavities. During acceleration to 920 GeV, the RF amplitude of the 208 MHz cavities is increased such that, at 920 GeV these systems mainly build up the RF buckets. In this case the RF kicks must be produced by an intervention into the RF control system of one 208 MHz cavity.

Since the technical assembly of both RF cavity control systems is different, this requires two different techniques for the RF kick production. To determine the techniques, some tests

and small modifications to the RF cavity control systems were necessary.

To generate two rectangular signals with programmable amplitude, width, and time between them, we used the four channel digital delay / pulse generator DG535 from Stanford Research. It was controlled, via a GPIB connection, by a UNIX workstation. This generator also provided a trigger signal, to start the fast longitudinal beam diagnostics.

### 10.1.1 52 MHz RF cavity control system

The 52 MHz RF cavity control system provides an input for an additional RF signal, to compensate beam loading. One can add an arbitrary signal to the RF control signal which drives the

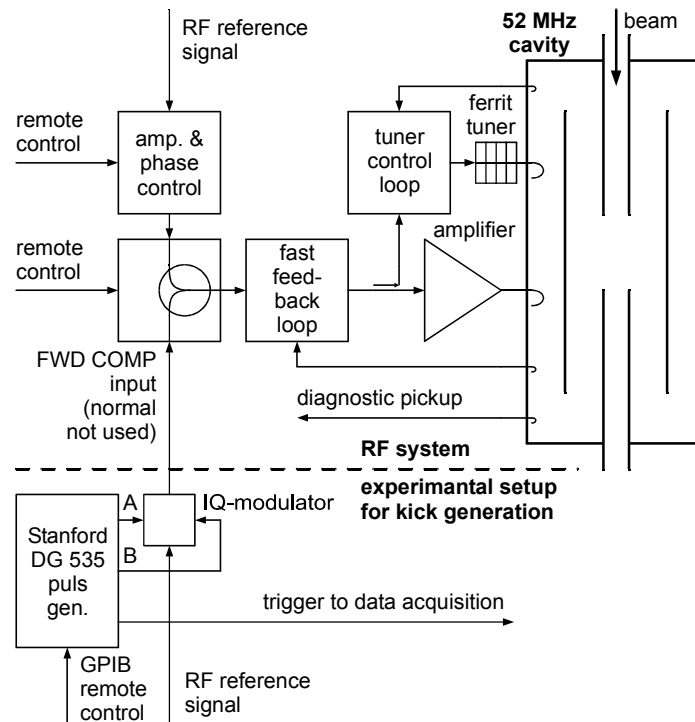


Figure 10.1: The 52 MHz RF System for the accelerating cavity and the modification for the RF kick generation.

final stage amplifier for the cavity. Two 52 MHz RF bursts are provided, using an I/Q modulator. The LO signal is provided by the 52 MHz RF reference. By supplying the I/Q demodulator at the I input with the first rectangular signal from the pulse generator, and at the Q input with the second one, two RF bursts with a phase relation of  $90^\circ$  are produced. The cable lengths are chosen such that the first burst produces a dipole kick and the second one a quadrupole kick. For the technical setup see figure 10.1.

Amplitude and phase are set at the 52 MHz RF cavity control system via a control without feedback, ‘amp. & phase control’ in figure 10.1. Therefore, the kicks, produced by using the feedforward compensation input, were not suppressed by a control loop.

For checking the RF kicks, we use the I/Q demodulation of the diagnostic pickup signal, described in chapter 6. A phase kick leads to a change of the imaginary part of the phasor and an amplitude kick leads to a change of the real part of the phasor, see figure 10.2. Figure 10.3 shows the phasor parts of the 52 MHz cavity no 1. Note, that the two RF bursts produce almost pure phase and amplitude kicks.



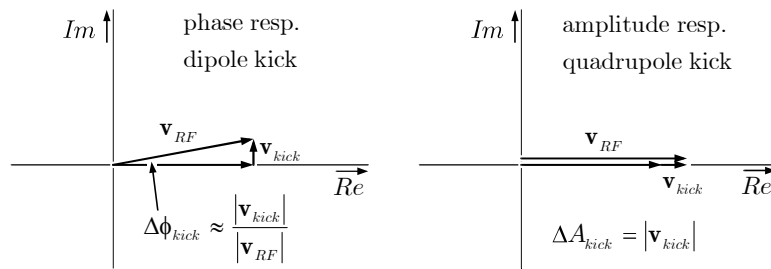


Figure 10.2: A phase, resp. dipole kick leads to a change of the imaginary part and the amplitude, resp. quadrupole kick to a change of the real part of the RF phasor.

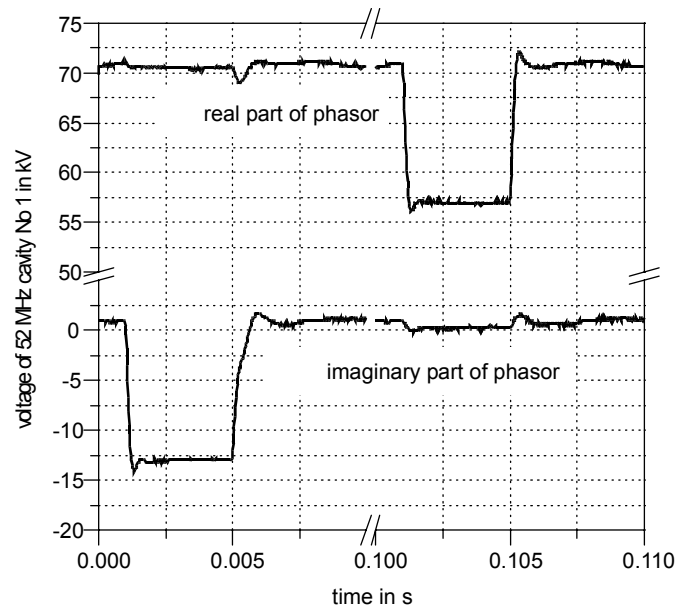


Figure 10.3: The I/Q demodulated 52 MHz pickup signal shows a dipole kick, followed by a quadrupole kick. For the dipole kick, a 4 ms long rectangular voltage step with 1 V was made, using the pulse generator, and for the quadrupole kick, a voltage step with 2 V.

### 10.1.2 208 MHz RF cavity control system

Initially, we proposed to produce the RF kicks at the 208 MHz RF cavity control system in the same way as at the 52 MHz system, i.e. via the feedforward compensation input. However, in contrast to the 52 MHz system, an amplitude and phase feedback control is implemented. It turned out that this feedback loop has a time constant shorter than the necessary kick duration of about 4 ms. This meant that it would suppress kicks produced by adding RF bursts via the feedforward compensation input.

A way out of this dilemma was a change of the set point of the amplitude and phase regulation loop [65], see figure 10.4.

Under normal conditions, the phase value set from the remote control, for a single 208 MHz cavity, is zero during the whole operation. The remote control was disconnected at this point and replaced by the pulse generator signal for the dipole kick.

One is able to add an amplitude modulation to the amplitude set point, chosen via the remote control at the condition unit, which was normally used to condition the cavity. Finally we were able to supply kicks, with sufficient rise times and power. The kicks are shown in figure 10.5.

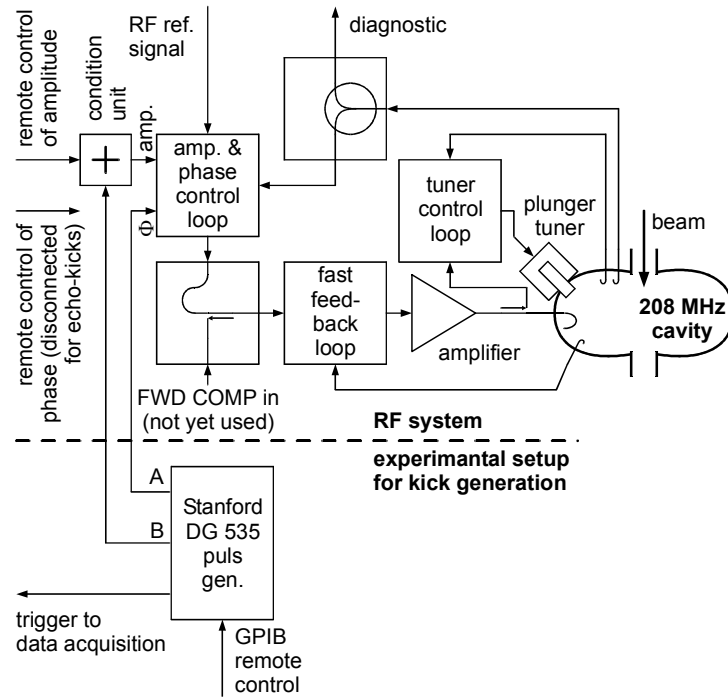


Figure 10.4: 208 MHz RF system of one cavity and the setup for the kick production.

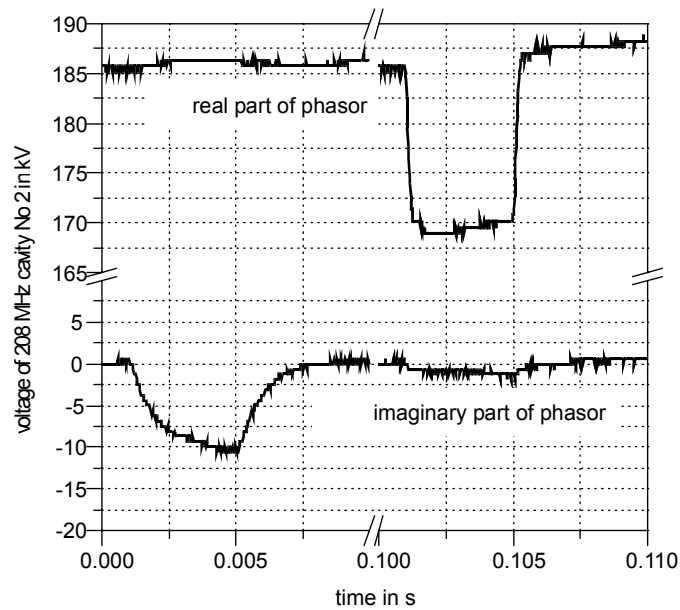


Figure 10.5: I/Q demodulated 208 MHz pickup signal with dipole and quadrupole kick. Both kicks were produced, by 4 ms long rectangular voltage steps with 0.5 V from the pulse generator.

## 10.2 Timing

Decoherence and echo measurements were carried out with single bunches only. This permits long observation times, because of the relatively high amount of ADC memory available. For example, we were able to observe the synchrotron oscillations of the bunch over a time of about 72 s. By reducing the observation time, we can increase the time resolution.

To measure the bunch phase and length at a certain time, we first sampled the signals in the dump gap, and directly afterwards, we measured the signals for the first bunch from the phase and the 208 MHz Fourier coefficient. By subtracting the values, obtained in the dump gap, from the bunch values, all offset errors are eliminated taking place at longer time scales than the time between both measurements. These are all unwanted signal modulations with frequencies lower than 1 MHz.

Performing such bunch phase and length measurements every 13th turn yields a sample frequency of 3.64 kHz. This is sufficiently high to observe synchrotron oscillations with frequencies of 20 Hz to 40 Hz, and bunch length oscillations with frequencies of 40 Hz to 80 Hz. In addition, this high sample frequency enables smoothing of the phase and amplitude curves by digital filters.

## 10.3 Errors of measured signals

For an estimation of the errors, we used measurements with an unperturbed bunch. By plotting a histogram of the differences between the individual measurements and the mean, one gets the error distribution function of the single shot measurements. One can reduce the measurement error by low pass filtering. In figure 10.6, the error distribution of bunch phase before and after filtering is shown.

In figure 10.7 one can see the error distribution of the bunch length measurement, from the raw data, and after filtering.

## 10.4 Observed beam echoes

In figure 10.8 and 10.9, typical beam echo signals in the HERA proton storage ring at 920 GeV, are shown. The dipole kick excites only dipole oscillations, there is no oscillation signal of the bunch length. The quadrupole kick only excites a quadrupole oscillation and no dipole oscillation.

Both kicks were 4 ms long, corresponding to one eighth of a synchrotron oscillation cycle. The dipole kick strength was about 40 kV and the quadrupole kick about 65 kV. With a cavity sum voltage of approximately 700 kV, one obtains the kick angle for the dipole kick

$$\Delta\phi_{\text{kick}} = \tan^{-1} \frac{40 \text{ kV}}{700 \text{ kV}} = 3.3^\circ.$$

We obtained a maximum amplitude of the synchrotron oscillation of about  $1^\circ$ . In the measurement shown, the dipole kick was applied 1 s after the trigger started the measurement, and the quadrupole kick at 1.8 s so that one can observe the echo at the time  $1 \text{ s} + 2 \times 0.8 \text{ s} = 2.6 \text{ s}$ . Filtering the data with a 100 Hz low pass filter delivers much cleaner conditions for further data analysis.

Figures 10.10 and 10.11 show a zoomed view of the beam response.

Figure 10.9 is evidence for an apparent bunch lengthening at the time of the dipole kick, caused by the onset of the filamentation process. In the subsequent sections, the mean bunch

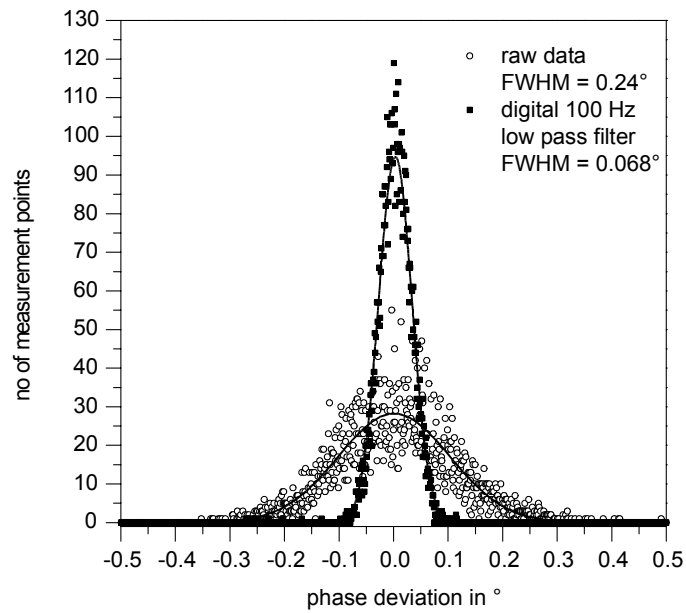


Figure 10.6: Error distribution of bunch phase measurement.

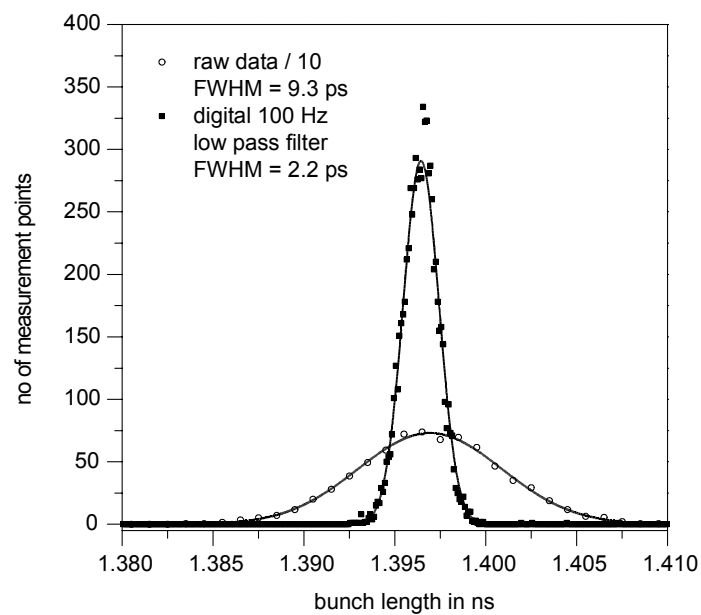


Figure 10.7: Error distribution of bunch length measurement.

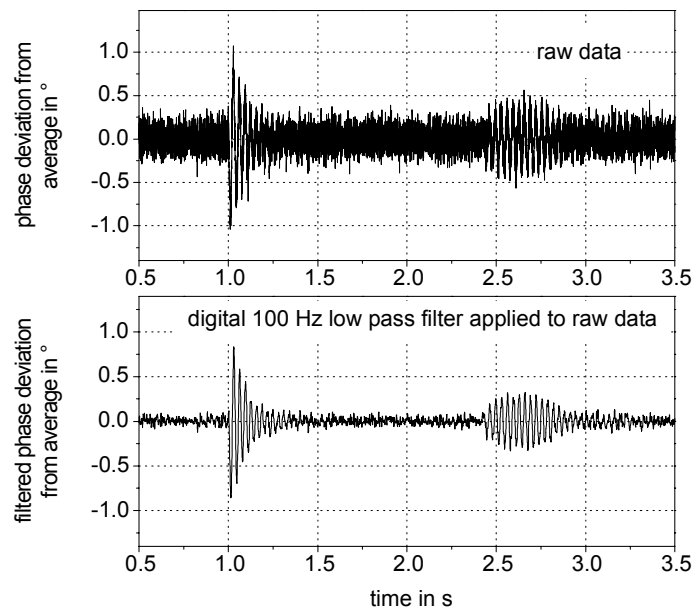


Figure 10.8: Bunch phase oscillation during a beam echo measurement.

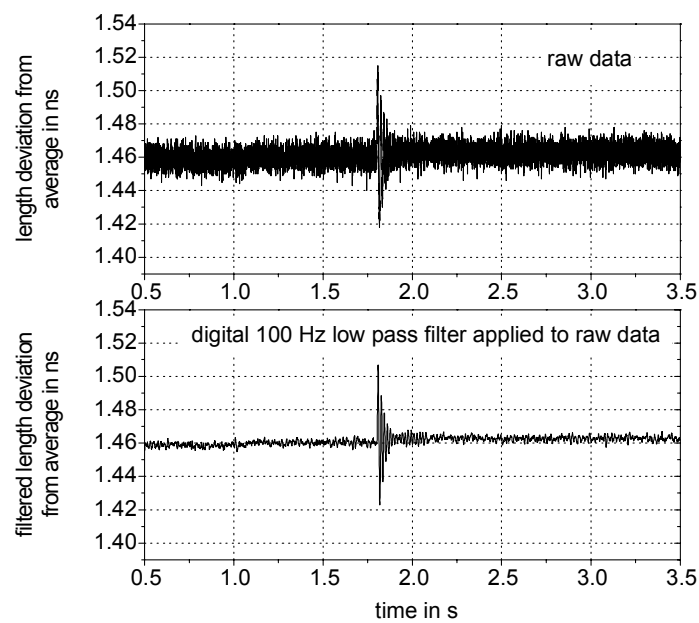


Figure 10.9: Bunch length oscillation during a beam echo measurement.

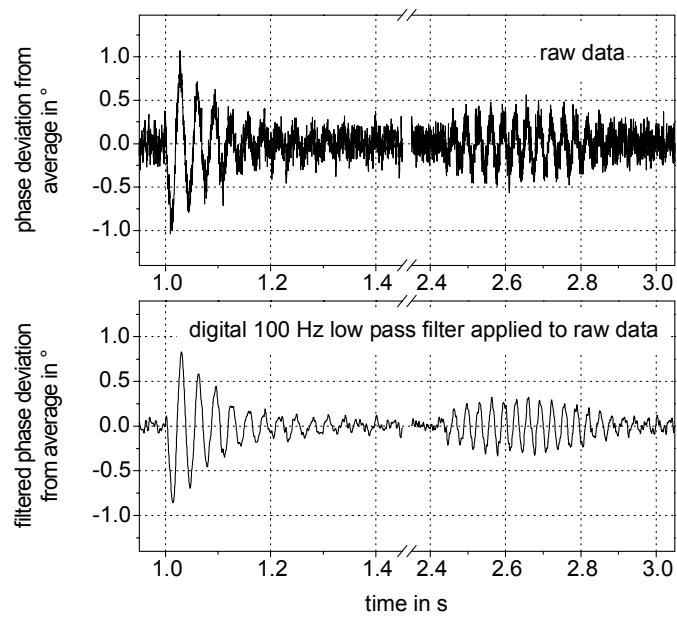


Figure 10.10: Zoomed view of bunch phase oscillation during a beam echo measurement (same data as figure 10.8).

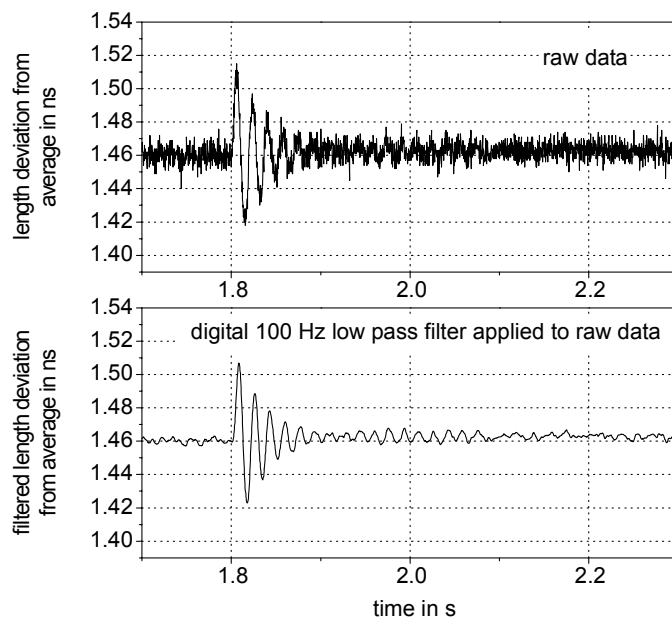


Figure 10.11: Zoomed view of bunch length oscillation during a beam echo measurement (same data as figure 10.9).

lengthening  $\Delta l$  is given for the measurements analyzed. This value is a measure of the influence of the kicks on the particle distribution within the bunch.

## 10.5 Decoherence

As already mentioned, an important stabilization effect for the longitudinal beam dynamic of a proton storage ring is the frequency spread within a bunch  $s_\omega$ , and with it Landau damping. From our measurements, we can derive the decoherence time  $\tau_d$  by fitting the decaying oscillation (section 8.2)

$$\Delta\phi(t) = \frac{\Delta\phi(0)}{1 + \left(2 \frac{0.6554}{\tau_d} t\right)^2} \sin[\omega_s t + \varphi] \quad (10.1)$$

to the beam phase oscillation response to the dipole kicks. From the decoherence time, we obtain the frequency spread with

$$|s_\omega| \propto \frac{1}{\tau_d}. \quad (10.2)$$

We will start our analysis at high energy, because the bucket potential is more sinusoidal than at low energy, and we can hope for a better agreement with our theoretical expectations.

At 920 GeV, the buckets are built up from three in-phase 208 MHz cavities, providing 540 kV, and the 52 MHz cavities, providing a voltage of 180 kV. The result is a nearly sinusoidal bucket potential, mainly defined by the 208 MHz cavities. Deviations of the bunch populations from a Gaussian distribution are not yet measurable. Considering this element of uncertainty, the estimated decoherence times in figure 10.12 agree with the values, calculated with the formulas from chapter 8.

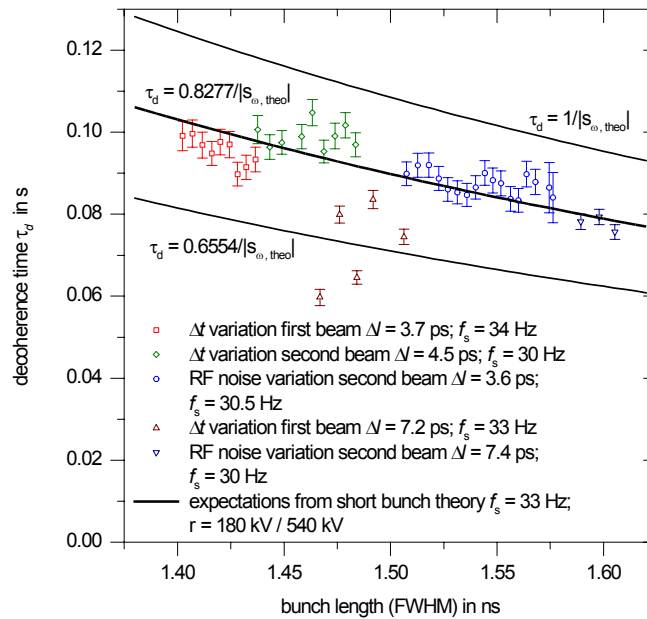


Figure 10.12: Decoherence time at 920 GeV.

For an accurate comparison we have first to calculate the frequency spread in dependence on the bunch length. For the given parameters and  $f_s = 33$  Hz we get

$$|s_\omega| \approx \frac{4.10}{s} \left( \frac{l_{FWHM}}{\text{ns}} \right)^2 \quad \text{at 920 GeV.} \quad (10.3)$$

From section 8.1, we know that the error in this calculation is smaller than 1%. The decoherence times from this frequency spread, with (8.27) i.e.  $\tau_d = 0.6554/|s_\omega|$ , are about 20% lower than the measured values. Decoherence times, calculated with the (8.25) i.e.  $\tau_d = 1/|s_\omega|$ , are 20% too large. Since the calculation of the frequency spread is one order of magnitude more accurate, we can assume, this is caused by deviations of the bunch shape from a Gaussian distribution. A good compromise for calculations may be the use of a curve in between. We simply use  $\tau_d = 0.8277/|s_\omega|$ , which fits well with the measured values.

Figure 10.13 shows decoherence time constants at 40 GeV, determined from different series of measurements. At this energy, the 52 MHz system builds up the bucket with a voltage of

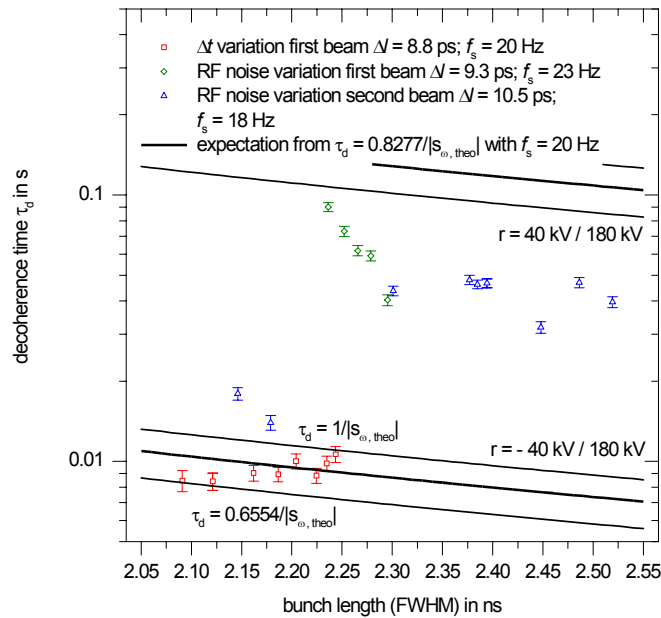


Figure 10.13: Decoherence time at 40 GeV.

180 kV. Three of the four 208 MHz cavities are in phase, and one runs with a phase shift of  $180^\circ$  and compensates most of the voltage of these three cavities. According to the set points in the accelerator control system, the remaining 208 MHz voltage should be 5 kV. With these parameters we would obtain, for  $f_s = 20$  Hz, a frequency spread within a bunch of

$$|s_\omega| \approx \frac{0.3784}{s} \left( \frac{l_{FWHM}}{\text{ns}} \right)^2 \quad \text{at 40 GeV and } r = \frac{5 \text{ kV}}{180 \text{ kV}}. \quad (10.4)$$

For a bunch length of  $l_{FWHM} = 2.3$  ns, this yields a decoherence time of

$$\tau_d \approx 0.8277/|s_\omega| = 0.41 \text{ s} \quad \text{at 40 GeV and } r = \frac{5 \text{ kV}}{180 \text{ kV}}. \quad (10.5)$$

Even the largest measured value is smaller than 0.1 s. This is at least a factor of four different from the expected values. This divergence allows only one conclusion: Something is wrong in



the calibrations of the cavity voltages at low energy. Other ratios of the RF voltages would lead to the frequency spreads

$$|s_\omega| \approx \frac{1.220}{\text{s}} \left( \frac{l_{FWHM}}{\text{ns}} \right)^2 \quad \text{at 40 GeV and } r = \frac{40 \text{ kV}}{180 \text{ kV}} \quad (10.6)$$

$$|s_\omega| \approx \frac{18.0}{\text{s}} \left( \frac{l_{FWHM}}{\text{ns}} \right)^2 \quad \text{at 40 GeV and } r = \frac{-40 \text{ kV}}{180 \text{ kV}}, \quad (10.7)$$

and with it, to decoherence times for  $l_{FWHM} = 2.3 \text{ ns}$  of

$$\tau_d = 0.8277/|s_\omega| = 0.128 \text{ s} \quad \text{at 40 GeV and } r = \frac{40 \text{ kV}}{180 \text{ kV}} \quad (10.8)$$

$$\tau_d = 0.8277/|s_\omega| = 8.68 \text{ ms} \quad \text{at 40 GeV and } r = \frac{-40 \text{ kV}}{180 \text{ kV}}. \quad (10.9)$$

This means, at injection energy we deal with a very non-parabolic bucket potential, leading to a large frequency spread, whereas we do not exact know, in which way this bucket is composed out of the two RF systems. But this large frequency spread leads to a good longitudinal stability, which makes injections much easier. The beam is less sensitive to steps in the RF voltages, caused by injection. We will come back to this topic in section 11.3.

## 10.6 Echo strength depending on kick delay

One motivation to set up beam echo measurements was to measure the dependence of the beam echo strength on the time delay between the dipole and quadrupole kick  $\Delta t = T_{\text{quadrupole}} - T_{\text{dipole}}$ . We hope to learn more about diffusive processes from the measured curve, such as intra-bunch scattering, processes caused by RF noise, etc.

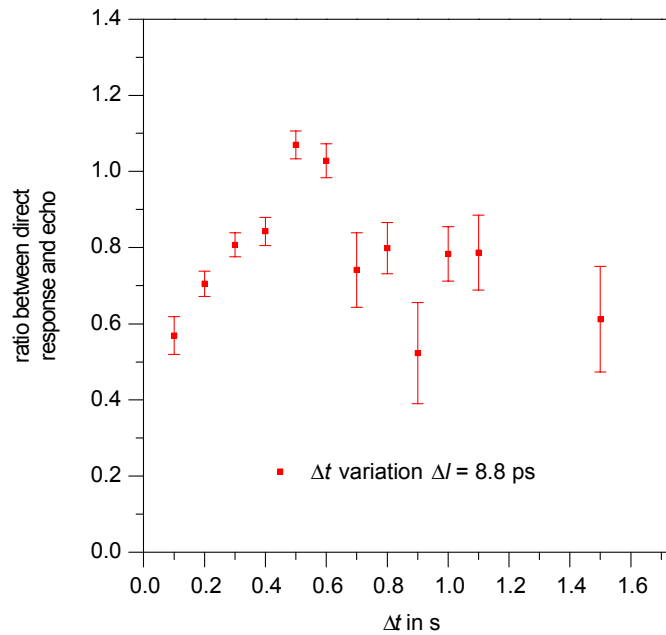


Figure 10.14: Echo strength as a function of the time delay between the two RF kicks at 40 GeV.

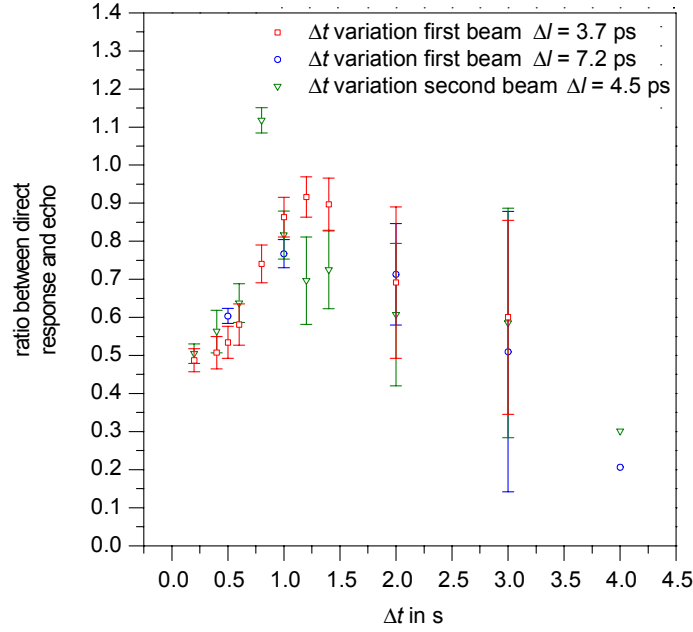


Figure 10.15: Echo strength versus the time delay between the two RF kicks at 920 GeV.

Unfortunately, the shape of the echo amplitude is very sensitive to the quadrupole kick strength<sup>1</sup>. Thus, the maximum amplitude of the echo per maximum amplitude of the initial dipole oscillation is not a very good indicator for the echo strength. The integral over the echo amplitude seems to depend less on the quadrupole kick strength<sup>2</sup>. Instead, for data analysis, the ratio of the integrals over the absolute value of the phase oscillations  $\Delta\phi(t)$  was used. The dipole kick response is

$$\Sigma_{\text{dipole}} = \int_{T_{\text{dipole}}}^{T_{\text{quadrupole}}} |\Delta\phi(t)| dt$$

and the echo strength

$$\Sigma_{\text{echo}} = \int_{T_{\text{quadrupole}}}^{T_{\text{quadrupole}} + 2\Delta t} |\Delta\phi(t)| dt.$$

By subtracting the noise

$$\frac{\Sigma_{\text{noise}}}{s} = \frac{\int_{T_0}^{T_{\text{dipole}}} |\Delta\phi(t)| dt}{T_{\text{dipole}} - T_0}$$

from the strength of the dipole kick

$$\Sigma_{\text{dipole,corr}} = \Sigma_{\text{dipole}} - (T_{\text{quadrupole}} - T_{\text{dipole}}) \frac{\Sigma_{\text{noise}}}{s}$$

and the echo

$$\Sigma_{\text{echo,corr}} = \Sigma_{\text{echo}} - 2\Delta t \frac{\Sigma_{\text{noise}}}{s},$$

<sup>1</sup>see figure 16 in [62]

<sup>2</sup>see again figure 16 in [62]

the ratio between direct response and echo was calculated

$$\frac{\Sigma_{\text{echo,corr}}}{\Sigma_{\text{dipole,corr}}}.$$

The fluctuation of the noise amplitude is equivalent to the uncertainty of the calculated kick strength.

Figure 10.14 shows the echo strength, divided by the dipole kick strength, versus the time deviation between the two RF kicks at 40 GeV.

At 920 GeV, three measurement series were taken with different parameters, the result is shown in figure 10.15.

Until now, we are not aware of a theory, describing bunched beam echoes in a double harmonic RF system, as used at the HERA proton ring. It is beyond the scope of this thesis to develop such a theory. A comparison of our results with theory may be carried out as soon as theoretical statements exist. For the multi-bunch stability of the HERA proton ring, this plays no role.

## 10.7 Echo strength depending on RF noise

In view of the presence of unbunched coasting beam, detected by the experiment HERA-B [64], the question arose whether noise in the RF system could cause coasting beam.

In principle, one can analyze the influence of RF noise on the bunched beam by observing the ratio of unbunched beam current to bunched beam current, over long time periods, during an application of a random modulation of RF. Such measurements are time consuming, since the ratio is slow in change. If one could observe the effect of RF noise on the echo strength, beam echo measurements could be used as a complementary, but much faster examination method.

In the measurements performed, we checked whether one can observe a change of the echo strength, as a function of applied RF noise, with constant time deviation between the kicks. Smaller echo strength at higher RF noise levels were expected, since higher RF noise causes more protons in a bunch to change their oscillation frequency and amplitude through scattering processes. The echo was therefore expected to be smaller.

We measured a noticeable bunch lengthening as long as RF noise was applied. But we observed no influence of RF noise on beam echoes. This could be due to the relatively short time delay between the kicks in combination with the relatively low noise levels. In the future, one could try to increase the time delay between the kicks, until one can no longer measure echoes.

Other ideas, to use the fast longitudinal diagnostic system for the examination of incoherent beam dynamical effects, are based on the use of extremely narrow band filters [66].

## 10.8 Results

We demonstrated that measurements of the longitudinal decoherence and bunched beam echoes are possible at the HERA proton storage ring. The signal quality received is rather good.

Echoes were measured at 40 GeV and at 920 GeV. In both cases the decoherence times were obtained. At 920 GeV, the measured decoherence times fit with our theoretical expectations. From the RF set points at 40 GeV we expected a much lower frequency spread within a bunch, and with that a larger decoherence time than measured. This gives rise to the hypothesis that there is something wrong in the cavity voltage calibration values at low energy. Nevertheless,

the large frequency spread leads to a good stability behavior for injection and is in principle desirable.

By changing the time delay between the RF kicks, a noticeable dependence of the echo strength on this time delay was observed. By using an automated measurement setup, one could expect good enough results to compare them with future theories. The dependence on RF noise resulted in a non uniform picture. Here, the time deviations between the kicks should be increased in future measurements.

## **Part IV**

# **Putting it All Together**



# 11 Causes of Beam Instability

To suppress the emittance growth, we may initially try to find the source of the unstable beam behavior. If we are able to locate this source, we can try to eliminate it and thus emittance achieve conservation.

A very useful method to identify possible sources for beam instabilities is, to estimate the so called effective impedance of every individual device [19]. The total impedance is a measure of the overall stability.

In this chapter, the strength of some selected impedances of the HERA proton ring is investigated. The inspection of all impedances in the storage ring is for itself a complete research work, which we do not carry out here. But the calculated values may set a scale for the complete impedance.

From the decoherence measurements, we can estimate the expected instability thresholds. We will discuss whether these thresholds fit with the observed beam instabilities.

## 11.1 The concept of effective impedances

In accelerator physics, it is convention to express the interaction of the beam with the environment in terms of ‘impedances’. We will consider the idea behind this treatment by means of a single bunch [67]. In Fourier space, the current distribution in the frequency domain is given by  $I(\omega)$  and induces in an impedance  $Z(\omega)$  the voltage

$$V(\omega) = I(\omega) Z(\omega). \quad (11.1)$$

The current distribution in the time domain  $I(t)$  can be expressed as a Fourier series, since it is periodic. This Fourier series consists of the DC component of the bunch current  $I_0$  and a summation, containing the frequency component  $I_p$ .  $I_p$  depends on the bunch shape, where  $p$  is the summation index of the series. With this series, one can calculate the average induced voltage  $\langle V \rangle$ , seen by a particle in a bunch [67]

$$\langle V \rangle = \frac{1}{I_0} \sum_{p=-\infty}^{\infty} |I_p(p\omega_{rev})|^2 Z(p\omega_{rev}). \quad (11.2)$$

This voltage leads to a energy loss per turn of

$$\frac{W}{T_{rev}} = \frac{I_0}{T_{rev}} \operatorname{Re} \langle V \rangle = q \operatorname{Re} \langle V \rangle. \quad (11.3)$$

Here,  $q$  is the bunch charge and  $T_{rev}$  the revolution time. Hence, any effect leading to a loss of the beam energy  $W$  can be expressed, with (11.2) and (11.3), in terms of an impedance  $Z(\omega)$ .

In the case of a beam consisting of  $M$  equally distributed Gaussian bunches, performing the coupled bunch oscillation  $l = 0, \dots, M - 1$ , we observe, at a fixed point in the accelerator, spectral lines at the frequencies

$$\omega_{p,l,m} = M\omega_{rev}p + \omega_{rev}l + \omega_s m \quad \text{with } p = -\infty, \dots, +\infty. \quad (11.4)$$

$m$  denotes the single bunch oscillation type. The amplitudes of the lines follows the single bunch mode power spectrum [19]

$$h_m(\omega) = \frac{(\omega \sigma)^{2m}}{\Gamma(m + \frac{1}{2})} \exp[-(\omega \sigma)^2]. \quad (11.5)$$

$\sigma = l_{FWHM} / 2\sqrt{\ln 4}$  is the  $\sigma$ -bunch length, expressed in units of time and  $\Gamma(z) = \int_0^\infty t^{z-1} e^{-t} dt$ . In frequency space, an interaction between the bunched beam and the impedance can appear only at the frequencies of the spectral lines (11.4). Hence, we may define an ‘effective impedance’, which takes this fact into account. It is given by

$$Z_{eff}^{(l,m)} = \frac{\sum_{p=-\infty}^{\infty} \frac{Z_L(\omega_{p,l,m})}{\omega_{p,l,m} / \omega_{rev}} h_{|m|}(\omega_p)}{\sum_{p=-\infty}^{\infty} h_{|m|}(\omega_{p,l,m})}. \quad (11.6)$$

It is convenient to divide impedances  $Z_L$  by the frequency, in terms of the revolution frequency  $n = \omega / \omega_{rev}$ , and call the result ‘normalized impedance’

$$\frac{Z_L}{n} \equiv \frac{Z_L(\omega)}{\omega / \omega_{rev}}.$$

In the special case when a normalized impedance obeys  $Z_L / n = const$ , it is equal to the effective impedance. For all other cases, one has to calculate the summations or may approximate them by integrations, if possible.

As already mentioned, a beam current induces a voltage in an impedance. This leads to a change of the sum voltage around the ring, providing the bucket potential. Hence, the synchrotron frequency is changed

$$\omega_s \longrightarrow \omega_s + \Delta\omega_{m,l}. \quad (11.7)$$

This coherent frequency shift  $\Delta\omega_{m,l}$ , expressed by the effective impedance, is [15, 19]

$$\frac{\Delta\omega_{m,l}}{\omega_s} = -i \frac{m}{m+1} \cdot \frac{I_0}{3 N_b h V_{RF}} \left( \frac{2\pi R}{c l_{full}} \right)^3 Z_{eff}^{(l,m)}. \quad (11.8)$$

The parameters in (11.8), for the HERA proton ring, are:

$\omega_s$	$\approx 2\pi 30 \text{ Hz}$	phase oscillation frequency
$m$	$= 1$	single bunch oscillation type (bunch phase oscillation)
$I_0$	$\approx 100 \text{ mA}$	total beam current
$N_b$	$= 180$	number of bunches
$M$	$= 220$	number of bunch positions
$h$	$= 1100$	harmonic number (at low energy)
	$= 4400$	(at high energy)
$V_{RF}$	$\approx 180 \text{ kV}$	voltage generating the bucket potential (at low energy)
	$\approx 700 \text{ kV}$	(at high energy)
$2\pi R$	$\approx 6.3 \text{ km}$	accelerator circumference
$c l_{full} = \frac{2c l_{FWHM}}{\sqrt{\ln 4}}$	$\approx 1.2 \text{ m}$	total resp. full bunch length (at low energy)
	$\approx 0.8 \text{ m}$	(at high energy)

From equations (11.8) and (7.4) we find, that the imaginary part of an effective impedance lead to a coherent frequency shift, whereas the real part is connected with the instability growth rate.



## 11.2 Which is the driving impedance?

In section 7.5, we determined frequency shifts for bunch phase oscillations ( $m = 1$ ) between  $1 \frac{1}{s}$  ( $l = 163$ ) and  $10 \frac{1}{s}$  ( $l = 74$ ) and, belonging to there, the instability growth rates  $1 \frac{1}{s}$  and  $0.5 \frac{1}{s}$ . With (11.8) we can now calculate the strength of effective impedances, driving these coupled bunch oscillations. The results are

$$Z_{eff}^{(l,m=1)} \approx i 0.36 \Omega \text{ s } \Delta\omega_{m=1,l} \quad (11.9)$$

$$Z_{eff}^{(l=163,m=1)} \approx 0.36 \Omega + i 0.36 \Omega \quad \begin{array}{l} \text{(common broad} \\ \text{band impedance?)} \end{array} \quad (11.10)$$

$$Z_{eff}^{(l=74,m=1)} \approx 0.18 \Omega + i 3.6 \Omega \quad \begin{array}{l} \text{(maybe narrow band} \\ \text{or actively driven).} \end{array} \quad (11.11)$$

Now we calculate some effective impedances to determine, whether their sum value is of the order of magnitude of the values (11.10) and (11.11).

### 11.2.1 Space charge impedance

A single particle in a bunch experiences a repulsive electrical force, due to all other charged particles in the beam. This leads to a defocussing of the beam, called ‘space charge effect’. Since the beam is moving, a single particle also suffers the attractive Lorentz force. It is weak for slow particles but for ultra relativistic particles it nearly cancels the repulsive electrical force. Both effects influence, on the one hand, the particle distribution within the bunches, but also the bunches as a whole. Since the beam is traveling in a beam pipe, mirror currents in the walls must also be considered. The effect on the bunches can be expressed as an impedance [15]

$$\frac{Z_L}{n} = i \frac{Z_0}{\beta \gamma^2} \left( 1 + 2 \ln \frac{b}{a} \right). \quad (11.12)$$

The parameters are:

$Z_0$	$= 376.73 \Omega$	free space impedance
$\beta = \frac{v}{c}$	$\approx 1$	with the beam velocity $v$ and speed of light $c$
$\gamma = \frac{1}{\sqrt{1-\beta^2}} = \frac{E_s}{E_0}$	$= 42.6$	at low energy
	$= 981$	at high energy
$E_s$	40 GeV to 920 GeV	energy of synchronous particle
$E_0$	$= 0.938 \text{ GeV}$	proton rest energy
$b$	$= 27.5 \text{ mm}$	radius of beam pipe
	$\approx 4.4 \text{ mm}$	r.m.s radius of beam (at low energy)
$a$	$\lesssim 1 \text{ mm}$	(at high energy)

We obtain

$$\frac{Z_L}{n} = i 0.97 \Omega \quad \text{at low energy} \quad (11.13)$$

$$\frac{Z_L}{n} = i 3.0 \text{ m}\Omega \quad \text{at high energy.} \quad (11.14)$$

Since  $Z_L / n = \text{const}$  (see last section), the effective impedances for all values of  $l$  and  $m$  are given by

$$Z_{eff}^{(l,m)} = i 0.97 \Omega \quad \text{at low energy} \quad (11.15)$$

$$Z_{eff}^{(l,m)} = i 3.0 \text{ m}\Omega \quad \text{at high energy.} \quad (11.16)$$

## 11.2.2 Resistive wall impedance

A bunched beam travelling in a beam pipe induces wall currents. Depending on the Fourier components of the beam, these wall currents flow through a layer, whose thickness is given by the skin depth. The wall currents dissipate power due to the resistivity of the beam pipe material, and also act back on the beam. Hence, the beam interacts with the so called ‘resistive wall impedance’.

In the HERA proton ring the beam pipe, inside the superconducting dipole magnets, consists of stainless steel with an inner copper layer of  $10 \mu\text{m}$  to  $15 \mu\text{m}$  thickness. The skin depth exceeds this layer for low frequency components. Therefore, we have to distinguish two cases: For low frequencies we assume, that the wall current flows completely through the copper layer. At high frequencies, it flows through a layer with the skin depth. We apply the well known expressions [68, 46]

$$\frac{Z_L}{n} = \left(1 + \frac{\omega}{|\omega|}i\right) \frac{L}{2\pi b d_c} \frac{1}{\sigma_c} \frac{\omega_{rev}}{\omega} \quad \text{for } \delta_{skin} > d_c \quad (11.17)$$

$$\frac{Z_L}{n} = \left(1 + \frac{\omega}{|\omega|}i\right) \frac{L}{2\pi b \delta_{skin}} \frac{1}{\sigma_c} \frac{\omega_{rev}}{\omega} \propto \frac{\omega_{rev}}{\sqrt{|\omega|}} \quad \text{for } \delta_{skin} < d_c \quad (11.18)$$

$$\delta_{skin} = \sqrt{\frac{2c}{Z_0 \sigma_c |\omega|}}. \quad (11.19)$$

The parameters are [46]:

$L$	$\approx 0.84 \cdot 2\pi R$	length of beam pipe (cold region)
	$\approx 0.16 \cdot 2\pi R$	length of beam pipe (warm region)
$2\pi R$	$\approx 6.3 \text{ km}$	accelerator circumference
$b$	$= 27.5 \text{ mm}$	radius of beam pipe (in cold region)
$d_c$	$\approx 10 \mu\text{m}$	thickness of copper layer
	$\approx 2 \cdot 10^9 (\Omega \text{ m})^{-1}$	specific conductivity of copper at 4.5 K
$\sigma_c$	$\approx 5.9 \cdot 10^7 (\Omega \text{ m})^{-1}$	specific conductivity of copper at 294 K
$\omega_{rev}$	$= 2\pi 47.3 \text{ kHz}$	revolution frequency
$c$	$\approx 3 \cdot 10^8 \frac{\text{m}}{\text{s}}$	speed of light $c$
$Z_0$	$= 376.73 \Omega$	free space impedance

We obtain for the cold beam pipe, inside the superconducting dipole magnets, the values

$$\frac{Z_L}{n} = \left(1 + \frac{\omega}{|\omega|}i\right) 1.53 \Omega \frac{\omega_{rev}}{\omega} \quad \text{for } |\omega| \lesssim 8 \frac{10^3}{\text{s}} \quad (11.20)$$

$$\frac{Z_L}{n} = \left(1 + \frac{\omega}{|\omega|}i\right) \frac{1.53 \Omega}{\sqrt{8 \frac{10^3}{\text{s}}}} \frac{\omega_{rev}}{\sqrt{|\omega|}} \quad \text{for } |\omega| > 8 \frac{10^3}{\text{s}}. \quad (11.21)$$

In the straight sections, the beam pipe changes its diameter several times, particularly near the interactions points. But for simplification, we take here the same radius for the beam pipe as in the cold region, and get

$$\frac{Z_L}{n} = \left(1 + \frac{\omega}{|\omega|}i\right) 9.9 \Omega \frac{\omega_{rev}}{\omega} \quad \text{for } |\omega| \lesssim 270 \frac{10^3}{\text{s}} \quad (11.22)$$

$$\frac{Z_L}{n} = \left(1 + \frac{\omega}{|\omega|}i\right) \frac{9.9 \Omega}{\sqrt{270 \frac{10^3}{\text{s}}}} \sqrt{\frac{\omega_{rev}}{|\omega|}} \quad \text{for } |\omega| > 270 \frac{10^3}{\text{s}}. \quad (11.23)$$

The normalized impedances depend on the frequency and we have to carry out the summations in (11.6) to calculate the effective impedance. We are interested in worst case approximations, therefore, we consider the following points: The resistive wall impedances have the strongest influence at low frequencies. Longer bunches have larger Fourier components at lower frequencies than shorter ones. Hence, we take for the power spectrum the bunch length  $l_{FWHM} = 2.4$  ns at low energy. Even for short bunches  $l_{FWHM} = 1.6$  ns, this power spectrum vanishes for  $m = 1$  at frequencies higher than 4 GHz. If we carry out the summations for safety up to 10 GHz, the summation index  $p$  for the spectral lines (11.4) has to run from -960 to +960. This summation can be easily done by a computer algebra system, like *Mathematica*. The results for the cold regions are

$$Z_{eff}^{(l,m=1)} = 2.8 \text{ m}\Omega + i 4.6 \text{ m}\Omega \quad \text{for } l = 1, 74, 163. \quad (11.24)$$

For the warm region, one obtains

$$Z_{eff}^{(l,m=1)} = 1.1 \text{ m}\Omega + i 6.1 \text{ m}\Omega \quad \text{for } l = 1, 74, 163. \quad (11.25)$$

The contribution of the resistive wall, to the over all impedance, is not able to drive coupled bunch oscillations.

### 11.2.3 Cavity impedances at fundamental frequencies

Likely candidates for impedances driving beam instabilities are accelerating cavities at their fundamental acceleration frequencies, because of the large shunt impedance  $R_s$  and the high quality factor  $Q_0$ . Fast feedback loops are mounted for the reduction of beam loading and transient RF voltage errors, see section 3.2. These loops significantly modify the impedance seen by the beam.

The impedance with a fast feedback loop is [15, 23]

$$Z_L = \frac{R_s}{1 + i Q_L \left( \frac{\omega_{cav}}{\omega} - \frac{\omega}{\omega_{cav}} \right) - A e^{-i \tau_{ff}}}, \quad (11.26)$$

where  $A$  is the feedback gain,  $Q_L$  is the ‘loaded quality factor’, accounting for the coupling between the final stage amplifier and the cavity, and  $\tau_{ff}$  is the signal propagation time through the loop. This signal propagation time is an integer multiple plus one half of the RF period  $\tau_{ff} = (\text{integer} + \frac{1}{2}) / f_{RF}$ . The factor  $\frac{1}{2}$  is needed for a RF phase advance of  $\pi$ , leading to a subtraction of the error signal from the loop drive signal. The impedance of the tetrode amplifiers, as seen from the cavities, is much higher than the cavity impedance. Hence, the ‘loaded quality factor’ is almost equal to the intrinsic quality factor of the cavity:  $Q_L \approx Q_0$  [23]. Table 3.1 contains the parameters of the RF systems of HERA. For the worst case approximation, we take for the cavity frequency the RF frequency plus the technically maximum possible frequency deviation, due to the tuners. These frequency deviations are smaller than the bandwidth, modified by the fast feedback loops. So, we can expect from the real values of the effective impedances information about the maximum possible Robinson effect.

The results for each of the 208 MHz cavities are, for any multi-bunch mode  $l$ :

$$\left| \text{Re } Z_{eff}^{(l,m=0)} \right| \lesssim 20 \text{ m}\Omega \quad \text{and} \quad \left| \text{Im } Z_{eff}^{(l,m=0)} \right| \lesssim 62 \text{ m}\Omega \quad \text{for 208 MHz} \quad (11.27)$$

$$\left| \text{Re } Z_{eff}^{(l,m=1)} \right| \lesssim 0.64 \Omega \quad \text{and} \quad \left| \text{Im } Z_{eff}^{(l,m=1)} \right| \lesssim 0.51 \text{ m}\Omega \quad \text{for 208 MHz} \quad (11.28)$$

Here, the sign of the tuning is responsible for the sign of the real part of the effective impedance. We get for one 52 MHz cavity the results (any  $l$ ):

$$\left| \operatorname{Re} Z_{eff}^{(l,m=0)} \right| \lesssim 0.17 \Omega \quad \text{and} \quad \left| \operatorname{Im} Z_{eff}^{(l,m=0)} \right| \lesssim i 0.28 \Omega \quad \text{for 52 MHz} \quad (11.29)$$

$$\left| \operatorname{Re} Z_{eff}^{(l,m=1)} \right| \lesssim 83 \text{ m}\Omega \quad \text{and} \quad \left| \operatorname{Im} Z_{eff}^{(l,m=1)} \right| \lesssim 26 \text{ m}\Omega \quad \text{for 52 MHz} \quad (11.30)$$

Detuned cavities are able to generate an instability, as observed. The value of their impedances, seen by the beam, are in the same order of magnitude as the impedance values, calculated from the growth rates (11.10) and (11.11). They drive preferred modes with numbers near  $l = 2$  and  $l = 218$ . For this calculation, we assumed that the signal propagation times in the fast feedback loops are perfectly adjusted. Deviations would cause larger values of the effective impedances.

From the real part we get the Robinson damping, respectively instability growth rate by inverting formula (11.9), respectively

$$\left| \frac{1}{\tau_{\text{Robinson}}} \right| = \frac{1}{0.36 \Omega \text{ s}} \left| \operatorname{Re} Z_{eff}^{(l,m=1)} \right|. \quad (11.31)$$

Higher modes of the cavities [34, 46] may also drive instabilities. If the damping antennas, cables or RF attenuators are damaged, one can expect here also a candidate for an impedance which drives instabilities.

## 11.2.4 Broad band impedances

The vacuum chamber in the HERA-*B* experiment constitutes a broad band impedance. We will discuss its possible influence on the HERA proton beam, because its RF properties are known [70].

The experiment HERA-*B* analyses *B* mesons, which are produced by the collision of protons from the bunch tails with wire targets. The particles produced leave the collision region at a small angle with respect to the flight direction of the proton bunches. The beam pipe widens its diameter at the collision region, to avoid that the secondary particles hit the wall. After about two meters the diameter is reduced back to the initial one by a sudden step. This structure forms a vessel, containing the vertex detector inside the vacuum region. From the point of view of accelerator physics it is a cavity with many resonant frequencies. To reduce the impedances seen by the beam, the beam orbit is shielded by thin strips of metal. The result are several broad band impedances, from 800 MHz to 2 GHz, with maximum impedances of 100  $\Omega$ .

The upper graph in figure 11.1 shows the real part of the longitudinal impedance of the vessel [70]. For the estimation of the effective impedance, we read from this picture the individual resonant frequencies  $f_{res,k}$ , the impedances  $R_{s,k}$ , and the relating band widths  $\Delta f_{res,k}$ . The impedance of the vessel is given by

$$Z_L = \sum_k \frac{R_{s,k}}{1 + i Q_k \left( \frac{\omega_{res,k}}{\omega} - \frac{\omega}{\omega_{res,k}} \right)} \quad \text{with} \quad Q_k = \frac{f_{res,k}}{2 \Delta f_{res,k}}. \quad (11.32)$$

The lower graph in figure 11.1 shows the real part of the created impedance model.

Since the resonant frequencies of the impedances are in the GHz region, short bunches may suffer more than longer ones. For a worst case estimation, we take therefore the bunch length

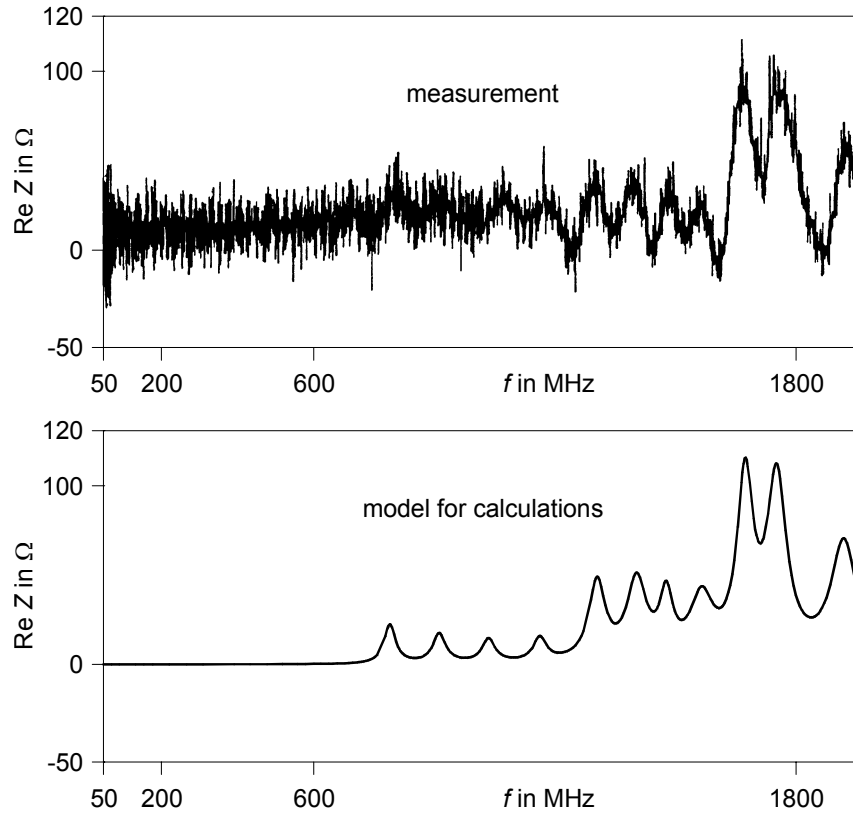


Figure 11.1: Impedance of the HERA-*B* vacuum vessel with four metal strips, for RF shielding of the proton beam orbit. The measurement is from [70].

of 1.6 ns, reached at 920 GeV, and theoretical achievable ones<sup>1</sup> of 0.6 ns. The results are for any mode number  $l$  and  $0 \leq m \leq 10$ :

$$\left| \operatorname{Re} Z_{eff}^{(l,m)} \right| \lesssim 10^{-9} \text{ m}\Omega \quad \text{and} \quad \left| \operatorname{Im} Z_{eff}^{(l,m)} \right| \lesssim 0.6 \text{ m}\Omega \quad \text{for } l_{FWHM} = 1.6 \text{ ns} \quad (11.33)$$

$$\left| \operatorname{Re} Z_{eff}^{(l,m)} \right| \lesssim 10^{-7} \text{ m}\Omega \quad \text{and} \quad \left| \operatorname{Im} Z_{eff}^{(l,m)} \right| \lesssim 0.7 \text{ m}\Omega \quad \text{for } l_{FWHM} = 0.6 \text{ ns} \quad (11.34)$$

From these results, we might expect that the well shielded HERA-*B* vessel does not have a negative influence on the HERA proton beam. But measurements of the beam induced RF spectrum in the vessel [71] showed several lines up to 600 MHz. Unfortunately, the installed loop antenna is not calibrated so that one can not determine the impedances. The measurements in the laboratory showed no lines in this range, compare figure 11.1. Since our estimations are based on these measurements, the impedances may be larger than the numbers given in (11.33) and (11.34).

<sup>1</sup>under the assumption of emittance preservation and a bunch lengths after injection of 2.4 ns

### 11.2.5 Other impedances

Other conceivable candidates [72], driving coupled bunch oscillations in the HERA proton ring, are (status until 2000 ):

- beam position monitors of any kind
- longitudinal restive gap monitors
- longitudinal beam current monitors - two types
- wire-scanner beam profile monitors
- rest-gas ionization monitors
- pumping ports
- collimators
- synchrotron radiation monitor
- luminosity monitors
- leading-proton spectrometers from high energy experiments
- transitions in the vacuum chamber profile - the HERA proton ring has 10 different chamber profiles
- photon window for luminosity monitor
- beam pipes inside the detectors
- beam pipes at separation regions of electron and proton beam

One may examine all these impedances by using approximation formulas [15], as we did for the impedances treated. More exact results can be expected by MAFIA calculations and measurements in the laboratory.

## 11.3 Is there sufficient Landau damping?

As already mentioned in section 7.1, a condition for de-coupling of coupled bunch oscillations is, that the coherent spread among the individual bunch synchrotron frequencies  $S_\omega$  exceeds the frequency shift  $\Delta\omega_{m,l}$ , caused by the coupling:

$$\text{coherent spread} > \text{shift} \quad (11.35)$$

$$S_\omega > |\Delta\omega_{m,l}| \quad \text{for de-coupling.} \quad (11.36)$$

The index  $m$  denotes the single bunch oscillation type and  $l$  the coupled bunch mode. But not only a sufficient spread between bunch synchrotron frequencies suppresses coupled bunch oscillations, but also the frequency spread within the bunches  $s_\omega$ , that is Landau damping. A rule-of-thumb, for suppression of an instability by Landau damping, is that this incoherent frequency spread should exceed four times the instability growth rate [73, 18]:

$$\text{incoherent spread} > 4 \times \text{growth rate} \quad (11.37)$$

$$\frac{s_\omega}{4} > \frac{1}{\tau} \quad \text{for suppression.} \quad (11.38)$$

A typical measured value for the frequency spread at low energy (40 GeV) is  $s_\omega \approx 28 \frac{1}{s}$ , and at high energy (920 GeV) we have  $s_\omega \approx 8 \frac{1}{s}$ , compare section 10.5. This means that an instability with a growth rate smaller than  $7 \frac{1}{s}$  is Landau damped at low energy and at high energy for a growth rate smaller than  $2 \frac{1}{s}$ . The assumption that the frequency spread is a monotonous function, between low and high energy of the storage ring, does not fit with the observation of instabilities during acceleration. The maximum estimated instability growth rate was  $1 \frac{1}{s}$ . With frequency spreads between  $28 \frac{1}{s}$  and  $8 \frac{1}{s}$  these instabilities should be suppressed.

Obviously, we lose Landau damping during ramping, from low to high energy, so that these weak instabilities can arise. Since Landau damping is mostly generated by the deviations of the bucket from a parabola, we have preferred to consider the RF voltages during ramping.

In section 10.5, we found a large disagreement between the decoherence time, calculated at low energy from the RF voltages, and the measured one. One may explain this by a wrong calibration of the voltage of the 208 MHz RF. Three cavities provide 70 kV each and the fourth compensates most of the RF voltage providing -205 kV. Small errors in the individual calibrations have a noticeable effect on the bucket form and thus on the frequency spread. If we assume, instead of 5 kV for the 208 MHz sum voltage, 40 kV or -40 kV, we get a better agreement between the computed and measured decoherence times, compare section 10.5. For the relating bucket potentials, see figure 11.2. Both possibilities represent two different voltage

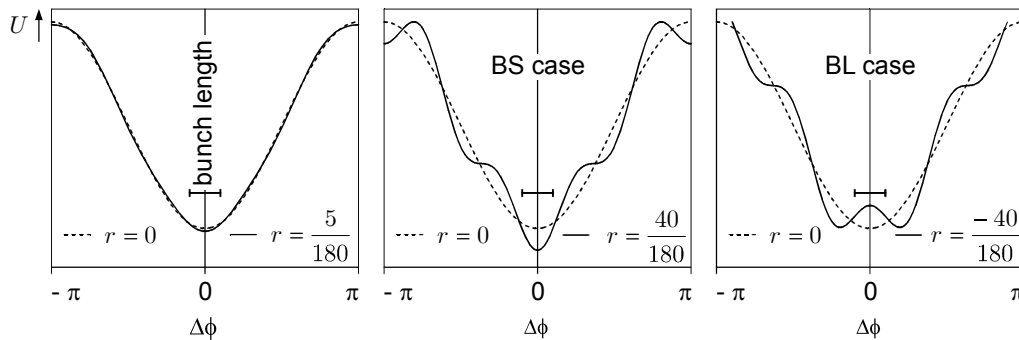


Figure 11.2: Bucket potentials at 40 GeV for different voltage ratios  $r = V_{208\text{MHz}} / V_{52\text{MHz}}$  of the 4th harmonic RF system in HERA.

ratios  $r = V_2 / V_1$  of a double harmonic RF system, namely  $r < 0$  and  $r > 0$ . These two possibilities represent the bunch lengthening (BL) and the bunch shortening (BS) case [50]. A more detailed examination of the frequency spread in dependence on the bunch length, as in section 8.1 shows that for the BS case the frequency spread grows continuously with the bunch length, however, not in the BL case [50]. This results from the dependence of the single particle synchrotron frequency on its amplitude, shown in figure 11.3. As a consequence, a beam in the BS case always stabilizes itself, with growing bunch lengths, whereas this is only valid for short bunches in the BL case. From such considerations and experimental experience [74] it is known that the HERA proton ring works always in the BS area. The case  $V_{208\text{MHz}} = -40\text{ kV}$  seems additional not reasonable, since viewing the resulting bucket shape, shown in figure 11.2, one would expect longer bunches, than observed.

To get a deeper understanding of the evolution of the frequency spread during acceleration, one first has to check the calibration values. The available Landau damping during the transition process from the 52 MHz to the 208 MHz RF buckets must be examined by calculations and decoherence measurements. Calculations of the frequency spread, as in section 8.1, disregard the influence of the bunch tails to Landau damping. Their influence must also considered in further examinations.

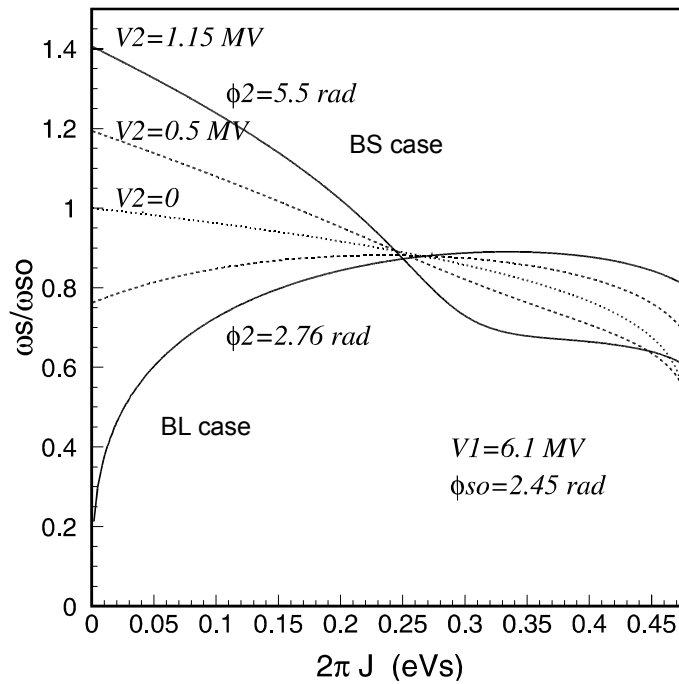


Figure 11.3: Normalized synchrotron frequency as a function of action, normalized to emittance, calculated for the 4th harmonic RF system of the CERN SPS [50].

The BTF measurements support the evidence that HERA has less damping between low and high energy. Typical BTF amplitudes are 100 at low energy (40 GeV) and 50 at high energy. But at the intermediate energy of 300 GeV we found BTF values larger than 250, compare chapter 9.



# 12 Active Measures against Emittance Dilution

The HERA proton ring was designed as a storage ring with low impedance. Hence, we did not expect a simple source of impedance, responsible for the unstable beam behavior. This expectation is confirmed. It is visible in the low values of the estimated effective coupling impedances in the range below  $1 \Omega$ .

A goal of this work was to provide a robust basis for active measures against beam instabilities, beside the diagnostic abilities. This chapter presents an overview of possible active measures against the proton emittance dilution in HERA.

## 12.1 Increase of coherent synchrotron frequency spread

According to Sacherer's rule (11.35), a larger spread in the synchrotron frequencies of the individual bunches decouples bunch oscillations. In HERA the beam loading transients, shown in figure 6.3, lead to individual bucket shapes of the bunches, and with that, to a coherent spread of the synchrotron frequencies. These individual buckets manifest themselves in a bunch-to-bunch variation of the synchronous phase, shown in the lower graph of figure 5.1. But obviously, the resulting coherent frequency spread of the order of 1.5 Hz is not sufficient to suppress coupled bunch oscillations, see section 7.4.

One may think first to increase the coherent frequency spread by increasing the beam loading transients. This can be achieved by reducing the gains of the fast feedback loops. But such a measure is counterproductive, since one then also increases the effective impedances of the cavities at the fundamental frequencies and, consequently, the bunch-to-bunch coupling. Larger beam loading transients also seriously interfere with clean bucket matching at injection. Hence, reducing the gains of the fast feedback loops is not advisable.

An appropriate increase of the frequency spread may be provided by an RF cavity, running at a different harmonic number [75], for example, one of the four 208 MHz cavities working at  $f_{4401} = 4401 f_{rev}$  instead of  $f_{RF4400} = 4400 f_{rev}$ . The 208 MHz voltage varies then, during one revolution, between  $V_{RF4401} - V_{RF4400}$  and  $V_{RF4401} + V_{RF4400}$ . As a result, the coherent frequency spread would be increased over the whole bunch population, depending on the voltage ratio  $V_{4401}/V_{4400}$ . As long as the difference of the harmonic numbers times the revolution frequency is in the tuning range of the cavities, this measure should not cause too much technical effort, except for a phase locked loop, to create the frequency with the different harmonic number.

This solution has some disadvantages. If we use, for example, only one 208 MHz cavity, this measure is effective when the buckets are mainly built up by the 208 MHz system, which is only the case at higher energies. A proper transition between both RF systems appears more difficult. An additional use of a 52 MHz cavity would decrease drastically the maximum available RF voltage at low energy. Furthermore, the bucket matching during injection has also to be changed over the bunch trains, certainly no trivial task.

## 12.2 Landau damping cavity

As shown in section 11.3, there is some loss of Landau damping at intermediate energies. A third RF system with a harmonic number 8800 (416.331 MHz), or even better, 17600 (832.662 MHz), would provide an additional incoherent frequency spread and enlarge Landau damping. Cavities for such purpose are commonly called ‘Landau damping cavities’ [75] and are often used to suppress coupled bunch instabilities in proton storage rings [50]. For an estimation of the required RF voltages, a detailed study of the bucket transition between 52 MHz and 208 MHz during acceleration is necessary.

From the technical point of view one may take an 832 MHz cavity, comparable to the 800 MHz cavities already used for the same purpose in the CERN SPS [50]. The accompanying RF control system requires an additional phase locked loop, locking an 832 MHz drive signal on the ‘HERA proton master frequency’ of 208 MHz - for this 208 MHz frequency, see section 3.1. In addition, one has to design a complete RF control system for the cavity, like these for the 208 MHz cavities. It has to be checked, whether a fast feedback loop can be used for impedance, respectively beam loading reduction.

## 12.3 Reduction of cavity impedance by RF feedforward

In section 11.2.3, we found that the impedance of the cavities, seen by the beam at the fundamental frequency, is able to drive coupled bunch oscillations as observed. An increase of the feedback gains  $A$ , for a further reduction of the cavity impedances, applying (11.26), is limited. According to Nyquist’s criterion [76], the upper limit of the feedback gain is given by [23]

$$A_{\max} = \frac{Q_L}{4 f_{cav} \tau_{ff}}, \quad (12.1)$$

where  $Q_L$  is the loaded quality factor,  $f_{cav}$  the cavity frequency and  $\tau_{ff}$  the signal propagation time through the loop. From this condition, we get an upper limit for the gain of about 130 for the 208 MHz RF system and about 230 for the 52 MHz system. Since the 208 MHz RF system already works with a gain of 100, see section 3.2, a further increase is not possible. At the 52 MHz system, working with a maximum gain of 50, this measure could be helpful. Unfortunately, this requires an intervention in the loop electronics, installed in the HERA tunnel. First one has to check whether this is technically possible. Increasing the gain results in an increased demand of RF power, to be supplied by the final stage amplifiers, so, additional amplifiers could be necessary.

A further reduction of the effective cavity impedance can be achieved with an RF feedforward control. The idea behind such a system is to estimate the beam loading transient before the beam passes the cavities, and feed a correction signal to the RF drive signal at the same time as the beam passes the cavities. The result is ideally a complete cancellation of the beam loading transient and a vanishing effective impedance [77].

To generate the correction a signal from a beam monitor, installed shortly after the injection point, can be used. The RF cavities are also installed near the injection point, but at the opposite side, see figure 1.3. As a result, an injected beam circulates once around the ring before it passes the cavities for the first time. During the revolution time, the signal from the beam monitor can be processed and the RF correction signals generated. Since the correction signal avoids the path around the ring, there is enough time for the calculations. After the first revolution, such a system acts as feedback system and considers automatically all occurring changes [41].

The HERA proton storage ring is now prepared for the implementation of such a feedforward system. The monitor signal is analog processed by the real time measurement. It supplies

analog input signals for analog to digital converters (ADC), necessary in front of digital signal processors (DSPs). These analog signals are described in chapter 4. From the two different filter frequencies of the diagnostic system, one can directly predict the beam loading transient of each individual bunch. Modulation units, controllable by digital to analog converters (DAC), exist to add corrections to the RF drive signals. A fast cavity field diagnostic is available to check whether the loop is working properly, see chapter 6. This cavity probe supplies information for an automated adjustment of the feedforward loop. This is necessary during acceleration, when the buckets change from 52 MHz to 208 MHz, and with that, the beam loading transients.

A feedforward is expected to reduce the emittance blow up during injection. Without beam loading transients, the bucket matching should be ideal. The low impedance should reduce the coupling, given by the cavities, and may reduce coupled bunch oscillations. A feedforward would also have a direct influence on the luminosity. As already mentioned, the beam loading transients cause individual bucket shapes and, as a result, a phase variation of the synchronous phase of up to  $5^\circ$ , see lower graph of figure 5.1. A phase shift of  $5^\circ$  correspond to a shift of the bunch center by 0.28 ns. A proton bunch would hit the opposing electron bunch 8 cm away from the interaction point (IP). Because of the small  $\beta$ -function, this reduces the luminosity at this collision by about 5% [78]. A feedforward which suppresses the beam-loading transients, would remove the phase shift and preserve the luminosity.

## 12.4 Coupled bunch feedback

A feedforward has the advantage of decreasing the cavity impedance, but the disadvantage of reducing the coherent frequency spread, which then supports inter bunch coupling caused by other impedances. A way out of this dilemma is the installation of a coupled bunch feedback system.

The detector side of a coupled bunch feedback system has been realized within this thesis. The oscillation of phase and length of each individual bunch can be measured with the real time measurement. As for a feedforward system, a coupled bunch feedback system consists of ADCs converting the preprocessed analog bunch signals and transmitting them to digital signal processors (DSPs). The processors filter first the measured data, to reduce noise and lower the threshold for detecting multi-bunch oscillations. Figure 10.6 demonstrates the improvement by a factor of about 3.5, achieved with a simple digital filter. The demand on the minimum necessary RF voltage  $V_{FB}$  for damping the oscillations depends on this threshold value,  $\delta\phi$  for bunch phase oscillations. In the case of bunch phase oscillations it is given by [73]

$$V_{FB} \geq 2 V_{RF} \frac{s_\omega}{\omega_s} \delta\phi, \quad (12.2)$$

where  $V_{RF}$  is the total RF voltage,  $s_\omega$  the incoherent frequency spread and  $\omega_s$  the synchrotron frequency. The factor  $s_\omega / \omega_s$  considers the fact, that we can counteract only coherent synchrotron oscillations. This means, we have to counteract a bunch oscillation before it vanishes due to the decoherence effect. Since  $V_{FB} \propto \delta\phi$ , one of the initial demands on the real time measurement was to reduce  $\delta\phi$  as much as possible. Considering the sum RF voltages, since then used, we get at low energy a minimum required feedback voltage of

$$V_{FB} \gtrsim 2 \cdot 200 \text{ kV} \frac{28 \frac{1}{s}}{126 \frac{1}{s}} 2\pi \frac{0.068^\circ}{360^\circ} \approx 105 \text{ V} \quad \text{at low energy,} \quad (12.3)$$

and

$$V_{FB} \gtrsim 2 \cdot 600 \text{ kV} \frac{8 \frac{1}{s}}{188 \frac{1}{s}} 2\pi \frac{0.068^\circ}{360^\circ} \approx 61 \text{ V} \quad \text{at high energy.} \quad (12.4)$$

In practice, one needs much larger voltages. Considering the maximum possible sum RF voltage, see table 3.1, results in

$$V_{FB} \gtrsim 2 \cdot 3.6 \text{ MV} \frac{28 \frac{1}{\text{s}}}{126 \frac{1}{\text{s}}} 2 \pi \frac{0.068^\circ}{360^\circ} \approx 2 \text{ kV} \quad \text{in practice.} \quad (12.5)$$

Another component of a longitudinal coupled bunch feedback is the ‘longitudinal kicker’, supplying the voltage  $V_{FB}$  for acting on the individual bunches. The bandwidth  $\Delta f_{FB}$  of such a device has to take into account the distance between subsequent bunches. Commonly, in electron and positron rings, the bandwidth is chosen to be one half of the bunch repetition frequency [79]. This results from frequency domain considerations requiring a ‘steady state’ coupled bunch oscillation. For a proper treatment of transient effects, I recommend for the HERA proton ring, that the bandwidth  $\Delta f_{FB}$  has to be significant larger than the bunch repetition frequency  $f_{rep}$ . A good choice may be

$$\Delta f_{FB} \gtrsim 2 \cdot f_{rep} \approx 20.8 \text{ MHz.} \quad (12.6)$$

The HERA proton beam shows large BTF amplitude values, see chapter 9, so that even small exciting signals lead to large bunch oscillations. In an unfavorable case, a feedback with too low kicker bandwidth would damp the oscillations of a selected bunch, but excite the subsequent bunches with the residual signals.

As a first attempt, one may try to circumvent the limited bandwidth of a 208 MHz cavity by adding a correction signal to the RF drive signal, consisting of two RF spikes with opposite voltage and a delay time of about  $1 / \Delta f_{FB}$ . Simulations show that this produces a RF kick in the cavity, with the desired signal rising and falling time. It has to be verified, whether the high peak power demand at the final stage amplifier is within the working specification and whether one can achieve sufficient kick voltages. A too narrow bandwidth of the amplifier chain could prevent the realization of this idea.

The proper solution is a specialized feedback kicker. Two different types of longitudinal feedback kickers are commonly used, for coupled bunch feedback systems. One is a stripline type kicker, for example installed in the LBNL ALS [80]. A more recent development are waveguide overloaded cavities, first used in the INFN DAΦNE [81]. The second principle has some advantages, regarding tuning, matching and higher order modes. Whether these principles are compatible with the requirements of the HERA proton ring, has to be examined. The kickers mentioned work at fundamental frequencies in the GHz range, whereas we need a frequency suitable to 52 MHz and 208 MHz.

# Conclusion and Outlook

The topic of this thesis is the design and assembly of a fast longitudinal diagnostic system, aimed at reducing the proton bunch length in HERA, to enable a further increase of the luminosity, after the luminosity upgrade. It provides also the sensor signals for possible control loops. By using this system, the occurrence of coupled bunch instabilities during acceleration from low to high energy has been demonstrated.

The fast longitudinal diagnostic system consists of several parts. A real time measurement setup is able to measure the phase and length of each individual proton bunch during one HERA revolution. Important parts of this setup are custom designed filters for measuring the 52 MHz and 208 MHz Fourier components of the individual bunch shapes.

The fast cavity field diagnostic permits the observation of the beam loading voltage and the accelerating voltage in each cavity. After down conversion of the cavity signals, the transient signals are separated by specially designed filters, to permit optimum resolution for both voltages.

A controllable timing system provides clock and trigger signals, for sampling the analog values.

The data allow the examination of longitudinal stability in the HERA proton ring. Measurements of the longitudinal proton beam emittance have been performed. The simultaneous appearance of coupled bunch oscillations and emittance blow up is evident.

Measurements of the longitudinal beam transfer function, which have been performed in collaboration with W. Kriens and U. Hurdelbrink, are needed for theoretical considerations and for the design of future feedback control loops.

From measurements of the decoherence times, the incoherent frequency spread can be examined. Hence, the available Landau damping can be evaluated. Beam echo experiments require nearly the same method. This provides the opportunity to explore incoherent beam dynamical effects, by means of beam echoes.

The fast longitudinal diagnostic system permits also the observation of transient effects, for example caused by injection or beam losses. Further insights on transient beam dynamics can be expected by exploring these possibilities. Other ideas relate to examination of noise on the RF and the beam, affecting the coasting beam production.

An estimate of the effective impedances of selected accelerator components leads to the conclusion that the coupled bunch oscillations are not driven by a single strong impedance. On the contrary, the sum of all impedances appears to be below the tolerable limit. At 40 GeV and at 920 GeV, the instability thresholds are not exceeded, but during acceleration the Landau damping is found to be reduced. The double harmonic RF system probably plays an important role in this respect.

To optimize the longitudinal stability, a careful programming of the RF voltages during acceleration is desirable. A careful tracking between the RF frequency and the field of the bending magnets should take place. This alone will not be sufficient to suppress the longitudinal emittance dilution. Hence, one has to think about the reduction of the cavity impedances, seen by the beam, through the implementation of RF feedforward control loops. The low power RF parts for such control loops are now available. An increase of the coherent frequency spread by a RF cavity, working at a different harmonic number, appears attractive for a test. Whether a

Landau damping cavity, or a coupled bunch feedback leads to shorter bunches at high energy, requires some consideration. Stabilization by Landau damping becomes less efficient for shorter bunches. A coupled bunch feedback should damp oscillations independent of the bunch length.

# Appendix

## A.1 Notation

### A.1.1 Radio frequency waves, phasors and vectors

In this work, ‘phasors’ and ‘vectors’ are used in several places. The definitions are given in the following section.

A radio frequency (RF) wave with amplitude  $V$ , frequency  $f = \frac{\omega}{2\pi}$  and phase  $\varphi$  is expressed as

$$v(t) = V \sin[\omega t + \varphi]. \quad (\text{A.7})$$

Using Euler’s relation

$$e^{i\theta} = \cos \theta + i \sin \theta, \quad (\text{A.8})$$

this wave can be expressed by

$$\begin{aligned} v(t) &= V \operatorname{Im} [e^{i(\omega t + \varphi)}] \\ &= \operatorname{Im} [(V e^{i\varphi}) e^{i\omega t}]. \end{aligned} \quad (\text{A.9})$$

The quantity  $V e^{i\varphi}$  in (A.9) is named the ‘phasor’ of the RF wave  $v(t)$ , it is a complex number, determined by the amplitude and the phase of the RF wave

$$\mathbf{v} = V e^{i\varphi} = V \cos \varphi + i V \sin \varphi. \quad (\text{A.10})$$

Usually, phasors are plotted as vectors in the complex plane. This representation is called a ‘phasor diagram’, shown in figure A.1.

Phasors are written in small bold letters like  $\mathbf{v}$ , to distinguish them from radio frequency waves  $v(t)$ , written in small italics letters. A phasor does not contain any information about the frequency of the RF wave, it is only determined by the amplitude and the phase.

The expression  $(V e^{i\varphi}) e^{i\omega t}$  in (A.9) is called a ‘rotating phasor’, it is a time-dependent complex number

$$\begin{aligned} \underline{v} &= \mathbf{v} e^{i\omega t} \\ &= V e^{i\varphi} e^{i\omega t} \\ &= V \cos[\omega t + \varphi] + i V \sin[\omega t + \varphi]. \end{aligned} \quad (\text{A.11})$$

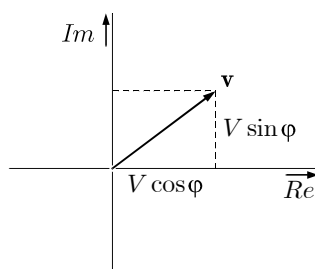


Figure A.1: Phasor diagram.

Rotating phasors are written in small italics and underlined letters, like  $\underline{v}$ . In contrast to a phasor, a rotating phasor contains in addition information about the frequency of the RF wave.

Rotating phasors are plotted at time  $t = 0$ , see figure A.2.

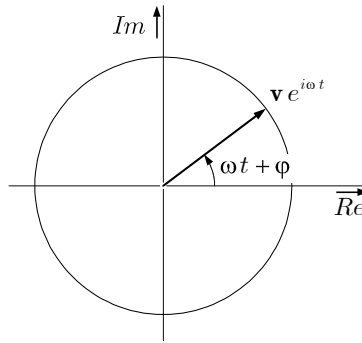


Figure A.2: Representation of a rotating phasor.

In digital communication systems, such as mobile radio, a similar description of a RF wave is used [83, 84]. A modulated RF wave can be written as

$$\begin{aligned} v(t) &= V(t) \sin[\omega t + \varphi(t)] \\ &= V(t) \sin[\omega t + \varphi - \Delta\varphi(t)] \\ &= \text{Im} [(V(t) e^{i\Delta\varphi(t)}) e^{i\varphi} e^{i\omega t}]. \end{aligned} \quad (\text{A.12})$$

The RF wave, determined by the time-independent phasor  $\mathbf{v}_{\text{car}} = e^{i\varphi}$ , is called the ‘carrier’. Modulations are described by the time-dependent phasor

$$\mathbf{v}_{\text{mod}}(t) = V(t) e^{i\Delta\varphi(t)}. \quad (\text{A.13})$$

In the case when the modulated RF wave is in phase with the carrier,  $\mathbf{v}_{\text{mod}}(t)$  is a real number.  $\mathbf{v}_{\text{mod}}(t)$  is an imaginary number, when the phasing between the modulated RF wave and the carrier is  $90^\circ$ , it is ‘out of phase’ or in ‘quadrature phase’. Therefore, the real part of the phasor  $\mathbf{v}_{\text{mod}}(t)$  is called the in-phase (I) part and the imaginary part the quadrature phase (Q) part. The modulation of the RF wave is also completely described by the ‘vector’ spanned by I and Q

$$\mathbf{v}_{\text{mod}}(t) = \begin{pmatrix} v_{\text{mod},I}(t) \\ v_{\text{mod},Q}(t) \end{pmatrix} = \begin{pmatrix} V(t) \cos \Delta\varphi(t) \\ V(t) \sin \Delta\varphi(t) \end{pmatrix}. \quad (\text{A.14})$$

The accompanying vector space is called the ‘IQ plane’, shown in figure A.3.

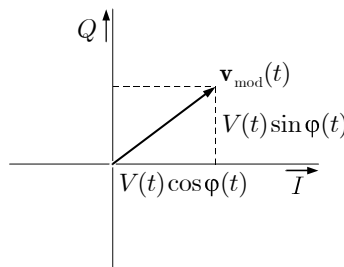


Figure A.3: Vector diagram or polar diagram.

One chooses  $\varphi = 0$  in technical installations. In this case one has only to replace ‘I’ by ‘Re’ and ‘Q’ by ‘Im’ to transform a vector in the IQ plane to a phasor in the complex plane.



By supplying the RF wave and a local oscillator (LO) wave, which is equivalent to the carrier, an IQ demodulator provides the vector components at the I and Q outputs. This is called ‘quadrature detection’ or ‘IQ detection’. By modulating the I and Q inputs of an IQ modulator, one modulates a RF signal, supplied to the RF input. This is normally called ‘vector modulation’ or ‘IQ modulation’.

### A.1.2 Other notation and expressions

The scalar product is

$$\mathbf{a} \cdot \mathbf{b} = \sum_i a_i b_i = a_i b_i, \quad (\text{A.15})$$

and  $\mathbf{a} \cdot \mathbf{b}$  denotes a dyadic product [85].

The heavy side function  $\Theta$  is given by

$$\Theta(t) = \begin{cases} 0 & \text{for } t < 0 \\ \frac{1}{2} & \text{for } t = 0 \\ 1 & \text{for } t > 0 \end{cases}. \quad (\text{A.16})$$

The expression ‘two frequencies are (phase) locked to each other’ does not imply two equal frequencies  $f_1$  and  $f_2$ . It means that the ratio of both frequencies is a fixed rational number, in the same way that cog numbers of gearwheels are fixed in a gear unit.

$$\frac{f_1}{f_2} = \frac{\text{integer}_1}{\text{integer}_2} = \text{const.} \quad (\text{A.17})$$

#### Some expressions:

‘Multi-bunch oscillation’: any bunch oscillation as soon as more than one bunch rotates in the storage ring.

‘Coupled bunch oscillation’: a bunch oscillation involving more than one bunch, forming common oscillation states. A coupled bunch oscillation is always a multi-bunch oscillation.

‘Coherent frequency spread’: spread of synchrotron oscillation frequencies between different bunches.

‘Coherent frequency shift’: shift of synchrotron oscillation frequencies of bunches.

‘Incoherent frequency spread’: spread of synchrotron oscillation frequencies of particles, within the individual bunches.

## A.2 Derivation of the luminosity reduction factor

For the luminosity upgrade, the colliding proton and electron beams in HERA are more strongly focussed at the interaction points (IPs). The bunch length and the  $\beta$ -function become comparable in magnitude. This leads to an enhancement of the effective cross section, compared to the cross section at the IPs, and the luminosity becomes dependent on the bunch length. This effect is called the hour-glass-effect. In section 1.2, the parameters for HERA were discussed. The formulas presented follow the treatments of [1].

The tri Gaussian density distributions of a proton bunch and an electron bunch are given by

$$\rho_p(x, y, s) = \frac{N_p}{(2\pi)^{3/2} \sigma_{px} \sigma_{py} \sigma_{ps}} \exp\left(-\frac{x^2}{2\sigma_{px}^2} - \frac{y^2}{2\sigma_{py}^2} - \frac{s^2}{2\sigma_{ps}^2}\right) \quad (\text{A.18})$$

$$\rho_e(x, y, s) = \frac{N_e}{(2\pi)^{3/2} \sigma_{ex} \sigma_{ey} \sigma_{es}} \exp\left(-\frac{x^2}{2\sigma_{ex}^2} - \frac{y^2}{2\sigma_{ey}^2} - \frac{s^2}{2\sigma_{es}^2}\right) \quad (\text{A.19})$$

with the total number of particles in a bunch  $N$  and the bunch size  $\sigma$ . The luminosity for the collision is given by the integral

$$\mathcal{L}_{col} = 2c \int ds dt dy dx \rho_p(x, y, s - ct) \rho_e(x, y, s + ct). \quad (\text{A.20})$$

Since bunch length and the  $\beta$ -function have comparable magnitude, the horizontal and vertical coordinates depend on the distance to the collision point ( $s = 0$ ). However the bunch length is independent of  $s$ :

$$\begin{aligned} \sigma_{px} &= \sigma_{px}(s) & \sigma_{ex} &= \sigma_{ex}(s) \\ \sigma_{py} &= \sigma_{py}(s) & \sigma_{ey} &= \sigma_{ey}(s) \\ \sigma_{ps} &= \text{const.} & \sigma_{es} &= \text{const.} \end{aligned} \quad (\text{A.21})$$

Carrying out the integrations over  $x$ ,  $y$  and  $t$ :

$$\frac{1}{2\pi \sigma_{px} \sigma_{ex}} \int_{-\infty}^{\infty} dx \exp\left(-\frac{1}{2} \left(\frac{1}{\sigma_{px}^2} + \frac{1}{\sigma_{ex}^2}\right) x^2\right) = \frac{1}{\sqrt{2\pi}} \frac{1}{\sqrt{\sigma_{px}^2 + \sigma_{ex}^2}}. \quad (\text{A.22})$$

The integration over  $y$  is similar:

$$\begin{aligned} \frac{1}{2\pi \sigma_{ps} \sigma_{es}} \int_{-\infty}^{\infty} dt \exp\left(-\frac{1}{2} \left(\frac{(s+ct)^2}{\sigma_{ps}^2} + \frac{(s-ct)^2}{\sigma_{es}^2}\right)\right) &= \\ &= \frac{1}{c} \frac{1}{\sqrt{2\pi}} \frac{1}{\sqrt{\sigma_{ps}^2 + \sigma_{es}^2}} \exp\left(-\frac{2s^2}{\sigma_{ps}^2 + \sigma_{es}^2}\right). \end{aligned}$$

The luminosity in terms of the bunch sizes  $\sigma = \sigma(s)$  near the interaction point is given by

$$\mathcal{L}_{col} = \frac{N_p N_e}{\pi \sqrt{2\pi} \sqrt{\sigma_{ps}^2 + \sigma_{es}^2}} \int_{-\infty}^{\infty} ds \frac{\exp\left(-\frac{2s^2}{\sigma_{ps}^2 + \sigma_{es}^2}\right)}{\sqrt{(\sigma_{px}^2(s) + \sigma_{ex}^2(s)) (\sigma_{py}^2(s) + \sigma_{ey}^2(s))}}. \quad (\text{A.23})$$

In the limit of short bunches ( $\sigma_s \ll \beta^*$ ) the bunch sizes are independent of the distance to the interaction point and equal to the values at the interaction point  $\sigma = \sigma^*$ :

$$\mathcal{L}_{col,0} = \frac{N_p N_e}{2 \pi \sqrt{(\sigma_{px}^{*2} + \sigma_{ex}^{*2})(\sigma_{py}^{*2} + \sigma_{ey}^{*2})}}. \quad (\text{A.24})$$

Assuming the bunch size depends on  $s$  like

$$\sigma = \sigma^* \left(1 + \frac{s^2}{\beta}\right) \quad (\text{A.25})$$

we substitute

$$u = \sqrt{\frac{2}{\sigma_{ps}^2 + \sigma_{es}^2}} \quad (\text{A.26})$$

in order to simplify equation (A.23) and to obtain the luminosity for long bunches

$$\mathcal{L}_{col} = \frac{N_p N_e}{2 \pi \sqrt{(\sigma_{px}^{*2} + \sigma_{ex}^{*2})(\sigma_{py}^{*2} + \sigma_{ey}^{*2})}} \int_{-\infty}^{\infty} du \frac{1}{\sqrt{\pi}} \frac{\exp(-u^2)}{\sqrt{\left(1 + \frac{u^2}{u_x^2}\right) \left(1 + \frac{u^2}{u_y^2}\right)}} \quad (\text{A.27})$$

with

$$u_x^2 = \frac{2(\sigma_{px}^{*2} + \sigma_{ex}^{*2})}{(\sigma_{ps}^2 + \sigma_{es}^2) \left(\frac{\sigma_{px}^{*2}}{\beta_{px}^{*2}} + \frac{\sigma_{ex}^{*2}}{\beta_{ex}^{*2}}\right)} \quad \text{and} \quad u_y^2 = \frac{2(\sigma_{py}^{*2} + \sigma_{ey}^{*2})}{(\sigma_{ps}^2 + \sigma_{es}^2) \left(\frac{\sigma_{py}^{*2}}{\beta_{py}^{*2}} + \frac{\sigma_{ey}^{*2}}{\beta_{ey}^{*2}}\right)}. \quad (\text{A.28})$$

This means, that the short bunch luminosity  $\mathcal{L}_{col,0}$  is reduced in the long bunch case  $\mathcal{L}_{col}$  by the luminosity reduction factor  $R$ , given by the ratio between (A.24) and (A.27):

$$R(u_x, u_y) = \frac{\mathcal{L}_{col,0}}{\mathcal{L}_{col}} = \int_{-\infty}^{\infty} du \frac{1}{\sqrt{\pi}} \frac{\exp(-u^2)}{\sqrt{\left(1 + \frac{u^2}{u_x^2}\right) \left(1 + \frac{u^2}{u_y^2}\right)}} \quad (\text{A.29})$$

At HERA, the vertical focussing is much larger than the horizontal; i.e.

$$\sigma_x = \sigma_x^* \quad \text{and} \quad \sigma_y = \sigma_y^* \left(1 + \frac{s^2}{\beta_y}\right) \quad (\text{A.30})$$

In this special case, the reduction factor can be evaluated analytically:

$$R(u_y) = \frac{\mathcal{L}_{col,0}}{\mathcal{L}_{col}} = \int_{-\infty}^{\infty} du \frac{1}{\sqrt{\pi}} \frac{\exp(-u^2)}{\sqrt{\left(1 + \frac{u^2}{u_y^2}\right)}} = \frac{u_y}{\sqrt{\pi}} \exp\left(\frac{u_y^2}{2}\right) K_0\left(\frac{u_y^2}{2}\right) \quad (\text{A.31})$$

Here,  $K_0$  is the modified Bessel function. Comparable derivations of this expression can be found in [86, 87].

### A.3 Microwave instability

It has long been known, through observations of longitudinal bunch shapes, that bunch shape oscillations take place during acceleration. Hence, the question arose, whether the HERA proton ring suffers from microwave instabilities similar to the CERN SPS in former times [88]. In normal operation, a narrow band microwave instability leads to micro-bunching and hence to emittance dilution. This is caused by impedances with high resonant frequencies, which for proton machines, like HERA, are typically in the order of GHz. During the HERA machine studies in December 1998, experiments were carried out to examine this effect [89].

To obtain stable conditions, the RF is first switched off. Then, the shapes of long bunches, injected from the pre-accelerator, are sampled several times with a fast frame oscilloscope. Micro-bunching would be visible if a sufficiently strong instability driving impedance is present. Fourier analysis of the bunch shapes gives indication of the resonant frequency from the impedance. With that information, the frequencies could be obtained [88].

W. Kriens provided the data of a typical measurement shown in figure A.4. These shapes

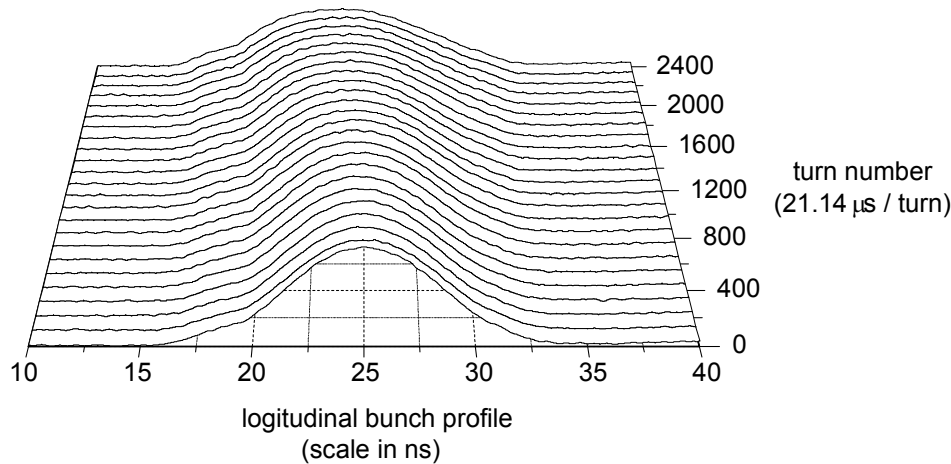


Figure A.4: Longitudinal bunch profiles taken to search for a possible microwave instability in the HERA proton ring.

were taken from a bunch consisting out of  $5 \cdot 10^{10}$  to  $6 \cdot 10^{10}$  protons. No micro-bunching is visible. Detailed examinations by Fourier transformation also showed no strong frequencies. This indicated that HERA does not suffer from micro wave instabilities up to bunch currents of 0.38 mA to 0.46 mA. These bunch current correspond to a beam current, for 180 bunches, of 69 mA to 83 mA.

### A.4 Details on the phase locked loop for injections

The orbit circumference  $2\pi R$  in a storage ring depends on the particle energy  $E_s$ , the RF frequency  $f_{RF}$  and the harmonic number  $h$ , see (3.1)

$$2\pi R = \frac{hc}{f_{RF}} \sqrt{1 - \left(\frac{E_0}{E_s}\right)^2}. \quad (\text{A.32})$$

Transferring the beam from PETRA to HERA does not change the particle energy. Hence, the ratio of the orbit circumferences in both accelerators is given by

$$\frac{2\pi R_{\text{HERA}}}{2\pi R_{\text{PETRA}}} = \frac{h_{\text{HERA}}}{h_{\text{PETRA}}} \frac{f_{\text{RF,PETRA}}}{f_{\text{RF,HERA}}}. \quad (\text{A.33})$$

For electrons, the ratio of the orbit circumference is equal to the ratio of the harmonic numbers, and one can choose equal RF frequencies. In practice, it is more flexible to choose two slightly different frequencies and accept small orbit deviations. Due to energy loss by synchrotron radiation and re-acceleration, these deviations disappear, called ‘damping by synchrotron radiation’.

PETRA accelerates protons and electrons in the same ring. Hence, protons have to bypass the electron RF cavities so that the proton beam quality is not affected by the cavity impedances. This bypass extends the proton orbit circumference in PETRA, and the ratio of the orbit circumference in both rings is not equal to the ratio of the harmonic numbers. To fulfill the condition (A.33), two different frequencies had to be chosen. The ratio is given by

$$\frac{f_{\text{RF,HERA}}}{f_{\text{RF,PETRA}}} = \frac{h_{\text{HERA}}}{h_{\text{PETRA}}} \frac{2\pi R_{\text{PETRA}}}{2\pi R_{\text{HERA}}} = \frac{1100}{400} \frac{2303.995 \text{ m}}{6335.825 \text{ m}} = 1.0000253. \quad (\text{A.34})$$

Two different frequencies result in a length deviation  $\Delta l_{\text{train}}$  of bunch trains in both accelerators. Considering the bunch filling scheme, see chapter 1.3, this deviation is  $\Delta l_{\text{train}} = 0.158 \text{ ns}$ . If the first bunch exactly hits the target bucket, then the last bunch has a phase, with respect to its target bucket, of

$$\Delta\phi = \frac{\Delta l_{\text{train}}}{\frac{1}{f_{\text{RF,HERA}}}} \frac{360^\circ}{2\pi} = \left( \frac{f_{\text{RF,HERA}}}{f_{\text{RF,PETRA}}} - 1 \right) 325 \frac{360^\circ}{2\pi} = 0.47^\circ. \quad (\text{A.35})$$

This is acceptable. Phase shifts caused by transient beam loading are one order of magnitude larger, compare section 5.3.

Nevertheless, the frequencies of both accelerators have to be phase locked during the transfer. Otherwise, even the buckets for the first bunch would not be synchronized. This is done with the phase locked loop, shown in figure A.5. Both frequencies are mixed down to the differ-

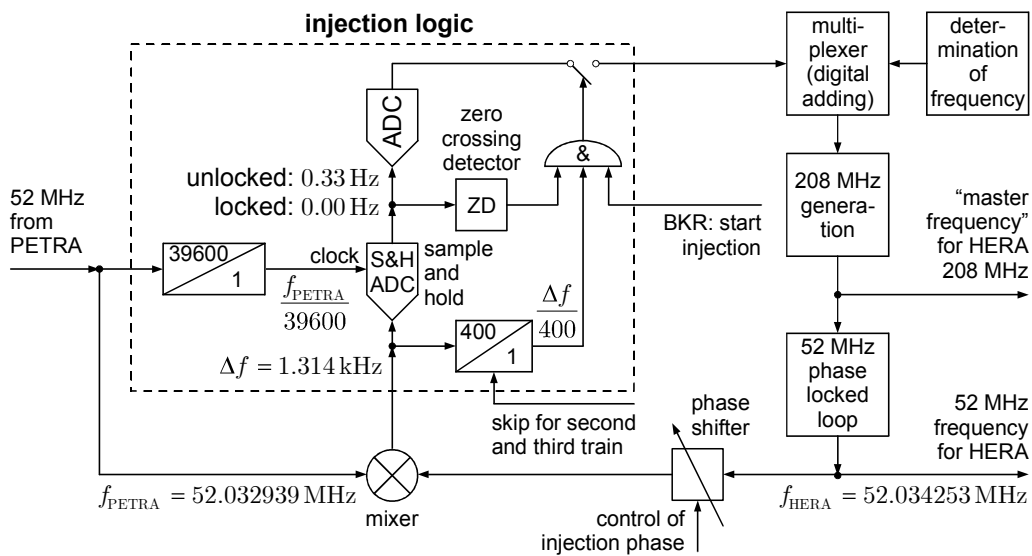


Figure A.5: Phase locked loop for the proton beam transfer from PETRA to HERA.

ence frequency of 1.314 kHz. Since the harmonic number of PETRA is 400, every 400th wave



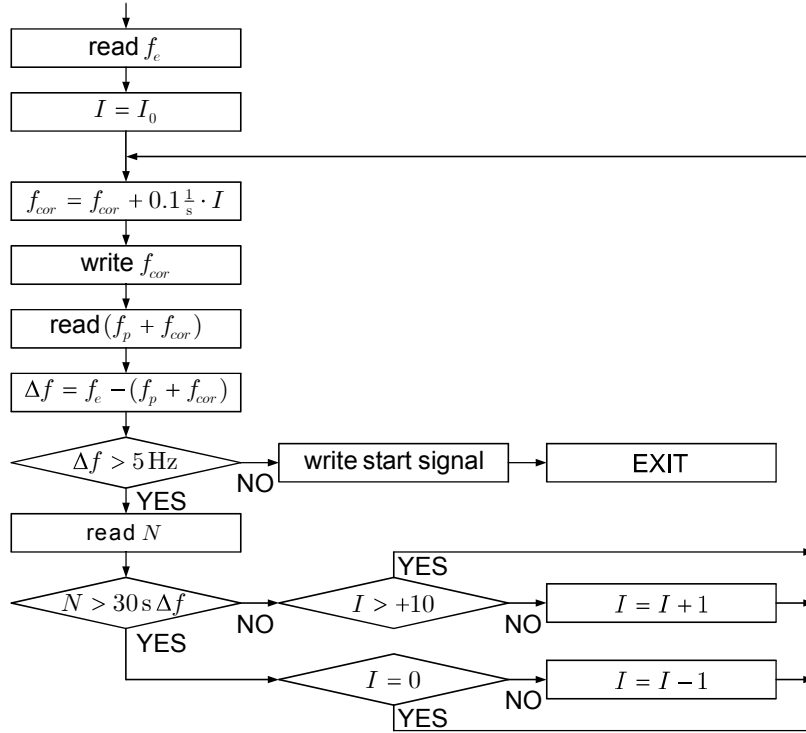


Figure A.7: This algorithm leads to a frequency approach during ep-synchronisation by keeping the ratio  $t_R = \frac{N}{\Delta f}$  constant.

As a the first step, the NORSK DATA computer calculates the difference frequency  $\Delta f$  from both frequencies. By sending the correction frequency  $f_{corr}$  to the multiplexer, it changes the generated frequency for the proton ring, and with it the difference frequency

$$\Delta f = f_e - f_p - f_{corr}. \quad (\text{A.37})$$

The correction frequency  $f_{corr}$  is increased until  $\Delta f \approx 250$  Hz.

From the 208 MHz reference signal of the proton ring, a 500 MHz signal is obtained by a phase locked loop. This frequency is used for the ep-synchronization. Mixing with the 500 MHz from the electron storage ring delivers the difference frequency  $\Delta f$ . The harmonic number of 500 MHz is at HERA 10560. A backwards counter (countdown), restarting counting after 10560 counts, counts the difference frequency waves. When the counter value  $N$  reaches 0, the bucket positions of both rings match. The remaining time  $t_R$  until the counter value reaches 0 and reset to 10560, is given by the actual number of remaining counts divided by the actual difference frequency

$$t_R = \frac{N}{\Delta f}. \quad (\text{A.38})$$

After reaching  $\Delta f = \Delta f_0 \approx 250$  Hz, the NORSK DATA computer waits until  $t_R = 30$  s. This is the case, when the counter value is given by

$$N_0 = 250 \text{ Hz} \cdot 30 \text{ s} = 7500. \quad (\text{A.39})$$

By further changing  $f_{corr}$ , the computer keeps  $t_R$  constant.

Assume, the computer needs the time  $\Delta t_{NORSK,0}$  after  $t_R = 30$  s has been reached, to take the next set of data, then the counter value has changed during this time to

$$N_1 = N_0 - \Delta f_0 \Delta t_{NORSK,0}. \quad (\text{A.40})$$

To keep  $t_R$  constant, the next difference frequency must be

$$\Delta f_1 = \frac{N_1}{30 \text{ s}} = \frac{7500 - \Delta f_0 \Delta t_{NORSK,0}}{30 \text{ s}}, \quad (\text{A.41})$$

et cetera. Altogether, we obtain

$$\Delta f_n = \frac{N_n}{30 \text{ s}}. \quad (\text{A.42})$$

This results in a correction frequency, transmitted to the multiplexer of

$$f_{corr,n} = f_e - f_p - \Delta f_n. \quad (\text{A.43})$$

The program of the NORSK DATA computer does not calculate the ratio (A.42) directly. In fact, it realizes the constant remaining time  $t_R$  by incrementing the correction frequency  $f_{corr}$ . The code implemented is shown in figure A.7. This procedure results in a smooth frequency approach of both accelerators, see figure A.8.

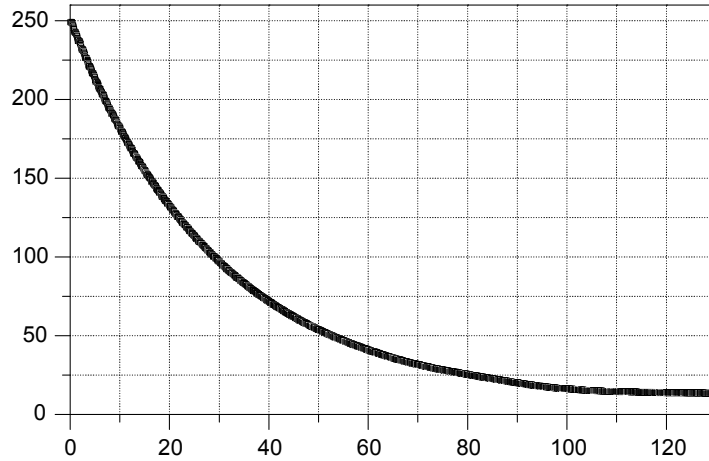


Figure A.8: Frequency approach during ep-synchronisation by keeping  $t_R = \frac{N}{\Delta f}$  constant.

Reaching the difference frequency tolerance of 5 Hz, this procedure is stopped and the computer enables the locking of the phase locked loop by sending ‘start’, i.e. a ‘true signal’ to an AND-gate. The second input of this gate will become true, when the counter value  $N$  reaches next time 0. In this case, the buckets correspond and the difference frequency is sufficiently small to phase lock the electron ring to the proton ring, resulting in a frequency jump in the electron ring of 5 Hz. Remember, by reaching the difference frequency of 5 Hz after the smooth approach, the remaining time  $t_R$ , until  $N$  reaches 0, is still 30 s. This mean, there is enough time for the computer to send ‘start’.

It is planned to replace this system in the future with a more flexible one [29].



## A.6 Stability investigations on the narrow band beam phase feedback systems

The two narrow band beam phase feedback systems, implemented in the HERA proton storage ring, represent implementations of two different concepts for damping synchrotron oscillations: Phase loop I implements a differential controller by feeding back a time delayed phase signal, this results in stability limits, but with the ability to damp batches of ten bunches independently from each other. Phase loop II implements an integral controller by changing the reference frequency, without any stability limits. In contrast to phase loop I, it damps only when all bunches oscillate in phase.

### A.6.1 The beam transfer function used for investigations

The stability investigations presented here are based on the simplified beam transfer function (BTF)

$$BTF(s) = \frac{1}{\frac{s^2}{\omega_s^2} + \frac{2\delta_{BTF}}{\omega_s}s + 1}, \quad (\text{A.44})$$

with damping  $0 \leq \delta_{BTF} \leq 1$  and synchrotron frequency  $\omega_s \geq 0$ . With this BTF, we ignore Landau damping and thus also the incoherent frequency spread. By using the damping value  $\delta_{BTF} = 0.005$ , representing coherent damping, we obtain a maximum BTF amplitude of 100. This amplitude is similar to those measured. For the synchrotron frequency we use  $\omega_s = 2\pi 30$  Hz. Figure A.9 shows the Bode diagram, consisting of the amplitude  $|BTF(i\omega)|$  and phase  $\arctan \frac{\text{Re}[BTF(i\omega)]}{\text{Im}[BTF(i\omega)]}$  response of the BTF.

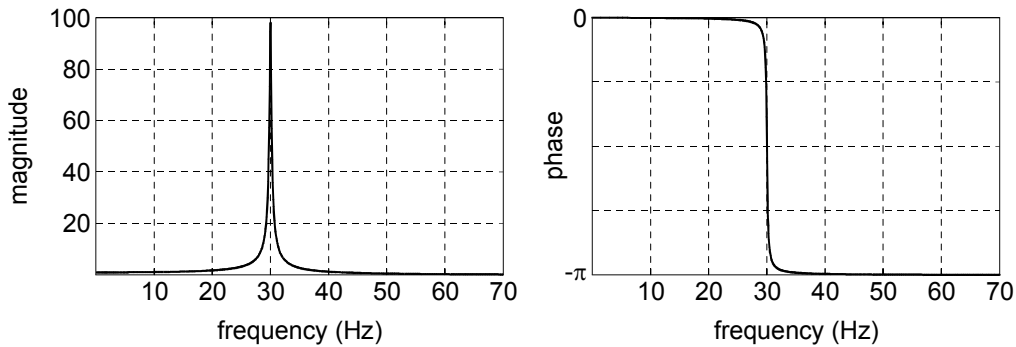


Figure A.9: Bode diagram of the BTF with  $\delta_{BTF} = 0.005$  and  $\omega_s = 2\pi 30$  Hz.

Even with this simple BTF, the operation mechanism of the phase loops can be investigated. These examinations may be extended to consider several beam dynamics effects.

### A.6.2 Phase loop I

From figure 3.8 we have first to determine the block diagram of phase loop I: Between the phase shifter and the phase detector, the behavior is given by the BTF. The essential part between the phase detector and the phase shifter is the  $90^\circ$  phase shift of the synchrotron oscillation signal. Figure A.10 shows the resulting block diagram.

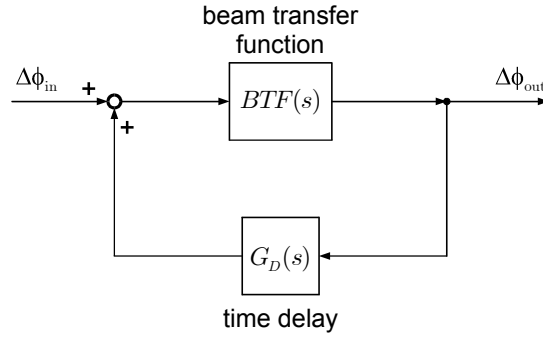


Figure A.10: Block diagram of phase loop I.

The phase shift of  $90^\circ$  is technically realized by the addition of three successive delayed phases signals [90, 91]

$$\Delta\phi_{\text{out}}(t) = g \left( -0.0175 \Delta\phi_{\text{in}}(t - T_s/2) + 0.9996 \Delta\phi_{\text{in}}(t - T_s) + 0.0175 \Delta\phi_{\text{in}}(t - 3T_s/2) \right), \quad (\text{A.45})$$

which can be approximated by

$$\Delta\phi_{\text{out}}(t) \approx g \Delta\phi_{\text{in}}(t - T_s). \quad (\text{A.46})$$

The resulting transfer function is

$$G_D(s) = g e^{-sT_s}. \quad (\text{A.47})$$

In practice, the delay time  $T_s$  is determined by measurements of the synchrotron frequency  $f_s$  and fixed at the value  $T_s = \frac{1}{4f_s}$ . During normal operation, this value is not changed. We assume, the value is  $T_s = \frac{1}{4 \cdot 30\text{Hz}}$ , for the following investigations.

From the block diagram A.10, we get the closed loop transfer function

$$G_{PLI}(s) = \frac{BTF(s)}{1 - BTF(s) G_D(s)} \quad (\text{A.48})$$

and hence the Bode plots with the loop gain  $g = 0.3$  at different synchrotron frequencies, shown in figure A.11. This plot gives approximately the damping of the loop

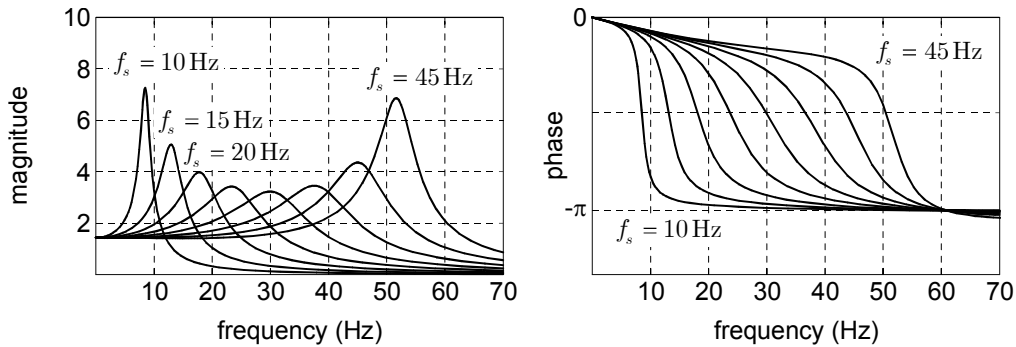


Figure A.11: Bode plot of the closed loop transfer function with loop gain  $g = 0.3$ , for synchrotron frequencies of 10 Hz, 15 Hz, 20 Hz, 25 Hz, 30 Hz, 35 Hz, 40 Hz and 45 Hz.

$$\delta_{PLI} \approx \frac{1}{2}g \quad (\text{A.49})$$

when the synchrotron frequency is near 30 Hz. Larger deviations of the synchrotron frequency from 30 Hz lead to less damping. It is clear, that at frequencies larger than  $2 \times 30$  Hz, the loop becomes unstable because of the negative feedback, caused by the fixed delay value of  $T_s = \frac{1}{4} \frac{1}{30 \text{ Hz}}$ .

For a more accurate stability investigation, the Nyquist criterion may be used. This is due to the fact that the denominator of the transfer function cannot be factorized and directly checked for zeros because of the exponential function.

Assuming a control loop with the open loop transfer function  $G(s)$  as figure A.12, the

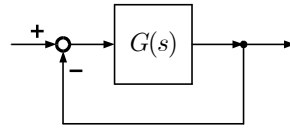


Figure A.12: A control loop with the open loop transfer function  $G(s)$ .

Nyquist diagram is obtained by plotting successive values of  $G(i\omega)$  as a function of the parameter  $\omega$ , running from 0 to infinity in the complex, so called  $G(s)$ -plane. For the resultant diagram, the Nyquist theorem says [76]: *The closed-loop system is stable if and only if the number of clockwise encirclements of the point  $s = -1 + i0$  by the Nyquist diagram of  $G(s)$  plus the number of poles of  $G(s)$  in the right half-plane is zero.*

In the case of the phase loop I, the open loop transfer function is given by

$$\begin{aligned} G(s) &= -BTF(s) G_D(s) \\ &= -\frac{g e^{-sT_s}}{\frac{s^2}{\omega_s^2} + \frac{2\delta_{BTF}}{\omega_s} s + 1} \end{aligned} \quad (\text{A.50})$$

and we get the Nyquist diagrams, shown in figure A.13, for several synchrotron frequencies.

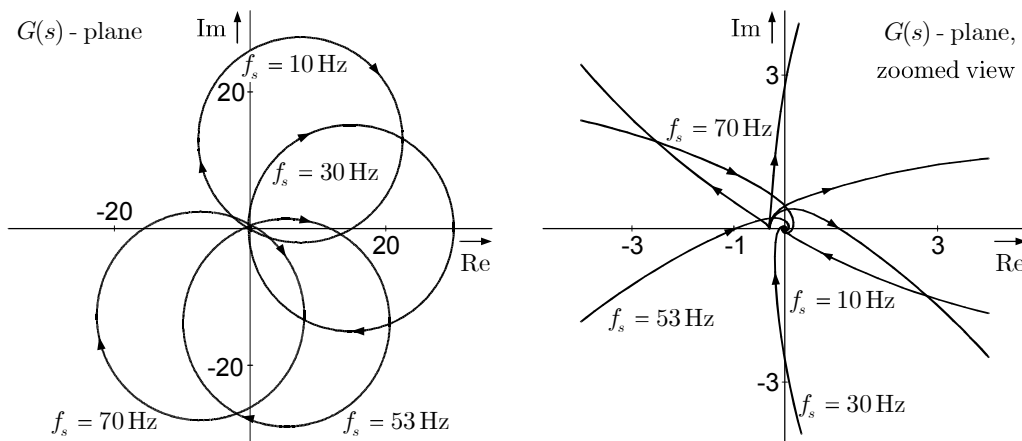


Figure A.13: Nyquist diagrams for the open loop transfer function of the phase loop I at  $\delta = 0.005$ ,  $g = 0.3$ ,  $T_s = \frac{1}{4} \frac{1}{30 \text{ Hz}}$  and synchrotron frequencies of 10 Hz, 30 Hz, 53 Hz and 70 Hz.

At synchrotron frequencies greater than 53 Hz, the Nyquist diagrams do not encircle the point  $s = -1 + i0$  and there are no poles in the right half- $s$ -plane. Frequencies above 53 Hz lead to

an encirclement of  $s = -1 + i0$ . This means, that the loop is stable for synchrotron frequencies below 53 Hz and unstable for synchrotron frequencies above 53 Hz.

Note, the starting point of the curves in the Nyquist diagram is  $G(i0) = -g + i0$ . One may increase the damping rate of the loop by increasing the gain  $g$ . But this leads to a more unstable behavior of the loop. By increasing the gain, the synchrotron frequency range of operation becomes smaller. A gain value of  $g$  greater than 1 makes the loop immediately unstable, because the starting point of the curves in the Nyquist diagram is then on the left hand side of  $s = -1 + i0$ .

### A.6.3 Phase loop II

Figure A.14 shows again the technical components of the phase loop II: To analyze stability we

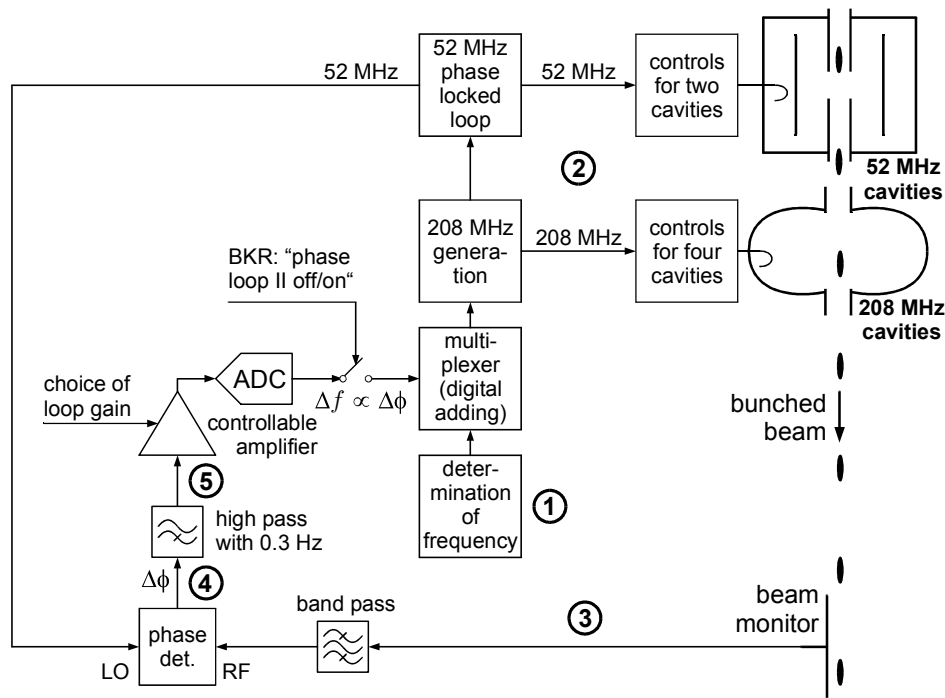


Figure A.14: Technical components of the phase loop II.

reduce this picture to a block diagram:

A phase change in the 208 MHz generation leads to an identical change in the 52 MHz phase locked loop and all radio frequency cavities (at point 2 in figure A.14). The connection between this point and the beam monitor, or the phase detector input (point 3), is given by the beam transfer function

$$BTF(s) = G_{23}(s) = \frac{1}{\frac{s^2}{\omega_s^2} + \frac{2\delta_{BTF}}{\omega_s}s + 1}, \quad (\text{A.51})$$

with  $0 \leq \delta_{BTF} \leq 1$  and  $\omega_s \geq 0$ . The reference of the phase detection is equivalent to 2, i.e. the output of the beam transfer function has to be subtracted by the bypassed input signal. We get from 2 to the phase detector output 4

$$G_{24}(s) = BTF(s) - 1. \quad (\text{A.52})$$

At the end of this section, we will discuss the fact that the high pass filter is an important component of the loop. But for simplicity it is first neglected

$$HP(s) = G_{45}(s) = 1.$$

The phase detector output is amplified, defining the gain  $g$ , and added to the frequency value  $\omega_{RF}$ , calculated from the magnetic field of the reference magnet. Therefore, the radio frequency is changed by  $\Delta\omega = g \Delta\phi$  and with it the phase of the radio frequency

$$\begin{aligned} v_{RF}(t) &= V_{RF}(t) \sin [(\omega_{RF} + \Delta\omega) t + \varphi_{RF}] \\ &= V_{RF}(t) \sin [\omega_{RF} t + g \Delta\phi t + \varphi_{RF}] \\ &= V_{RF}(t) \sin [\omega_{RF} t + \Delta\varphi(t) + \varphi_{RF}]. \end{aligned} \quad (\text{A.53})$$

From this approach, we obtain the change of the radio frequency phase at point 2 in dependence on the beam phase at 5 as

$$\frac{\Delta\varphi}{\Delta\phi} = g t \quad (\text{A.54})$$

which is equivalent to an integration

$$G_I(s) = G_{52}(s) = \frac{g}{s} \quad (\text{A.55})$$

with  $g \geq 0$ . Combining all these elements, we get the block diagram, shown in figure A.15.

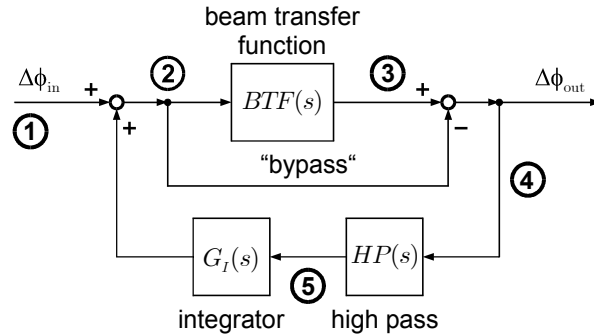


Figure A.15: Control theoretical block diagram of phase loop II.

To investigate the stability, we have to calculate the transfer function of the whole loop:

$$\begin{aligned} G_{PLII}(s) &= \frac{BTF(s) - 1}{1 - (BTF(s) - 1) HP(s) G_I(s)} \\ &= \frac{BTF(s) - 1}{s^2 + 2 \delta_{BTF} \omega_s s} \\ &= \frac{BTF(s) - 1}{s^2 + (2 \delta_{BTF} \omega_s + g) s + 2 \delta_{BTF} \omega_s g + \omega_s^2}. \end{aligned} \quad (\text{A.56})$$

The poles of the loop transfer function are given by the roots of the denominator

$$s_{p1} = -\frac{1}{2} \left( 2 \delta_{BTF} \omega_s + g - \sqrt{(2 \delta_{BTF} \omega_s + g)^2 - 4(2 \delta_{BTF} \omega_s g + \omega_s^2)} \right) \quad (\text{A.57})$$

$$s_{p2} = -\frac{1}{2} \left( 2 \delta_{BTF} \omega_s + g + \sqrt{(2 \delta_{BTF} \omega_s + g)^2 - 4(2 \delta_{BTF} \omega_s g + \omega_s^2)} \right). \quad (\text{A.58})$$

We have to distinguish two cases, namely a negative and a positive argument of the root, with  $0 \leq \delta_{BTF} \leq 1$  and  $g \geq 0$  in mind. A negative argument leads to imaginary poles and hence to oscillatory behavior of the loop and a positive one to purely exponential behavior.

$$g < 2(1 + \delta_{BTF})\omega_s \quad \text{oscillations} \quad (\text{A.59})$$

$$g > 2(1 + \delta_{BTF})\omega_s \quad \text{exponential behaviour} \quad (\text{A.60})$$

The loop is stable and will damp synchrotron oscillations, if the real parts of the poles are negative. This is the case for all limited and non-vanishing values of the synchrotron frequency  $\omega_s$ . Figure A.16 shows the positions of the poles  $s_{p1}$ ,  $s_{p2}$  and zeros  $s_{n1}$ ,  $s_{n2}$  in the complex  $s$ -plane in dependence on the loop gain and the damping parameter  $\delta_{BTF}$ .

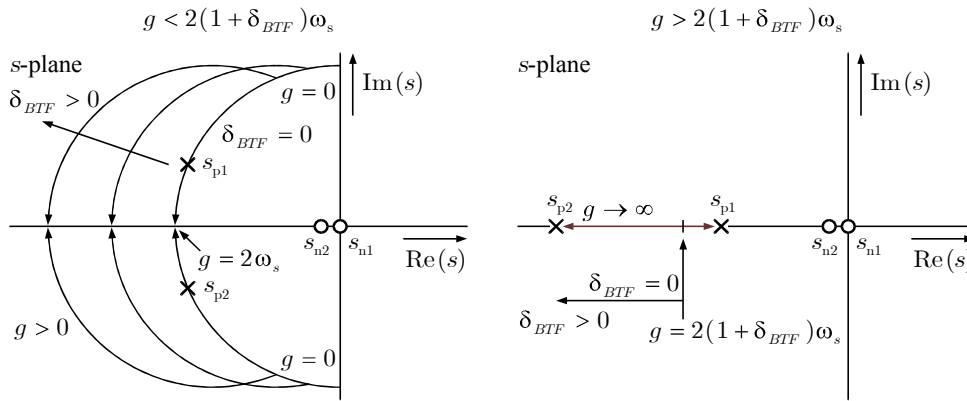


Figure A.16: Poles and zeroes of the closed loop transfer function of the phase loop II.

We calculate the damping rate using the inverse Laplace transformation

$$\begin{aligned} G_{PLII}(t) &= \frac{1}{2\pi i} \oint G_{PLII}(s) e^{st} ds \\ &= \sum_{j=1}^n \text{Res} [G_{PLII}(s_{pj}) e^{s_{pj}t}] \end{aligned} \quad (\text{A.61})$$

where  $n$  is the number of poles. In the case  $\delta_{BTF} = 0$ , we get

$$\text{Res} [G_{PLII}(s) e^{st}; s_{p1}] = -\frac{(\sqrt{g^2 - 4\omega_s^2} + g)^2}{4\sqrt{g^2 - 4\omega_s^2}} \exp \left[ \frac{1}{2} (-\sqrt{g^2 - 4\omega_s^2} - g) t \right] \quad (\text{A.62})$$

$$\text{Res} [G_{PLII}(s) e^{st}; s_{p2}] = \frac{(\sqrt{g^2 - 4\omega_s^2} - g)^2}{4\sqrt{g^2 - 4\omega_s^2}} \exp \left[ \frac{1}{2} (\sqrt{g^2 - 4\omega_s^2} - g) t \right]. \quad (\text{A.63})$$

These expressions supply the damping of the phase loop II directly:

$$\begin{aligned} \delta_{PLII} &= \frac{1}{2} g && \text{for } g < 2\omega_s \text{ and } \delta_{BTF} = 0 \\ \delta_{PLII} &= \frac{1}{2} (g + \sqrt{g^2 - 4\omega_s^2}) && \text{for } g > 2\omega_s \text{ and } \delta_{BTF} = 0 \end{aligned} \quad (\text{A.64})$$

Aside: In the pure damping case, the second pole  $s_{p2}$  plays no role because

$$\lim_{g \rightarrow \infty} \text{Res} [G_{PLII}(s) e^{st}; s_{p2}] = 0. \quad (\text{A.65})$$

Since this loop influences the frequency of the RF-system, we have to investigate whether this loop has an unwanted effect on the cavity frequencies. This can be estimated by considering the transfer function from the frequency generation to the cavity frequency. For calculating this transfer function, we have to rearrange the block diagram, figure A.15, as follows: The input is still point 1, but for the output we have to choose point 2. This result in the block diagram shown in figure A.17.

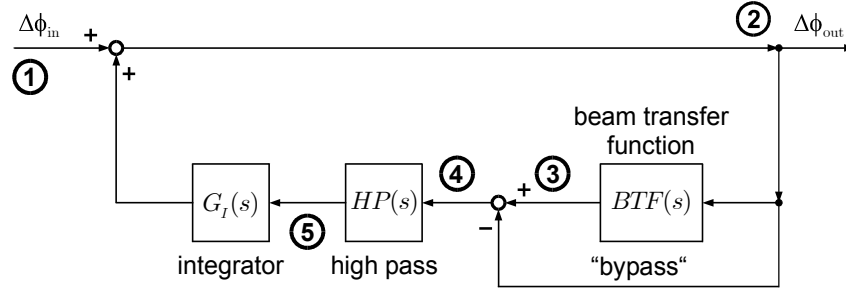


Figure A.17: Block diagram of the phase loop II, in view of the cavities.

The transfer function is

$$\begin{aligned} G_{PLII,cav}(s) &= \frac{1}{1 - (BTF(s) - 1) HP(s) G_I(s)} \\ &= \frac{1}{s^2 + 2 \delta_{BTF} \omega_s s + \omega_s^2} \\ &= \frac{1}{s^2 + (2 \delta_{BTF} \omega_s + g) s + 2 \delta_{BTF} \omega_s g + \omega_s^2}. \end{aligned} \quad (\text{A.66})$$

An adiabatic change i.e.  $s = i\omega \rightarrow 0$  of the input  $\Delta\omega_{RF,in}$  frequency and with it the input phase  $\Delta\phi_{in} = \Delta\omega_{RF,in} t$  leads to a change of the output phase  $\Delta\phi_{out}$ . The ratio is given by the transfer function

$$\left. \frac{\Delta\phi_{out}}{\Delta\phi_{in}} \right|_{s=i\omega \rightarrow 0} = \lim_{s \rightarrow 0} G_{PLII,cav}(s) = \frac{\omega_s^2}{2 \delta \omega_s g + \omega_s^2}. \quad (\text{A.67})$$

We get a not vanishing ratio between the cavity frequency and the required frequency, determined by (3.3):

$$\frac{\Delta\omega_{RF,cavity}}{\Delta\omega_{RF,required}} = \frac{\omega_s^2}{2 \delta \omega_s g + \omega_s^2} \quad (\text{A.68})$$

For typical values of  $\omega_s = 2\pi 30$  Hz,  $\delta_{BTF} = 0.005$  and  $g = 200$ , the result is 0.99, which leads to a 9 mm larger average orbit radius  $R$  at the end of acceleration. Compare the main principle of the frequency ramp in chapter 3.1. Even at low energies, during the largest frequency changes, the  $\sigma$ -emittance of the proton beam is about  $4.4 \text{ mm} / 1 \sigma$ . A minimum aperture of  $5\sigma$  is needed for a sufficiently large life time of the beam. With the beam pipe radius of 27.5 mm, the aperture will be decreased from  $\frac{27.5 \text{ mm}}{4.4 \text{ mm}/\sigma} = 6.25 \sigma$  to  $\frac{27.5 \text{ mm} - 4 \text{ mm}}{4.4 \text{ mm}/\sigma} = 4.2 \sigma$  which leads to an enormous beam loss. Larger damping  $\delta_{BTF}$  of the beam itself increases this effect, for example Robinson and Landau damping.

This problem can be solved by using the high pass filter, already mentioned above. Its transfer function is given by

$$HP(s) = G_{45}(s) = \frac{\tau_{HP} s}{\tau_{HP} s + 1}, \quad (\text{A.69})$$

with the filter time-constant  $\tau_{HP} = 1 / \omega_{HP}$ . In this case, the transfer function is

$$G_{PLII,cav}(s) = \left[ 1 + \frac{g \tau_{HP} s^2 + 2 \delta_{BTF} \omega_s g \tau_{HP} s}{\tau_{HP} s^3 + (1 + 2 \delta_{BTF} \omega_s \tau_{HP}) s^2 + (2 \delta_{BTF} \omega_s + \omega_s^2 \tau_{HP}) s + \omega_s^2} \right]^{-1}. \quad (\text{A.70})$$

With it, the frequency ratio becomes

$$\frac{\Delta \omega_{RF,cavity}}{\Delta \omega_{RF,required}} = \frac{\Delta \phi_{out}}{\Delta \phi_{in}} \Big|_{s=i\omega \rightarrow 0} = \lim_{s \rightarrow 0} G_{PLII,cav}(s) = 1 \quad (\text{A.71})$$

and the frequency error is eliminated.

In reality, the time constant of  $\tau_{HP} \approx 0.5$  s i.e.  $f_{HP} \approx 0.3$  Hz was chosen for the high pass filter [29]. Phase loop II does not lose the excellent stability behavior due to the filter implementation.

During development of phase loop II, tests were undertaken, using a loop operation without high pass filter. Already after starting the ramp process, the beam was lost [29]. This agrees well with the above done statements.



## A.7 Picture gallery

The following pages show some photographs of the hardware described in this work.

Figure A.18 show the racks, containing the fast longitudinal diagnostic system, whose components are labeled in figure A.19. Figures A.20 to A.23 show some low power RF components of the system, and figure A.24 shows a part of the timing system. Figures A.25 to A.29 are photographs of particular sections of the HERA proton ring, such as the superconducting magnets, the transfer line, the resistive gap monitor and the RF cavities. Figure A.30 shows the 208 MHz cavity controls.

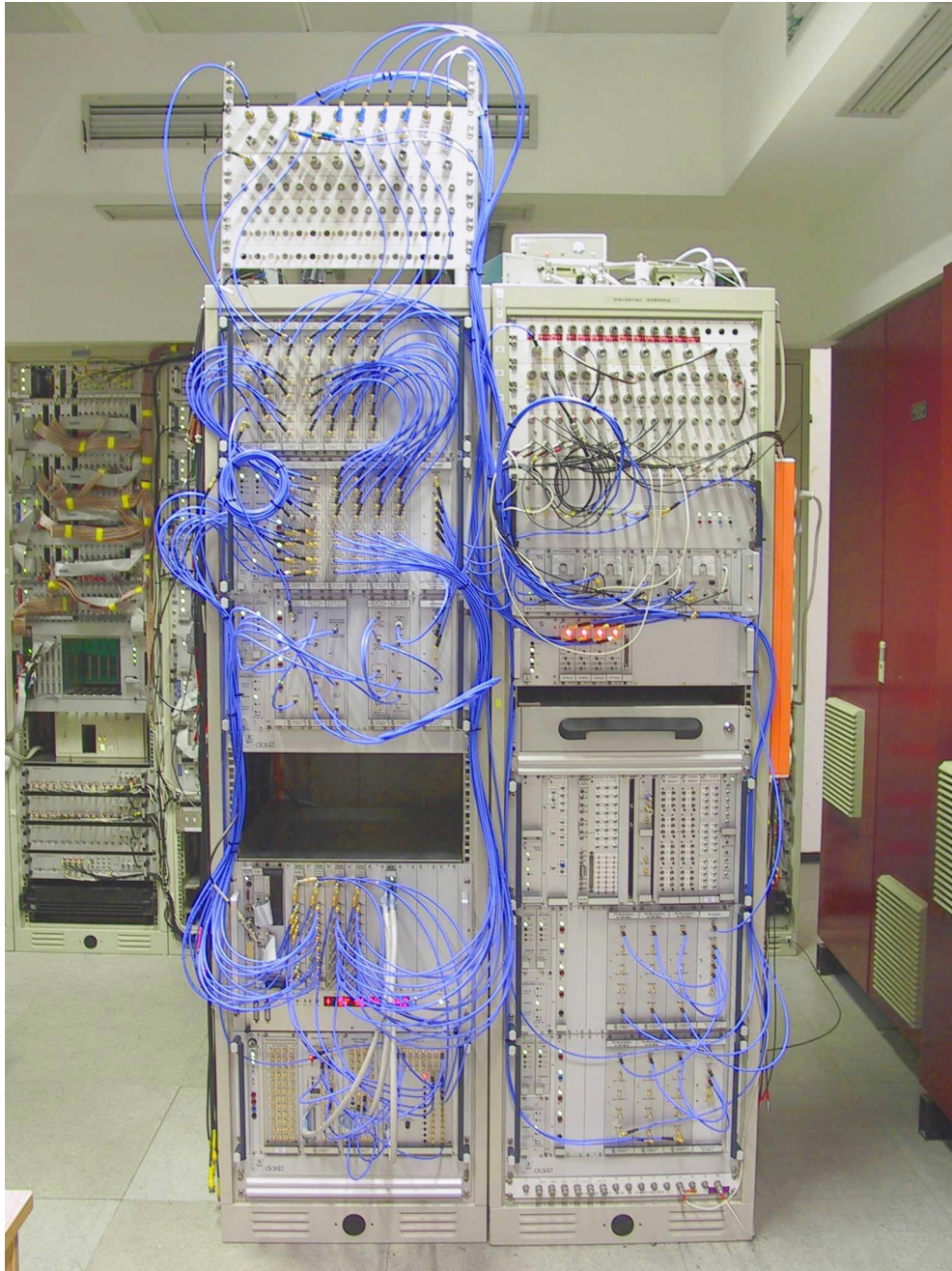


Figure A.18: The fast longitudinal diagnostic system.

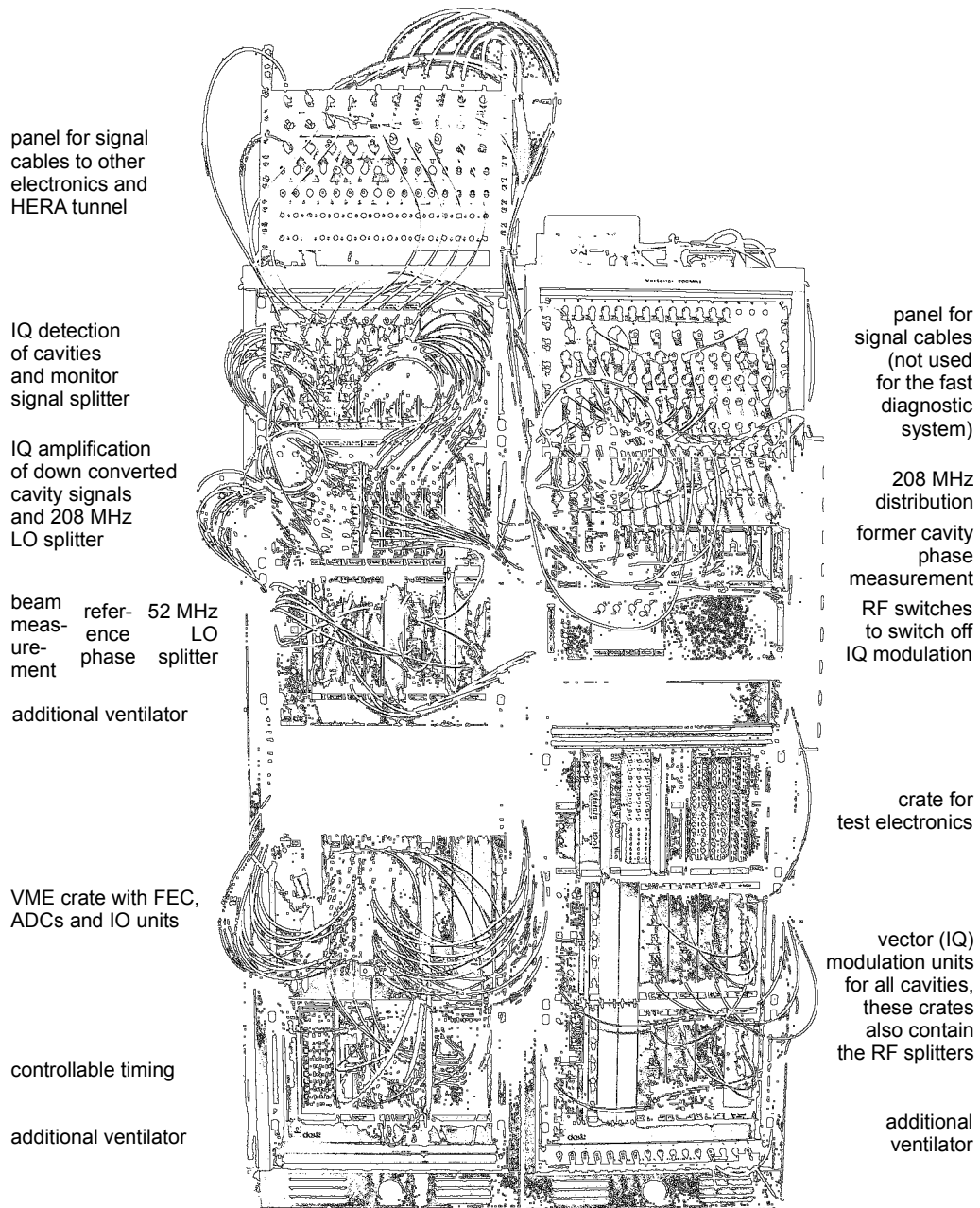


Figure A.19: Scheme of the racks containing the fast longitudinal diagnostic system.

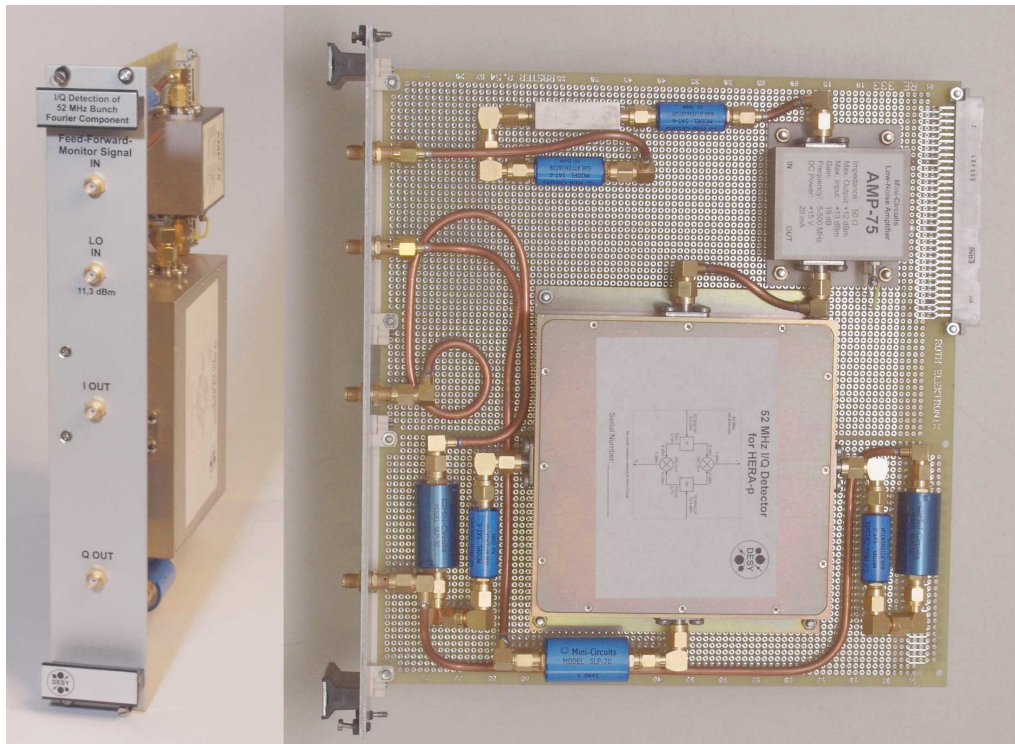


Figure A.20: RF parts for the bunch phase measurement mounted as a plug-in unit for a crate, supplying the different voltages needed for amplifiers. Interference from the environment is prevented by using semi rigid cables and RF-proof solid aluminum cases.

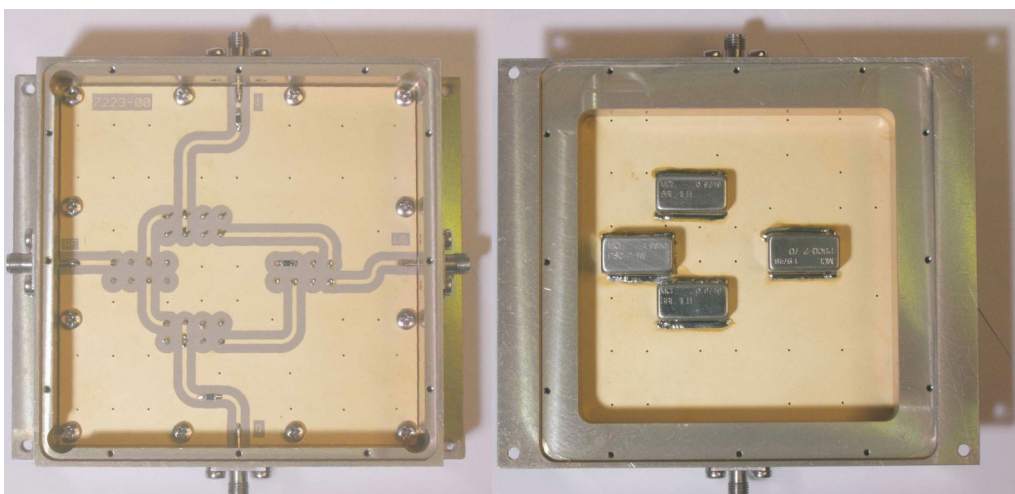


Figure A.21: A view inside a vector modulator - IQ detectors look similar. Striplines on the board with gold-coated copper conductor ensure an impedance of  $50\ \Omega$ . This prevents signal reflections.



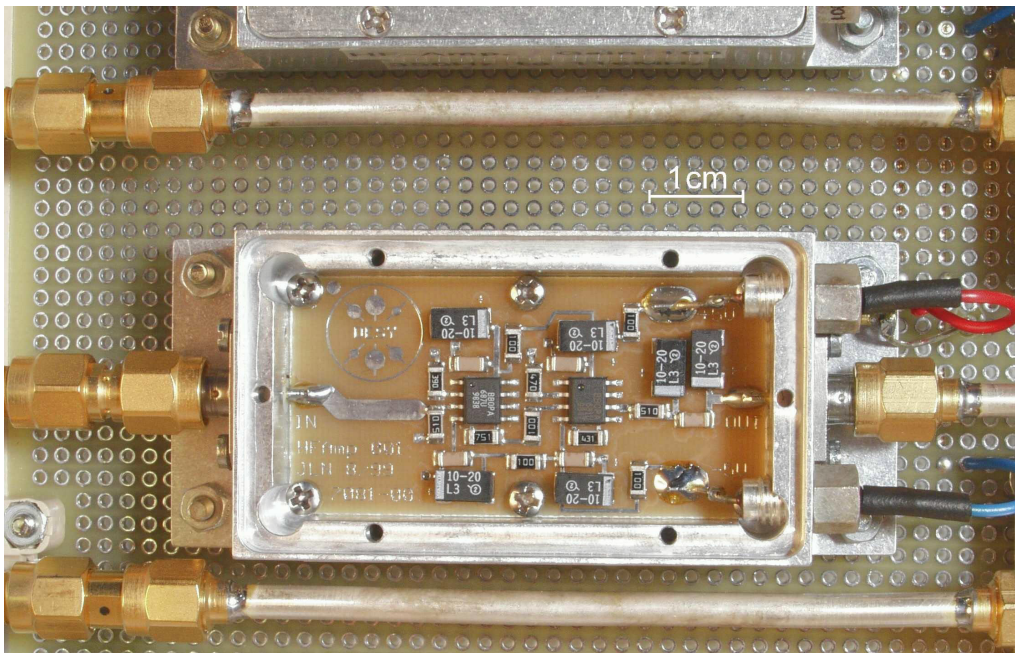


Figure A.22: ADC preamplifier to increase the signal levels for optimum use of the dynamic range of the ADCs. All preamplifiers are installed in RF-proof solid aluminum cases to prevent interference from the environment. By using surface mounted parts, small dimensions are achieved. (Circuit design: J. Lund-Nielsen)

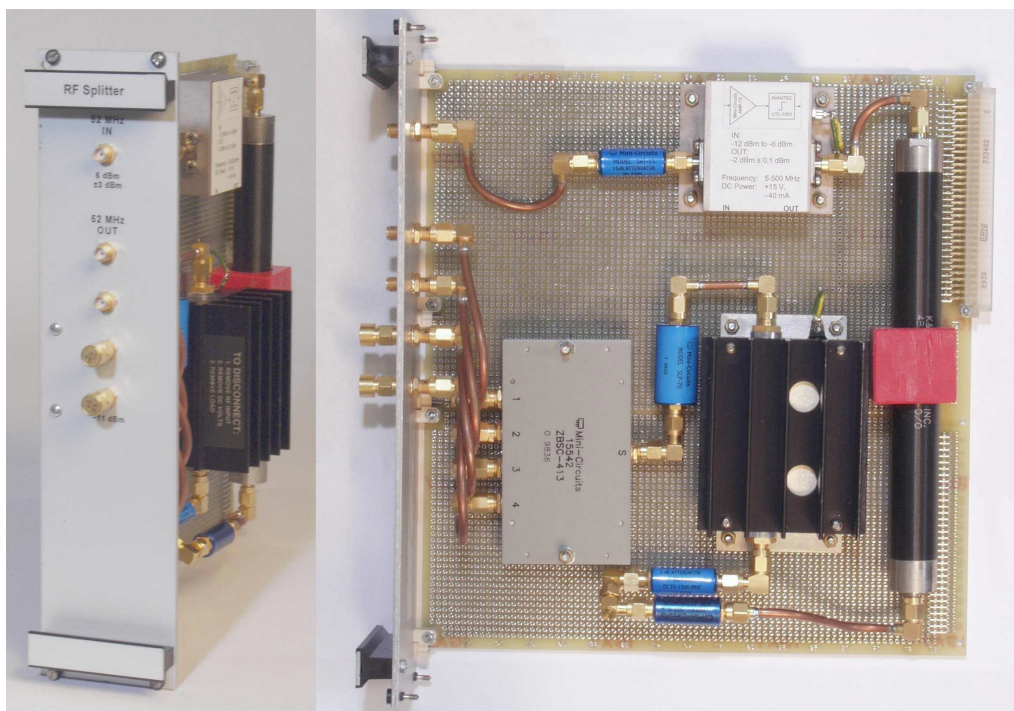


Figure A.23: RF splitters, respectively LO splitters supply RF reference signals with constant power levels.

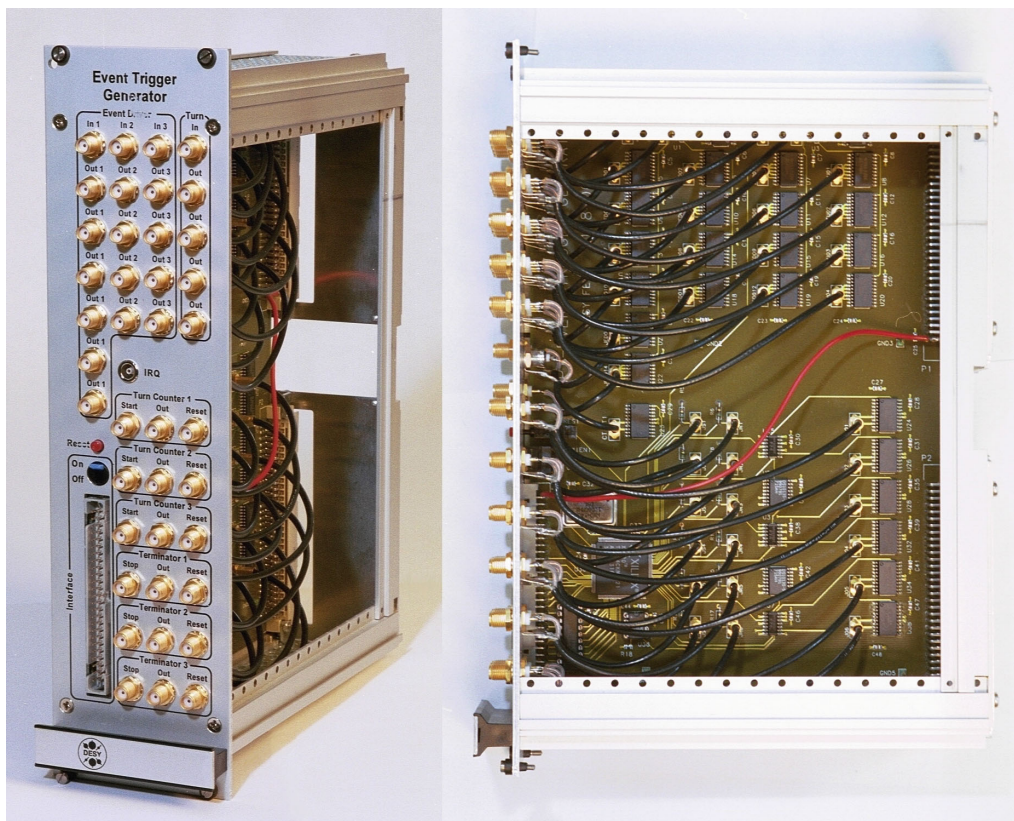


Figure A.24: A plug-in unit of the remote controllable timing system. SMA connectors and double shielded cables are used to prevent radiation of high frequency signal components of the timing signals. Such signal components disturb analog signals. (Circuit design: group FEA)



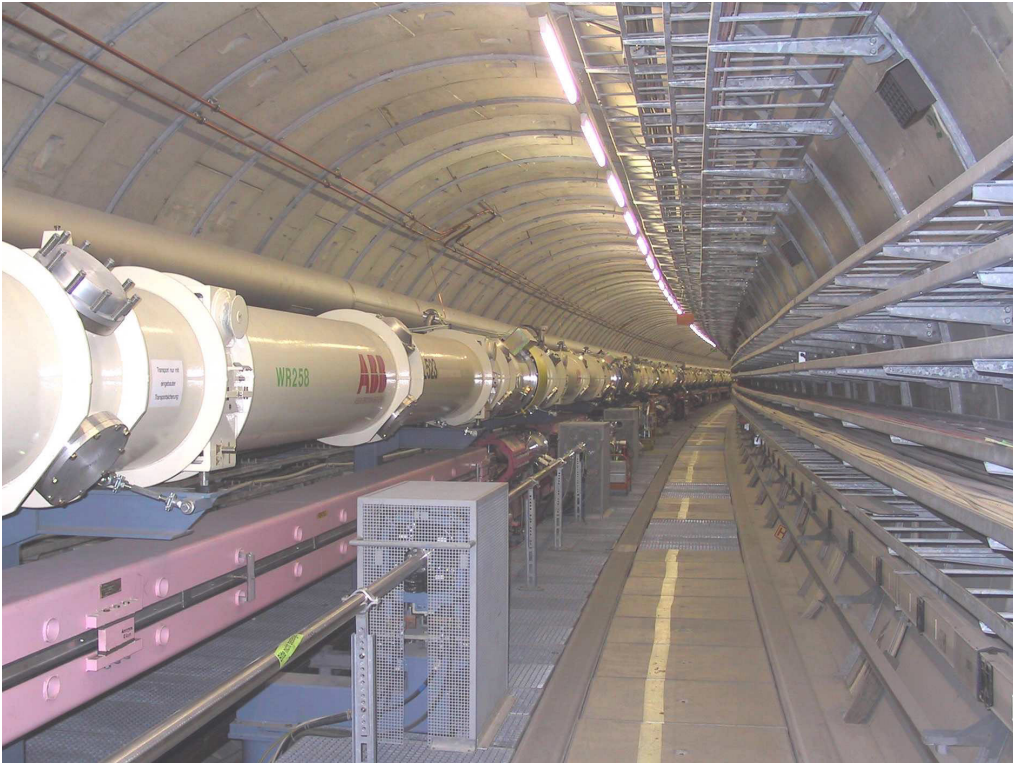


Figure A.25: A view inside HERA, in the arc from west to north. The superconducting dipole magnets of the proton storage ring (large pipe) are mounted above the normal conducting magnets of the electron, respectively positron storage ring (rectangular structure below pipe).

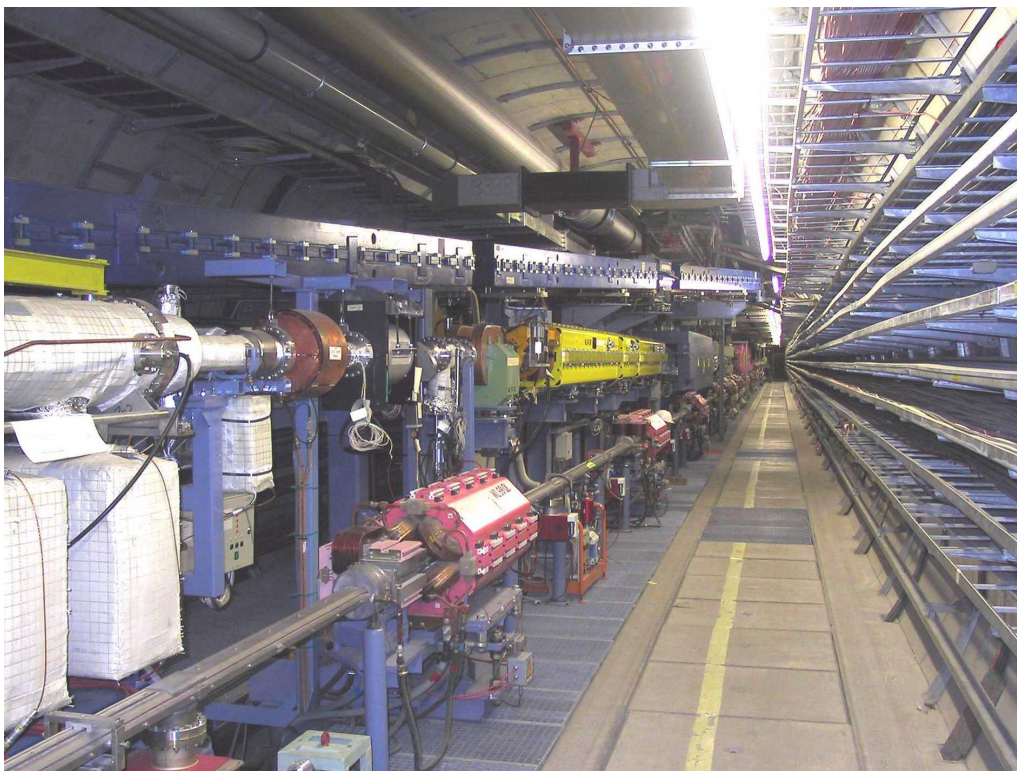


Figure A.26: Injection line to HERA, from PETRA. The magnets descending from the ceiling are the transfer path from the proton pre-accelerator PETRA II to the proton storage ring.



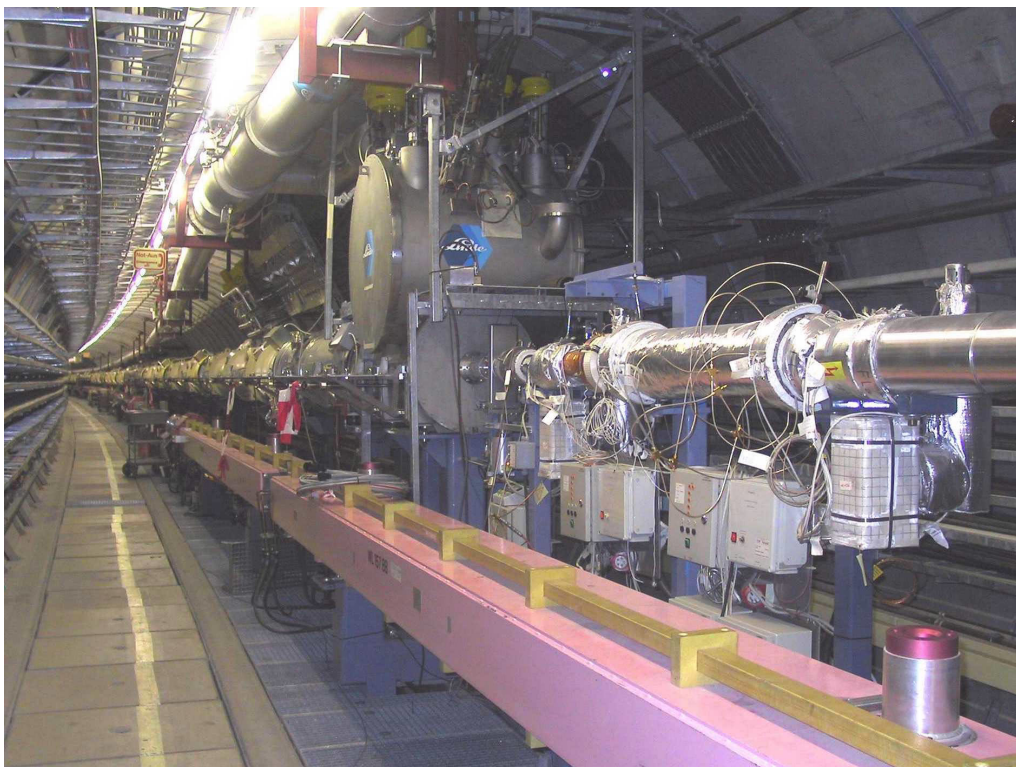


Figure A.27: The thick silver pipe with the semi rigid cables is the resistive gap monitor. It is located shortly before the beginning of the arc from west to south.



Figure A.28: The two 52 MHz cavities build up the proton buckets at the injection energy of 40 GeV.

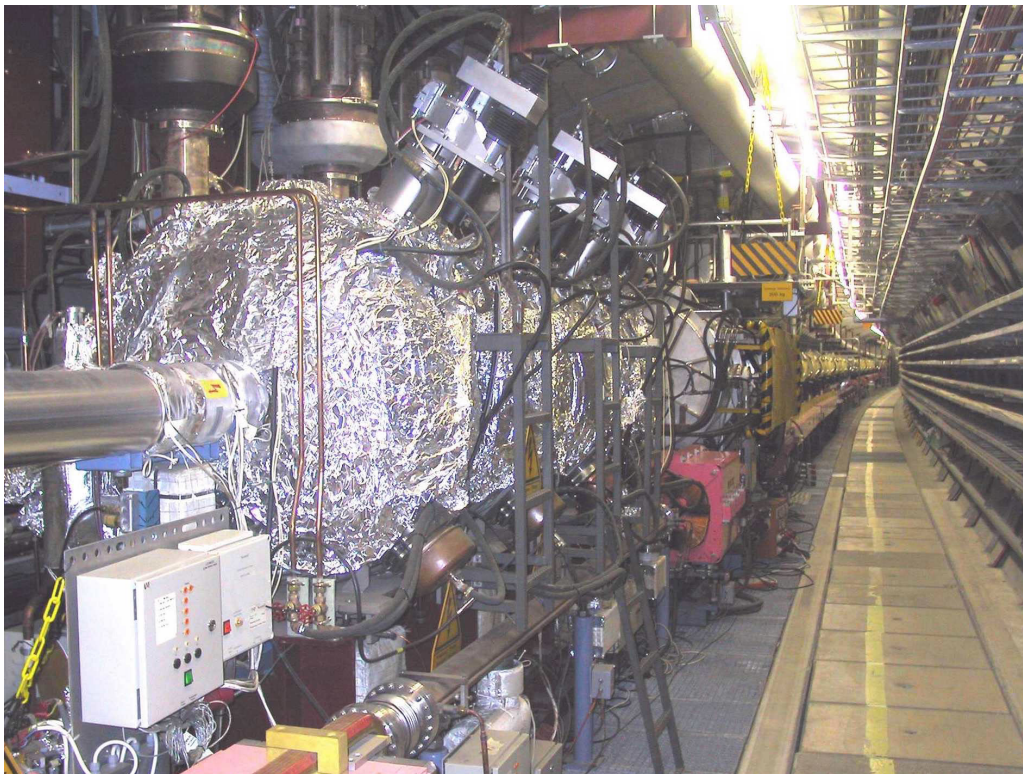


Figure A.29: During acceleration from 40 GeV to 920 GeV, the four 208 MHz cavities shown take over the build-up of the proton buckets from the 52 MHz cavities. At the left flanges, the final stage amplifiers are mounted, and at the right flanges you can see the tuners.



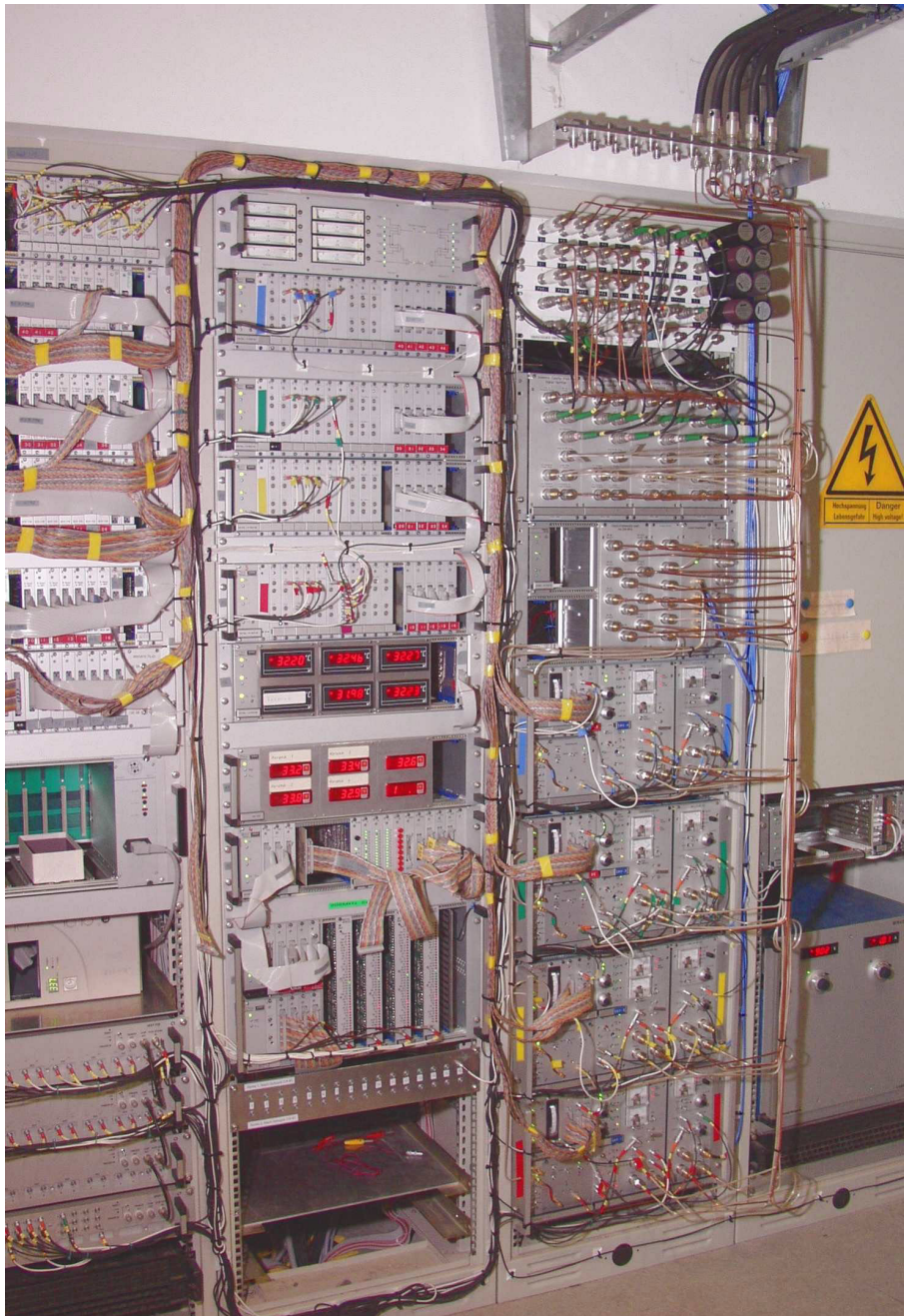


Figure A.30: These racks contain the 208 MHz cavity controls. The cable bridge on top leads to the fast longitudinal diagnostic system.



# Bibliography

- [1] M. A. Furman, 'The hourglass reduction factor for asymmetric colliders', Asymmetric B-Factory collider Note No. SLAC-ABC-41-REV (1991)
- [2] R. Hofstadter and R. McAllister, 'Electron scattering from the Proton', *Physical Review* 98, 217 (1955)
- [3] E. E. Chambers and R. Hofstadter, 'Structure of the Proton', *Physical Review* 103, 1454 (1996)
- [4] V. Chiochia, E. Lohrmann, J. Naumann, 'Traveling to the Heart of Matter with HERA', <http://www.desy.de/f/hera/engl/index.html>
- [5] Yuval Ne'eman, Yoram Kirsh, *Die Teilchenjäger*, Übersetzt von Bernhardt Simon (Springer-Verlag Berlin Heidelberg, 1995)
- [6] P. Schmüser, H. Spitzer, 'Particles', in L. Bergmann, C. Schaeffer, *Constituents of Matter* (Walter de Gruyter, Berlin, New York, 1997)
- [7] Donald H. Perkins, *Introduction to High Energy Physics* (4th Ed, Cambridge University Press, 2000)
- [8] C. Berger, *Teilchenphysik - Eine Einführung* (Springer Verlag Berlin Heidelberg, 1992)
- [9] R. D. Kohaupt, 'Multi-bunch systems at DESY', in *Proceedings of the Particle Accelerator Conference, Dallas, USA, 1995*, (DESY Report No. DESY M 95-08, 1995)
- [10] W. Kriens, 'PETRA Bunch Rotation', in *Proceedings of the Particle Accelerator Conference, Vancouver, Canada, 1997*, (DESY Report No. DESY-M-97-10N, 1997)
- [11] G. Wiesenfeldt, 'Untersuchungen zur longitudinalen Strahlanpassung beim Protonentransfer von PETRA nach HERA', Diplomarbeit, University of Hamburg (1995)
- [12] G. H. Hoffstaetter, 'Future Possibilities for HERA', in *Proceedings of the European Particle Accelerator Conference, Vienna, Austria, 2000*
- [13] personal communication with J. Rümmler, DESY (1999)
- [14] personal communication with G. H. Hoffstaetter, DESY (2001)
- [15] A. W. Chao and M. Tigner, *Handbook of Accelerator Physics and Engineering* (World Scientific, 1999)
- [16] E. Shaposhnikova, 'Analysis of coupled bunch instability spectra', CERN Report No. CERN-SL-99-040 HRF, (1999)
- [17] J. Fox, H. Hindi, R. Larsen, S. Prabhakar, D. Teytelman, A. Young, A. Drago, M. Serio, G. Stover, 'Multi-Bunch Longitudinal Dynamics and Diagnostics via a Digital Feedback System at PEP-II, DAΦNE, ALS and SPEAR', in *Proceedings of the Particle Accelerator Conference, Stockholm, Sweden, 1998*, (1998)

- [18] F. J. Sacherer, 'A longitudinal stability criterion for bunched beams', to be presented to the *1973 Particle Accelerator Conference San Francisco*, 5-7 March 1973 (CERN Report No. CERN-MPS-Int. BR-73-3, 16. February 1973)
- [19] F. Ruggiero, 'Single-Beam Collective Effects in the LHC', CERN Report No. CERN SL/95-09 (AP) (1995); <http://wwwslap.cern.ch/~rgo/lhc95/lhc95.html>
- [20] G. Lopez *et al*, 'Observation of Proton Bunch Behavior in HERA', in *Int. J. Mod. Phys. A*, Proc. Suppl. 2A, p. 251 (1993), identical with *Proceedings of International Conference on High Energy Accelerators, Hamburg, Germany, 1992*
- [21] D. Bussard, 'Schottky Noise and Beam Transfer Function Diagnostics', in *Proceedings of CERN Accelerator School - Fifth Advanced Accelerator Physics Course, Rhodes, Greece, 1993* (CERN Report No. CERN-95-06-vol.2, p. 758, 1995)
- [22] Personal communication with M. Wendt from DESY. His signal combination method is based on an idea already used at CERN. (2000)
- [23] A. Gamp, 'Servo Control of RF Cavities under Beam Loading', in *Proceedings of CERN Accelerator School - RF Engineering for Particle Accelerators, Oxford, United Kingdom, 1991* (CERN Report No. CERN-92-03-vol.2, p. 396, 1992)
- [24] W. Kriens, 'Neue Kontrollen für die Frequenz- und Transfersteuerung bei HERA', in *DESY Accelerator Operation Seminar Grömitz, Germany, 1999* (DESY Report No. DESY-HERA-99-04, p. 405, 1999)
- [25] W. Kriens, 'Neue Kontrollen für die Frequenzsteuerung und Synchronisation bei HERAp', in *DESY Accelerator Operation Seminar Grömitz, Germany, 2000* (DESY Report No. DESY-M-00-05, 2000)
- [26] <http://t.home.cern.ch/t/tomograp/www/>
- [27] S. Hancock, P. Knaus, M. Lindroos, 'Thomographic Measurements of Longitudinal Phase Space Density', in *Proceedings of the European Particle Accelerator Conference, Stockholm, Sweden, 1998*
- [28] S. Hancock, S. Koscielniak, M. Lindroos, 'Longitudinal Phase Space Tomography with Space Charge', CERN Report No. CERN-PS-2000-021-RF (2000)
- [29] detailed personal communication with W. Kriens, DESY (2001)
- [30] personal communication with R. Wagner, DESY (1998)
- [31] personal communication with R. Wagner, DESY (2001)
- [32] WWW home page from proton RF group at DESY, <http://desyntwww.desy.de/mhf/mhf-p/>, DESY (2001)
- [33] not published measurements together with R. Wagner, DESY (1998)
- [34] C. Fox, 'Dämpfung höherer Moden in den 52 MHz Resonatoren des HERA Speicherrings', Diplomarbeit, University of Hamburg (1991), (DESY Report No. DESY-HERA-91-18, 1991)
- [35] personal communication with A. Gamp, DESY (1998)

- [36] C. Boccard, T. Bogey, J. P. Papis and L. Vos, 'Intensity and Bunch Length Measurement for Lepton Beam in the Injection Lines of the SPS and LEP', in *Proceedings of Second European Workshop on Beam Diagnostics and Instrumentation for Particle Accelerators (DIPAC'95), Lübeck-Travemünde, Germany, 1995*, (CERN Report No. CERN SL/95-58 (AP), 1995)
- [37] Y. Chernousko suggested this idea, DESY (1999)
- [38] D. A. Edwards, M. J. Syphers, *An Introduction to the Physics of High Energy Accelerators* (John Wiley & Sons, 1993)
- [39] W. Pirkel, 'Longitudinal Beam Dynamics', in *Proceedings of CERN Accelerator School - Fifth Advanced Accelerator Physics Course, Rhodes, Greece, 1993* (CERN Report No. CERN-95-06-vol.1, p. 233, 1995)
- [40] E. Vogel, 'Real Time Measurement of Single Bunch Phase and Length at the HERA Proton Storage Ring and the Observation of Multi Bunch Oscillations', DESY Report No. DESY-HERA-00-08 (2000)
- [41] E. Vogel, 'Ingredients for an RF Feedforward at HERAp', in *DESY Accelerator Operation Seminar Grömitz, Germany, 1999* (DESY Report No. DESY-HERA-99-04, p. 398, 1999)
- [42] A. Hofmann, 'Single-beam collective phenomena - longitudinal', (CERN Report No. CERN 77-13 1977)
- [43] J. M. Byrd, 'Single Beam Collective Phenomena in CESR', A Dissertation Presented to the Faculty of the Graduate School of Cornell University, May 1992
- [44] K. Balewski, R. D. Kohaupt, 'Analytic Evaluation of the Effective Impedance for Coupled Bunch Instabilities', DESY Report No. DESY 90-152 (December 1990)
- [45] R. D. Kohaupt, 'On Multi-Bunch Instabilities for Fractionally Filled Rings', DESY Report No. DESY M 85-139 (December 1985)
- [46] R. Wanzenberg, 'The Impedances of Selected Components of the HERA Proton Ring', DESY Report No. DESY HERA 95-07 (November 1995)
- [47] S. Prabhakar, R. Claus, J. Fox, H. Hindi, I. Linscott, J. Olsen, W. Ross, D. Teytleman, 'Observation and modal analysis of coupled bunch longitudinal instabilities via a digital feedback control system', SLAC Report No. SLAC-PUB-7717 (December 1997)
- [48] J. L. Liu, D. D. Caussyn, M. Ellison, S. Y. Lee, D. Li, A. Riabko and L. Wang, 'Analytic Solution of Particle Motion in a Double RF System', *Particle Accelerators*, 1995, Vol. 49, pp. 221-251 (1995)
- [49] A. Hofmann, S. Myers, 'Beam Dynamics in a Double RF System', presented at *XIth International Conference on High Energy Accelerators, Geneva Switzerland, 1998* (CERN Report No. ISR-TH-RF/80-26, 1980)
- [50] T. Bohl, T. Linnecar, E. Shaposhnikova and J. Tuckmantel, 'Study of Different Operating Modes of the 4th RF Harmonic Landau Damping System in the CERN SPS', in *Proceedings of the European Particle Accelerator Conference, Stockholm, Sweden, 1998* (CERN Report No. SL-98-026 RF, 1998)

- [51] L. D. Landau, E. M. Lifschitz, *Lehrbuch der theoretischen Physik*, 10 Bde., Bd. 1, *Mechanik*, 14. Aufl. (Verlag Harri Deutsch, 1997) or older editions
- [52] V. I. Arnold, *Gewöhnliche Differentialgleichungen* (Deutscher Verlag der Wissenschaften, Berlin, 1991)
- [53] D. Sagan, 'On the physics of Landau damping', CNLS Report No. CLNS 93/1185, (1993)
- [54] S. Koscielniak, H. J. Tran, 'Decoherence of Displaced Binomial Amplitude Distribution', in *Proceedings of the European Particle Accelerator Conference, Barcelona, Spain, 1996* (TRIUMF Report No. TRI-PP-96-30, 1996)
- [55] R. D. Kohaupt, 'What is Landau-damping? : plausibilities, fundamental thoughts, theory', DESY Report No. DESY M 86-02 (March 1986)
- [56] R. D. Kohaupt, 'Longitudinal instabilities of a single bunch and the observation of reduced Landau damping in DORIS', DESY Report No. DESY 75/26 (August 1975)
- [57] R. D. Kohaupt, 'Landau damping', in *Proceedings of CERN Accelerator School - Advanced Accelerator Physics Course, Uppsala, Sweden, 1989* (CERN Report No. CERN 90-04, p. 67, 1990)
- [58] H. Wiedemann, *Particle Accelerator Physics II - Nonlinear and Higher-Order Beam Dynamics* (Springer-Verlag, Berlin, Heidelberg, New York, 1995)
- [59] M. Chanel, U. Oeftiger, 'Results from beam transfer function measurements at the low-energy antiproton ring (LEAR)', *Workshop on Beam Cooling and Related Topics, Montreux, Switzerland, October 1993* (CERN Report No. CERN PS 93-44 AR)
- [60] M. G. Minty, F. Zimmermann, 'Longitudinal beam-transfer-function measurements at the SLC damping rings', *Proceedings of the Particle Accelerator Conference, Vancouver, Canada, 1997* (SLAC Report No. SLAC-PUB-7467 1997)
- [61] Charles P. Slichter, *Principles of Magnetic Resonance, Third Enlarged and Updated Edition* (Springer-Verlag, Berlin, Heidelberg, New York, 1990)
- [62] G. Stupakov and S. Kauffmann, 'Echo Effect in Accelerators', Superconducting Super Collider Laboratory Report No. SSCL-587 (1992)
- [63] O. Bruening et. al., 'Beam Echoes in the CERN SPS', *Proceedings of the Particle Accelerator Conference, Vancouver, Canada, 1997* (CERN Report No. CERN-SL-97-023-AP 1997)
- [64] K. Ehret et. al. - HERA-B Target Group., 'Observation of coasting beam at the HERA Proton-Ring', hep-ex/0002002, DESY Report No. DESY 00-018 (February 2000)
- [65] personal communication with R. Wagner, DESY (August 2000)
- [66] S. Ivanov, O. Lebedev, 'Coasting Beam in HERA-p Ring', DESY Report No. DESY HERA 01-03 (October 2001)
- [67] A. Hofmann, 'Beam Instabilities', in *Proceedings of CERN Accelerator School - Fifth Advanced Accelerator Physics Course, Rhodes, Greece, 1993* (CERN Report No. CERN-95-06-vol.1, p. 307, 1995)

- [68] K. Balewski, 'Instabilitäten in HERA-p und PETRA-p', in *HERA Seminar 1994 Bad Lauterberg, Harz, Germany*, 1994 (DESY Report No. DESY-HERA-94-03, p. 424, 1994)
- [69] personal communication with K. Balewski, DESY (2001)
- [70] F. Klefenz, 'Die Hochfrequenz-Abschirmung des HERA-B Vertexdetektors', Diplomarbeit, University of Heidelberg (1997), (DESY Report No. DESY M 98-01, January 1998)
- [71] R. Wanzenberg, M. Wendt, 'Measurements of the Modes in the HERA-B Vertex Chamber excited by the HERA Proton Beam', in *Proceedings of the European Particle Accelerator Conference, Stockholm, Sweden*, 1998, (1998)
- [72] F. Galluccio, 'The Impedance Budget of HERA-p; a Preliminary Selection of Contributing Elements', DESY Report No. DESY M 94-10 (December 1994)
- [73] D. Bussard, D. Brandt and L. Vos, 'Is a longitudinal feedback system required for LHC', LHC Project Note 205, November 5, (1999)
- [74] personal communication with F. Willeke, DESY (2001)
- [75] S. Stahl, S. A. Bogacz, 'Coupled Bunch Instabilities in Fermilab Booster and Possible Cures - Longitudinal Phase-Space Simulation', FNAL Report No. FN-460 (September 1987)
- [76] C. E. Rohrs, 'The Nyquist Stability Test', in *The Control Handbook*, edited by William S. Levine (CRC and IEEE Press, ISBN 0-8493-8570-9, 1996)
- [77] T. Bohl, 'Measures against longitudinal instabilities and beam loading', CERN Report No. OPEN-99-058 (January 1999)
- [78] personal communication with G. H. Hoffstaetter, he calculated this value, DESY (2001)
- [79] E. Kikutani, J. Flanagan and M. Tobiyama, 'Limitations of Multibunch Feedback Systems and Extrapolation', in *Proceedings of the European Particle Accelerator Conference, Vienna, Austria*, 2000
- [80] J. N. Corlett, J. Johnson, G. Lambertson, F. Voelker, 'Longitudinal and Transverse Feedback Kickers for the ALS', in *Proceedings of the European Particle Accelerator Conference, London, Great Britain*, 1994, Vol. 2, pp. 1625-1627, (1994)
- [81] R. Boni, A. Gallo, A. Ghigo, F. Marcellini, M. Serio and M. Zobov, 'A Waveguide Overloaded Cavity as Longitudinal Kicker for the DAΦNE Bunch-By-Bunch Feedback System', *Particle Accelerators*, 1996, Vol. 52, pp. 95-113, (1996)
- [82] F. Moeller, H. Frohne, K.-H. Löcherer, H. Müller, *Grundlagen der Elektrotechnik*, 18. Auflage (B. G. Teubner Stuttgart, 1996)
- [83] 'Digital Modulations in Communication Systems - An Introduction', Application Note 1298, Hewlett-Packard Company, 1997
- [84] 'An Introduction to Digital and Vector Modulation', Application Note 2050, IFR, Inc., 2000
- [85] N. I. Bronstein, K. A. Semendjajew, *Taschenbuch der Mathematik*, 23. Auflage (Verlag Harri Deutsch Thun und Frankfurt / Main, 1987)

- 
- [86] F. Willeke, 'HERA Luminosity Upgrade Commissioning', in *DESY Accelerator Operation Seminar Grömitz, Germany*, 2000 (DESY Report No. DESY-M-00-05, 2000)
- [87] personal communication with G. H. Hoffstaetter, DESY (2001)
- [88] T. Bohl, T. Linnecar, E. Shaposhnikova, 'The Fine Structure of the Longitudinal Impedance Observed with Single Bunches', CERN Report No. CERN SL-97-029 (1997)
- [89] T. Bohl, E. Shaposhinkova from CERN and W. Kriens from DESY did these examinations (1998)
- [90] A. Gamp, 'Servo Control of Cavities under Beam Loading', DESY Report No. DESY-HERA-00-04 (2000)
- [91] personal communication with A. Gamp, DESY (2001)



# Acknowledgments

I want to express my gratitude to the DESY directorate, for giving me the opportunity to write a thesis in the field of accelerator physics and for financial support.

I would like to thank Prof. Dr. Peter Schmüser and Dr. Ferdinand Willeke, for their continuous interest, advice and support and for making this thesis possible.

I benefited greatly from Dr. Alexander Gamp by his confidence in my hardware designs. He was responsible for granting the financial and human resources, indispensable for this work. For continuing support, regarding this aspect, I would also like to thank Dr. Stefan Choroba.

With sincerest appreciation I would also like to mention Wilhelm Kriens. Discussions with him were always very fruitful, and I profited very much from his experience with analog low power RF systems. We also made successful measurements together with Uwe Hurdelbrink.

For further helpful discussions, on technical designs and measurement methods, I would also like to thank Dr. Michiko Minty and Dr. Stefan Simrock. Discussions with Dr. Stefan Simrock led to a hardware design, which will work with digital signal processors (DSPs) for future control tasks.

I would also like to thank Dr. Klaus Balewski for his willingness to talk about his experience on coupled bunch oscillations.

For talks about theory, such as describing incoherent beam dynamics, I would like to thank Dr. Georg Hoffstätter.

Many people were involved in the realization of the hard- and software. It is not possible to do justice to all of them, but I would particularly like to thank Peter Albrecht, Ralf Apel, Josef Baran, Wolfgang Bensch, Yuri Chernousko, Bernd Closius, Guenter Delfs, Philip Duval, Hans-Thomas Duhme, Peter Gasiorek, Serguei Goloborodko, Torsten Grevsmuehl, Steve Herb, Gerd Hochweller, Andrej Kholodniy, Manfred Luehmann, Jorgen Lund-Nielsen, Tomasz Plawski, Willi Radloff, Rainer Saust, Victor Soloviev, Andreas Sommer, Klaus-Ulrich Tode, Richard Wagner, Manfred Wendt, Hong Gong Wu and Xiang Zeng.

I would especially like to mention Hong Gong Wu. He programmed the ADC-Server, supplying the pre-possessed data. This was a sophisticated task, due to the large amount of data involved. There were many fruitful discussions about the best way to take and supply the data to the accelerator control system.

I would like to thank all my colleagues from the FDET and MPY groups for providing a stimulating and friendly work environment.

I offer my thanks to Dr. Nicholas John Walker, Susan Wipf, Dr. John Maidment, Dr. Michiko Minty and Dr. Bernhard Holzer for reading parts of my thesis.

I would like to thank Margitta Mueller for taking the photographs of my hardware setup.

The weather in Hamburg became tolerable, when I started to take active part in the Akademischer Segler-Verein Hamburg. Sailing trips, boat races and maintenance of the club boats were ideal recreational activities, particularly together with nice people.

Last but not least, I would like to express my gratitude to my family who supported me during a difficult time, working on this thesis.